

**Forschungsbericht 2009-13**

**Multi-Channel Azimuth Processing  
for High-Resolution Wide-Swath  
SAR Imaging**

Nicolas Gebert

Deutsches Zentrum für Luft- und Raumfahrt  
Institut für Hochfrequentechnik und  
Radarsysteme  
Oberpfaffenhofen



**DLR**

**Deutsches Zentrum  
für Luft- und Raumfahrt e.V.**  
in der Helmholtz-Gemeinschaft



*Herausgeber*

Deutsches Zentrum  
für Luft- und Raumfahrt e.V.  
Bibliotheks- und  
Informationswesen  
D-51170 Köln  
Porz-Wahnheide  
Linder Höhe  
D-51147 Köln

*Telefon*  
*Telefax*

(0 22 03) 6 01- 32 01  
(0 22 03) 6 01- 47 47

Als Manuskript gedruckt.  
Abdruck oder sonstige Verwendung  
nur nach Absprache mit dem DLR gestattet.

ISSN 1434-8454

**Forschungsbericht 2009-13**

**Multi-Channel Azimuth Processing  
for High-Resolution Wide-Swath  
SAR Imaging**

Nicolas Gebert

Deutsches Zentrum für Luft- und Raumfahrt  
Institut für Hochfrequenztechnik und  
Radarsysteme  
Oberpfaffenhofen

215 Seiten  
132 Bilder  
15 Tabellen  
99 Literaturstellen



**DLR**

**Deutsches Zentrum  
für Luft- und Raumfahrt e.V.**

in der Helmholtz-Gemeinschaft



# **Multi-Channel Azimuth Processing for High-Resolution Wide-Swath SAR Imaging**

Zur Erlangung des akademischen Grades eines

**DOKTOR-INGENIEURS**

von der Fakultät für  
Elektrotechnik und Informationstechnik  
der Universität Fridericiana Karlsruhe (TH)

genehmigte

**DISSERTATION**

von

**Dipl.-Ing. Nicolas Gebert**  
geb. in München

Tag der mündlichen Prüfung:  
Hauptreferent:  
Korreferent:

04.06.2009  
Prof. Dr.-Ing. habil. Alberto Moreira  
Prof. Dr.-Ing. Dr. h.c. Dr.-Ing. E.h. Werner Wiesbeck



# Vorwort

Die vorliegende Dissertation entstand während meiner Tätigkeit als wissenschaftlicher Mitarbeiter am Institut für Hochfrequenztechnik und Radarsysteme des Deutschen Zentrums für Luft- und Raumfahrt (DLR) in Oberpfaffenhofen. Mein Dank gilt besonders Institutsdirektor Prof. Dr.-Ing. Alberto Moreira, ohne dessen Unterstützung als Referent die vorliegende Arbeit nicht möglich gewesen wäre, sowie Prof. Dr.-Ing. Werner Wiesbeck vom Institut für Höchstfrequenztechnik und Elektronik (IHE) der Universität Karlsruhe (TH) für die Übernahme des Korreferats.

Von den jederzeit hilfsbereiten Kollegen am DLR gilt es, meine Abteilungs- und Fachgruppenleiter Marian Werner, Dr.-Ing. Gerhard Krieger und Dr.-Ing. Marwan Younis hervorzuheben. Ihnen möchte ich vor allem für ein stets angenehmes Arbeitsklima und für die immer gerne gewährte fachliche Unterstützung danken. Erst die zahlreichen anregenden Diskussionen mit Dr.-Ing. Gerhard Krieger, in denen ich von seinem großen technischen Fachwissen und seiner großen Erfahrung profitieren konnte, haben diese Dissertation in der vorliegenden Form ermöglicht. In Bezug auf die kritische Durchsicht der Arbeit und den damit verbundenen wertvollen Anregungen und Verbesserungen, möchte ich Dr.-Ing. Gerhard Krieger und besonders Dr.-Ing. Marwan Younis erwähnen. Vielen Dank an die zahlreichen hier ungenannten Kollegen, die mir mit ihren Kommentaren, Korrekturen und Ideen ebenso eine große Hilfe waren.

Nicht zuletzt bedanke ich mich bei meinen Kollegen Marc Rodríguez Cassolà sowie Dr. Federica Bordoni, die immer zur guten Atmosphäre im Büro 081 beigetragen haben und stets zur Diskussion technischer Probleme bereit waren; insbesondere Marc, der sich immer die Zeit genommen hat, mir zu helfen.

Abschließend möchte ich mich bei EADS Defence Electronics in Ulm bedanken, die meine Arbeit im Rahmen einer Kooperation mit dem DLR finanziell unterstützt hat.

München, Juni 2009

Nicolas Gebert





# Contents

<b>Zusammenfassung</b>	<b>v</b>
<b>Abstract</b>	<b>vii</b>
<b>Acronyms and Symbols</b>	<b>ix</b>
<b>1 Introduction</b>	<b>1</b>
1.1 State-of-the-Art: Synthetic Aperture Radar Remote Sensing .....	2
1.2 Motivation, Scope, and Structure of this Work.....	5
<b>2 Conventional SAR Systems – Fundamentals and Constraints</b>	<b>9</b>
2.1 Geometry and Principle.....	9
2.2 SAR Signal Model .....	12
2.3 Pulsed Signal Acquisition .....	17
2.3.1 Azimuth Ambiguities .....	17
2.3.2 Range Ambiguities .....	19
2.4 Constraints.....	20
<b>3 Multi-Channel SAR – An Overview</b>	<b>23</b>
3.1 Multiple Aperture Reception.....	23
3.2 Overview of Historical Developments.....	24
3.3 First System Concepts.....	26
3.3.1 Multiple Apertures in Elevation .....	26
3.3.2 Displaced Phase Center Antenna in Azimuth .....	26
3.3.3 Quad Array Antenna .....	27
3.4 Processing Strategies.....	27
3.4.1 Scan-on-Receive in Elevation (SCORE).....	28

3.4.2	Multi-Channel Reconstruction Algorithm in Azimuth.....	28
3.4.3	Multi-Channel Phase Correction in Azimuth .....	29
3.4.4	Minimum Variance Distortionless Beamformer .....	29
3.5	Alternative Approaches.....	29
3.5.1	Multiple Beam SAR .....	30
3.5.2	Spread Spectrum Waveforms .....	31
3.5.3	Sparse Array SAR Constellations.....	31
<b>4</b>	<b>Multi-Channel SAR in Azimuth</b>	<b>33</b>
4.1	Multi-Channel Reception in Azimuth .....	33
4.2	Multi-Channel Impulse Response and Quadratic Approximation .....	35
4.3	Spatial Sampling.....	38
4.3.1	Effective Phase Center, Virtual Sample Position and Spatial Sampling .....	38
4.3.2	Uniform Sampling .....	40
4.3.3	Special Sampling Scenarios.....	41
<b>5</b>	<b>Multi-Channel Azimuth Processing: Reconstruction Algorithm</b>	<b>43</b>
5.1	Theoretical Background .....	44
5.2	Illustration of Principle.....	47
5.3	Multi-Channel Reconstruction in the Framework of STAP .....	49
5.4	Two-Dimensional Reconstruction and Processing.....	50
5.4.1	Multi-Channel Range Cell Migration.....	50
5.4.2	Reconstruction Filter Mismatch .....	52
5.4.3	Two-Dimensional Multi-Channel Reconstruction .....	53
5.5	Signal Power .....	54
5.6	Residual Reconstruction Error and Azimuth Ambiguities: $AASR_N$ .....	56
5.7	$SNR$ Scaling in Digital Beamforming Networks: $\Phi_{bf}$ .....	60
5.8	Noise Equivalent Sigma Zero ( $NESZ$ ) in Multi-Channel SAR .....	66
<b>6</b>	<b>Demonstration With Airborne Measured Data</b>	<b>69</b>
6.1	Reconstruction of E-SAR Measured Data.....	69
6.2	Reconstruction of F-SAR Measured Data.....	73
6.2.1	System Setup .....	74
6.2.2	Processing Results .....	76
<b>7</b>	<b>System Design Example</b>	<b>83</b>
7.1	Requirements and Timing .....	83

7.2	System Parameters .....	85
7.2.1	Azimuth Parameters .....	85
7.2.2	Cross-Track Parameters .....	88
7.3	Simulation Environment .....	89
7.4	System Performance.....	89
7.4.1	Azimuth-Ambiguity-to-Signal Ratio: $AASR_N$ .....	90
7.4.2	Geometric Resolution in Azimuth: $\delta_{az}$ .....	92
7.4.3	Signal Peak Power: $p_{s,max}$ .....	93
7.4.4	SNR Scaling – Prediction and Simulation .....	93
7.4.5	Azimuth Loss: $L_{az}$ .....	96
7.4.6	Noise Equivalent Sigma Zero : $NESZ$ .....	97
<b>8</b>	<b>Optimization Potentials</b> .....	<b>99</b>
8.1	Error Sources and Optimization Approaches .....	99
8.2	Optimized Parameter Setup: Adaptation of Processed Doppler Bandwidth .....	101
8.3	Adaptive <i>PRF</i> Management in Sparse Array Systems.....	102
8.4	Pattern Tapering on Transmit.....	103
8.5	Optimized System Design Example.....	107
8.6	Phase Center Adaptation on Transmit.....	109
8.6.1	System Architecture and Basic Principle .....	109
8.6.2	Analytic Description.....	111
8.6.3	Performance Analysis.....	113
8.7	Cascaded Beamforming Networks.....	115
8.7.1	System Architecture and Extended System Model .....	116
8.7.2	Phase Center Adaptation .....	119
8.7.3	Compensation for Power Loss in Analog Networks .....	122
8.7.4	Signal Power .....	122
8.7.5	Residual Reconstruction Error and Azimuth Ambiguities: $AASR_{N,BD}$ .....	124
8.7.6	SNR Scaling in Cascaded Beamforming Networks: $\Phi_{bf,c}$ .....	125
8.7.7	Performance Analysis I - Analog Pre-Beamshaping on Receive .....	127
8.7.8	Performance Analysis II - Adapted Digital Beamforming .....	130
<b>9</b>	<b>Multi-Channel Reconstruction in Burst Mode Operation</b> .....	<b>139</b>
9.1	Motivation of Multi-Channel Burst Mode Systems .....	139
9.2	Burst Mode Operation.....	141
9.2.1	ScanSAR Timing.....	141

9.2.2	Burst Mode Target Signal Spectrum .....	141
9.3	Burst Mode Signal Power.....	143
9.4	Azimuth Ambiguities in Burst Mode Operation: $AASR_{N,B}$ .....	144
9.5	$SNR$ Scaling in Burst Mode Operation: $\Phi_{bf,B}$ .....	145
9.6	System Design Example – Multi-Channel ScanSAR.....	145
9.6.1	Timing and System Parameters .....	146
9.6.2	Performance Analysis.....	148
9.7	Multi-Channel TOPS Mode .....	150
9.7.1	Performance Analysis.....	151
9.7.2	Adaptively Squinted Multi-Channel Processing for TOPS .....	153
<b>10</b>	<b>Discussion</b> .....	<b>157</b>
10.1	Conclusion – Achieved Objectives of the Work .....	157
10.2	Summary of Results .....	158
10.3	Outlook.....	160
	<b>Bibliography</b> .....	<b>163</b>
<b>A</b>	<b>History of Spaceborne SAR Missions</b> .....	<b>171</b>
<b>B</b>	<b>Spherical SAR Geometry</b> .....	<b>173</b>
<b>C</b>	<b>Quadratic Approximation of Range History</b> .....	<b>177</b>
<b>D</b>	<b>Analogy of Null-Steering and Multi-Channel Reconstruction</b> .....	<b>183</b>
<b>E</b>	<b><math>SNR</math> in Multi- and Mono-Aperture Systems</b> .....	<b>187</b>
<b>F</b>	<b><math>SNR</math> Scaling – Further Interpretations</b> .....	<b>191</b>

# Zusammenfassung

Radar mit synthetischer Apertur (SAR) ist eine seit vielen Jahren bewährte Methode zur Fernerkundung. SAR ist aufgrund seiner Fähigkeit, nahezu unabhängig von Lichtverhältnissen und Wetter eine hoch aufgelöste Abbildung der Erdoberfläche zu gewährleisten, zum vielseitigen Einsatz in der Erdbeobachtung geeignet. Allerdings sind bisherige, „konventionelle“ SAR-Systeme, die nur auf einer einzelnen Sende- sowie Empfangsantenne basieren, nicht in der Lage, die zunehmenden Anforderungen hinsichtlich verbesserter geometrischer Auflösung einhergehend mit vergrößerter abgebildeter Streifenbreite zu erfüllen. Um diese inhärente Systembeschränkung zu überwinden, wurden verschiedene neuartige Verfahren vorgeschlagen, die alle auf einer Mehrzahl von Empfangskanälen basieren. Dadurch werden gleichzeitig mehrere Signale empfangen und somit im Vergleich zu konventionellen Systemen zusätzliche Informationen gesammelt, die es erlauben, einen breiten Streifen abzubilden und dabei gleichzeitig eine hohe geometrische Auflösung zu gewährleisten (*high-resolution wide-swath imaging*). Die vorliegende Arbeit fasst in einem ersten Schritt die vorgeschlagenen Systemarchitekturen und Konzepte zusammen, wobei der Schwerpunkt auf mehreren Kanälen in Flugrichtung („Azimut“) liegt. Danach wird ein innovativer Algorithmus vorgestellt, der geeignet ist, die von solchen Multi-Kanal-Systemen empfangenen Daten zu prozessieren. Es folgt die umfassende Analyse dieses Multi-Kanal-Rekonstruktions-Algorithmus, beginnend mit einer theoretischen Untersuchung, wie die Systemleistung durch die Signalverarbeitung beeinflusst wird. In einem weiteren Schritt werden die Anwendbarkeit und das Potential des Algorithmus anhand von gemessenen Flugzeug-SAR-Daten sowie simulierten SAR-Daten verifiziert. Die Simulationsergebnisse werden im Rahmen eines vollständigen Systementwurfs für ein *high-resolution wide-swath* SAR präsentiert, wobei der direkte Zusammenhang zwischen Systemarchitektur und Multi-Kanal-Prozessierung verdeutlicht wird. Darauf aufbauend werden verschiedene neue Methoden zur Systemoptimierung vorgestellt und ihr Potential zur Erhöhung der Flexibilität sowie zur Verbesserung der Leistungsfähigkeit bewertet. In diesem Kontext werden die theoretische Beschreibung der Systemleistung auf die optimierten Verfahren erweitert und die Gültigkeit der hergeleiteten Zusammenhänge in Simulationen bestätigt. Der letzte Teil der Arbeit untersucht schließlich Systeme mit mehreren Empfangskanälen, die in einem sogenannten „burst“ Modus wie beispielsweise TOPS (*Terrain Observation with Progressive Scan*) oder ScanSAR betrieben werden. Dieser neuartige Multi-Kanal-Betriebsmodus erlaubt, dass eine bisher nicht dagewesene Kombi-

nation von sehr breitem Streifen mit hoher Auflösung mit kompakten Antennengrößen erreicht wird. Abschließend zeigt ein Ausblick das große Potential der behandelten Methoden und Algorithmen im Hinblick auf ihre Anwendbarkeit in zukünftigen Systemen, wie etwa Reflektorantennen mit *feed arrays* oder verteilte SAR-Systeme, bestehend aus mehreren kooperierenden Sensoren auf jeweils unabhängigen Satelliten.

# Abstract

Synthetic Aperture Radar (SAR) is a well-established imaging technique for remote sensing. It enables versatile and detailed imagery of the Earth's surface almost independently of light and weather conditions, such as clouds, fog, and rain. However, nowadays conventional SAR systems with a single transmit and receive antenna are not capable of fulfilling the increasing demands for improved spatial resolution and wider swath coverage. To overcome these system-inherent limitations, several new techniques have been proposed which employ multiple receive apertures to gather additional information along the synthetic aperture. This work reviews the proposed systems and techniques with particular emphasis on multiple channels in azimuth. Furthermore, it introduces an innovative processing algorithm that is suited to cope with the challenges posed by multi-channel data. Comprehensive analysis of this novel "multi-channel reconstruction algorithm" covers the theoretical investigation of its impact on system performance as well as its verification with measured and simulated data. The simulation results are given in the context of a complete high-resolution wide-swath SAR system design which highlights the intricate relationship between the system architecture and the multi-channel azimuth processing algorithm. Subsequently, the potential of different innovative optimization strategies to improve the system performance and increase the operational flexibility is demonstrated. Theoretical system performance analysis and description is extended to these approaches and verified in simulations. Furthermore, multi-channel systems operating in burst modes such as TOPS (Terrain Observation with Progressive Scan) and ScanSAR are investigated as a solution to new imaging modes enabling for compact antenna dimensions an unprecedented combination of an ultra-wide swath with reasonable geometric resolution in azimuth. Finally, future potentials are highlighted when applying the presented techniques to reflector-based antennas with multi-feed arrays or multi-satellite configurations forming a sparse array of SAR sensors.





# Acronyms and Symbols

In this work identical notation is used for real and complex quantities.

## List of Constants

$c_0$	speed of light in vacuum	$2.997925 \cdot 10^8$ m/s
$k$	Boltzmann's constant	$1.38 \cdot 10^{-23}$ J/K
$\pi$	Pi	3.141592
$R_E$	mean Earth radius	6371 km

## Mathematical Notations, Symbols and Functions

$j$	imaginary number	$j = \sqrt{-1}$
$\cos(x)$	cosine function	
$\text{rect}((f-f_0)/B)$	rectangular window function of width $B$ around center $f_0$	
$\sin(x)$	sine function	
$\text{sinc}(x)$	$\sin(x)/x$ function	
$\tan(x)$	tangent function	
$\mathcal{F}\{u\}$	Fourier transform of $u$	
$\mathcal{F}^{-1}\{U\}$	inverse Fourier transform of $U$	
$W(I)$	rectangular window function confining interval $I$	
$E[\cdot]$	expectation (for statistical values) / mean value (for deterministic values)	
$\max\{a,b\}$	maximum of values $a$ and $b$	
$\Sigma$	sum	
$\cap$	intersection / overlap of intervals	
$\mathbb{N}$	set of positive integer numbers	

---

$\mathbb{Z}$	set of integer numbers
$\mathbb{C}$	set of complex numbers
$\sim$	indicates approximate value of a variable
$\approx$	indicates approximation in an equation
$\in$	relates single element with corresponding set of values
$\propto$	relates directly proportional values
*	denotes complex conjugate of (scalar or vector) quantity
H	denotes conjugate transpose of vector quantity
T	denotes transpose of vector quantity

## Acronyms

Italic letters indicate that the acronym is also used as a variable.

<i>AASR<sub>N</sub></i>	Azimuth Ambiguity-to-Signal Ratio (in multi-channel systems of <i>N</i> receivers)
A/D	Analog-to-Digital (Converter)
ABF	Adapted Beamforming
ADC	Analog-to-Digital Conversion
BF	Beamforming
DBF	Digital Beamforming
DPCA	Displaced Phase Center Antenna
<i>HPBW</i>	Half Power Beamwidth
HRWS	High-Resolution Wide-Swath (as referring to a specific system)
LNA	Low Noise Amplifier
MBBM	Multi-Beam Burst Mode
MMSE	Minimum Mean Squared Error
<i>NESZ</i>	Noise Equivalent Sigma Zero
PBS	Pre-Beamshaping
PN	Pseudo-noise
<i>PRF</i>	Pulse Repetition Frequency
radar	Radio Detection and Ranging
<i>RASR</i>	Range-Ambiguity-to-Signal Ratio
RCMC	Range Cell Migration Correction
RF	Radio Frequency

Rx	Receiver
SAR	Synthetic Aperture Radar
SCORE	Scan On Receive
SNR	Signal-to-Noise Ratio
SRTM	Shuttle Radar Tomography Mission
STAP	Space-Time Adaptive Processing
T/R	Transmit/Receive (module)
TOPS	Terrain Observation with Progressive Scan
Tx	Transmitter

## Lower Case Letters

	Unit	
$\underline{a}$		vector containing optimum beamforming weights
$a(t)$		joint Tx/Rx antenna pattern and signal envelope of mono-aperture system in time domain, $\mathcal{F}^{-1}\{A(f)\}$
$b$		complex factor accounting for amplitude and phase of free-space attenuation, losses and radar cross section
$d_{el}$	m	length of individual receiving element in azimuth dimension
$d_{az,rx}$	m	length of receive aperture in azimuth dimension
$d_{az,tx}$	m	length of transmit aperture in azimuth dimension
$d'_1$	m	effective receive aperture length in azimuth dimension in cascaded networks
$d_1$	m	receiver phase center spacing in azimuth dimension in cascaded networks
$dc$		duty cycle
$d_{ev,rx}$	m	height of receive aperture in elevation dimension
$d_{ev,tx}$	m	height of transmit aperture in elevation dimension
$e_{k,j}(f)$		residual ambiguous contribution of order $k$ in channel $j$
$e_{c,k}$		residual ambiguous contribution of order $k$ for cascaded networks
$e_k$		residual ambiguous contribution of order $k$
$e_{\Sigma}(f)$		sum over all residual ambiguous contributions
$f$	Hz	Doppler/azimuth frequency
$f_0$	Hz	center Doppler frequency
$f_{0,k}$	Hz	center Doppler frequency of $k$ -th continuation of $U_j(f)$
$f_{0,m}$	Hz	center Doppler frequency of sub-band $m$

$f_{0,t}$	Hz	center frequency of target spectrum in burst mode
$f_{a,k}$	Hz	ambiguous Doppler frequencies of $k$ -th continuation of $U_j(f)$
$f_{\text{off},B}$	Hz	Doppler frequency offset corresponding to cycle time in burst mode
$f_r$	Hz	range domain frequency
$f_s$	Hz	sampling rate in range domain
$f_x$	Hz	spatial (Doppler) frequency (Fourier pair with azimuth dimension $x$ )
$h_{\text{ev}}$	m	overall antenna height in elevation dimension
$h_s$	m	sensor (orbit) height above ground
$h_s(t)$		mono-aperture azimuth response function for a point-like target, $\mathcal{F}^{-1}\{H_s(f)\}$
$h_{s,j}(t)$		multi-channel azimuth response function for a point-like target, $\mathcal{F}^{-1}\{H_{s,j}(f)\}$
$h_j(t)$		function relating mono- and multi-channel azimuth response for a point-like target, $\mathcal{F}^{-1}\{H_j(f)\}$
$i$		index, in general referring to individual receiving element $i$
$j$		index, in general referring to receiver $j$
$k$		discrete-time variable or index, in general referring to periodic continuation of Doppler spectrum by $k \cdot PRF$
$l_{\text{az}}$	m	antenna length in azimuth dimension
$l_{\text{az,eff}}$	m	effective overall antenna length in azimuth dimension
$m$		index, in general referring to sub-band $m$
$\underline{n}$		vector containing noise components
$n(f)$		overall noise in the reconstructed data
$n_{j,p}(f)$		periodic continuation of $n_j(f)$ with a period of $PRF$
$n_j(f)$		thermal noise of channel $j$
$n_{j,B}(f)$		additive white receiver noise of channel $j$ with respect to bandwidth $B$
$n_{q,j}(f)$		quantization noise of channel $j$
$n_{q,i}(f)$		quantization noise of element $i$
$\underline{n}_{\text{sp}}$		vector containing spatially structured noise
$\underline{n}_{\text{w}}$		vector containing spectrally white receiver noise
$p_a$	W	azimuth ambiguous power
$p_{a,B_s,i}$	W	azimuth ambiguous power originating from band $B_{s,i}$
$p_{n,\text{el},j}$	W	input noise power of channel $j$
$p_{n,\text{el}}$	W	input noise power at a receiving element
$p_n$	W	overall noise power in reconstructed data
$p_{n,B_s,i}$	W	output noise power originating from band $B_{s,i}$

$p_{n,rx,j}$	W	thermal receiver noise power of channel $j$
$p_{n,rx}$	W	thermal receiver noise power
$p_{n,c,rx}$	W	thermal receiver noise contributions in cascaded networks
$p_{n,q}$	W	quantization noise power
$p_{n,q,an}$	W	quantization noise after analog pre-processing
$p_{n,q,d}$	W	quantization noise after digital pre-processing
$p_{s,el,j}$	W	input signal power of channel $j$
$p_{s,el}$	W	input signal power of single receiving element
$p_s$	W	output signal power (after reconstruction)
$p_{s,c}$	W	output signal power in cascaded networks
$p_{s,B_{s,i}}$	W	output signal power resulting from the band $B_{s,i}$
$p_{s,max}$	W	signal peak power after compression/focusing
$\underline{s}$		steering vector
$t$	s	azimuth (slow) time
$t_n$	s	particular azimuth time specified by index $n$
$t_r$	s	range (fast) time
$u_{tx}(t)$		transmitted waveform in time domain
$u_{tx,b}(t)$		transmitted baseband waveform in time domain
$u_s(t)$		scene reflectivity in time domain, $\mathcal{F}^{-1}\{U_s(f)\}$
$u_{rx}(t)$		mono-aperture SAR signal in time domain before down-conversion
$u(t)$		mono-aperture SAR baseband signal in time domain, $\mathcal{F}^{-1}\{U(f)\}$
$u_i(t)$		multi-channel SAR signal at receive aperture $i$ in time domain, $\mathcal{F}^{-1}\{U_i(f)\}$
$u_j(t)$		multi-channel SAR signal of receiver channel $j$ in time domain, $\mathcal{F}^{-1}\{U_j(f)\}$
$u_{out,j}[k]$		discrete-time output signal of channel $j$
$u_{out}[k]$		discrete-time output signal
$v_e$	m/s	equivalent velocity in azimuth dimension
$v_g$	m/s	beam velocity on ground in azimuth dimension
$v_s$	m/s	sensor velocity in azimuth dimension
$w_{ij}(f)$		complex weighting for input signal of element $i$ with output to channel $j$
$x$	m	azimuth dimension (sensor track or on ground)
$x_e$	m	equivalent azimuth dimension
$x_{tx}(t)$	m	transmit antenna phase center position in azimuth dimension
$x_{tx,max}$	m	outermost position for transmit aperture phase center in azimuth dimension

## Capital Letters

	Unit	
$\mathbf{A}(f)$		inverse matrix of $\mathbf{V}(f)$
$A_{\text{ant}}$	$\text{m}^2$	antenna area
$A(f)$		joint Tx/Rx antenna pattern and signal envelope of mono-aperture system in Doppler domain, $\mathcal{F}\{a(t)\}$
$A_0(f)$		normalized point-target signal envelope $A(f)$
$A_j(f)$		point-target signal envelope of multi-aperture system in Doppler domain
$B$	Hz	analog system bandwidth
$B_{\text{az}}$	Hz	bandwidth of azimuth modulation (“Doppler bandwidth”)
$B_{\text{B}}$	Hz	Doppler bandwidth of single burst
$B_{\text{D}}$	Hz	processed Doppler bandwidth for focusing
$B_{\text{rg}}$	Hz	bandwidth of transmitted chirp signal
$B_{\text{s},i}$	Hz	reflected Doppler band of specific target in burst mode
$C_{\text{UA}}$		constant relating $U(f)$ and $A(f)$ in a way to ensure the correct unities
$F_j$		noise figure (power) of LNA in channel $j$
$F$		noise figure (power) of all LNAs
$G_j$		power gain of LNA in channel $j$
$G$		power gain of all LNAs
$G_{\text{rx},j}$		power gain of single receive aperture $j$
$G_{\text{rx}}$		power gain of receive antenna
$G_{\text{rx},c}$		equivalent power gain of receive antenna in cascaded networks
$G_{\text{tx}}$		power gain of transmit antenna
$H_{\text{s}}(f)$		mono-aperture azimuth response function for a point-like target, $\mathcal{F}\{h_{\text{s}}(t)\}$
$H_{\text{s},j}(f)$		multi-channel azimuth response function for a point-like target, $\mathcal{F}\{h_{\text{s},j}(t)\}$
$H_j(f)$		function relating mono- and multi-channel azimuth response for a point-like target, $\mathcal{F}\{h_j(t)\}$
$H_{jk}(f)$		$H_j(f)$ shifted by $k \cdot \text{PRF}$
$\mathbf{H}(f)$		system matrix containing the functions $H_j(f)$
$\mathbf{I}$		unity matrix
$I_m$		Doppler sub-band of width $\text{PRF}$ centered around $f_{0,m}$
$I_{\text{S}}$		Doppler system band
$K$		number of individual receiving elements

$L$		losses (atmospheric, system, receiver noise, 2-way)
$L_{az}$		azimuth loss factor (referred to mean power)
$L_{az,co}$		azimuth compression loss (referred to peak power)
$L_p$		normalized loss of peak power
$L_{sa}$	m	synthetic aperture length (extension on ground)
$M_j(f)$		system functions of pre-processing stage in cascaded networks
$N$		number of receive apertures in azimuth dimension
$N_{0,B}$	W/Hz	noise power spectral density with respect to bandwidth $B$
$N_{az}$		number of focused pulses in azimuth dimension
$N_B$		number of bursts
$N_{ch,i}$		number of channels of element $i$ after power splitter
$N_{el}$		number of Rx apertures in elevation dimension
$N_{rg}$		number of focused samples in range dimension
$P_j(f)$		reconstruction filter function of channel $j$
$P_{jm}(f)$		reconstruction filter function of channel $j$ on sub-band $m$
$\mathbf{P}(f)$		matrix containing the reconstruction filter functions $P_j(f)$
$\mathbf{P}_0(f_0)$		matrix defined by extract of $\mathbf{P}(f)$ at frequency $f_0$
$P_{mf}(f)$		matched filter function for SAR compression/focusing
$P_{tx}$	W	transmit peak power
$R$	m	slant range dimension
$\mathbf{R}$		noise covariance matrix
$R(t)$	m	time varying distance between sensor and a specific target, “range history”
$R_0$	m	minimum slant range distance (closest approach)
$\mathbf{R}_{sp}$		covariance matrix of spatially structured noise
$R_g$	m	ground range dimension
$T$	K	system temperature
$T_B$	s	illumination time of a single burst
$T_C$	s	cycle time in burst mode operation
$T_{sa}$	s	synthetic aperture length (time duration)
$U_s(f)$		scene reflectivity in Doppler domain, $\mathcal{F}\{u_s(t)\}$
$U(f)$		mono-aperture SAR signal in Doppler domain, $\mathcal{F}\{u(t)\}$
$U_j(f)$		multi-channel SAR signal of channel $j$ in Doppler domain, $\mathcal{F}\{u_j(t)\}$
$U_{j,p}(f)$		continuation of $U_j(f)$ with a period of $PRF$

$U_{jk}(f)$		$U_j(f)$ shifted by $k \cdot PRF$
$U_i(f)$		multi-channel SAR signal at receive element $i$ in Doppler domain, $\mathcal{F}\{u_i(t)\}$
$U_{i,\text{split}}(f)$		split multi-channel SAR signal at receive element $i$ after power divider
$U_{c,j}(f)$		intermediate signal after pre-processing stage in cascaded networks; input signal of “virtual” channel $j$
$U_c(f)$		equivalent monostatic signal of $U_{c,j}(f)$
$U_{c,k}(f)$		$U_c(f)$ shifted by $k \cdot PRF$
$U_{e,k}(f)$		residual ambiguity of order $k$ in the focused image
$\mathbf{V}(f)$		matrix containing characteristic beamforming vectors of linear array
$W_g$	m	swath width on ground

## Greek Symbols

	Unit	
$\alpha$		TOPS steering coefficient
$\gamma_j$	rad	correction phase of channel $j$
$\delta_{\text{az}}$	m	geometric resolution in azimuth dimension
$\delta_{\text{rg}}$	m	geometric resolution in ground range dimension
$\Delta t_j$	s	delay of effective phase center of receiver $j$ to transmitter phase center
$\Delta x$	m	antenna spacing in azimuth dimension
$\Delta x_e$	m	antenna spacing in equivalent azimuth dimension
$\Delta x_j$	m	separation between phase centers of receiver $j$ and transmitter
$\Delta x_{\text{step}}$	m	pulse-to-pulse shift of sample position in azimuth dimension
$\Delta x_{\text{step,tx}}$	m	pulse-to-pulse shift of Tx aperture phase center in azimuth dimension
$\Delta R$	m	range cell migration (one-way)
$\Delta R_{0,j}$	m	relative slant range offset (two-way) of receiver $j$ from reference value
$\Delta R_{\text{curv},j}$	m	differential range curvature (two-way) with respect to reference curvature
$\Delta \varphi_j$	rad	phase mismatch for reconstruction of range compressed signal
$\Delta \varphi_{\tau,j}$	rad	phase mismatch for reconstruction of uncompressed signal
$\varepsilon_{\text{bw}}$		ratio of Doppler system bandwidth to processed bandwidth
$\Theta$	rad	azimuth angle
$\Theta_{\text{az}}$	rad	3-dB power beamwidth of antenna pattern in azimuth dimension
$\Theta_{\text{ev}}$	rad	3-dB power beamwidth of antenna pattern in elevation dimension



$\Theta_i$	rad	incident angle
$\Theta_r$	rad	radar look angle
$\lambda$	m	carrier wavelength
$\sigma^2$	W	power of white noise
$\tau$	s	pulse duration
$\varphi(t)$	rad	point target azimuth phase modulation
$\Phi_{\text{bf}}$		<i>SNR</i> scaling factor of beamforming network
$\Phi_{\text{bf},B}$		<i>SNR</i> scaling factor of beamforming network in burst mode operation
$\Phi_{\text{bf},B_D}$		<i>SNR</i> scaling factor of beamforming network after focusing
$\Phi_{\text{bf},c}$		<i>SNR</i> scaling factor of cascaded beamforming network

## Superscripts and Subscripts

0	denotes reference value or indicates center value
a	relates quantity to azimuth ambiguity
az	denotes azimuth dimension
B	relates quantity to burst mode operation
$B_{xx}$	relates quantity to bandwidth $B_{xx}$
$B_D$	quantity after focusing with processed Doppler bandwidth $B_D$
bf	relates quantity to beamforming network
c	relates quantity to cascaded networks
co	quantity after focusing (“compression”)
el	relates quantity to individual receiving element
ev	denotes elevation dimension
g	denotes ground range dimension
i	denotes incident geometry
$i$	relates quantity to receiver element $i$
in	relates quantity to input variable
$j$	relates quantity to receiver channel $j$
$k$	indicates a shift by $k \cdot PRF$
$m$	denotes sub-band $m$
max	denotes maximum value
min	denotes minimum value

n	relates quantity to noise signal
$N$	relates quantity to multi-channel system of $N$ receivers
opt	denotes optimum value
out	relates quantity to output variable
p	indicates periodically continued quantity
qa	indicates quadratic approximation of quantity
rg	denotes (ground) range dimension
rx	relates quantity to receiver or receive aperture
s	relates quantity to wanted signal or denotes sensor
sa	denotes synthetic aperture
sgl	denotes singular value
sp	indicates spatially structured (noise) quantity
tx	relates quantity to transmitter or transmit aperture
uni	relates quantity to uniform sampling
w	indicates spectrally white (noise) quantity

# 1 Introduction

James C. Maxwell's theoretical work on electromagnetic fields from 1864 established the fundamentals for the development of radio detection and ranging (radar) systems. Based on Maxwell's and Michael Faraday's scientific knowledge, in 1887 Heinrich H. Hertz experimentally proved the propagation of electromagnetic waves through free space and their reflection by metallic and dielectric objects, enabling the future development of radar. In 1904, Christian Hülsmeyer demonstrated the primal radar system, the so-called "telemobiloscope", which enabled the detection of ships and marked the beginning of radar history [1]. Through the next decades, the radar technique developed, leading to the first early warning radar systems at the end of the 1930s. During World War II, rapid development was ongoing, with a focus on military systems. After the war the first civilian applications arose in the field of air traffic control, but radar was still mainly used for object detection and not for imaging of the Earth's surface.

The Synthetic Aperture Radar (SAR) principle discovered by Wiley in the early 1950s [2][3] enabled NASA to put into operation the first spaceborne imaging radar in 1978 (cf. Fig. 1): the Seasat oceanographic satellite [4]. The SAR principle is based on a pulsed operation of the radar and benefits from the sensor's motion over the scene, yielding the coherent reception of multiple echo pulses while the sensor illuminates a specific target. Processing results in an effective beam which is very narrow, permitting detailed imagery as e.g. a geometric resolution of 25 m in the

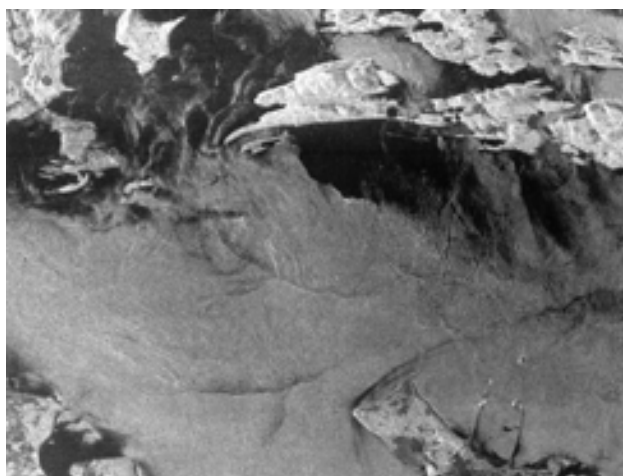


**Fig. 1. Strait of Georgia (Canada) imaged with a geometric resolution of 25 m by the first spaceborne SAR satellite Seasat ([5], © NASA/JPL).**

case of Seasat [5]. In the following years, SAR was developed more extensively and numerous satellites for Earth observation were launched by the European Space Agency (ESA), the Japanese Aerospace Exploration Agency (JAXA), the Canadian Space Agency (CSA), and, last but not least, NASA's Jet Propulsion Laboratory (JPL). These satellites include ESA's ERS-1/2 in 1991 and 1995, respectively, and ENVISAT (2002), as well as JERS-1 launched by JAXA in 1992, and the Canadian's Radarsat-1 (1995). As well, NASA's space shuttle has carried SAR sensors during the SIR-A and SIR-B missions in the 1980s, followed by SIR-C/X-SAR (1994) and the Shuttle Radar Topography Mission (SRTM) in 2000, the latter carried out in cooperation with the German Aerospace Center (DLR) and the Italian Space Agency (ASI) (cf. summary in Appendix A). In addition, several airborne platforms carrying SAR sensors have been developed and are in operation at the present time.

Now, after more than 100 years of radar history [6], SAR is an established technique for remote sensing of the Earth and other planets of our solar system, and progress is ongoing as numerous missions are planned to be launched within the next decade and new airborne sensors are put into service. Radar remote sensing and especially SAR imagery have proven to be suited for a large number of very versatile applications such as disaster management, land and sea traffic observation, wide area surveillance, and environmental monitoring to name only a few. These applications can include a radiometric mapping of the area of interest for cartographic purposes as well as interferometric applications to provide information on terrain heights, change detection or moving object identification. Further, in contrast to optical sensors, all applications are ensured independently of weather and light conditions, as clouds, fog, and rain, have almost negligible effect on the propagation of the electromagnetic waves of the radar.

## 1.1 State-of-the-Art: Synthetic Aperture Radar Remote Sensing

The current state-of-the-art for spaceborne SAR is represented by a number of SAR sensors put into orbit very recently such as TerraSAR-X [7], COSMO-SkyMed [8], and Radarsat-2 [9] which were launched in 2007 by Germany, Italy, and Canada, respectively. In addition, ALOS PalSAR [10], launched by Japan in 2006, is mentioned as an L-band representative. All these sensors are based on a phased array antenna and rely on transmit-receive (T/R) modules. As a consequence, the instruments offer sophisticated beamsteering capability by an analog real-time weighting of the phased array signals both on receive and on transmit, thus enabling advanced imaging modes such as spotlight [12], ScanSAR [13],[14] and TOPS [15].

Table 1 summarizes selected system parameters and performance figures for the above mentioned SAR sensors, to give an idea of their capabilities. Further, Fig. 2 to Fig. 5 illustrate the versatile use of spaceborne SAR imagery. They show TerraSAR-X images enabling agricultural monitoring in the Noerdlinger Ries (Swabia, Germany), ship detection and coastal surveillance in the Strait of Gibraltar, climate change detection by means of the forecast of glacier calving at the Larsen Ice Shelf (Antarctica), and the mapping of urban areas close to the pyramids of Gizeh (Egypt), respectively.

Sensor	Launch	Band	Stripmap		Spotlight/Fine Resolution		ScanSAR/Wide Swath	
			Resolution	Swath	Resolution	Scene	Resolution (looks)	Swath
TerraSAR-X	Jun 07	X	3 m	30 km	1 m 2 m	5 x 5 km <sup>2</sup> 5 x 10 km <sup>2</sup>	16 m	100 km
COSMO-SkyMed	Jun 07	X	3 m	40 km	1 m	10 x 10 km <sup>2</sup>	16 m 30 m	100 km 200 km
Radarsat-2	Dec 07	C	9 m	50 km	3 m	20 km	28 m (4) 50 m (2)	100 km 300 km
ALOS PalSAR	Jan 06	L	5 m	70 km	n/a	n/a	100 m (4)	350 km

**Table 1. Parameters and performance of spaceborne state-of-the-art SAR sensors [7]-[11]. Figures for single polarization and single look, otherwise number of looks is given in brackets.**

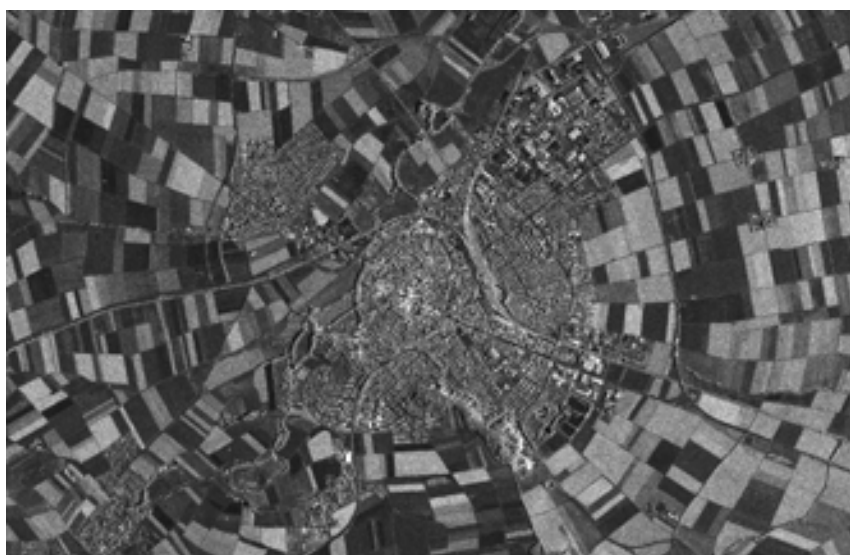


**Fig. 2. Noerdlinger Ries: Agricultural monitoring and harvest management with TerraSAR-X [7].**

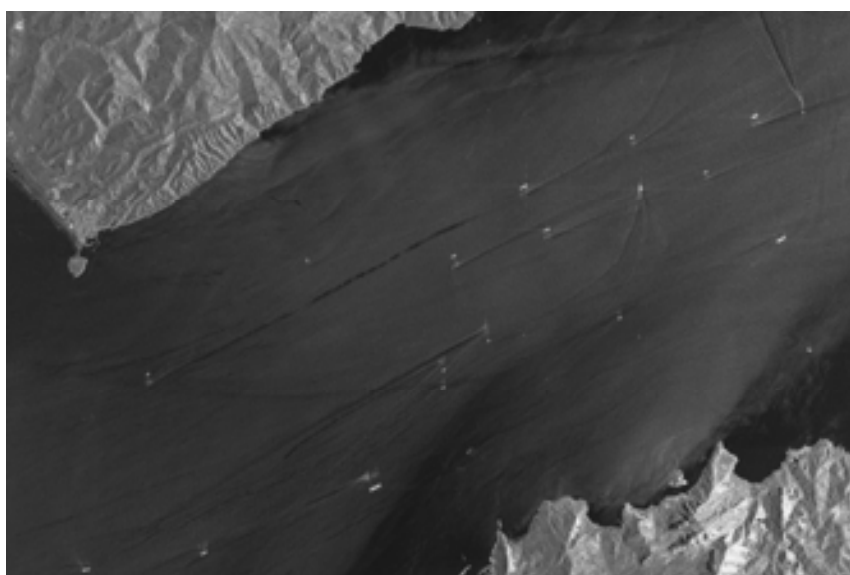


**Fig. 3. TerraSAR-X image of the Strait of Gibraltar: Coastal surveillance and ship detection [7].**

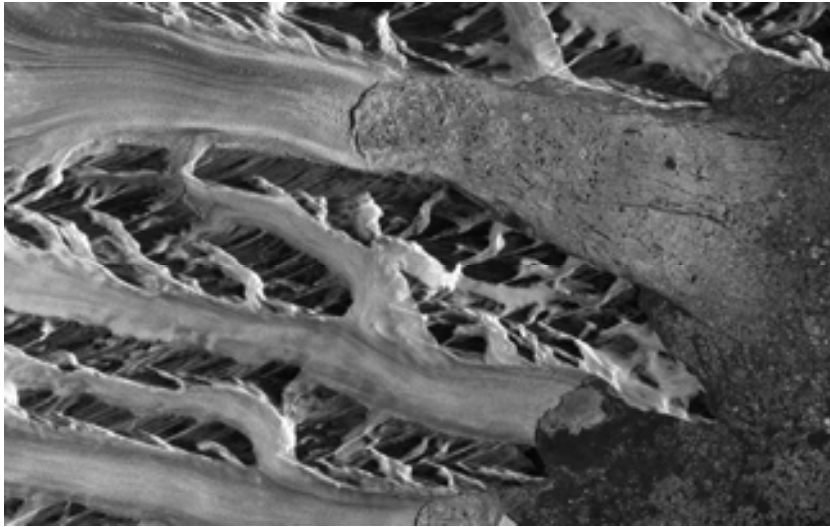


**Fig. 4. TerraSAR-X [7]: Detection and monitoring of climate changes of the Larsen Ice Shelf.**



**Fig. 5. Mapping/cartography of urban areas: TerraSAR-X image of the pyramids of Gizeh [7].**

As previously mentioned, all sensors allow for sophisticated beamsteering. Nevertheless, all beamforming and beamsteering is effectuated by an analog real-time weighting and combination of the antennas multiple receiving chains without storing the individual signals, thus depriving the sensor of the ability to apply “digital beamforming”, i.e. an a-posteriori digital multi-channel processing. Only Radarsat-2 allows for nominal two-channel reception [16], but solely for polarimetric applications and moving target indication and thus its digital beamforming capability is limited.<sup>1</sup>

---

<sup>1</sup>TerraSAR-X is capable of being experimentally operated with an antenna split into two sub-apertures (“dual-receive antenna mode”), which in principle also allows for basic digital multi-channel processing [17]. Strictly speaking, TerraSAR-X and Radarsat-2 can be considered as “rudimentary” multi-channel systems, but in terms of the requirements to future SAR missions this capability can only be regarded as a first step.

Table 1 clearly shows that all state-of-the-art sensors allow either for high resolution in combination with a narrow swath or can ensure wide-swath coverage with coarse geometric resolution. As will be derived later in detail, this is caused by a limitation inherent to single-aperture SAR systems, which permits improvement in resolution only at the cost of a narrower swath and vice versa, as optimization of one of the two performance parameters inevitably results in a degradation of the other [18], [19]. Fig. 6 visualizes the relation between swath width and resolution, making clear the trade-off between both parameters and indicating the upper bound for achievable system performance by the gray-shaded area. It becomes obvious that SAR systems based on a single transmit and receive aperture, do not allow for high-resolution and wide-swath imaging at the same time.

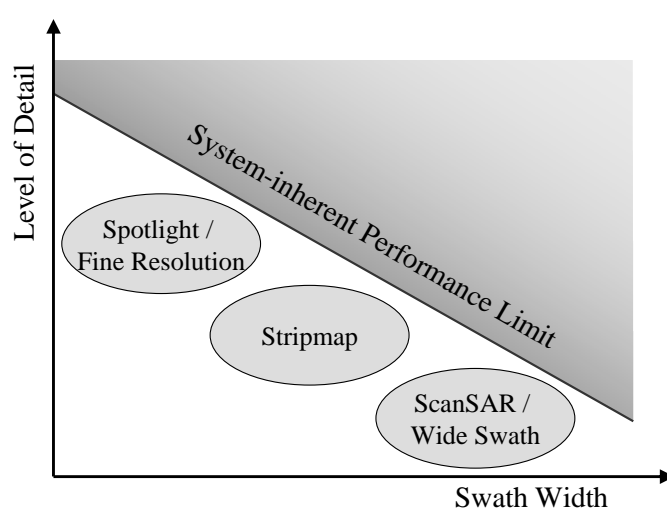


**Fig. 6. Relation between swath width and level of detail defined by the (inverse) geometric resolution in conventional SAR systems. The gray-shaded area marks the limitation of achievable swath width and resolution as a given swath width cannot be imaged with an arbitrarily good resolution and vice versa.**

## 1.2 Motivation, Scope, and Structure of this Work

As introduced before, SAR is a well-proven imaging technique for the observation of the Earth. However, “conventional” SAR sensors, i.e. systems based on a single transmit and receive aperture, are inherently limited as they cannot provide high geometric resolution and wide-swath coverage at the same time (cf. [18] and Fig. 6). Nevertheless, especially in recent years, Earth remote sensing applications increasingly demand sensors that are capable of continuous global coverage and, in addition, provide detailed imagery. Thus, conventional SAR is not capable of meeting the rising demands of future remote sensing missions, and innovative concepts are needed to ensure the imaging of a wide swath with high resolution. The most promising of these concepts employ multiple receive apertures and are listed in chronological order by [20]-[60].<sup>2</sup>

<sup>2</sup>Chapter 3 provides a detailed overview on the different system concepts, methods and processing techniques.

This allows for the simultaneous reception by multiple channels, compared to conventional systems with only a single receiving channel. The basic idea is, hence, to use the multiple receivers to gather additional information and to benefit from this information to overcome the above restrictions of conventional SAR systems. In general, the multiple receivers can be either arranged in flight direction (“along-track”) [24], perpendicular to it (“cross-track”) [23], or in both dimensions [25]. Accordingly, processing methods for signals in elevation dimension are introduced [29]-[33], [38], [51] as well as along-track multi-channel data are considered [35], [39]-[41], [45], [48]-[50], or both dimensions are combined, using a joint approach [26], [28], [34], or by exploiting the SAR geometry [20]-[22].

The present work focuses on sensors with multiple apertures in the along-track direction. In such systems, the spatial separation of the data gathered for a single transmit pulse is determined by the spacing between the different receivers, while the distance between two subsequent pulses is defined by the pulse repetition frequency (*PRF*) and the sensor velocity. In consequence, the *PRF* affects the spatial distribution of the gathered data (“samples”) for a fixed antenna length in azimuth [36], [37]. When conventional SAR algorithms are applied to such data, system analysis reveals that the performance varies depending on the spatial sample distribution and is hence sensitive to unavoidable variations of operational parameters like the applied *PRF*. This means that conventional SAR processing will fail, and thus novel methods of processing the received multi-channel data are required [52], [53]. So far, the problem of developing an algorithm which is suited to ensure full system performance independently of the applied system parameters has not yet been answered satisfactorily.

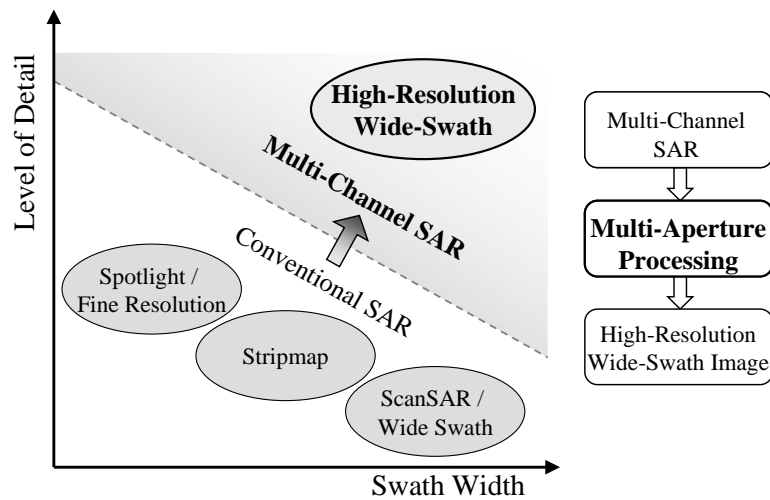


**Fig. 7. Multi-channel SAR system in combination with innovative digital multi-channel processing overcomes the limitation of conventional SAR and allows for high-resolution wide-swath imaging.**

The scope of this work is to introduce and analyze an innovative processing algorithm for azimuth data of multi-channel SAR systems in order to allow for high-resolution wide-swath imaging albeit with a varying *PRF* [42]-[44]. This work presents the derivation and verification of the novel algorithm as well as its analytical description allowing for the prediction of system performance [46], [47]. A detailed analysis in the frame of a system design example demon-



strates the capability to enable high-resolution wide-swath imagery and reveals the limitations of the algorithm which can be overcome by various innovative optimization strategies that are presented and analyzed in the second part of the work [52]-[57]. In a final step, the algorithm is extended to burst mode operation enabling a completely new class of SAR systems which is capable of imaging so far unprecedented ultra-wide swaths with reasonable geometric resolution [58]-[60], [65].

In summary, the present work provides an innovative and very flexible “toolbox” with respect to multi-channel processing in azimuth. This includes the possibility of novel modes as well as introducing an exceptional flexibility and reconfigurability of SAR systems, thus enabling hitherto unprecedented performance in combination with a dramatically increased area of application. In consequence, the innovative processing algorithm in azimuth opens a completely new field of SAR operation, which allows for flexibly answering the needs of future remote sensing requirements. Especially if embedded in the frame of advanced imaging concepts [61]-[65], the presented azimuth processing methods show huge potential to become an indispensable component for the next decade of SAR.

This dissertation is organized as follows. It begins with an introduction to the basic principles, relationships and constraints in conventional SAR systems to give a basic understanding of the topic and to stress the necessity for new SAR concepts (cf. Chapter 2). Then, Chapter 3 introduces the idea of multi-channel reception as a possible solution to overcome the system-inherent limitations of conventional approaches, followed by a detailed overview of the historical development of multi-channel SAR from its beginnings to state-of-the-art systems, concepts, and techniques. Focus is then turned to the azimuth dimension in Chapter 4, which presents a multi-channel SAR signal model. Furthermore, the properties of the spatial sampling in azimuth specific to multi-channel systems are summarized in order to provide a better understanding of the signal processing analysis in azimuth. In Chapter 5, theory and the principle of the innovative digital beamforming algorithm in azimuth are presented, and the algorithm is incorporated in the classical space-time adaptive processing (STAP) framework. Then, the one-dimensional processing approach is embedded in the two-dimensional SAR processing scheme. Further, a detailed theoretical analysis is carried out showing how signal, ambiguities and noise are affected by the digital processing network. This provides analytic expressions to estimate the respective parameters in multi-channel SAR systems thus enabling a prediction of the system performance.

A proof-of-concept in Chapter 6 demonstrates the applicability and potential of the presented algorithm to multi-channel data obtained with the German Aerospace Center’s airborne sensors E-SAR and F-SAR.

Chapter 7 presents the design and performance analysis of an example system which enables the imaging of a swath width of 100 km with a resolution better than 1 m. Simulation results for various performance parameters in combination with a comparison to alternative azimuth processing techniques demonstrate the great potential of the multi-channel reconstruction algorithm. In addition, the results allow for verification of the theory derived in Chapter 5. At the same time, the analysis illustrates the intricate connection between mission performance requirements and system parameters and highlights the resulting limitations.

In a next step, system optimization is discussed in Chapter 8 with the goal of overcoming the aforementioned limitations by improving the performance and increasing the flexibility of multi-channel SAR systems. At first, error sources are identified and innovative strategies are derived. Next, it is illustrated how an adaptation of the processed Doppler bandwidth and an adaptive management of the *PRF* in sparse array systems allow for an optimization of the system performance. Then, optimization concepts concerning the transmit side, such as pattern tapering on transmit and an innovative strategy based on the patented adaptive pulse-to-pulse shift of the transmit antenna phase center [56], [57], are explained. Afterwards, focus is turned to the receive side, and a new concept based on a cascaded structure of processing networks is introduced and analyzed. In this context, the theoretical examination of signal power, residual errors, ambiguities and scaling of the noise power is extended to the class of cascaded beamforming systems. The investigation of the cascaded beamforming technique is completed by a system performance analysis. In this framework, an analog representation of a cascaded network called “pre-beamshaping on receive” as well as a digital pre-processing approach are presented, and their performance is evaluated.

In a further step, the applicability of the multi-channel reconstruction algorithm to ScanSAR and TOPS-SAR is investigated and characteristic effects of multi-channel processing in burst mode systems are analyzed in Chapter 9. In this regard, a design example for such an innovative system concept is presented that enables the remote sensing of ultra-wide swaths of 400 km with a geometric resolution of 5 m.

This dissertation closes with a discussion containing an outlook on further issues like sparse array systems (cf. Chapter 10).

## 2 Conventional SAR Systems – Fundamentals and Constraints

This chapter introduces the geometry and basic parameters of SAR and explains the characteristic of SAR operation, followed by a derivation of the signal model of a single-aperture (“conventional”) system, where attention is drawn to azimuth dimension, as the work focuses on these aspects. Then, based on the derived model, the relationships between system parameters and performance figures are deduced, leading to the system-inherent limitation to provide detailed (“high-resolution”) imagery and wide coverage (“wide-swath”) at the same time. For an in-depth analysis and a wider description of SAR, the reader is referred to e.g. [18] or [66].

### 2.1 Geometry and Principle

Synthetic Aperture Radar consists of side looking radar on a moving platform, being ground-based, air- or spaceborne. The radar is emitting pulses with a frequency denoted by  $PRF$  (Pulse Repetition Frequency). The pulses are then backscattered by the illuminated area on ground and coherently received and stored by the sensor. The data are downlinked to the ground

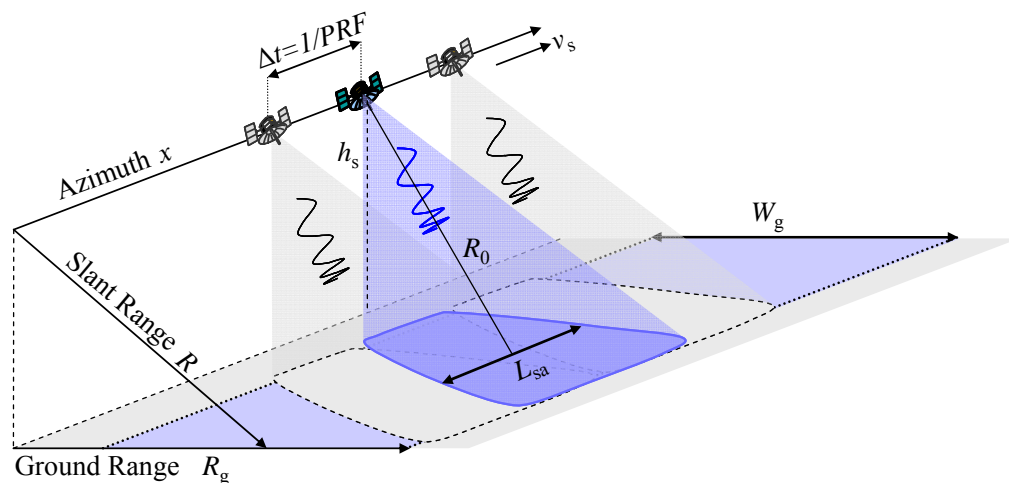


**Fig. 8. SAR geometry.** Side-looking radar sensor moving along azimuth dimension  $x$  with velocity  $v_s$  and transmitting pulses in slant range direction  $R$  with repetition frequency  $PRF$ . The antenna footprint covers a swath width  $W_g$  on ground and a length  $L_{sa}$  in azimuth (“synthetic aperture”).

where appropriate processing is performed in order to generate a map of the reflectivity of the ground, i.e. a radar “image” of the scene.

Fig. 8 depicts the basic geometry of SAR. The sensor is traveling in a height  $h_s$  with constant velocity  $v_s$  and the direction of the sensor’s movement is called along-track or azimuth dimension, which is denoted by  $x$ . The radar look direction perpendicular to along-track is referred to as slant range dimension  $R$ . The projection of the slant range dimension on the Earth is indicated by the index  $g$  yielding the ground range  $R_g$ . The slant range depends on the angular direction in which the antenna beam is pointing. It is given by the radar look angle  $\theta_r$ , while the angle between the incident wave emitted by the radar and the normal of the surface is denominated incident angle  $\theta_i$  (cf. Fig. 9). Note that  $\theta_r$  and  $\theta_i$  are different in orbital SAR geometry, as depicted in the left part of Fig. 9. Only in flat Earth approximation and assuming the absence of terrain slope they become identical, as shown on the right part of Fig. 9.

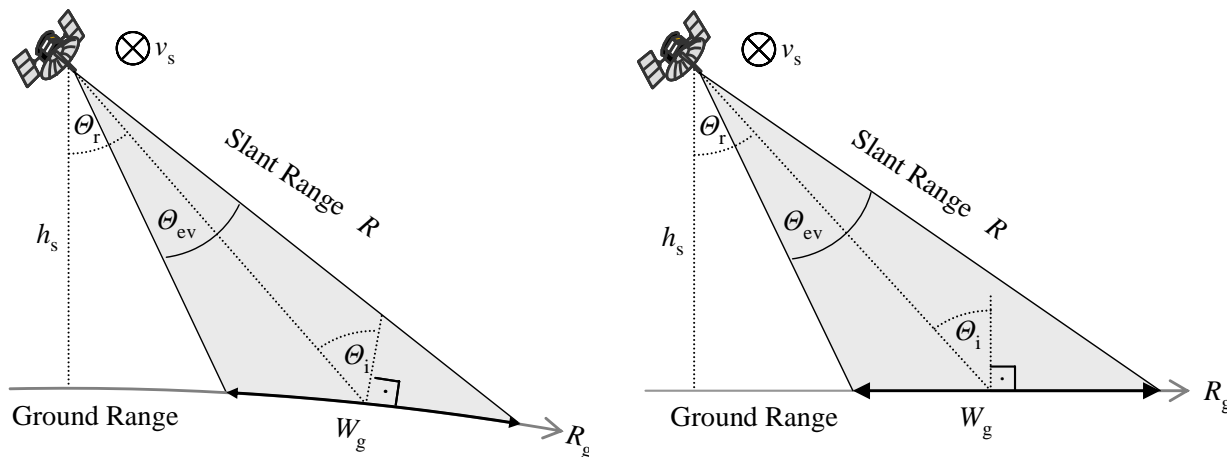


**Fig. 9.** Crosscut showing range dimension with radar look angle  $\theta_r$  and incident angle  $\theta_i$ . The antenna beam of angular width  $\theta_{ev}$  illuminates a swath of width  $W_g$  on ground. Left shows the curved Earth surface while right depicts the flat-Earth approximation.

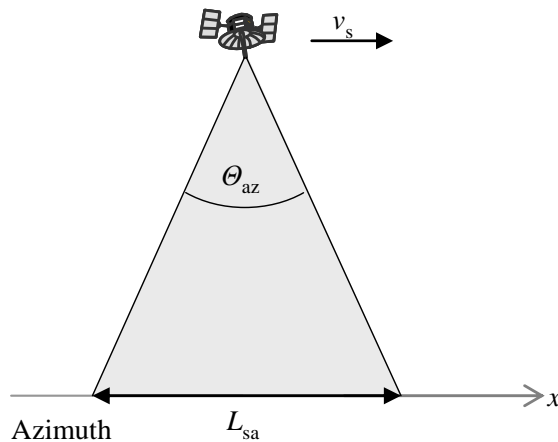


**Fig. 10.** Crosscut showing azimuth dimension with antenna beamwidth  $\theta_{az}$  resulting in an illuminated area of length  $L_{sa}$  on ground.

The flat-Earth geometry provides a valid estimate for airborne sensors, but spaceborne configurations require a modeling that better approximates the “round-like” shape of the Earth, being it by a simple spherical approximation or by a more accurate elliptical modeling of the Earth’s surface. For more details on the geometrical relationships in spaceborne scenarios, the reader is referred to [67] and [68].

The area on ground illuminated by the antenna is characterized by  $\Theta_{\text{ev}}$  and  $\Theta_{\text{az}}$ , respectively, representing the 3-dB beamwidth of the two-way antenna pattern in the respective dimension. Finally,  $\Theta_{\text{ev}}$  and  $\Theta_{\text{az}}$  lead to a swath of width  $W_g$  in ground range dimension and length  $L_{\text{sa}}$  (“synthetic aperture length”) in azimuth dimension, respectively (cf. Fig. 9 and Fig. 10).

The SAR principle is based on the movement of the sensor with respect to a specific target while emitting pulses. Consequently, the backscattered echoes of this target contribute to the received signal as long as the target is illuminated by the antenna. This illumination time and the corresponding length on ground are denoted by  $T_{\text{sa}}$  and  $L_{\text{sa}}$ , respectively, and will be referred to as “synthetic aperture” in the following. In terms of the received signal, the synthetic aperture is built by all the pulses which are backscattered and received coherently during the illumination time.

The characteristic of the SAR configuration is the varying distance between the sensor and a specific target while the platform travels along the synthetic aperture. As mentioned, the sensor moves with constant velocity  $v_s$  on a spherical flight track of height  $h_s$ . Further, the relation between time  $t$  and along-track dimension is defined as  $x(t) := v_s \cdot t$ , i.e.  $x$  follows the sensor’s spherical flight path. Finally, without restriction of generality, the target position in azimuth on ground is assumed at  $x=0$  and the rotation of the Earth is neglected according to [68]. This leads to the following expression for the slant range distance  $R(t)$  between the sensor and the target, where  $R_E$  is the mean Earth radius.

$$R(t) = \sqrt{(R_E + h_s)^2 + R_E^2 - 2 \cdot (R_E + h_s) \cdot R_E \cdot \cos(\Theta_E) \cdot \cos\left(\frac{v_s \cdot t}{R_E + h_s}\right)} \quad (1)$$

$\Theta_E$  represents the angle between the straight lines from the geocenter to the sensor and the target, respectively, and corresponds to the difference between radar look angle and incident angle.<sup>3</sup>

$$\Theta_E = \Theta_i - \Theta_r \quad (2)$$

Applying a Taylor expansion of second order to (1) yields the quadratic approximation of the signal path as follows, where  $v_g$  describes the velocity of the antenna footprint on ground as derived in detail in Appendix B.<sup>4</sup>

<sup>3</sup>The equations are given in dependency on  $\Theta_E$  as this allows for a more compact notation. For the reformed expression in dependency on the incident angle  $\Theta_i$ , the reader is referred to Appendix B.

<sup>4</sup>It should be noted that the quadratic approximation allows for an easier interpretation, but might not be accurate enough for the later development. For a detailed analysis, refer to Appendix C.

$$R(t) \approx R_0 + \frac{v_g \cdot v_s}{2 \cdot R_0} \cdot t^2 \quad (3)$$

One obtains a quadratic variation of the slant range distance between sensor and target, where  $R_0$  is the point of closest approach, which is obtained by inserting  $t=0$  into (1) according to the target position  $x=0$ .

$$R_0 := R(t_0) = \sqrt{(R_E + h_s)^2 + R_E^2 - 2 \cdot (R_E + h_s) \cdot R_E \cdot \cos(\Theta_E)} \quad (4)$$

As already mentioned, the above expressions consider the orbital geometry that is valid for spaceborne configurations. If the orbital flight track can be approximated by a straight path,  $v_g = v_s$  can be assumed and (1) simplifies to the well-known expression for the slant range variation.

$$R(t) = \sqrt{R_0^2 + x(t)^2} \approx R_0 + \frac{v_s^2}{2 \cdot R_0} \cdot t^2 \quad (5)$$

## 2.2 SAR Signal Model

The waveform of a single pulse transmitted by the SAR shall be given by  $u_{tx}(t)$ . The pulse can be separated into the baseband signal  $u_{tx,b}(t)$  and a carrier defined by the wavelength  $\lambda$ , where  $c_0$  denotes the speed of light in vacuum and  $t$  gives the time:

$$u_{tx}(t) = u_{tx,b}(t) \cdot \exp\left[j \cdot 2\pi \frac{c_0}{\lambda} \cdot t\right] \quad (6)$$

Then, the signal  $u_{rx}(t)$  received from a point-like target at distance  $R(t)$  is defined by the delayed and attenuated transmit signal, where – for convenience – the complex coefficient  $b$  summarizes free-space attenuation and further losses as well as the target's phase and radar cross section. Further, the weighting by the joint Tx/Rx antenna pattern in azimuth is expressed by  $a(t)$ .

$$u_{rx}(t) = b \cdot a(t) \cdot u_{tx}\left(t - \frac{2 \cdot R(t)}{c_0}\right) \quad (7)$$

After down-conversion, the received signal in baseband,  $u(t)$ , is obtained:

$$u(t) = b \cdot a(t) \cdot u_{tx,b}\left(t - \frac{2 \cdot R(t)}{c_0}\right) \cdot \exp\left[-j \cdot 2\pi \underbrace{\frac{2 \cdot R(t)}{\lambda}}_{=\varphi(t)}\right] \quad (8)$$

The signal  $u(t)$  can be separated into the transmitted baseband waveform  $u_{tx,b}(t)$  delayed according to the two-way path  $R(t)$  from the sensor to the target and an additional phase term  $\varphi(t)$  that remains from the delayed and down-converted carrier as given by (8).

Firstly, attention is given to the received raw data signal and its two-dimensional arrangement after storage in the memory of the radar system. Consider a transmitted chirp signal of duration  $\tau$  and an isolated point-like scatterer at azimuth position  $x_0$ , reflecting the pulses during the illumination time  $T_{sa}$ . This means that for each azimuth position, an echo of extension  $\tau$  is received, which is stored according to the respective range delay time (“range time”) resulting from the actual distance between sensor and target. Taking further into account that echoed pulses are received in azimuth during the illumination time  $T_{sa}$ , yields the two-dimensional raw data array for a point target as shown below on the left.

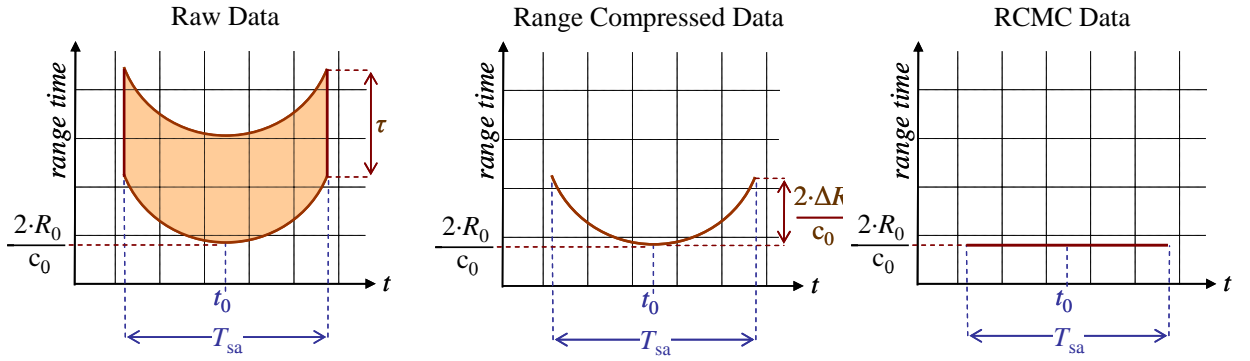


**Fig. 11. Two-dimensional SAR data array defined by range delay (“range time”) and azimuth (“ $t$ ”). Raw data (left) and range compressed data (middle) and signal after range cell migration correction (right).**

In a next step, range compression is taken into account, but only treated shortly, as the present work focuses on azimuth dimension. A detailed description can be found e.g. in [69]. This means that for each azimuth position the echo is convolved with a replica of the transmit pulse. As a result, nearly the complete energy of the pulse is concentrated on the locus according to the distance between target and sensor (cf. Fig. 11, middle). As it can be observed, the signal energy of a point-like target is supported from a range time interval governed by the slant range variation  $\Delta R$ , which is in general larger than a single range resolution cell (“range bin”). Hence, the signal of a single target spans several pixels in range (“range cell migration”). This requires range cell migration correction (RCMC) [69] to align the echoes of a specific target in a single range bin (cf. Fig. 11, right), thus enabling an isolated one-dimensional consideration of the azimuth signal.

In the following, focus is turned to the signal variation in azimuth dimension. One recognizes that the remaining phase term is independent from the waveform of the transmitted signal  $u_{tx,b}(t)$  and varies only over azimuth according to the varying distance between sensor and target causing a phase modulation. This azimuth modulation of the signal is represented by the function  $h_s(t)$  which gives the azimuth response for a point-like target situated at azimuth position  $x=0$  (cf. (9)).

$$h_s(t) = \exp\left[-j \cdot \frac{4\pi}{\lambda} \cdot R(t)\right] \quad (9)$$

Assuming a scene reflectivity  $u_s(t)$ , the received SAR signal is given by the correlation of  $u_s(t)$  with the impulse response function  $h_s(t)$ , taking into account the azimuth pattern  $a(t)$  [70]. In Doppler frequency domain, this correlation can be carried out by a multiplication of the respective Fourier transforms  $U_s(f)$ ,  $H_s(f)$ , and  $A(f)$ . Note that the joint antenna Tx/Rx pattern in azimuth  $A(f)$  also represents the azimuth signal envelope. The obtained SAR signal is then given by  $u(t)$  and  $U(f)$ , respectively, as indicated by the following block diagram:

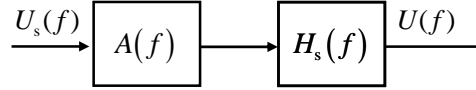


**Fig. 12. Azimuth block diagram of SAR signal acquisition. The scene characterized by its reflectivity  $U_s(f)$  is filtered by the “SAR channel” defined by the impulse response function  $H_s(f)$  and the signal envelope  $A(f)$ , leading to the SAR signal  $U(f)$ .**

Having a closer look on the phase term  $\varphi(t)$  describing the modulation in azimuth, it is recognized that  $\varphi(t)$  is determined by constant system parameters and the slant range  $R(t)$ . In consequence,  $\varphi(t)$  can also be expressed using quadratic approximation according to (3), allowing for a separation of the modulation into a constant phase term defined by  $R_0$  and a quadratic part describing the phase variation depending on azimuth time  $t$ .

$$\varphi(t) = -\frac{4\pi}{\lambda} R(t) \approx -\frac{4\pi}{\lambda} \left( R_0 + \frac{v_g \cdot v_s}{2 \cdot R_0} \cdot t^2 \right) \quad (10)$$

A visualization of the range history of a point-like target and the related phase versus azimuth time  $t$  is given in Fig. 13, where  $T_{sa}$  defines the time corresponding to the length of the synthetic aperture. As it facilitates understanding the derivation of the basic principles, the signal envelope in azimuth is estimated by the generic case of a rectangular shaped pattern in the following. This means that the envelope of the signal is approximated to be equal to 0 outside the antenna footprint given by  $\Theta_{az}$  and equal to 1 within.

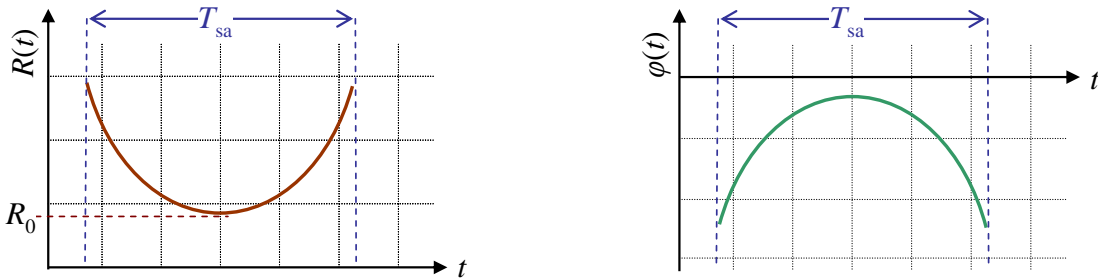


**Fig. 13. Left: Range variation  $R(t)$  between sensor and target. Right: Resulting phase modulation.**

The phase modulation of the target response over the synthetic aperture can be interpreted as a frequency variation, the so called Doppler frequency  $f$  that is defined in (11).

$$f(t) = \frac{1}{2\pi} \cdot \frac{\partial}{\partial t} \varphi(t) \quad (11)$$



Under the above assumption of quadratic approximation, evaluation of (11) yields a linear Doppler frequency characteristic of the target as given in (12) and depicted in Fig. 14 on the left.

$$f(t) \approx -\frac{2 \cdot v_g \cdot v_s}{\lambda \cdot R_0} \cdot t \quad (12)$$

Inserting (12) into (10), and representing  $h_s(t)$  in terms of  $f(t)$ , yields the characteristic chirp of the azimuth signal as follows in (13). It is visualized in Fig. 14 on the right.

$$h_s(t) \approx \exp[j \cdot 2\pi \cdot f(t) \cdot t] \quad (13)$$

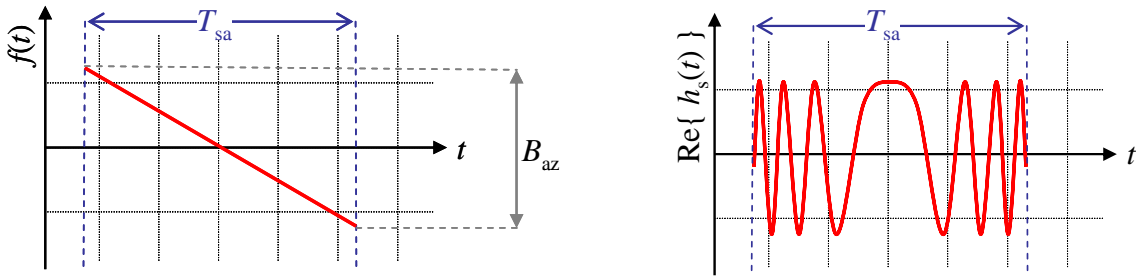


**Fig. 14. Characteristic of Doppler frequency  $f$  (after demodulation) vs. azimuth time  $t$  (left) and corresponding real part of chirp signal in azimuth after down-conversion (right).**

The bandwidth  $B_{az}$  of this azimuth modulation is determined by the length of the synthetic aperture  $L_{sa}$  or equivalently the maximum illumination time  $T_{sa} = L_{sa}/v_g$ . Note that the relation is given by the footprint velocity on ground,  $v_g$ , as this defines how long the target is illuminated.

$$B_{az} = f\left(\frac{T_{sa}}{2}\right) - f\left(-\frac{T_{sa}}{2}\right) = \frac{2 \cdot v_g \cdot v_s}{\lambda \cdot R_0} \cdot T_{sa} \quad (14)$$

As a rule of thumb, the length of the synthetic aperture  $L_{sa}$  is set equal to the extension of the antenna footprint on ground in azimuth dimension. In real patterns, the footprint is defined by the half power antenna beamwidth  $\Theta_{az}$ . For small angles,  $\Theta_{az}$  is approximated by (15), where  $l_{az}$  represents the antenna length in azimuth. Then, the antenna angle  $\Theta_{az}$  scaled with the slant range distance  $R_0$  yields  $L_{sa}$  and  $T_{sa}$ , respectively (cf. (16)).

$$\Theta_{az} \approx \frac{\lambda}{l_{az}} \quad (15)$$

$$T_{sa} = \frac{L_{sa}}{v_g} \approx \frac{R_0 \cdot \lambda}{v_g \cdot l_{az}} \quad (16)$$

Inserting (16) in (14), one obtains the basic relationship between antenna dimension and received Doppler bandwidth.

$$B_{az} \approx \frac{2 \cdot v_s}{l_{az}} \quad (17)$$

This means that the signal bandwidth in azimuth is only determined by the antenna size and the geometry, where a small antenna in azimuth illuminates a large area on ground entailing a high Doppler bandwidth and vice versa.

In the following, the signals obtained by two different antennas are regarded, taking into account the processing to show the impact on the geometric resolution of the SAR image. Therefore, a large and a small antenna are considered. As shown on the left part of Fig. 15, the large antenna results in a short synthetic aperture  $T_{sa,1}$  and entails a small Doppler bandwidth  $B_{az}$ . In contrast, the small antenna leads to a long illumination time  $T_{sa,2}$  and, correspondingly, a large Doppler bandwidth of the signal, as given on the right part of Fig. 15.

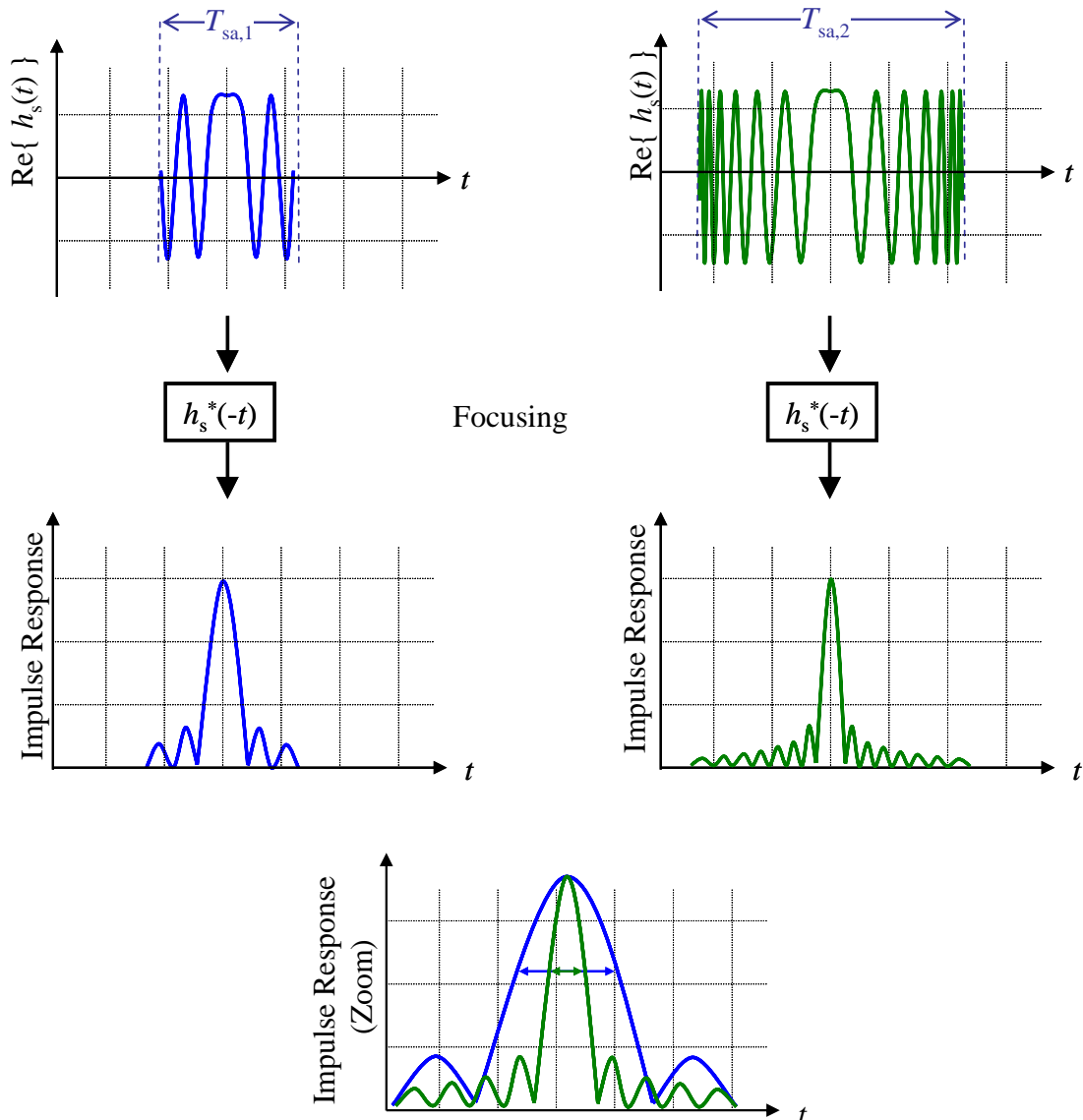


**Fig. 15.** Modulation of azimuth signal (top) and resulting point target impulse response (middle) after focusing. The left part considers a short and the right part a long illumination time  $T_{sa}$ . The 3 dB width of the mainlobe defines the geometric resolution  $\delta_{az}$  which becomes the narrower the longer  $T_{sa}$  is (bottom).

Processing of the received chirp to focus the signal in azimuth is then done by correlation with an expected impulse response (“matched filter”), i.e. the function of the focusing filter is chosen to  $h_s^*(-t)$ , where  $*$  denotes the complex conjugate.<sup>5</sup> This basically corresponds to a compensation of the phase of each sample followed by a summation of the respective samples.

For the considered generic case of a rectangular shaped pattern, one obtains a  $\sin(x)/x$  shaped function as an impulse response for a point-like target (cf. Fig. 15, bottom). Further, the geometric resolution in azimuth – defined by the 3 dB beamwidth of the mainlobe and denoted by  $\delta_{az}$  – becomes the better, the higher the bandwidth of the chirp signal is.

In consequence, the geometric resolution in azimuth is inversely proportional to the corresponding antenna dimension.<sup>6</sup> For the used approximation of a rectangular pattern, the resolution is related to Doppler bandwidth as given in (18). Using the equality of (17), the Doppler bandwidth can be replaced by the corresponding antenna dimension in azimuth, yielding the well-known relation between geometric resolution in azimuth and aperture size [66].

$$\delta_{az} \approx 0.89 \cdot \frac{v_g}{B_{az}} \approx 0.89 \cdot \frac{v_g}{v_s} \cdot \frac{l_{az}}{2} \approx \frac{l_{az}}{2} \quad (18)$$

Note that the factor 0.89 relates the half power beamwidth and the integration time for the special case of rectangular patterns and assumed a full resolution SAR. If the antenna pattern is no longer approximated by rectangles, this factor varies slightly, but the basic relation between resolution and Doppler bandwidth remains valid. Further, a reduction of the processed bandwidth, i.e.  $B_D < PRF$ , results in a coarsened resolution. In any case, half of the antenna length provides a first rough estimate for the geometric resolution in azimuth. In general, the resolution is above this value as can be seen at the example of TerraSAR-X, where an antenna of 4.8 m leads to a resolution of 3 m.

## 2.3 Pulsed Signal Acquisition

After the general considerations discussed above, the pulsed operation of the radar is taken into account and its impact on the system performance is derived. In particular, ambiguous returns in azimuth and range dimension are considered and how they are related to system geometry and  $PRF$ .

### 2.3.1 Azimuth Ambiguities

As mentioned, the pulses are transmitted – and then received – with a repetition frequency of  $PRF$ . This is equivalent to a sampling of the azimuth signal by this frequency and, consequently, discrete-time signal theory is to be considered. This requires for the  $PRF$  a value greater or equal

<sup>5</sup>Further,  $h(t) = h(-t)$  due to symmetry. Hence, the filter function can equivalently be chosen to  $h^*(t)$ .

<sup>6</sup>This considers a full resolution SAR, i.e. the complete Doppler bandwidth within the antenna footprint is focused. In other words, the bandwidth of the filter function  $h_s^*(-t)$  is equal to the acquired signal bandwidth. Of course, the bandwidth of  $h_s^*(-t)$  can be set to a smaller value.

to the Doppler bandwidth  $B_{az}$  (cf. (17)), to fulfill the Nyquist-Shannon sampling theorem [71]. If the Nyquist-Shannon theorem is violated by a too low  $PRF$  (so-called “sub-sampling”), ambiguous targets will occur in the SAR image.

At first,  $PRF > B_{az}$  is assumed and, hence, the azimuth signal is properly sampled. This means that each frequency component is “displayed” correctly after the sampling. The respective case is depicted exemplarily on the right side of Fig. 16, showing the chirp signal after sampling (top), its Doppler frequency characteristic (middle) and the impulse response after focusing (bottom).

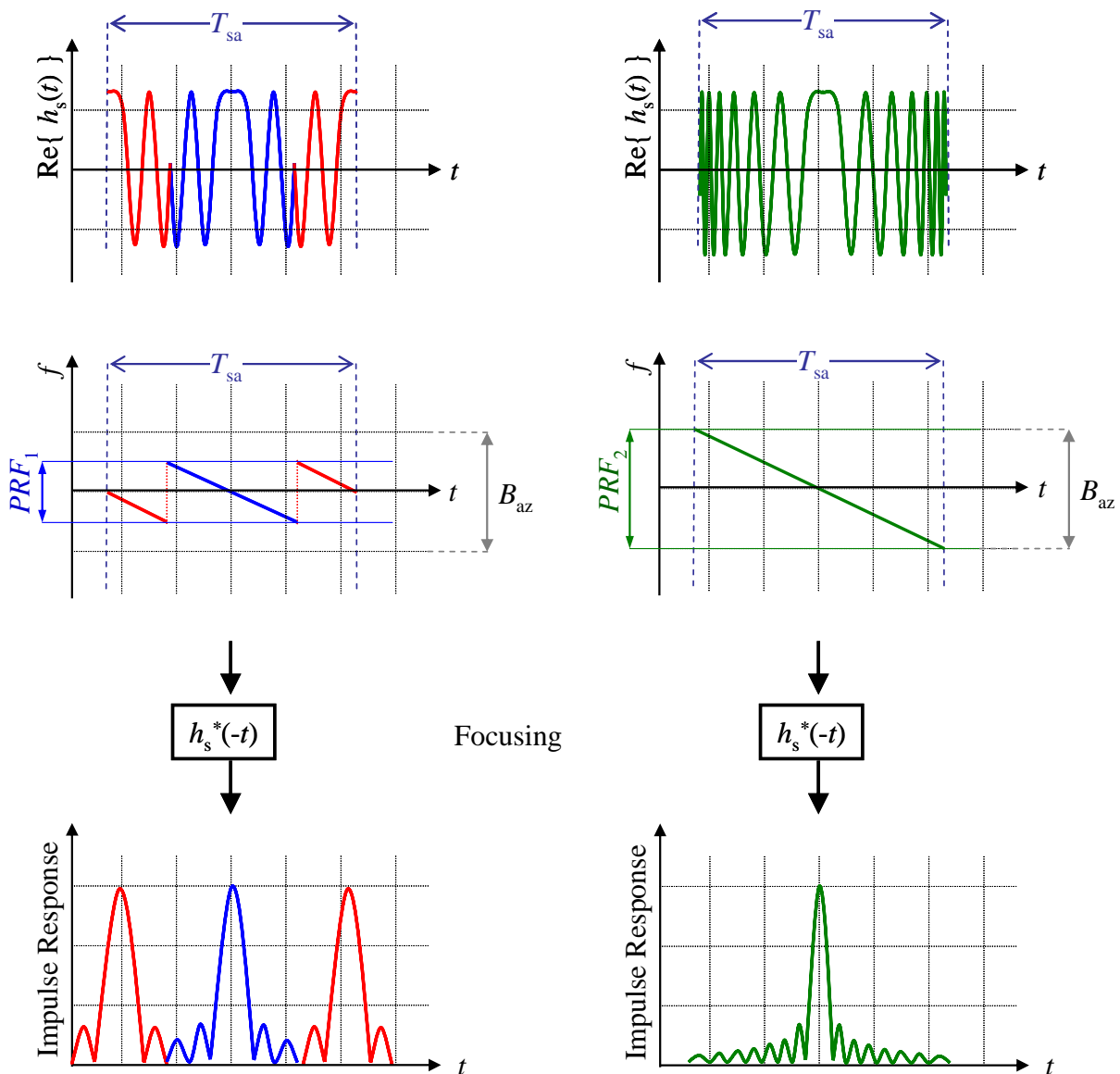


**Fig. 16.** Azimuth modulation of a point-like target (top), corresponding Doppler frequency characteristic after sampling (middle), and impulse response after focusing (bottom). **Left:** Under-sampling with  $PRF_1 < B_{az}$ . Backfolding of frequencies  $|f| > PRF_1/2$  into the Doppler band  $[-PRF_1/2, PRF_1/2]$ , leading to ambiguities in the focused image. **Right:** Sampling with  $PRF_2 > PRF_1$  according to Nyquist: The ambiguous returns are avoided.

In contrast, for the case where  $PRF < B_{az}$  holds true, the signal is sub-sampled and as a result frequencies  $f$  with  $|f| > PRF/2$  are no longer displayed correctly, but reduced by integer multiples of the  $PRF$ , i.e. a frequency  $f=0.8 \cdot PRF$  will be displaced after sampling to  $f-PRF=0.2 \cdot PRF$ . This leads to a backfolding of the Doppler spectrum (“aliasing”), that is spectral parts of the signal outside the band  $[-PRF/2, PRF/2]$  are falsely considered as the echoes of different targets and give rise to ambiguous targets in azimuth in the SAR image. An example for such a sub-sampled signal is shown on the left part of Fig. 16, where the top shows the sub-sampled chirp, followed by the back-folded Doppler frequency characteristic (middle), finally resulting in ambiguous returns after focusing (bottom).

As a conclusion, the required resolution does not only require a certain antenna length to illuminate an appropriately large Doppler bandwidth, but also a sufficiently high  $PRF$  to unambiguously sample this bandwidth. This means that (18) can be extended as follows:

$$\delta_{az} \approx 0.89 \cdot \frac{v_g}{v_s} \cdot \frac{l_{az}}{2} \approx 0.89 \cdot \frac{v_g}{B_{az}} \geq 0.89 \cdot \frac{v_g}{PRF} \quad (19)$$

In consequence, antenna dimension in azimuth and  $PRF$  have to be coordinated to ensure the required resolution while avoiding azimuth ambiguities. Thus, for a given antenna length, a minimum  $PRF$  is required to sufficiently suppress azimuth ambiguities. Vice versa, a certain  $PRF$  needs a minimum antenna length to keep azimuth ambiguous returns at a tolerable level.

In other words, resolution and ambiguity suppression in azimuth impose a lower bound on the system  $PRF$ , and the higher it is, the better the achievable azimuth resolution becomes and the smaller ambiguous returns will be. Unfortunately, a high  $PRF$  causes problems in range dimension as will be explained in the following section.

### 2.3.2 Range Ambiguities

Switching to the slant range dimension, one recognizes that the echoes of different transmit pulses might be received simultaneously if the two-way slant range distances between the respective ambiguous targets correspond to integer multiples of the interpulse period. Accounting for the round-trip by a factor “1/2”, the slant range distance between these so-called range-

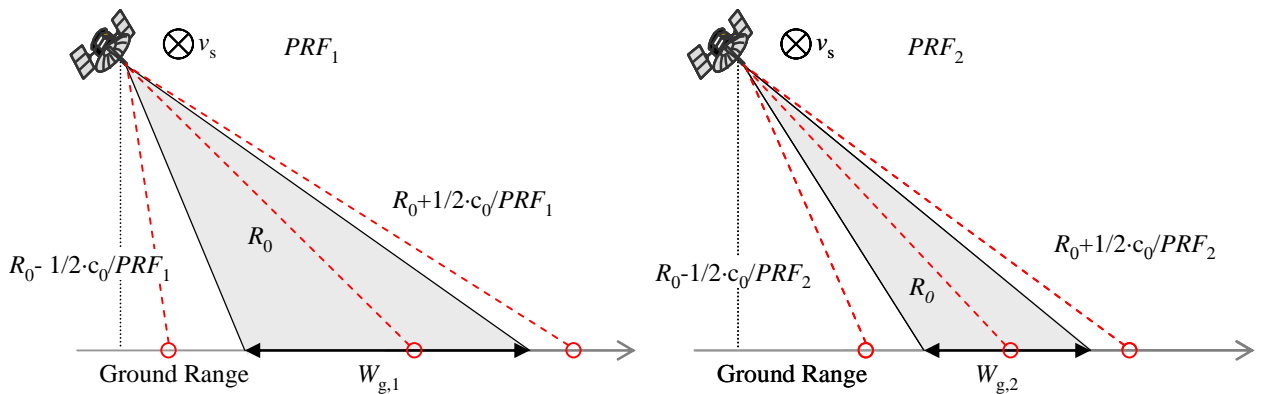


**Fig. 17. Relation between range-ambiguous returns and swath width on ground. A low  $PRF_1$  results in a large separation of the ambiguous returns allowing for a wide swath  $W_{g,1}$  (left), while a high  $PRF_2$  leads to closer ambiguous returns entailing a narrow swath  $W_{g,2}$  (right).**

ambiguous targets is given by  $1/2 \cdot c_0 / PRF$  (cf. Fig. 17, dashed red lines). In a next step, this distance can be translated into an angular separation, which determines the illumination by the antenna pattern in elevation and consequently the power of the ambiguous return. Hence, avoiding these returns requires adapting antenna height and  $PRF$  in a way that no range ambiguities occur within the antenna footprint in range. Effectively, this corresponds to a limitation of the imaged swath on ground, as a low  $PRF$  results in a large angular separation of the ambiguity and allows for a small antenna height enabling the illumination of a wide swath (cf. Fig. 17, left), while for a high  $PRF$  the ambiguous returns get closer requiring a higher antenna to guarantee a sufficient suppression which results in a smaller swath (cf. Fig. 17, right) [18].

This means that the higher the  $PRF$  the smaller the swath width becomes and vice versa. The relation between the maximum imaged swath on ground,  $W_g$ , and the system parameters is given in (20) where  $\Theta_i$  represents the incident angle. The equation gives an upper bound of the swath that can be imaged for a given  $PRF$ .

$$W_g < \frac{c_0}{2 \cdot \sin(\Theta_i) \cdot PRF} \quad (20)$$

Equivalently, (20) can be reformed easily to give an upper bound for the  $PRF$  in dependency on a predetermined swath width.

## 2.4 Constraints

As shown, a good azimuth resolution requires a short antenna of length  $l_{az}$  to illuminate a long synthetic aperture which results in high Doppler bandwidth  $B_{az}$ . This calls for a high  $PRF$  to sample the Doppler spectrum according to the Nyquist criterion (cf. (19)). In contrast, a low  $PRF$  is favorable to unambiguously image a wide swath on ground ( $W_g$ ) that is illuminated by a small antenna in elevation of height  $h_{ev}$  (cf. (20) and Fig. 17).

To obtain a figure of merit for the SAR image, the size of the imaged area and its level of detail, i.e. geometric resolution, are considered. Consequently, the swath width and the reciprocal resolution are combined by dividing (20) by (19), leading to a figure representing the number of imaged cells. Obviously, a system is the better the more cells are imaged, i.e. the higher the value of this figure is. This yields expression (21) which is only determined by the system geometry, but independent of adjustable system parameters.

$$\frac{W_g}{\delta_{az}} < \frac{c_0}{2 \cdot \sin(\Theta_i) \cdot 0.89 \cdot v_g} \quad (21)$$

Equation (21) can be reformed to the well-known minimum antenna area constraint [18], if the considerations start from a given  $PRF$  which entails a minimum antenna dimension in azimuth to limit the Doppler spectrum as well as a minimum antenna height to avoid range ambiguities.<sup>7</sup> The combination of these two constraints results in a minimum area  $A_{ant}$  for the antenna.

<sup>7</sup>As mentioned, this is valid for the assumed full resolution SAR. A relaxation – without solving the inherent constraint – can be achieved at the cost of a performance loss [19].

Equivalently to the figure of merit in (21),  $A_{\text{ant}}$  is given by the geometry and cannot be adjusted by system parameters (cf. (22)).

$$A_{\text{ant}} = h_{\text{ev}} \cdot l_{\text{az}} > \frac{4 \cdot \lambda \cdot R_0 \cdot v_s \cdot \tan(\Theta_i)}{c_0} \quad (22)$$

This means, the SAR system parameters are subject to a trade-off, as the resolution can only be enhanced at the cost of a decreased swath width or vice versa. In other words, in conventional SAR systems the unambiguous swath width and the achievable azimuth resolution pose contradicting requirements on system design, and consequently SAR systems allow only for a concession between resolution and swath-width. This is illustrated in Fig. 18 where the middle shows a compromise between swath width and azimuth resolution. If the system is optimized for a high resolution, the antenna length in azimuth decreases while increasing the *PRF*. The higher *PRF* requires a larger antenna height in elevation and entails a decreased swath (cf. Fig. 18, left). If the focus is turned to an enlarged swath, the antenna height has to be decreased. This rises the necessity for a decreased *PRF*, which requires an increased azimuth dimension of the antenna (cf. Fig. 18, right).

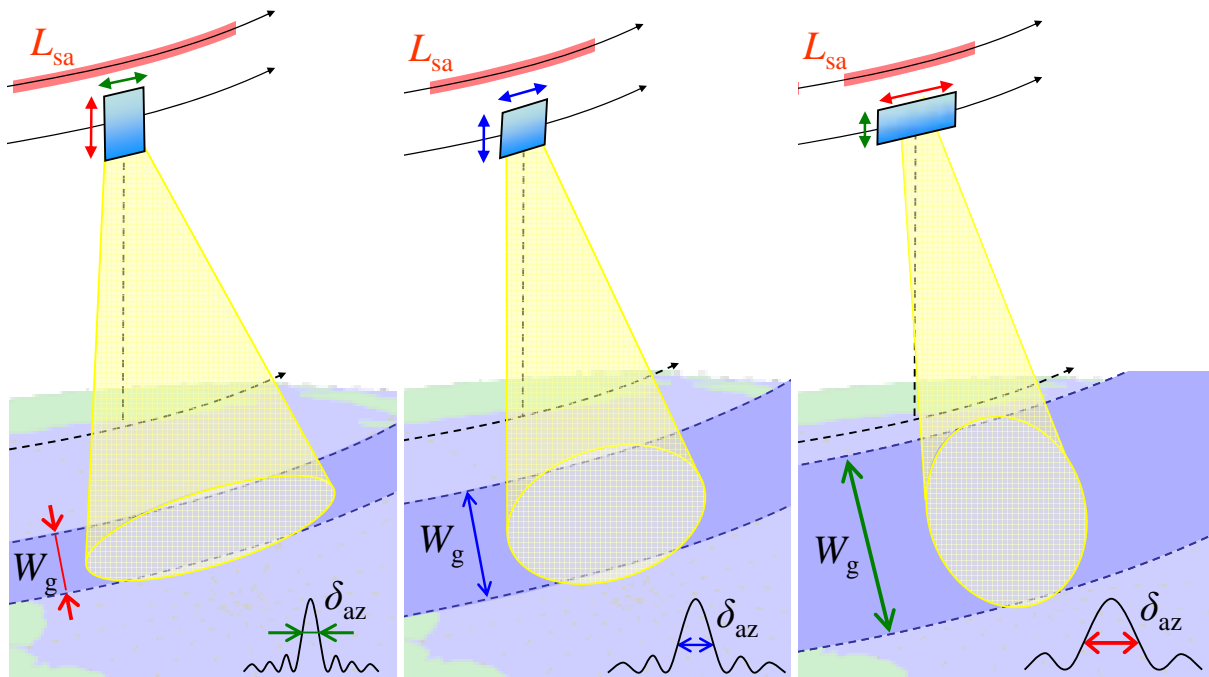


**Fig. 18. Left: System designed for high-resolution imaging. Middle: Stripmap mode with a trade-off between resolution and coverage. Right: Focus on wide-swath imaging.**

Alternative SAR imaging modes push this trade-off only further into one direction or another without resolving the underlying system-inherent constraint: the Spotlight mode yields a high azimuth resolution, but no sufficient coverage [12], while burst modes as ScanSAR [13],[14] and TOPS-SAR [15] map a wide swath but provide only a coarse resolution in azimuth dimension.

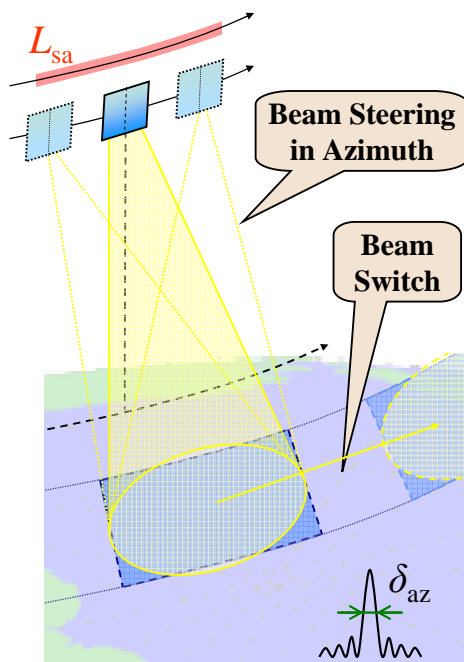


**Fig. 19. Spotlight mode: Increased illumination time (i.e. extended synthetic aperture) by beam steering in azimuth dimension.**

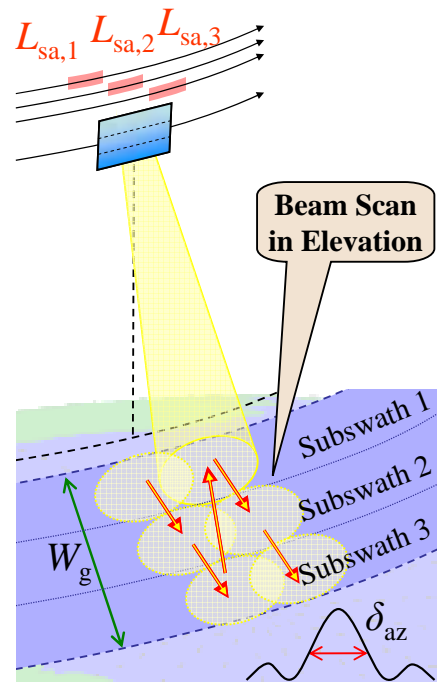


**Fig. 20. Burst mode (ScanSAR): Increased imaged swath by sensing multiple sub-swaths of coarsened resolution each.**

The increased resolution in Spotlight mode is achieved by steering the antenna footprint against flight direction to keep a defined area on ground illuminated as long as possible. This leads to an increased Doppler bandwidth of the received signal, but the switch of the antenna footprint from the outermost steering angles results in blind areas of the swath that are not imaged (cf. Fig. 19). In contrast, in burst modes operation the antenna footprint is continuously switched between multiple sub-swaths. As a result, the overall swath width consists of all sub-swaths, but is at the cost of a reduced illumination time per sub-swath leading to the coarsened azimuth resolution. A system operating in ScanSAR as an example for such a burst mode is depicted in Fig. 20.



## 3 Multi-Channel SAR – An Overview

As indicated in the introduction, increasing demands are arising to radar remote sensing, especially regarding the high image quality in combination with a continuous and frequent coverage of the Earth. The preceding chapter derived the system-inherent limitation of single-aperture SAR with respect to high-resolution wide-swath imaging, which prevent these “conventional” systems from satisfying the standards which will be requested in the future (cf. Section 2.4). In consequence, new system concepts are needed to fulfill the rising demands made to future SAR.

This chapter presents the basic idea of multi-channel SAR and how these systems are suited to “answer” the challenges of next generation radar remote sensing. In this context, Section 3.1 introduces the principle of employing multiple distinct apertures on receive to gather additional information thus enabling enhanced geometrical resolution in azimuth and/or an enlarged swath. The following sections give a compendium of the different concepts and processing strategies for the various multi-channel configurations. This comprises approaches based on multiple receivers in elevation as well as in azimuth which are sometimes combined with an appropriate processing.<sup>8</sup> In this context, Section 3.2 starts with a short overview of the historical development. Then, Sections 3.3 and 3.4 briefly present the principle and underlying idea of each of the suggested individual system concepts and processing techniques, respectively. The chapter is completed by describing alternative concepts that are no longer based on classical side-looking SAR geometry (cf. Section 3.5). Note that a detailed presentation of all techniques and concepts is beyond the scope of this work, but more information can be found in the corresponding references.

### 3.1 Multiple Aperture Reception

Numerous innovative concepts are presented to enable high-resolution wide-swath imaging whereof the most promising employ a single transmit antenna in combination with multiple channels on receive. This means that these systems have a receiving antenna which is split into multiple sub-apertures with independent receiver chains that are interpreted as individual channels. A similar technique is the distribution of the receiver apertures on multiple platforms that

---

<sup>8</sup>Note that this chapter presents the state-of-the-art of concepts and ideas, while Section 1.1 referred to existing systems that are already being operated.

are grouped to a formation of space- or airborne sensors leading to a multistatic SAR. Either on a single platform or distributed, all apertures illuminate the same area on the ground. Consequently, it is common to all of these methods that the backscattered signal is received simultaneously by multiple apertures, which are mutually displaced in azimuth and/or in elevation dimension. The different receive aperture positions introduce spatial diversity in the received echoes. Effectively, this corresponds to the reception of multiple signals. Compared to a conventional system – which receives only a single signal – the multi-aperture system architecture allows for gathering additional data. This supplementary information permits to overcome the aforementioned inherent limitations of conventional SAR systems.

The basic concept of a multi-channel SAR system is illustrated in Fig. 21: The system consists of  $N$  receiver chains, each interpreted as an individual channel. The received sub-aperture signals are down-converted and then combined in an additional digital signal processing stage, which shall be generally denoted by “Digital Beamforming”. Depending on the respective approach, the applied processing ranges from a simple temporal interleaving of the channels to a real-time beamsteering or even to an a posteriori digital processing of the previously stored and digitized data.<sup>9</sup> Independently of the applied beamforming, a single output signal is obtained which combines – in the optimum case – the information of all the input signals. In the following, classic monostatic SAR algorithms are applied to focus the signal.

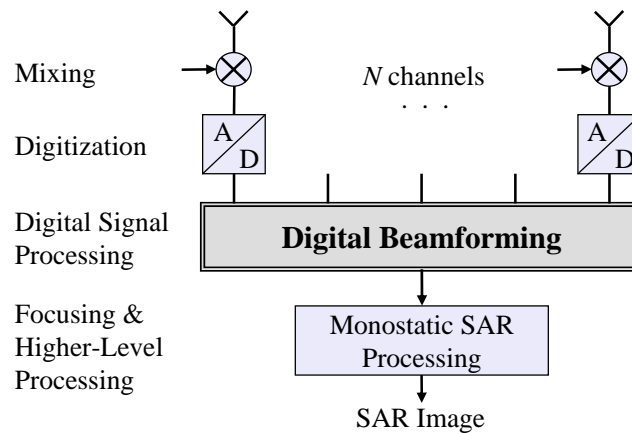


**Fig. 21. Multi-channel system block diagram. Each aperture is interpreted as an individual channel whose signals are mixed, digitized and combined in an additional signal processing stage (“Digital Beamforming”).**

## 3.2 Overview of Historical Developments

Although of course not really separable, the development can be roughly divided into earlier approaches, which focus on the system concept and give a general idea, followed by more spe-

<sup>9</sup>It should be noted that some of the suggested techniques do not imperatively require digital processing, as e.g. the SCORE algorithm [29] could also be realized by analog phase shifters. Nevertheless, digital processing is possible and reasonable in all of the presented methods and concepts.

cific and increasingly sophisticated techniques, which are based on the principles of the systems presented before but focus on the processing of the multi-channel signals and require more complex system configurations in general. A further distinction can be made between systems that rely on “classical” side-looking and pulsed SAR systems and alternative approaches that strike different paths to overcome the challenge of high-resolution wide-swath SAR imaging.

Concerning classical side-looking multi-channel SAR systems, the development started in 1991 with proposing a planar array antenna in elevation to suppress range-ambiguous returns [23] and the idea of splitting the antenna in azimuth direction to reduce azimuth ambiguities [24] followed by the combination of both [25]. Then, at the end of the 90s, the complexity of the systems increased and interest turned to more sophisticated processing strategies enabling so-called “software-defined radars”, where the multi-channel SAR signal is processed in azimuth, elevation or both dimensions [27]-[55]. In addition, innovative concepts relying on reflector antennas with feed arrays were discussed, which allow for digital processing in elevation [30], [62] as well as in azimuth dimension [61].

Starting in 2001, [29] and [31] present an innovative processing approach in elevation dimension. The so-called HRWS (High-Resolution Wide-Swath) SAR system is built on an array antenna consisting of multiple elements in elevation that allow on receive for a real-time scanning of a narrow beam in order to follow the echo of the transmitted signal on ground. This enables the suppression of range-ambiguous returns and ensures a high antenna gain. Follow-on investigations can e.g. be found in [33] and [38].

Regarding the azimuth dimension, [36], [40], and [48] specify dedicated algorithms for multi-channel SAR processing. The approach presented in [40] and further elaborated in [45] introduces a phase correction that is applied to the raw data to resample the signal in azimuth, while the technique presented in [36] proposes an algorithm based on a generalization of the sampling theorem that allows for the unambiguous recovery of the azimuth spectrum from multiple aliased sub-aperture signals. The method is elaborated in several follow-on papers [42]-[44], [46], [47], [52], [55] and later extended to burst mode operation [58]-[60], [65]. Finally, [48]-[50] bring up another space-time approach for application in small satellite constellations forming a sparse array. The basic idea is to minimize the combined power of white and colored noise by a trade-off between a spatial filtering of the azimuth signal to suppress Doppler ambiguities – which corresponds to the method presented in [36] – and a matched filter.

Besides, alternative concepts that do not directly build on conventional SAR have been proposed. One idea is based on steering multiple beams to different azimuth directions and assigning each of the corresponding footprints to a different slant range, as proposed by the multi-beam concepts of [20] and [21] and the squinted SAR configuration described by [22]. Further, a very general approach based on a multi-satellite constellation forming a sparsely distributed radar sensor is developed and an optimum way of processing in the space-time domain is derived in [26], [28], and [34]. Last but not least, [35] and [41] present the “SAR train” consisting of a multi-satellite constellation that is distributed in along-track direction and uses a spread spectrum waveform for transmission.

### 3.3 First System Concepts

Although system concepts and processing techniques are not always clearly separable, the present section focuses on the early developments of multi-channel systems while Section 3.4 summarizes different processing methods.

#### 3.3.1 Multiple Apertures in Elevation

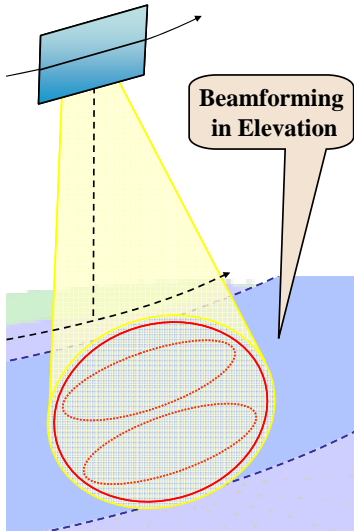


**Fig. 22. Adaptive null-steering in elevation to suppress range ambiguous returns.**

In 1991, Griffiths and Mancini [23] proposed a system consisting of an array antenna split in elevation (cf. Fig. 22). The overall dimension of this antenna is smaller than implied by the minimum antenna area constraint for SAR systems yielding a broad beam in elevation dimension that covers a wide swath on ground but at the same time gives rise to range-ambiguous echoes. The basic idea is now to apply the processing in terms of an appropriate weighting and combination of the signals received by the different apertures. This allows for suppressing range ambiguities by adaptively steering nulls in the antenna pattern in elevation to the directions of the ambiguous returns. Consequently, a widened swath is obtained. In a monostatic system the swath may become no longer contiguous as blind ranges are introduced when the receiver is switched off during transmission. Such restrictions could be overcome by bistatic radar systems allowing for simultaneous transmission and reception [37] and hence, short compact antennas could be used for high-resolution SAR systems with continuous wide area coverage.

#### 3.3.2 Displaced Phase Center Antenna in Azimuth

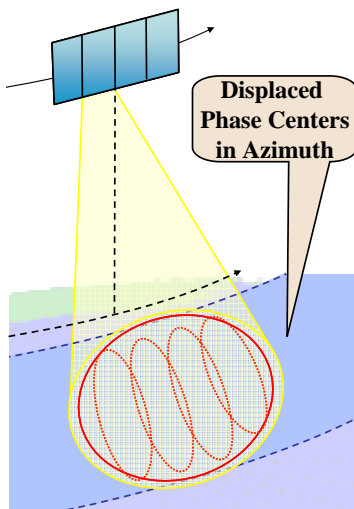


**Fig. 23. Multiple phase centers in azimuth to reduce azimuth ambiguities.**

A different approach was proposed in 1992 in [24]. The so-called Displaced Phase Center Antenna (DPCA) technique is based on dividing the receive antenna in along-track direction into multiple sub-apertures (cf. Fig. 23), each receiving, down-converting and digitizing the radar echo. Hence, for every transmitted pulse the system receives multiple pulses in the along-track direction. This means that additional samples are gathered, thus increasing the effective sampling rate on receive according to the number of sub-apertures. As a result, either the resolution can be improved while the swath width remains constant, or the *PRF* can be reduced without rising azimuth ambiguities or impairing the resolution, by this enabling a wider swath. In consequence, the system benefits from the whole antenna length regarding azimuth ambiguity suppression while azimuth resolution is determined by the dimension of a single sub-aperture, thus decoupling the hitherto restrictions for high-

resolution wide-swath imaging, as will be discussed in detail in Section 4.1. Note that this technique proposes to recover the azimuth signal by simply interleaving the samples of the different receiving channels without any further processing. As will be shown in Chapter 4, this imposes a stringent timing requirement on the system regarding the relation between sensor velocity,  $PRF$  and antenna length. These parameters have to be adjusted in order to obtain a signal that is equivalently sampled as a single-aperture signal of the same effective sampling rate. Unfortunately, this constraint will be unavoidably violated, as a system cannot be operated with only a single  $PRF$ . As a result, the sample positions deviate from the ideal positions entailing a degraded performance.

### 3.3.3 Quad Array Antenna

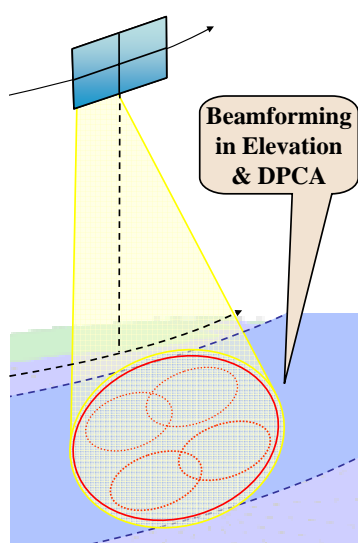


**Fig. 24. Combination of adaptive null-steering in elevation and multiple phase centers in azimuth.**

The Quad Array approach presented in [25] is based on an antenna split into two rows and two columns yielding a four-element array as shown in Fig. 24. Basically this concept can be understood as a combination of the two approaches presented before as the displaced sub-apertures in azimuth are complemented by multiple sub-apertures in elevation. This idea combines the advantages of gathering additional samples in azimuth to suppress azimuth ambiguities and simultaneously enabling an enlarged swath for a fixed  $PRF$  as resulting range ambiguities are suppressed by an adequate null-steering of the antenna pattern in elevation. As already mentioned above, the proposed system in elevation will result in an imaged swath with blind ranges that are introduced when the receiver has to be switched off for transmission. Further, as mentioned in the section on the DPCA method, the system underlies the stringent timing constraint to ensure a uniform spatial distribution of the gathered samples in azimuth dimension.

## 3.4 Processing Strategies

Subsequently, attention is turned from the system concepts to the further development of the processing strategies of a multi-channel SAR signal, both in elevation and in azimuth. Depending on the available data rate and data storage capacities, the processing is either to be conducted directly in real-time on board of the sensor or can be carried out on ground using the stored signal. While the on-board processing offers the possibility to combine the signals of a large number of individual receiver channels, a prior storage of the signals allows for a complete a-posteriori and consequently very flexible and reconfigurable processing.

Although the techniques are derived and developed either for a single-platform system or multi-satellite systems, it should be noted that the algorithms are in general applicable to both approaches, though entailing different challenges.

### 3.4.1 Scan-on-Receive in Elevation (SCORE)

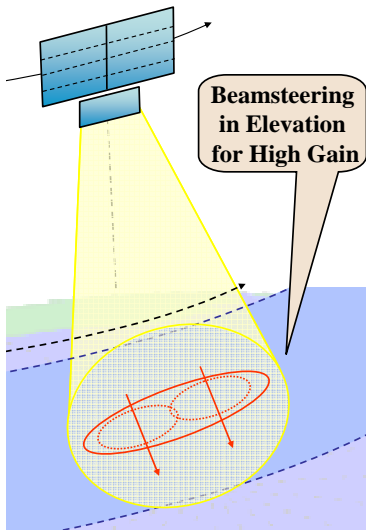


**Fig. 25. Real-time beam scanning in elevation to suppress range ambiguities and provide high gain.**

The High-Resolution Wide-Swath SAR (HRWS SAR) system introduced in [29] and established in several follow-on publications [31], [33], [38] is based on an array antenna split into a number of azimuth panels, each sub-divided into multiple elements in elevation (cf. Fig. 25). This allows for combining multi-channel sampling in azimuth with a time-variant beamsteering approach in elevation. In the suggested system, particular attention is only turned to the elevation dimension while in azimuth the different channels are only interleaved without any processing.

The processing concept combines the echoes from the sub-apertures in elevation in a way to form a narrow beam in elevation which “scans” the ground in real-time in order to follow the reflected radar pulse as it travels on the ground. This “scan-on-receive in elevation” (SCORE) enables the coverage of a wide swath by using a large receiver aperture with high gain. Hence the system is capable of compensating the unavoidably poor gain of a passive large area illuminator and to provide a sufficient suppression of range-ambiguous returns. However, this technique requires

knowledge of the observed terrain topography, because otherwise a mispointing of the narrow elevation beam may occur, resulting in severe gain loss [64]. Another important issue is the lack of any azimuth processing strategy. Although relying on an array antenna in azimuth, the gathered samples in azimuth are only interleaved and no further processing is applied entailing a degraded performance if the system is operated with a non-optimum *PRF*. The application of an appropriate processing algorithm – as will be proposed in Chapter 5 – can solve this problem.

Specific aspects of the HRWS system concept have been investigated in detail in several follow-on studies [51], [52].

### 3.4.2 Multi-Channel Reconstruction Algorithm in Azimuth

This processing concept of the multi-channel azimuth signal was first proposed in [36]. It is based on a generalization of the sampling theorem, which states that a signal spectrum can be unambiguously reconstructed if the Shannon-Nyquist theorem is fulfilled in average without requiring equally spaced samples in space-time [72], [73]. The technique describes the signal acquisition of a multi-channel SAR system by a system of linear filters. The corresponding set of linear equations then enables to determine a set of weighting functions which allow for the unambiguous recovery of the formerly aliased azimuth spectrum. It will be derived and investigated in detail in Chapter 5. Together with [40] – and apart from [26] which treats the subject of non-uniform sampling in a general way – this concept was the first to address the inconveniences arising from non-uniformly spaced samples in azimuth dimension. But in contrast to [40], it allows for effectively solving the problem of azimuth ambiguities as will be seen from the system performance calculations (cf. Chapter 7).

### 3.4.3 Multi-Channel Phase Correction in Azimuth

First presented in [40] and elaborated in [45], this method is based on an analysis of the multi-channel signal's phase compared to the phase of a monostatic and uniformly sampled signal. This yields a Doppler frequency dependent phase difference between the multi-channel signals and the monostatic signal. Hence, by applying an appropriate phase correction to the data of each individual channel, the phase of the multi-channel signal is adjusted in a way such that the resulting phase corresponds to the monostatic and uniformly sampled signal.

### 3.4.4 Minimum Variance Distortionless Beamformer

Another space-time approach for application in small satellite constellations forming a sparse array is brought up in [48]-[50]. Similar to classical STAP (Space-Time Adaptive Processing) approaches, the basic idea is to consider azimuth ambiguous energy as colored noise and then adapt the processing to minimize the combined power of white and colored noise by a trade-off between a spatial filtering of the azimuth signal to suppress azimuth ambiguities and a matched filter to optimize the *SNR* with respect to white noise. The azimuth ambiguities are suppressed by the adaptive adjustment of the weighting coefficients of the single azimuth apertures to steer the nulls in the resulting joint antenna pattern to the angles corresponding to the ambiguous Doppler frequencies.<sup>10</sup> This approach for ambiguity suppression is combined with a matched filter, basically yielding the minimum variance distortionless beamformer as e.g. presented in [74] or [75].

In comparison to a mere ambiguity suppression, such a combined method yields an improved *SNR* at the cost of a degraded ambiguity suppression, which can be afforded if the ambiguities remain within the noise floor. Nevertheless, this requires the correct estimation of the ratio of ambiguous to white-noise power, and consequently this method is no longer data independent.

## 3.5 Alternative Approaches

To complete the overview of systems aiming at high-resolution wide-swath SAR imaging, it is necessary to mention two early approaches from 1979 and 1983 based on a SAR in “multiple beam” operation [20]-[22] that builds on an array antenna in a squinted configuration and two further multi-satellite concepts and their processing strategies. Different from the ones presented above, the subsequent methods are not based on classical side-looking SAR sensors with pulsed operation.

---

<sup>10</sup>As it will be shown in Appendix D, this adaptive null-steering is under certain approximations included in the multi-channel reconstruction algorithm introduced in 3.4.2 and described in detail in Chapter 5.

### 3.5.1 Multiple Beam SAR

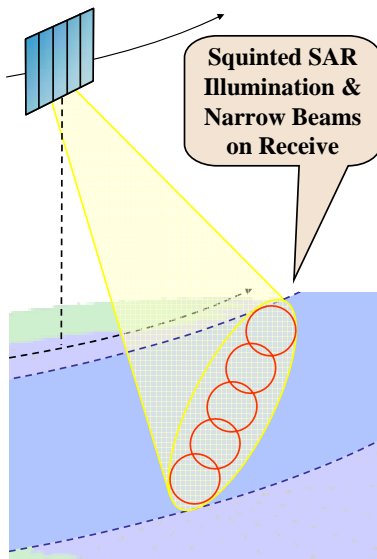


**Fig. 26. Squinted SAR configuration with narrow beams to image a wide swath.**

In contrast to classical SAR systems, the multiple beam SAR approach [22] is not strictly side-looking as the sensor is squinted around the axis perpendicular to the ground as indicated in Fig. 26. The squinted geometry is combined with a receiving antenna split into multiple sub-apertures in azimuth that allow for beamforming.

An appropriate coherent – either analog or digital – combination of the individual sub-apertures' signals enables to form multiple antenna beams. The respective footprints are determined by the overall antenna dimensions in azimuth and elevation which lead, respectively, to an illuminated area on ground much smaller than the wished swath. The squinted configuration of the antenna ensures that each of the formed sub-beams illuminates an area of different ground range distance, yielding – after stringing together the sub-beams – wide-swath coverage. In other words, the footprint of each beam steered to a different squint angle corresponds to a different sub-swath of the overall

imaged region. As the elevation dimension of the antenna is large compared to the imaged swath, range ambiguities are well suppressed thus allowing for a *PRF* high enough to suppress azimuth ambiguities. However, a problem of this approach is the coarsened resolution and impaired performance arising from the high squint angles that are needed. For details refer to [22].

A similar approach was introduced by Jain in 1979 [21]. The proposed SAR is also based on a multi-beam approach with each beam illuminating a separate range and azimuth footprint. In contrast to the method described above, multiple receive apertures are neither explicitly mentioned to be required nor excluded. Further, [21] proposes a slightly different illumination in a way that for a specific pulse the echoes from different beams are received at different interpulse periods. This results in an increased swath, but includes blind ranges corresponding to the times where the antenna transmits, according to 3.3.1.



### 3.5.2 Spread Spectrum Waveforms

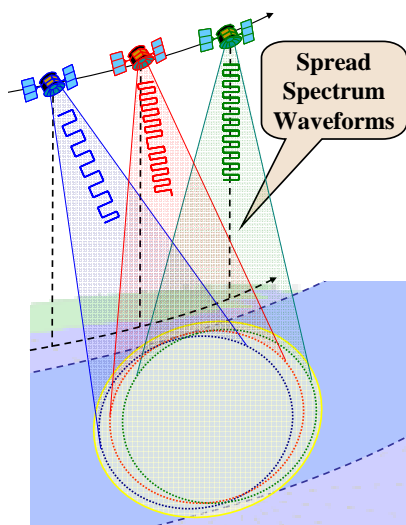


**Fig. 27. “SAR train” emitting spread spectrum waveforms.**

A further technique is presented in [35] and [41]. The “SAR train” consists of multiple individual satellites that are distributed in along-track direction and whose signals are combined coherently to improve the system performance. In this context, a fully active system is addressed as well as the special case of a single transmitter system in combination with multiple receivers. In a first step, pulsed operation with no specific processing of the individual signals is suggested. Thus a fixed relation between sensor positions, velocity, and *PRF* is required to ensure a uniform distribution of the received samples in azimuth. This imposes a stringent requirement on the accuracy of the individual satellite positions, as any violation entails non-equally spaced samples leading to severely degraded ambiguity suppression (cf. Chapter 4). As a new approach, continuous spread spectrum waveforms are suggested instead of transmitting “conventionally” pulsed waveforms. As indicated in Fig. 27, mutually uncorrelated pseudo-noise (PN) codes are emitted, which allow for relaxing the stringent timing constraint, as the ambiguous energy is no longer locally concentrated in peaks but spread. In the case of unrepeated PN code, this yields a constant pedestal of ambiguous energy spread over all image pixels, while for a repeatedly transmitted PN sequence, a comb-like distribution is obtained according to the sequence length. Finally, this technique ensures a coherent summation of the signal while the ambiguous parts only add incoherently. This yields improved ambiguity suppression in case of a non-optimum satellite spacing and, as explicitly pointed out in [35], even for distributed targets.

### 3.5.3 Sparse Array SAR Constellations

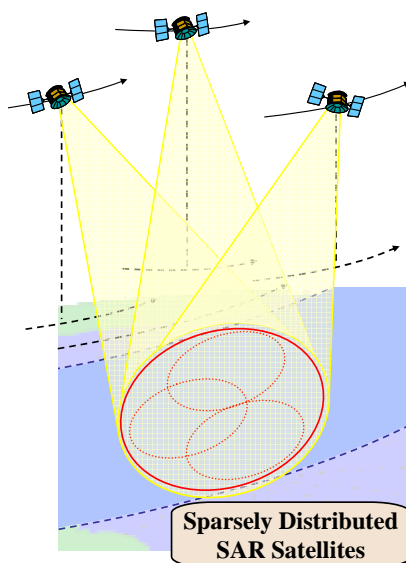


**Fig. 28. Sparse array configuration of multiple satellites.**

A more general approach is proposed in [26] and further investigated in a couple of follow-up publications as e.g. [28] and [34]. The concept considers an arbitrarily distributed spaceborne array of radar satellites that do not necessarily build a formation that is aligned in along-track dimension (cf. Fig. 28). The satellites are then regarded as a sparse array of antennas that, in addition to range-Doppler data, collect also angle-of-arrival information. This additional independent information enables wide-swath imaging with enhanced resolution. The processing of the irregularly spaced and sparsely distributed samples of the array then requires a space-time minimum mean-squared error (MMSE, i.e. Wiener) estimator as traditional approaches like matched filtering typically do not yield adequate imaging results.



## 4 Multi-Channel SAR in Azimuth

In the following, the focus is turned to the azimuth signal of multi-channel SAR as the work concentrates on these aspects. Firstly, this chapter introduces the principle of multiple signal reception in azimuth dimension and elaborates how this allows for overcoming the restrictions of single-aperture SAR architectures. Then, Section 4.2 derives the multi-channel impulse response in azimuth and shows the relation to single-aperture SAR. This is followed by Section 4.3, which recalls and derives basic relationships between the sensor geometry and system parameters and how this determines the spatial distribution of the acquired signal (“spatial sampling”).

### 4.1 Multi-Channel Reception in Azimuth

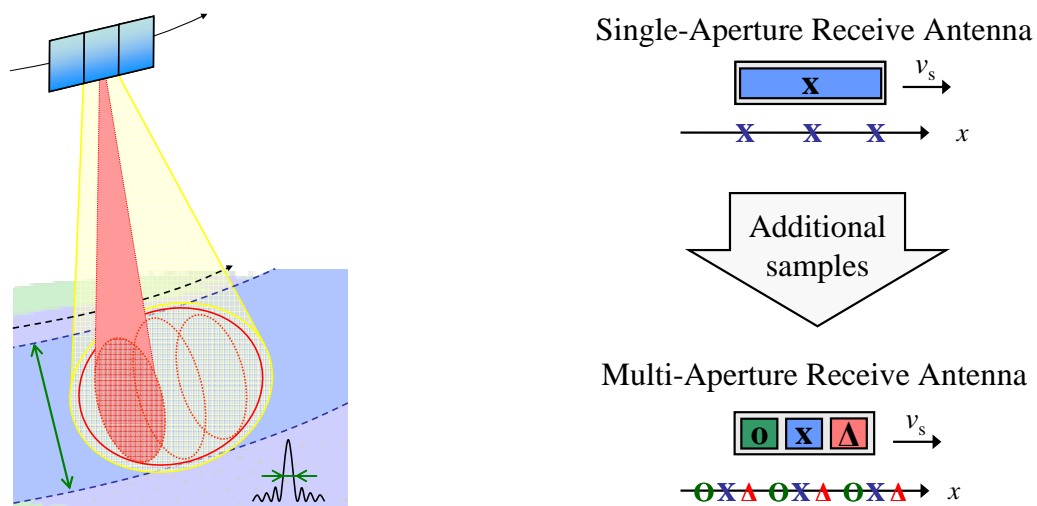


**Fig. 29. Left:** Multi-channel azimuth system enabling high-resolution wide-swath imaging. **Right:** Azimuth samples gathered by a single-aperture system (top) and increased sampling rate obtained for the same *PRF* with multiple receive apertures (bottom). The spacing of the gathered samples is given by half of the Rx phase center distance as will be derived in Section 4.3.

Multi-channel SAR systems in azimuth have a single transmit aperture and a receiving antenna that is subdivided into  $N$  individual apertures in azimuth dimension (cf. Fig. 29, left). Each of the receive apertures and the transmit antenna illuminate the same area on ground. Consequently, for each transmitted pulse such a sensor receives a number of  $N$  pulses at mutually dis-

placed positions as illustrated in the right part of Fig. 29. This means that additional samples are gathered along the synthetic aperture and as a result, the effective sampling rate of the azimuth signal is increased to  $N \cdot PRF$  while the transmit  $PRF$  remains unaltered. Recalling the limitation of conventional systems, this means that (20) remains valid regarding the range-ambiguous returns, but the necessary minimum  $PRF$  to fulfill the Nyquist criterion decreases by a factor of  $N$  according to (23).

$$N \cdot PRF \geq B_{az} \quad (23)$$

Compared to a mono-aperture system, transmit  $PRF$  and effective sampling rate are “decoupled” by a factor of  $N$ . Consequently, for the same  $PRF$  an  $N$ -times higher Doppler bandwidth can be sampled allowing for an improved geometric resolution while keeping the range ambiguities constant. Or, alternatively, the  $PRF$  can be reduced by  $1/N$  without an increase of azimuth ambiguities and degradation of the resolution while increasing the unambiguous slant range by a factor of  $N$  thus enabling the imaging of a wider swath.

Analogously to the figure of merit for conventional systems (cf. Section 2.4), (23) in combination with (18) allows for deriving the figure of merit for a multi-channel system, which is relaxed by a factor of  $N$ :

$$\frac{W_g}{\delta_{az}} < \frac{N \cdot c_0}{2 \cdot \sin(\Theta_i) \cdot 0.89 \cdot v_g} \quad (24)$$

As will be explained in detail in the following sections, the spatial distribution of the gathered samples has to be accounted for and the above presented “decoupling” by a factor of  $N$  is only valid without restrictions for a specific relation between antenna dimensions and  $PRF$ . In any other case, an additional processing step is required in order to achieve a coherent combination of the  $N$  sub-sampled and hence aliased channels to a single output signal sampled with  $N \cdot PRF$  and free of aliasing. Due to restrictions imposed by the timing, it is in general not possible to operate a SAR system with only a single  $PRF$  as for example certain  $PRF$  values would require temporally coinciding transmission and reception, which is not possible. Consequently, the application of an appropriate digital processing network is mandatory for the successful operation of a multi-channel SAR system and thus the multi-channel system block diagram modifies to Fig. 30: Each of the  $N$  receiver channels’ signals is mixed, digitized and stored. Then, a posteriori, digital processing (“Multi-Channel Azimuth Processing”) is carried out by a joint spatiotemporal processing of the recorded sub-aperture signals, before classic monostatic SAR algorithms are applied to focus the signal. In terms of the joint antenna pattern resulting from the weighted combination of the individual channels, this can be interpreted as the formation of narrow “virtual” – i.e. digitally formed – beams that are used to gain supplementary information about the direction of arrival of the backscattered signals (Fig. 30, right). As all processing is done a posteriori, multiple arbitrary beams can be formed one after another. In simple words, the azimuth processing aims at combining  $N$  input channels – each sub-sampled with  $PRF$  and aliased – to a single output channel of  $N \cdot PRF$  that is free of aliasing.

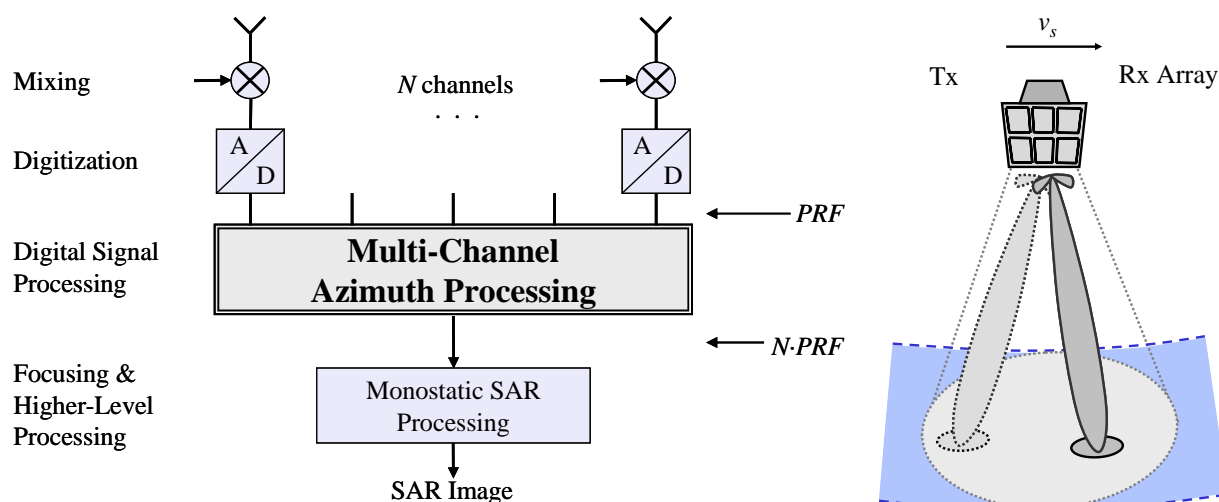


**Fig. 30. Multi-channel azimuth system with formation of different narrow beams (right) and corresponding system block diagram (left): Each aperture is interpreted as an individual channel whose signals are digitized and stored before they are combined coherently a posteriori in a digital signal processing stage.**

A suited multi-channel processing algorithm, which allows for relaxing the imposed constraints on system design and operation will be presented and analyzed starting from Chapter 5.

## 4.2 Multi-Channel Impulse Response and Quadratic Approximation

In conventional mono-aperture SAR, the varying path length and the resulting phase modulation of the signal (cf. (1) and (9), respectively) are determined by twice the distance between sensor and target (cf. Fig. 31, left). In a multi-channel configuration, transmitter and receiver are separated and consequently the way from the transmitter to the target and the way back are different and the spacing between the transmit (Tx) and receive (Rx) aperture has to be taken into account (cf. Fig. 31, right).

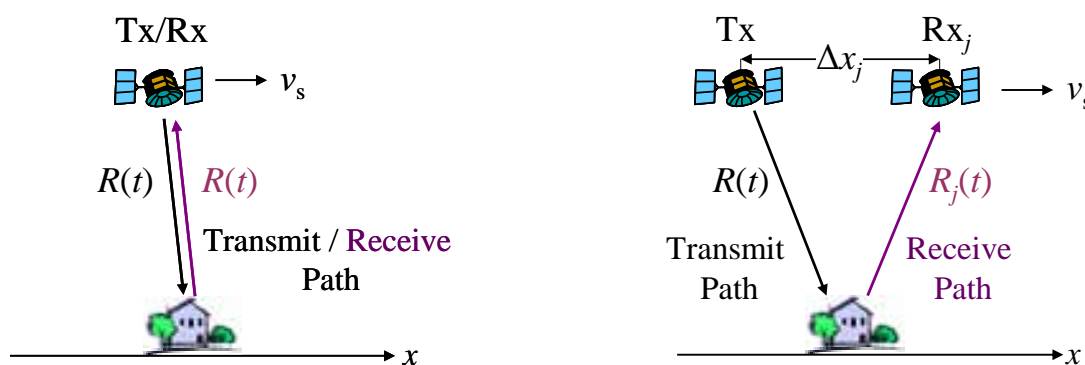


**Fig. 31. Transition from the monostatic path length (left) to the multi-channel path, where the receive path changes to  $R_j(t)$  as the Tx-Rx spacing given by  $\Delta x_j$  has to be considered (right).**

As mentioned, focus is on azimuth dimension. Consequently, along-track separations between transmitter and receiver will be considered and the impact on the signal model will be derived in analogy to the monostatic signal model of Chapter 2.

For a given receiver  $j$  separated by  $\Delta x_j$  in azimuth from the transmitter, the azimuth response  $h_{s,j}(t)$  for a point-like target at azimuth position  $x=0$ , minimum slant range  $R_0$  and for a carrier wavelength  $\lambda$  is described by (25). The phase of  $h_{s,j}(t)$  is determined by the lengths of transmit and respective receive path  $j$  which are given by  $R(t)$  and  $R_j(t)$ , respectively.

$$h_{s,j}(t) = \exp\left[-j \cdot \frac{2\pi}{\lambda} (R(t) + R_j(t))\right] \quad (25)$$

With the assumption of the same radius for both the transmit and receive aperture track, the relation between  $R(t)$  and  $R_j(t)$  is defined as follows:

$$R_j(t) = R\left(t - \frac{\Delta x_j}{v_s}\right) \quad (26)$$

In a next step, the joint Tx/Rx $_j$  antenna patterns in azimuth defined by  $a_j(t)$  are taken into account. The respective Fourier transforms are given by  $A_j(f)$ , where  $f$  denotes Doppler frequency. As a homogeneous scene of reflectivity  $u_s(t)$  and  $U_s(f)$ , respectively, is assumed, the azimuth frequency envelope of the SAR signal at channel  $j$  is also given by  $A_j(f)$ . This leads to the following expression for a multi-channel SAR system, where  $H_{s,j}(f)$  represents the Fourier pair of the impulse response function  $h_{s,j}(t)$ , and  $U_j(f)$  describes the received SAR signal at channel  $j$ .

$$U_j(f) = U_s(f) \cdot A_j(f) \cdot H_{s,j}(f) \quad (27)$$

Transferred to a block diagram, one obtains:

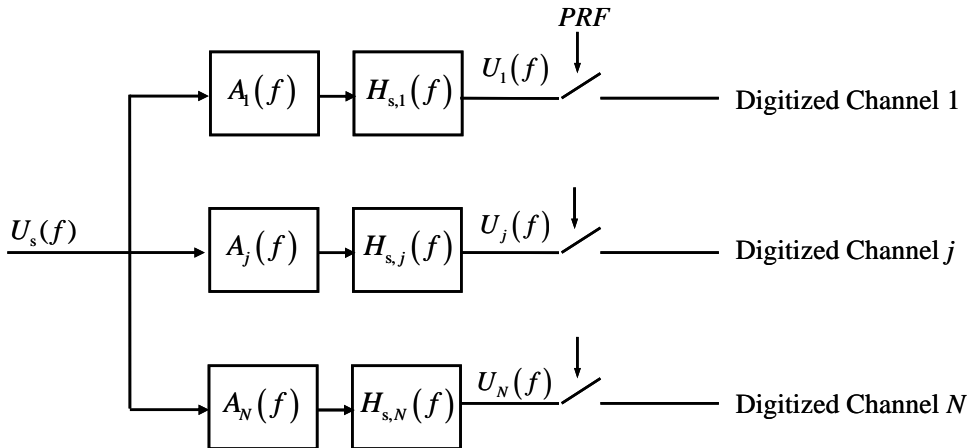


**Fig. 32. Block diagram of a multi-channel SAR where the filter function  $H_{s,j}(f)$  and the azimuth signal envelope  $A_j(f)$  characterize the respective channel  $j$  in Doppler domain, leading to a SAR signal  $U_j(f)$ . The “input” signal  $U_s(f)$  gives the scene reflectivity.**

Taylor expansion of both paths from (25) to the order of two yields the quadratic approximation of the multi-channel impulse response function in azimuth.

$$h_{s,j}(t) \cong \exp\left[-j \cdot \frac{4\pi}{\lambda} R_0\right] \cdot \exp\left[-j \cdot \frac{v_g}{v_s} \frac{\pi \cdot \Delta x_j^2}{2 \cdot \lambda \cdot R_0}\right] \cdot \exp\left[-j \cdot \frac{2\pi \cdot v_g \cdot v_s}{\lambda} \frac{\left(t - \left(\frac{\Delta x_j}{2 \cdot v_s}\right)\right)^2}{R_0}\right] \quad (28)$$

Comparing (28) to the approximated monostatic impulse response  $h_s(t)$  defined by (12) and (13), one recognizes that the multi-channel point target response evolves from the monostatic response  $h_s(t)$  by

1. a constant phase shift  $\Delta\varphi_j = -\pi \cdot v_g \cdot \Delta x_j^2 / (2 \cdot v_s \cdot \lambda \cdot R_0)$  and
2. a time delay  $\Delta t_j = \Delta x_j / (2 \cdot v_s)$ .

As a result, the multi-channel impulse response function in azimuth can be rewritten as:<sup>11</sup>

$$h_{s,j}(t) \cong h_s(t - \Delta t_j) \cdot e^{j\Delta\varphi_j} \quad (29)$$

In Doppler frequency domain, this relation between monostatic impulse response  $H_s(f)$  and the multi-channel response of channel  $j$ ,  $H_{s,j}(f)$ , is described by a simple multiplication with the filter  $H_j(f)$ , where  $H_s(f)$  and  $H_j(f)$  are the Fourier pairs of  $h_s(t)$  and  $h_{s,j}(t)$ , respectively (cf. (30)).

$$H_{s,j}(f) \approx H_j(f) \cdot H_s(f) \quad (30)$$

The multi-channel response can hence be separated into the influence of the multi-channel system described by  $H_j(f)$  and the conventional SAR impulse response given by  $H_s(f)$ . Transferring (29) to Doppler frequency domain,  $H_j(f)$  consists of the constant phase  $\Delta\varphi_j$  and a phase ramp corresponding to the shift by  $\Delta t_j$  in time domain.

$$H_j(f) = \exp\left[-j \cdot \underbrace{\frac{v_g}{v_s} \cdot \frac{\pi \cdot \Delta x_j^2}{2 \cdot \lambda \cdot R_0}}_{\Delta\varphi_j}\right] \cdot \exp\left[-j \cdot 2\pi \cdot f \cdot \underbrace{\frac{\Delta x_j}{2 \cdot v_s}}_{\Delta t_j}\right] \quad (31)$$

Accordingly, a single branch of the block diagram simplifies as follows:

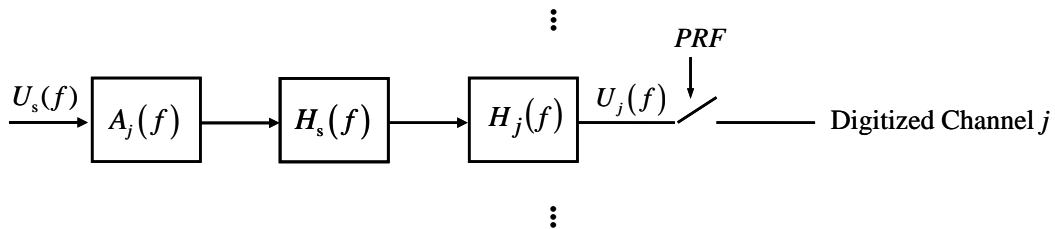


**Fig. 33. Block diagram of branch  $j$  after quadratic approximation. The impulse response function  $H_{s,j}(f)$  is expanded into the monostatic impulse response function  $H_s(f)$  and a “channel function”  $H_j(f)$ .**

<sup>11</sup>Although the quadratic approximation of (28) is not always applicable without restrictions, the derived expression (29) which relates mono- and multistatic range histories by a time shift and a constant phase is valid in all considered scenarios. For a detailed discussion refer to Appendix C.

Further, for single-platform systems, the same azimuth characteristic can be assumed for each channel  $j$  and consequently  $A_j(f)$  simplifies to  $A(f)$  and its time domain representation  $a(t)$ . Recalling Fig. 12, filtering of the scene with  $A(f) \cdot H_s(f)$  yielded the monostatic SAR signal in Doppler domain,  $U(f)$ , with its time domain representation  $u(t)$ . Hence, the description of a conventional SAR – given by  $A(f)$ ,  $H_s(f)$  and  $U(f)$  – is decoupled from the characterization of the multi-channel system defined by  $H_j(f)$ . Finally, this yields the block diagram shown subsequently.

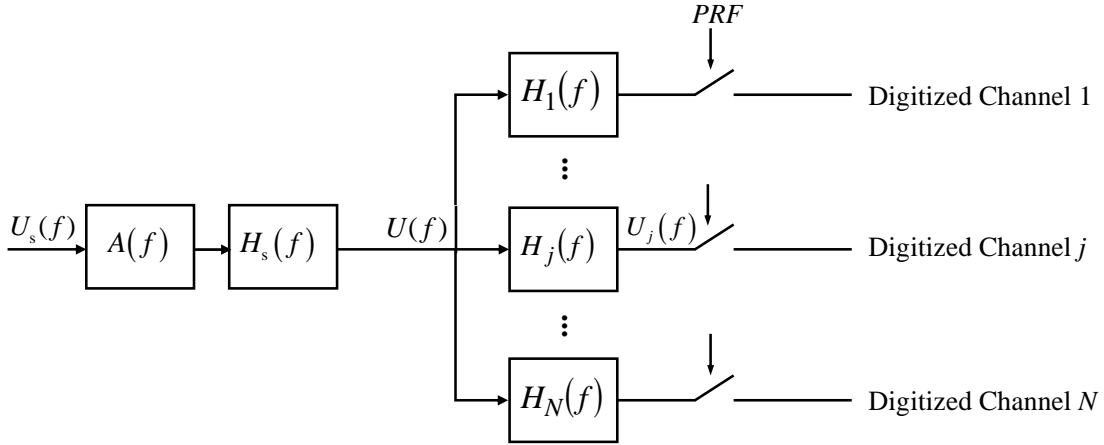


**Fig. 34. Block diagram of a multi-channel SAR interpreted as a monostatic SAR system followed by a set of  $N$  linear filter functions  $H_j(f)$ . In Doppler frequency domain, each  $H_j(f)$  represents the relationship between the monostatic SAR signal  $U(f)$  and the respective multi-channel SAR signal  $U_j(f)$ .**

Analytically, this means that the multi-channel SAR signal of channel  $j$  – denoted by  $U_j(f)$  and  $u_j(t)$  – is related to  $U(f)$  and  $u(t)$  by  $H_j(f)$  according to (32) and its time domain representation  $h_j(t)$ , respectively.

$$U_j(f) = H_j(f) \cdot U(f) \quad (32)$$

### 4.3 Spatial Sampling

In order to provide a better understanding, the present section recalls and derives the basic relationships of multi-channel systems regarding the spatial positions in along-track (“azimuth”) dimension of the gathered information (“spatial sampling”). The relation between transmit and receive aperture position and the location of the corresponding sample is derived and the dependencies on system parameters are given. Finally, special sampling scenarios for a train of pulses are presented.

#### 4.3.1 Effective Phase Center, Virtual Sample Position and Spatial Sampling

The phase center of an antenna or aperture represents the “effective” position of the transmitted or received signal and it is in general situated in the center of area of the aperture. In conven-



tional systems usually the same antenna is used for transmission and reception and consequently the phase center of both are the same. As mentioned in the preceding sections, in a multi-channel system a single transmit antenna is combined with a number of receiving channels and hence, in general, the positions of transmitter and receiver do not coincide. As derived above, the impulse response function of such a system evolves from a monostatic one by a time shift corresponding to half the spacing between transmitter and receiver and a constant additional phase (cf. (29)). Hence, these systems of spatially separated transmit and receive apertures can be approximated by a virtual system where both coincide and lie midway between the transmitter and respective receive aperture and a constant phase term is added. This position is called “effective phase center” and represents the spatial position of the received signal of the respective transmitter-receiver pair. As derived in Section 4.2, this interpretation of the effective phase center is based on a Taylor expansion of the path length from the transmitter to the target and back to the receiver. It should be kept in mind that the validity of the effective phase center approximation midway between transmitter and receiver depends on the accuracy of the Taylor expansion to describe the path length. This approximation is very good in single-platform systems, but it might become invalid for very large separations between transmit and receive antenna.

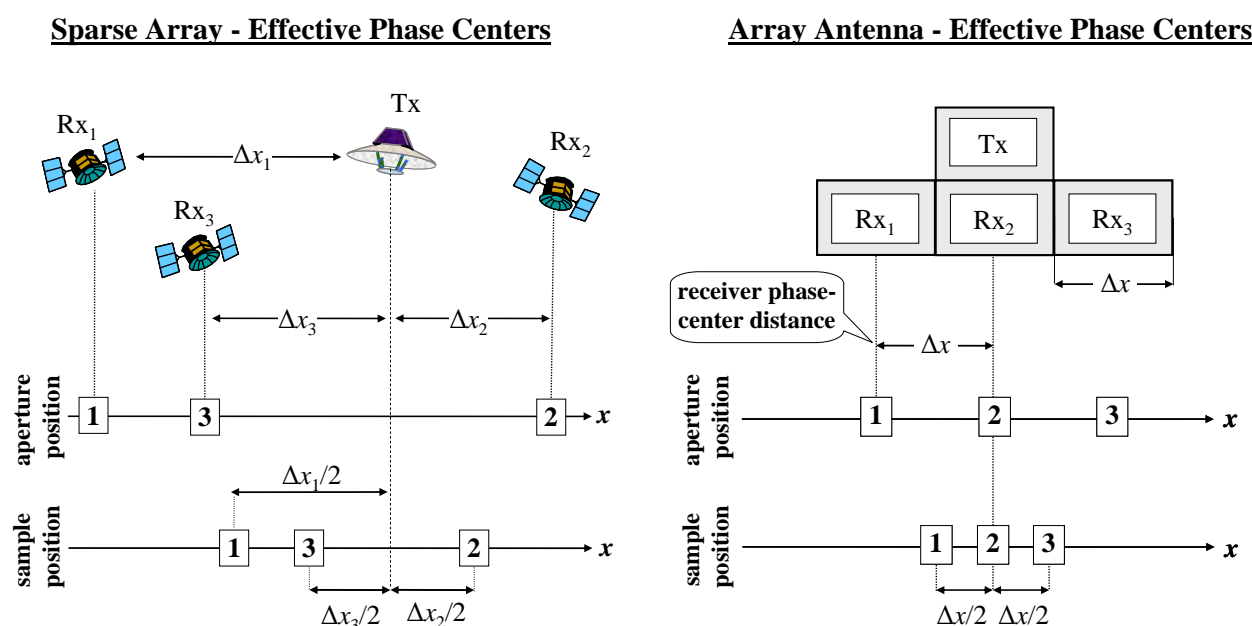


**Fig. 35. Position of transmit (Tx) and multiple receive apertures (Rx<sub>j</sub>) in azimuth direction  $x$  and corresponding effective phase center giving the spatial sample position. The sample position is determined by the distance  $\Delta x_j$  between Tx and respective receiver Rx<sub>j</sub>. Right shows a single-platform system while left gives a multi-satellite configuration.**

The positions of the effective phase centers in azimuth of a single-platform system with exemplary 3 receivers – denoted from Rx<sub>1</sub> to Rx<sub>3</sub> – are shown in the right part of Fig. 35. In this case the spacing of the samples is equal to half of the receive aperture spacing  $\Delta x$ , which corresponds also to the size of a single receive aperture. Note, that all adjacent samples are spaced equally as all adjacent receive apertures show the same distance. In contrast, in a sparse array system the offset between adjacent receivers is no longer constant and consequently the resulting

sample positions are distributed in azimuth with non-equal spacing, which is determined by the different distances  $\Delta x_j$  of the respective receiver  $j$  to the transmitter (Tx) (cf. Fig. 35, left).

Consider now the system moving with constant velocity  $v_s$  and the transmitter emitting a train of pulses with a pulse repetition frequency  $PRF$ . Then the spatial distribution of samples (“spatial sampling”) as shown in Fig. 36 is obtained. For every transmitted pulse,  $N$  signals are received whose positions in azimuth are determined by the positions of the receivers with respect to the transmitting aperture and consequently the distances of the samples received for a single pulse are defined by the spacing between the receiving apertures. Further, the system travels in along-track the distance of  $v_s/PRF$  between successive transmit pulses and as a consequence the spacing of subsequent samples corresponding to a specific receive aperture is determined by the system parameters  $v_s$  and  $PRF$ . Note, that for a sparse array configuration a receiver-spacing larger than the distance between subsequent pulses might cause spatially adjacent samples which neither originate from adjacent receivers nor from the echo of the same transmit pulse (cf. Fig. 36, left). In the following, the relation between spatial sampling and the system parameters as aperture position, sensor velocity and  $PRF$  is derived and the most relevant cases are presented.

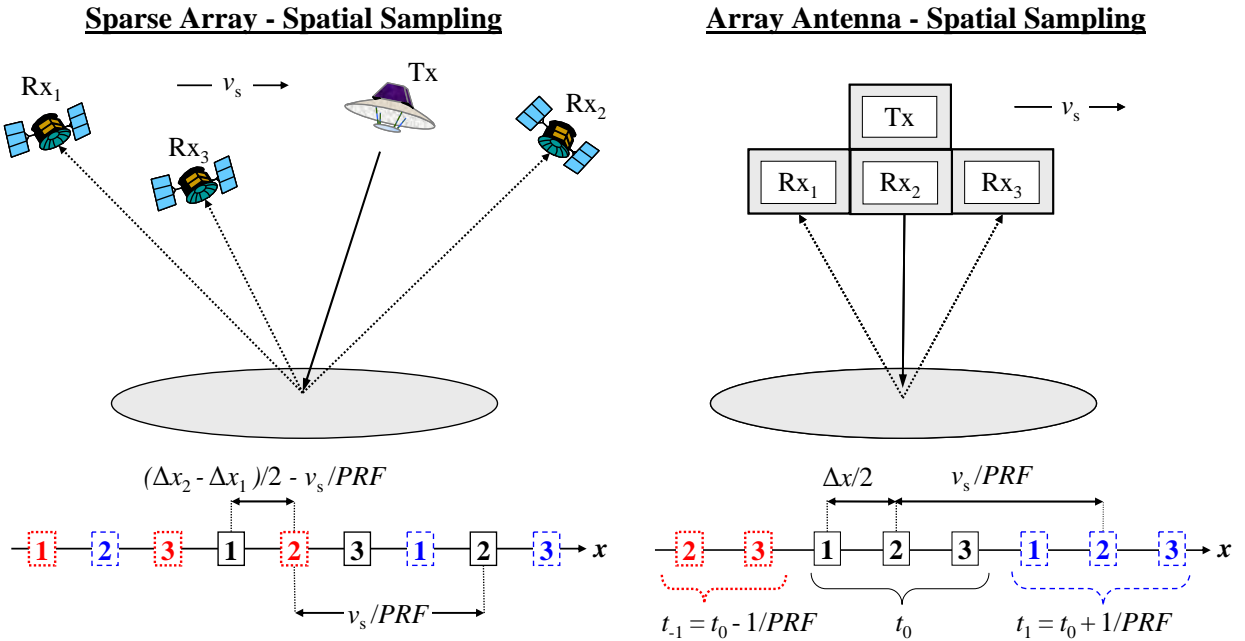


**Fig. 36.** Spatial sampling for three subsequent pulses transmitted at  $t_{-1}$  (dotted red),  $t_0$  (solid black) and  $t_1$  (dashed blue) for a single-aperture system (right) and a multi-satellite system (left). The intersample spacing for a single transmit pulse is determined by the aperture distance  $\Delta x$  while the distance between samples of subsequent pulses is given by the sensor velocity  $v_s$  and the  $PRF$ .

#### 4.3.2 Uniform Sampling

The optimum case is given by a scenario where all gathered samples are distributed uniformly along the synthetic aperture. In the general case of a sparse array of receive apertures, this means that the distance between adjacent receivers has to result in a phase center distance of  $1/N$ -th of the distance between subsequent pulses given by  $v_s/PRF$ . Hence, to ensure equally

spaced samples for a given  $PRF$  in a multi-satellite configuration moving with  $v_s$ , the following conditions for the along-track displacement of the receive apertures to the transmit aperture,  $\Delta x_j$ ,  $j \in \{2, \dots, N\}$  relative to the offset  $\Delta x_1$  of receiver 1 have to be fulfilled:

$$\Delta x_j - \Delta x_1 = \frac{2 \cdot v_s}{PRF} \left( \frac{j-1}{N} + k_j \right) \quad ; \quad k_j \in \mathbb{Z} \quad (33)$$

The integer  $k_j$  accounts for the fact that spatially neighbored samples might originate from temporally different transmit pulses. One recognizes that in general (33) possibly cannot be fulfilled for all receivers  $j$  at the same time and hence there might be no optimum  $PRF$  ensuring uniformly distributed samples. For a single-platform system with an array antenna, the along-track displacement between adjacent sub-apertures is constant and denoted by  $\Delta x$  and all  $k_j$  of (33) become zero. Consequently, (33) simplifies to:

$$\Delta x = \frac{2 \cdot v_s}{PRF \cdot N} \quad (34)$$

Taking into account that the overall antenna length in azimuth  $l_{az}$  is made up of  $N$  apertures, each of length  $\Delta x$ , the optimum  $PRF$  can be directly derived from system parameters according to (35). Equation (35) imposes a stringent requirement on the system as it states that to ensure equal spacing between all the samples in azimuth the  $PRF$  has to be chosen such that the SAR platform moves just one half of its antenna length  $l_{az}$  between subsequent radar pulses. This optimum  $PRF$  will be referred to as “uniform”  $PRF_{uni}$  as it fulfills the timing requirement for uniformly spaced samples in azimuth (“uniform sampling”).

$$PRF_{uni} = \frac{2 \cdot v_s}{N \cdot \Delta x} = \frac{2 \cdot v_s}{l_{az}} \quad (35)$$

A uniformly sampled data array represents the optimum case as it yields a data array equivalent to that of a single-aperture (“monostatic”) system operated with  $N \cdot PRF$  and hence conventional SAR algorithms can be applied to process the multi-channel SAR data. In reverse, any deviation from the relations of (33) and (35), respectively, will result in a non-equally sampled data array along the synthetic aperture (“non-uniform sampling”) that is no longer equivalent to a monostatic signal and cannot be processed by conventional monostatic algorithms without performance degradation. This means that classic multi-channel systems where the antenna is split in azimuth dimension either are subject to stringent operational requirements or need appropriate pre-processing algorithms to correct for perturbations caused by non-uniformly spaced samples. In general, timing constraints do not allow for operating a system with a single  $PRF$  thus requiring suitable digital processing algorithms to the multi-channel signals (cf. Chapter 5).

### 4.3.3 Special Sampling Scenarios

To complete this section, two more special sampling scenarios are shortly presented. Firstly, certain  $PRF$  values may result in an interleaving of samples originating from different transmit pulses in a way such that again all samples are spaced equally, yielding a “uniform sampling of higher order” (cf. Fig. 37, left). In contrast to (33) this means that not with the subsequent pulse

but only after  $k$  pulses the first sample of the array has traveled half of the antenna length yielding other possible  $PRF$  values of uniform sampling that are denoted by  $PRF_{uni,k}$  and given by (36) a). Further, in this case it is required that no samples are located at the same azimuth position as ensured by the inequality for  $k$  given in (36) b), which excludes those values where samples coincide spatially.

$$PRF_{uni,k} = k \cdot \frac{2 \cdot v_s}{N \cdot \Delta x} = k \cdot PRF_{uni} \quad \text{a)}$$

$$k \neq \frac{p \cdot N}{m} \quad \text{where } m \in \{1, \dots, N-1\}; p, k \in \mathbb{N} \quad \text{b)}$$

A second case to be mentioned arises when samples of different transmit pulses received by apertures  $j$  and  $i$  coincide spatially as sketched in Fig. 37 on the right. This condition is defined generally in (37), where  $p$  and  $q$  denote the number of pulses after which the samples of channel  $i$  and  $j$  coincide, respectively. Equation (37) simplifies to (38) for a single-platform system yielding the respective  $PRF_{sgl}$  specified by  $m$  and  $n$ . Note that the spatial sampling in this case passes into uniform sampling if one of the coinciding channels is “switched off” and only a reduced number of channels is considered. In the example given in Fig. 37 this would mean skipping the samples corresponding to receiver 3, thus yielding a uniformly sampled system with a reduced number of  $N=2$  receive apertures.

$$\frac{\Delta x_i}{2} + p \cdot \frac{v_s}{PRF_c} = \frac{\Delta x_j}{2} + q \cdot \frac{v_s}{PRF_c}; \quad \text{where } p, q \in \mathbb{N} \quad (37)$$

$$PRF_{sgl,n,m} = \frac{2 \cdot v_s}{\Delta x} \cdot \frac{n}{m} = \frac{PRF_{uni}}{N} \cdot \frac{n}{m}; \quad m \in \{1, \dots, N-1\}; n \in \mathbb{N} \wedge n < m \cdot N \quad (38)$$

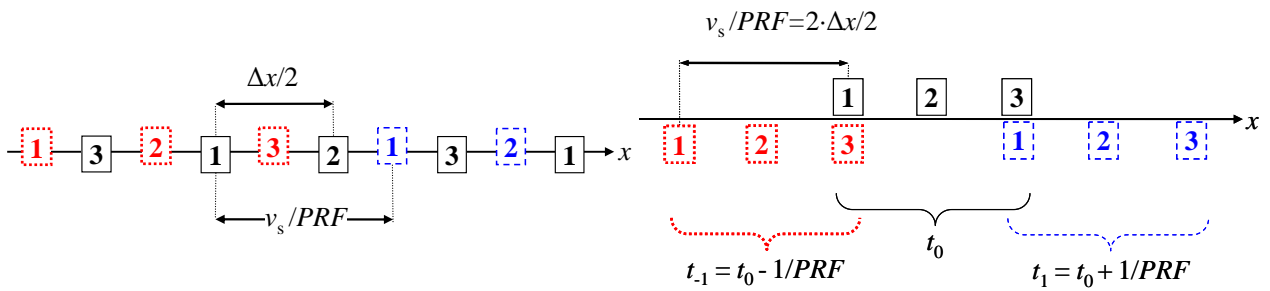


**Fig. 37.** Spatial distribution of samples in azimuth direction  $x$  originating from three subsequent transmit pulses separated by  $\Delta t = PRF^{-1}$  and emitted at  $t_{-1}$  (dotted red),  $t_0$  (solid black), and  $t_1$  (dashed blue) yielding interleaved uniform sampling (left) and spatially coinciding samples of channels 1 and 3 (right).

## 5 Multi-Channel Azimuth Processing: Reconstruction Algorithm

As presented in Chapter 3, most of the suggested systems so far propose to simply operate a multi-channel antenna in azimuth by interleaving the samples of the different receiving channels without further specific processing steps [16], [24], [25], [31]. As further elaborated in Chapter 4, this requires a stringent timing according to (35) to be fulfilled, in order to obtain a signal that is equivalent to a monostatic signal of  $N$  times the  $PRF$ . In any other case the sample positions deviate from the ideal positions, but they are treated as if the signal was sampled uniformly which leads to a degradation of the system performance (increased ambiguities, coarsened resolution, etc.) as it will be discussed in this chapter. In this case, further processing of the signal is required before conventional monostatic SAR algorithms are applied to focus the signal.

The present chapter is dedicated to a technique called *Multi-Channel Reconstruction Algorithm* that is suited to process multi-channel signals in azimuth. This algorithm is built on a generalized sampling theorem according to [72] and [73], and its first application to SAR data was proposed in [36]. The technique is based on solving a system of linear equations to unambiguously recover the formerly aliased azimuth spectrum even in case of non-uniformly spaced data samples. This means that constant performance of the multi-channel system is ensured also for non-optimum  $PRF$  values violating the timing requirement. This chapter starts with a detailed derivation of the algorithm and an illustrative approach to its principle in Sections 5.1 and 5.2, followed by regarding the proposed algorithm in the framework of STAP processing in Section 5.3. In a next step, the one-dimensional azimuth reconstruction is embedded in a two-dimensional processing scheme, proving its applicability for regular SAR processing (cf. Section 5.4). This is followed by an investigation of the algorithm's impact on signal power, residual ambiguous energy, and noise power, yielding analytic expressions for the azimuth ambiguity-to-signal ratio ( $AASR_N$ ) and variations of the signal-to-noise ratio ( $\Phi_{bf}$ ) in multi-channel systems (cf. Sections, 5.5-5.7). Based on the result for the  $SNR$  variation induced by the multi-channel processing, the well-known expression for the Noise Equivalent Sigma Zero ( $NESZ$ ) is extended to multi-channel SAR systems (cf. Section 5.8).

It should be noted that the algorithm has great potential for any multi-channel SAR system, be it a sparse array consisting of multiple distributed satellites or a single-platform system relying on the displaced phase center technique, like the high-resolution wide-swath (HRWS) SAR

[31] or the dual receive antenna approach with TerraSAR-X [17] or Radarsat-2 [16]. In the following, focus is turned a single-platform system; basic considerations on the characteristics of distributed systems are given in Section 5.4 and in the outlook in Chapter 10.

## 5.1 Theoretical Background

As introduced in Section 2.3, the SAR echoes obtained from the subsequently transmitted chirp pulses are interpreted as a discrete-time azimuth signal that is sampled with a frequency given by the  $PRF$ . According to the sampling theorem formulated by Nyquist and Shannon [71], this allows for a maximum azimuth (“Doppler”) bandwidth of  $PRF$  that can be recovered from the discrete-time data without loss of information. The sampling theorem can be illustratively interpreted by having a look at the signal spectra. According to signal theory, sampling with a frequency of  $PRF$  leads to a spectrum that consists of the periodic repetition of the original spectrum with a period defined by the sampling frequency. Consequently, only signal bandwidths  $B_{D,i}$  smaller than the sampling frequency result in a discrete-time Fourier transform of the signal where the individual spectra do not overlap and the original spectrum can be recovered by low-pass filtering (cf. Fig. 38, top). If  $B_{D,i}$  exceeds the  $PRF$ , sampling leads to an overlap of the spectra (cf. Fig. 38, bottom) making it impossible to separate the original spectrum from its repetition. As a result, information is lost. For a thorough discussion of discrete-time signals and processing, refer to e.g. [76].

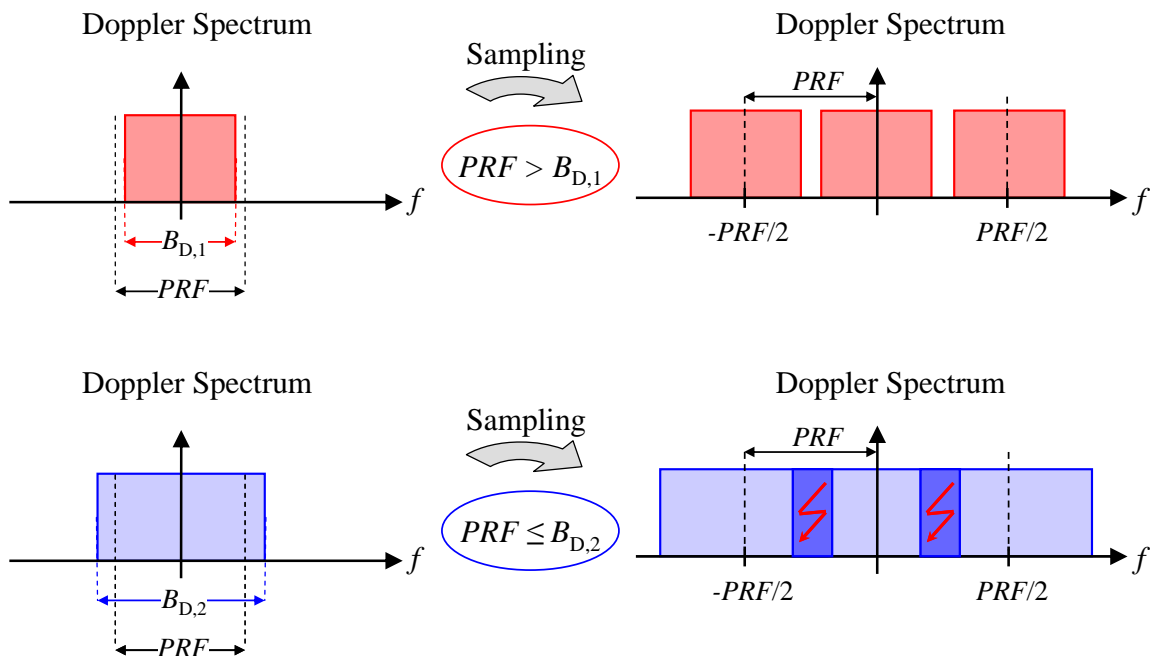


**Fig. 38. Illustration of Shannon-Nyquist sampling theorem. Top: A “properly” sampled signal spectrum ( $B_{D,1} \leq PRF$ ) which can be recovered as the discrete-time spectra can still be discerned. Bottom: Sub-sampled signal ( $B_{D,2} > PRF$ ) whose periodically continued spectra partly overlap (cf. red lightning) in discrete-time domain and can hence not be recovered without loss of information.**

The multi-channel reconstruction algorithm that will be derived in the following is founded on a generalization of the “classical” sampling theorem described in short words above. According to this generalization,  $N$  independent representations of a signal, each sub-sampled at  $1/N$  of the signal’s Nyquist frequency, allow for the unambiguous “reconstruction” of the original signal from the aliased Doppler spectra of the  $N$  representations. This means that any band-limited signal  $U(f)$  is uniquely determined in terms of the responses  $H_j(f)$  of  $N$  linear systems with input  $U(f)$  each, resulting in an output signal  $U_j(f)$ , sampled at  $1/N$ -th of the Nyquist frequency. The functions  $H_j(f)$  may be chosen in a quite general way, but not arbitrarily [72], [73]. In simple words, this means that it is sufficient to fulfill the Nyquist sampling rate in average, i.e. a sufficient number of samples per time is enough, independent from their spatial distribution as long as the samples do not coincide in space.

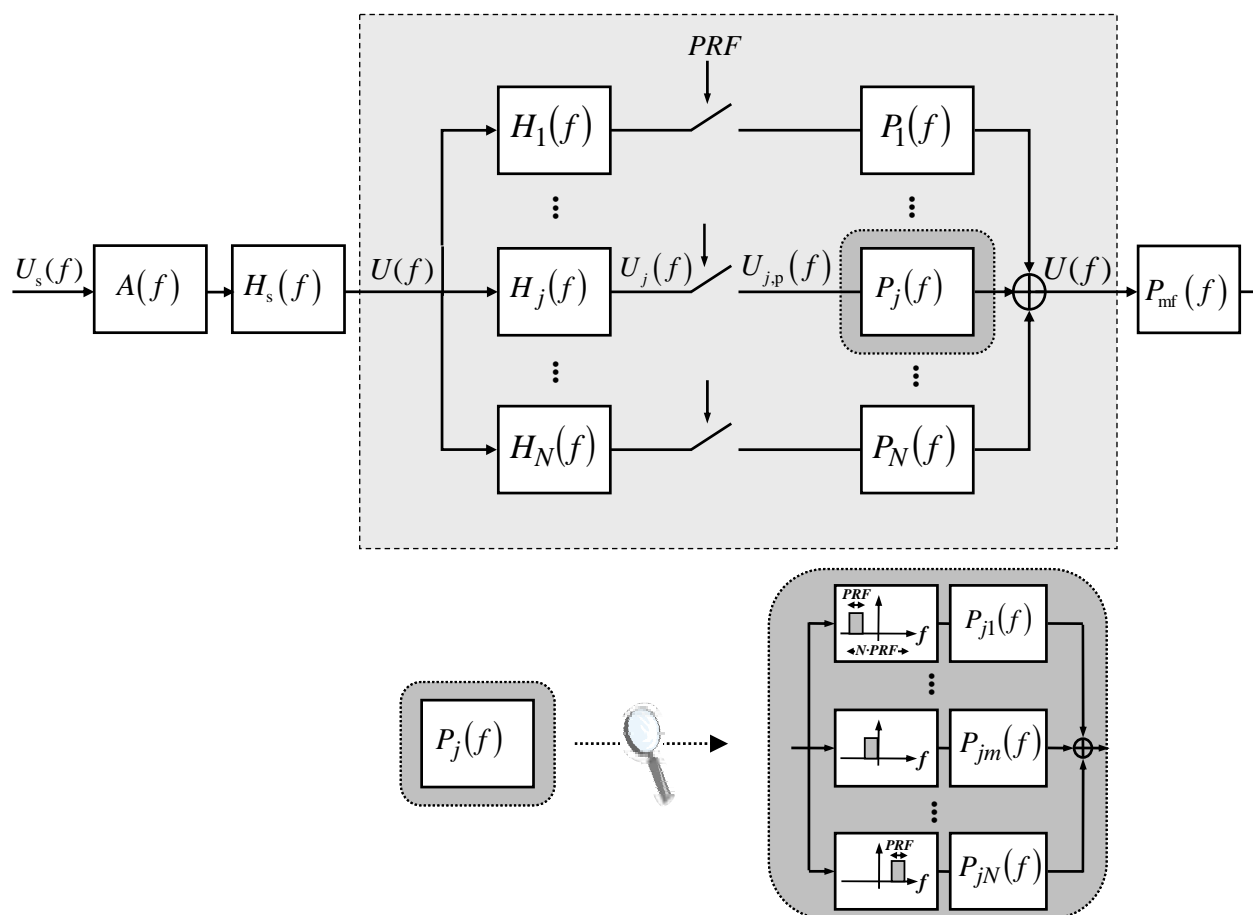


**Fig. 39. Top:** Block diagram of a multi-channel SAR system with “reconstruction” of  $N$  sub-sampled channels by filters  $P_j(f)$ . **Bottom (zoom):** Each  $P_j(f)$  consists of  $N$  bandpass filters  $P_{jm}(f)$  valid on a sub-band of width  $PRF$ .

Transferred to a multi-channel SAR system and applied to the system model originally introduced in Fig. 34 and extended to Fig. 39,  $U(f)$  gives the equivalent monostatic SAR signal. The functions  $H_j(f)$  represent the channel between the transmitter and each receiver  $j$  with respect to the monostatic impulse response yielding the multi-channel SAR signals  $U_j(f)$  according to (32). Note that in principle the complete multi-channel SAR signal model including the two-way

patterns of the respective channels can be used for reconstruction. This means that the channel functions  $A_j(f) \cdot H_{s,j}(f)$ , which relate  $U_s(f)$  and its representations  $U_j(f)$  according to (27), are used to calculate the reconstruction filters. In this case, not the SAR signal  $U(f)$  but the scene reflectivity  $U_s(f)$  is directly obtained, i.e. the focusing is already included in the reconstruction. For reasons of simplicity, only the quadratically approximated system model of Fig. 39 will be considered in the following.

After reception, each signal is sampled in azimuth by  $PRF$  and hence the maximum signal bandwidth is  $N \cdot PRF$  according to the effective sampling rate. A compact characterization of the whole system is then given by the system matrix  $\mathbf{H}(f)$ , that contains all channel representations  $H_j(f)$  shifted by integer multiples of the  $PRF$  according to (39).

$$\mathbf{H}(f) = \begin{bmatrix} H_1(f) & \cdots & H_N(f) \\ H_1(f + PRF) & \cdots & H_N(f + PRF) \\ \vdots & \ddots & \vdots \\ H_1(f + (N-1) \cdot PRF) & \cdots & H_N(f + (N-1) \cdot PRF) \end{bmatrix} \quad (39)$$

Then, as shown in [73], the inversion of  $\mathbf{H}(f)$  yields a matrix  $\mathbf{P}(f)$  that contains in its rows  $N$  functions  $P_j(f)$  that are decomposed by the columns in  $N$  functions  $P_{jm}(f)$ . Each  $P_{jm}(f)$  is defined on a sub-band  $m$  of width  $PRF$  around a center frequency  $f_{0,m} = (-N/2 + m - 1/2) \cdot PRF$  (cf. Fig. 39, bottom). The corresponding interval is denoted by  $I_m$ :

$$I_m = f_{0,m} \pm \frac{PRF}{2} = \left[ \left( -\frac{N}{2} + m - 1 \right) \cdot PRF, \left( -\frac{N}{2} + m \right) \cdot PRF \right] ; \quad m = 1, \dots, N \quad (40)$$

Consequently, all  $I_m$  make up the complete Doppler spectrum of the system and, accordingly, all  $P_{jm}(f)$  make up  $P_j(f)$ , where each function  $P_j(f)$  represents the filter for the multi-channel processing of channel  $j$ .

$$\mathbf{P}(f) = \mathbf{H}^{-1}(f) = \begin{bmatrix} P_{11}(f) & P_{12}(f + PRF) & \cdots & P_{1N}(f + (N-1)PRF) \\ P_{21}(f) & P_{22}(f + PRF) & \cdots & P_{2N}(f + (N-1)PRF) \\ \vdots & \vdots & \ddots & \vdots \\ P_{N1}(f) & P_{N2}(f + PRF) & \cdots & P_{NN}(f + (N-1)PRF) \end{bmatrix} \quad (41)$$

Note that in the considered case the matrix  $\mathbf{H}(f)$  is invertible as long as samples of different receive apertures do not coincide spatially. By investigating the properties of  $P_{jm}(f)$ , it is observed that the absolute value within each of the sub-bands  $I_m$  is not varying with Doppler frequency, i.e. the following holds true.

$$|P_{jm}(f)| = \text{const.} \quad (42)$$

The aliased frequencies in the Doppler spectra of the individual channels are then suppressed and consequently the original signal  $U(f)$  is recovered by filtering each channel  $j$  with its appropriate ‘‘reconstruction’’ filter  $P_j(f)$  and subsequent coherent combination of all weighted receiver channels (cf. Fig. 39). To complete Fig. 39, the conventional monostatic SAR focusing filter  $P_{jm}(f)$  is included. Note that the reconstruction filter functions  $P_j(f)$  vary for a given system with



the  $PRF$ , i.e.  $P_j(f, PRF)$  would be a more accurate notation. Nevertheless, for reasons of a succinct notation the explicit expression will be omitted, while keeping in mind the dependency on the  $PRF$ .

## 5.2 Illustration of Principle

In this section, an illustrative approach to explain the principle and limitations of the multi-channel reconstruction algorithm is given. Consider a system as shown in Fig. 39 with exemplary  $N=2$  apertures and  $U(f)$  describing a monostatic SAR signal, while  $U_j(f) = H_j(f) \cdot U(f)$  represents the received SAR signal at aperture  $j$ . At first, assume  $U(f)$  limited to  $[-PRF, PRF]$ . Then, Fig. 40 on the left shows the spectrum of the band-limited signal “seen” at the receiver  $j$  before sampling (top) and its periodic continuation after sampling with  $PRF$  (middle) yielding  $U_{j,p}(f)$ , given in (43). For convenience the notation  $U_{jk}(f) = U_j(f+k \cdot PRF)$  is introduced, where the index  $k$  indicates a shift by  $k \cdot PRF$  in Doppler frequency domain.

$$U_{j,p}(f) = \sum_{k=-\infty}^{\infty} U_j(f+k \cdot PRF) = \sum_{k=-\infty}^{\infty} U_{jk}(f) = \sum_{k=-\infty}^{\infty} U(f+k \cdot PRF) \cdot H_j(f+k \cdot PRF) \quad (43)$$

As can be observed, for any frequency, the sub-sampled and aliased signal consists of not more than two (in general  $N$ ) shifted and superimposed spectra, as not more than one spectrum (in general  $N-1$  spectra) of the periodic continuation overlaps with the original spectrum. Hence, the spectra  $U_1(f)$  and  $U_2(f)$  can be weighted and combined in such a way, that the component of the original spectrum is recovered, while the shifted component is cancelled. With  $P_{jm}(f)$  denoting the reconstruction filter for receiver  $j$  on the interval  $I_m$  (cf. Fig. 39), this requires the following equations to hold in the interval  $I_1$  (cf. Fig. 40, middle, left):

$$\begin{aligned} P_{11}(f) \cdot H_1(f) \cdot U(f) + P_{21}(f) \cdot H_2(f) \cdot U(f) &\stackrel{!}{=} U(f) \\ P_{11}(f) \cdot H_1(f+PRF) \cdot U(f+PRF) + P_{21}(f) \cdot H_2(f+PRF) \cdot U(f+PRF) &\stackrel{!}{=} 0 \end{aligned} \quad (44)$$

The first equation of the system in (44) recovers the original spectrum while the second equation forces the cancellation of the aliased parts caused by the back-folded/shifted spectra. The cancellation is done by adjusting the phases of the  $P_{jm}(f)$  in a way to eliminate the ambiguous spectral components. As explained in Appendix D, this corresponds to steering nulls in the joint antenna pattern to the direction of the azimuth ambiguous returns. The magnitude of the filters  $P_{jm}$  is set to ensure a recovery of the original magnitude of the signal spectrum. Of course, different scaling factors can be chosen, but will not affect the performance of the system.

By setting up the corresponding equations for the other interval, one obtains:

$$\begin{aligned} P_{12}(f) \cdot H_1(f) \cdot U(f) + P_{22}(f) \cdot H_2(f) \cdot U(f) &\stackrel{!}{=} U(f) \\ P_{12}(f) \cdot H_1(f-PRF) \cdot U(f-PRF) + P_{22}(f) \cdot H_2(f-PRF) \cdot U(f-PRF) &\stackrel{!}{=} 0 \end{aligned} \quad (45)$$

In order to combine the equations of all intervals in one linear system, they have to be expressed for the same interval. Without loss of generality,  $I_1$  is chosen as the reference interval for solving the linear system. Consequently, the relationships of (45) are shifted to  $I_1$ , yielding:

$$\begin{aligned} P_{12}(f + PRF) \cdot H_1(f + PRF) + P_{22}(f + PRF) \cdot H_2(f + PRF) & \stackrel{!}{=} 1 \\ P_{12}(f + PRF) \cdot H_1(f) + P_{22}(f + PRF) \cdot H_2(f) & \stackrel{!}{=} 0 \end{aligned} \quad (46)$$

The combination of (44) and (46) in matrix notation then yields the linear system introduced in (39) and (41):

$$\mathbf{H}(f) \cdot \mathbf{P}(f) = \mathbf{1} \Leftrightarrow \mathbf{P}(f) = \mathbf{H}^{-1}(f) \quad (47)$$

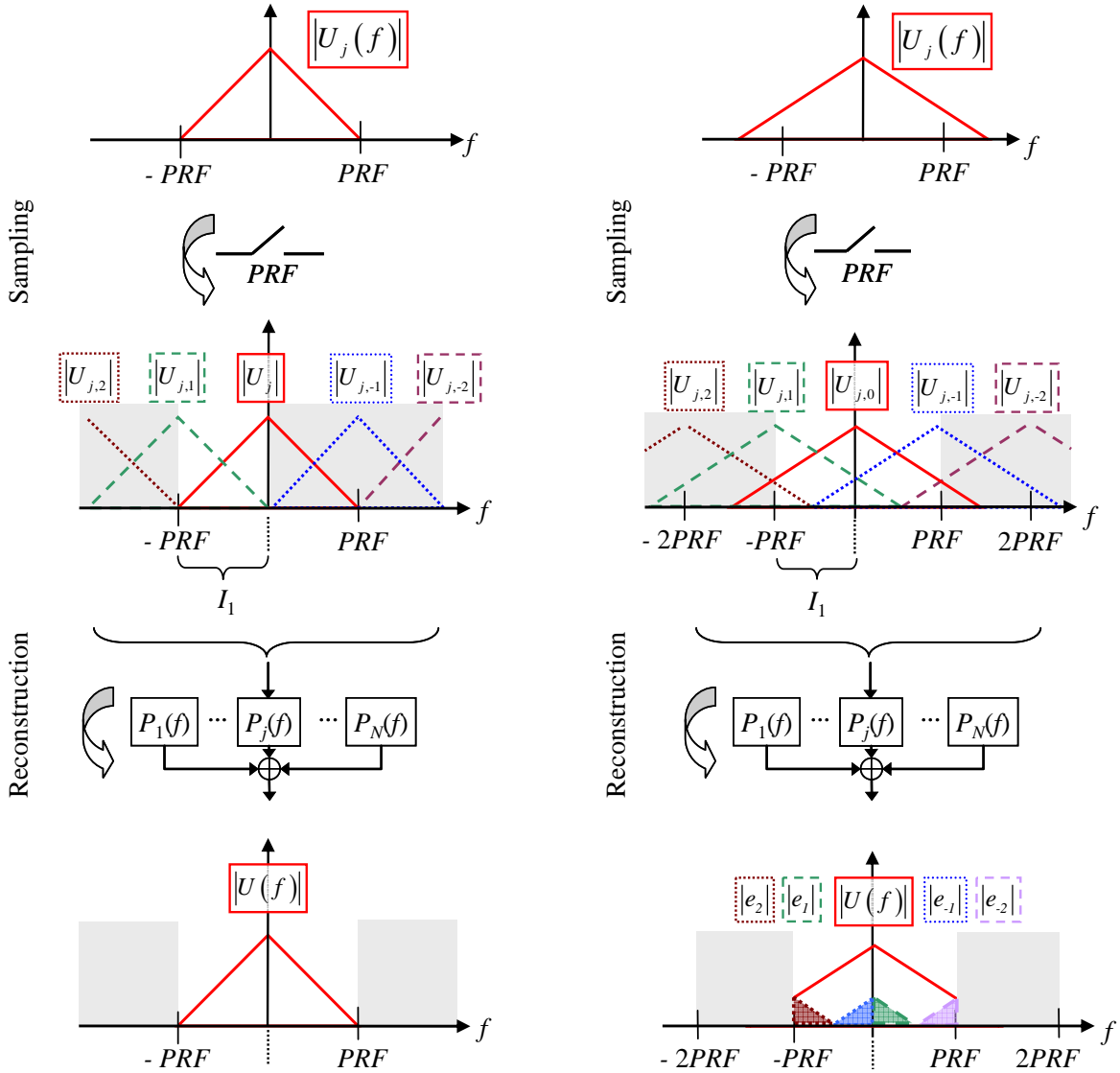


**Fig. 40.** Spectrum of signal at receiver  $j$  before (top) and after (middle) sampling with  $PRF$  and after reconstruction (bottom) taking into account all receivers. Left side shows a signal band-limited to  $[-PRF, PRF]$  that is correctly recovered while the signal bandwidth on the right side exceeds  $[-PRF, PRF]$  and is superimposed by erroneous contributions  $e_k$ .

In a next step, a scenario is analyzed, where the bandwidth of the signal exceeds  $N \cdot PRF$ . For  $N=2$ , an example for the spectrum of such a signal is given in Fig. 40 on the right, before (top) and after (middle) sampling. In contrast to the former case, it is observed that for each frequency the sampled signal  $U_{j,p}(f)$  consists of up to three contributions, as the spectra of the periodic continuation may overlap. For the general case, this means that more than  $N$  spectra may coincide at a certain Doppler frequency. From the mathematical point of view this results in a linear system of equations that is under-determined and consequently the original spectrum in general cannot be reconstructed exactly. As it was shown in the theoretical approach presented in [46], a complete suppression of the contributions from the shifted spectra is not achieved, due to the fact that the filters  $P_j(f)$  are determined as if the signal bandwidth was limited to  $\pm N \cdot PRF/2$ . Hence only the ambiguous energy within the band  $[-N \cdot PRF/2, N \cdot PRF/2]$  of the original signal is cancelled by the reconstruction. All energy outside this band is not well suppressed and finally gives rise to ambiguities in the reconstructed signal as will be derived in the following section. How the ambiguous energy can be reduced, e.g. by selecting appropriate sub-bands or weighting of the azimuth spectrum during the reconstruction, will be discussed in Chapter 8.

### 5.3 Multi-Channel Reconstruction in the Framework of STAP

According to [74], a multi-channel beamforming system consisting of  $N$  channels is considered. Each channel  $i$  is described by its input signal  $s_i$ , noise component  $n_i$  and weighting function  $a_i$  that are summarized by  $\underline{s} = [s_1, \dots, s_N]^T$ ,  $\underline{n} = [n_1, \dots, n_N]^T$  and  $\underline{a} = [a_1, \dots, a_N]^T$ , respectively. The output  $y$  of the system can then be described by the sum of two scalar products, which represent the weighted and summed input signals and noise components, respectively:

$$y = \underline{a}^T \cdot \underline{s} + \underline{a}^T \cdot \underline{n} \quad (48)$$

Further, if an incident plane wave is assumed and quasi-parallel approximation is applied, each  $s_i$  can be related to  $s_1$  by a phase term that accounts for the azimuth angle-dependent path difference between receivers  $i$  and 1. Hence,  $\underline{s}$  simplifies to a steering vector, where  $\Theta$  gives the azimuth angle and  $\Delta x_i$  denotes the distance of receiver  $i$  to receiver 1. Without loss of generality  $\Delta x_1 = 0$  is assumed leading to (49).

$$\underline{s} = \left[ 1, \exp\left[j \cdot \frac{2\pi}{\lambda} \sin(\Theta) \Delta x_i\right], \dots, \exp\left[j \cdot \frac{2\pi}{\lambda} \sin(\Theta) \Delta x_N\right] \right]^T \quad (49)$$

If colored noise  $\underline{n}$  is assumed, the optimum beamforming weights  $\underline{a}$  to minimize the noise power are defined as follows [74]:

$$\underline{a}^* = \frac{\mathbf{R}^{-1} \cdot \underline{s}}{k_0} \quad (50)$$

Where  $*$  denotes the complex conjugate,  $k_0$  represents a normalization factor and  $\mathbf{R}$  describes the noise covariance matrix that consists of the covariance matrix  $\mathbf{R}_{sp}$  of the spatially structured noise  $\underline{n}_{sp}$  and the unity matrix  $\mathbf{I}$  representing the white noise  $\underline{n}_w$  of power  $\sigma^2$ :

$$\mathbf{R} = \mathbb{E}[\underline{n} \cdot \underline{n}^H] = \mathbb{E}[\underline{n}_{\text{sp}} \cdot \underline{n}_{\text{sp}}^H] + \mathbb{E}[\underline{n}_{\text{w}} \cdot \underline{n}_{\text{w}}^H] = \mathbf{R}_{\text{sp}} + \sigma^2 \mathbf{I} \quad (51)$$

In the special case when interpreting the ambiguous Doppler frequencies as a jammer arriving from the respective azimuth angle and further assuming that no white noise is present, i.e.  $\sigma = 0$ , it was shown that (52) holds true, if  $k_0$  is chosen to ensure unitary gain and the dependency on the azimuth angle  $\Theta$  is replaced by Doppler frequency  $f$  [77].

$$\underline{a}^*(f) = \frac{\mathbf{R}(f)^{-1} \cdot \underline{s}(f)}{k_0} = \frac{\mathbf{R}_{\text{sp}}(f)^{-1} \cdot \underline{s}(f)}{k_0} = \mathbf{P}^*(f) \quad (52)$$

Where matrix  $\mathbf{P}(f)$  represents the reconstruction filter functions derived in Section 5.1, but neglecting the constant phase terms  $\Delta\phi_j$  according to (29). Hence, the – simplified –  $\mathbf{P}(f)$  contains in its  $i$ -th line the weighting function  $a_i$  and thus offers an alternative way of deriving the optimum beamformer to suppress azimuth ambiguities that are interpreted as jammers in the STAP context.

In conclusion, the multi-channel reconstruction represents the optimum solution to suppress azimuth ambiguities of a band-limited signal, while the STAP solution additionally incorporates a matched filter component and thus minimizes the joint power of both azimuth ambiguities and white noise. However, the STAP approach requires knowledge or estimation of the ratio between noise and ambiguous power, while the multi-channel reconstruction is data independent.

## 5.4 Two-Dimensional Reconstruction and Processing

So far, the unambiguous reconstruction of the azimuth signal has been investigated. In the present section, the two-dimensional data reconstruction is analyzed with regard to the impact of range cell migration [43]. In this context, basically two aspects deserve consideration. Firstly, possible differences between the channels' range histories have to be taken into account, and, secondly, the impact of range migration on the reconstruction per se is analyzed.

### 5.4.1 Multi-Channel Range Cell Migration

As discussed in Section 2.2, the range history of a point-like target migrates over several range resolution cells, thus spanning a range from  $R_0$  to  $R_0 + \Delta R$ . In addition, in multi-channel systems the situation becomes more complicated as the same target is “seen” under different minimum slant range distances and with varying range curvatures, depending on the respective distance to the transmit aperture. As a result, the range cell migration might be different for each receive aperture as illustrated below.

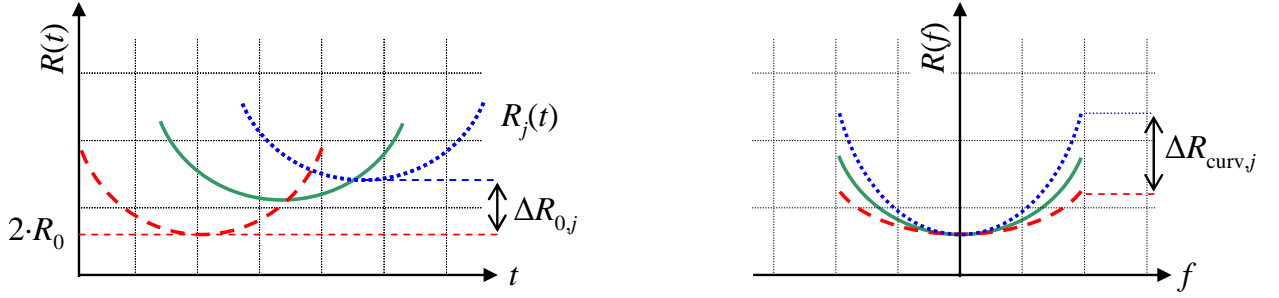


**Fig. 41. Multi-channel range cell migration: Depending on the receiver position, the same target shows different range histories. Left shows the relative two-way slant range offset  $\Delta R_{0,j}$  for three receivers while right illustrates the varying curvature vs. Doppler frequency resulting in an offset  $\Delta R_{\text{curv},j}$  (two-way, each curve normalized to its respective  $R_0$ ).**

The unambiguous azimuth signal is obtained by separately reconstructing each range bin, i.e. each line of the data array. This means that in a first step it has to be ensured that the contributions from a specific target in range-Doppler domain are co-registered to the same “reference” range bin in all receivers’ signal memories. In this regard, firstly, a large receiver spacing might result in a large relative range offset  $\Delta R_{0,j}$ , which exceeds the range resolution, thus requiring a range shift to correct for. Secondly, the differential range curvature  $\Delta R_{\text{curv},j}$  might also be in the order of a range resolution cell. As a consequence, the echo of a specific target is stored in different range bins according to the respective receiver’s position, thus precluding correct reconstruction. It should be noted that  $\Delta R_{0,j}$  as well as  $\Delta R_{\text{curv},j}$  consider the two-way path difference, as this is relevant for the different delay times.

The variation in slant range can be directly derived from the effective phase center definition, which includes the addition of a constant phase (cf. Section 4.2). This phase originates from the above discussed differences regarding the minimum slant range of the range history. Hence, the constant phase term from (31) defines – in quadratic approximation – the phase resulting from the modified slant range, leading for the two-way distance to the analytic expression as follows.

$$\Delta R_{0,j} = \frac{v_g}{v_s} \cdot \frac{\Delta x_j^2}{4 \cdot R_0} \quad (53)$$

In order to evaluate the impact of the different range cell migrations, one single-platform system and one distributed constellation are analyzed for L-band as well as X-band and a slant range of 735 km. In this context the maximum receiver separation describes the largest distance with respect to a reference receiver at the transmitter position. As the range curvature depends also on the illumination time, a value is chosen which ensures an azimuth resolution in the order of 1 m. Further, for the following considerations a range resolution in the same order is assumed. The relative range offsets and differences in range curvature obtained are investigated in detail in Appendix C. The respective results are summarized in the subsequent table which also contains the reconstruction phase errors from the analysis following in Section 5.4.2.

Parameter	Single-platform System		Multi-platform System	
	X-Band	L-Band	X-Band	L-Band
Maximum receiver separation	10 m		500 m	
Differential range curvature $\Delta R_{\text{curv},j}$ (two-way)	$< 10^{-8}$ m	$< 10^{-6}$ m	$< 10^{-5}$ m	$< 10^{-3}$ m
Relative range offset $\Delta R_{0,j}$ (two-way)	$< 10^{-4}$ m		$< 0.1$ m	
Maximum Range Migration $\Delta R_j$	$< 50$ m	$< 2700$ m	$< 50$ m	$< 2700$ m
$\Delta\phi_{\tau,j}$ (uncompressed, $\tau = 10\mu\text{s}$ )	$< 10^{-2}$ °	$< 10^{-3}$ °	$< 5$ °	$< 1.5$ °
$\Delta\phi_j$ (range compressed)	$< 10^{-4}$ °	$< 10^{-3}$ °	$< 0.1$ °	$< 0.6$ °

**Table 2. Range migration in multi-channel SAR and resulting reconstruction filter mismatch.**

Regarding the differential range curvatures, Table 2 shows for both systems and bands an error far below the range resolution and consequently this effect can be neglected. This is good news, as a correction of the curvature could only be carried out in Doppler frequency domain. Hence, on the one hand the full – i.e. unaliased – Doppler spectrum would be required, but on the other hand correction would be necessary prior to reconstruction, which is a contradiction in terms.

Concerning the relative range offset, a negligible value is encountered in single-platform systems, but a sparse array constellation might require compensation. For each channel, the respective offset is a constant value independent on Doppler frequency but with slight variation in dependency of the slant range according to (53). As the differential curvature is minor, this means that all range histories obtained at a certain  $R_0$  can be aligned correctly by a constant shift of the received pulse in range time domain. As a pixel-wise shift cannot ensure correctly aligned range histories over the complete range migration, the alignment has to be performed by a phase ramp in range frequency domain yielding a time shift according to  $\Delta R_{0,j}$ . This leaves the azimuth phase unchanged thus not affecting the following azimuth processing steps. For example, the shift can be directly incorporated in the range compression by using an appropriately shifted replica, which has to be adapted to the respective  $R_0$  to ensure exact solution. In a brute force approach, this would mean that for each slant range the compression is performed separately. As this entails huge computational load and as the variation of  $\Delta R_{0,j}$  over  $R_0$  is slow, one could think of a range compression in sections. An investigation of optimized correction algorithms is beyond the scope of this work as the focus of the research is directed to single-platform systems.

#### 5.4.2 Reconstruction Filter Mismatch

In a second step, the reconstruction filter functions  $P_j(f)$  are taken into account, which are adapted to the respective slant range  $R_0$ . As a preliminary step, the filters' dependency on  $R_0$  is derived. As can be seen from (39) in combination with (31), the system matrix  $\mathbf{H}$  can be decomposed into a matrix  $\mathbf{H}'$  multiplied by a diagonal matrix  $\mathbf{D}$  whose elements represent the dependency on  $R_0$ . The diagonal elements at position  $(j,j)$  are given as follows:

$$(\mathbf{D})_{j,j} = \exp \left[ -j \cdot \frac{v_g}{v_s} \cdot \frac{\pi \cdot \Delta x_j^2}{2 \cdot \lambda \cdot R_0} \right] \quad (54)$$

Thus, according to basic matrix algebra the matrix  $\mathbf{P}$  is made up of the inverse from  $\mathbf{H}'$  multiplied by  $\mathbf{D}^{-1}$  which simply consists of the inverse diagonal elements. As a result, the dependency of each channel  $j$  on  $R_0$  is characterized as follows:

$$P_j(f) \propto \exp \left[ j \cdot \frac{v_g}{v_s} \cdot \frac{\pi \cdot \Delta x_j^2}{2 \cdot \lambda \cdot R_0} \right] \quad (55)$$

As the range history spans several range bins, a signal obtained for a target at  $R_0$  will be partly reconstructed by filters calculated for  $R_0 + \Delta R_j$ . Thus, range migration introduces a mismatch between the signal and the reconstruction. As differential range curvature can be neglected and the relative range offset is assumed to be corrected, this mismatch is only determined by the maximum range migration  $\Delta R_j$  of channel  $j$  from the range history from  $R_0$ . Note that in this context the one-way slant range is relevant.

$$\Delta \varphi_j = \frac{v_g}{v_s} \cdot \frac{\pi \cdot \Delta x_j^2}{2 \cdot \lambda} \left( \frac{1}{R_0} - \frac{1}{R_0 + \Delta R_j} \right) = \frac{v_g}{v_s} \cdot \frac{\pi \cdot \Delta x_j^2}{2 \cdot \lambda} \left( \frac{\Delta R_j}{R_0 \cdot (R_0 + \Delta R_j)} \right) \quad (56)$$

This result enables to convert the range migration of Table 2 in respective phase errors, where  $\Delta \varphi_j$  refers to the compressed pulse, while  $\Delta \varphi_{\tau,j}$  considers the uncompressed pulse. Here, a pulse length  $\tau = 10 \mu\text{s}$  is assumed and correspondingly the maximum range mismatch is increased by  $\tau \cdot c_0 = 3 \text{ km}$ . Both possibilities are analyzed, as in principle the aliased data of each channel can either be range compressed before reconstruction, or afterwards. Nevertheless, the obtained values (cf. Table 2) allow for the conclusion that the phase errors are negligible for range compressed data but have to be considered for uncompressed data gathered by multi-platform systems with large receiver separations. Consequently, from the reconstruction point of view, range compression prior to reconstruction is favorable, as the extension of the target echo is reduced by the pulse length and the effective  $\Delta R$  will be smaller.

### 5.4.3 Two-Dimensional Multi-Channel Reconstruction

In summary, in single-platform systems the different range histories and the errors introduced by applying the azimuth reconstruction subsequently for each range line are negligible. Thus a direct application of the one-dimensional multi-channel reconstruction algorithm in a two-dimensional processing approach is possible to such systems without further correction steps. In multi-platform constellations, a large receiver separation might lead to non-negligible slant range offset. This requires compensation which can be achieved by an appropriate range shift of the data which can e.g. be incorporated in the range compression. After correction, multi-channel reconstruction can be applied with minor errors similar to single-platform systems.

As a conclusion, this allows for stating that the isolated one-dimensional consideration of the multi-channel reconstruction represents a valid approximation for the application of the algorithm to two-dimensional data, according to the following processing flow: After range compres-

sion and – if necessary – applying a shift to each channel’s data, line-by-line reconstruction is carried out. After complete reconstruction of all range bins, conventional SAR processing follows, i.e. single channel range cell migration correction is performed, and, finally, monostatic azimuth focusing results in the SAR image [43].

## 5.5 Signal Power

In the following, the signal power is defined as the mean energy of the unambiguous azimuth signal, which is limited by the system bandwidth in azimuth  $I_S = N \cdot PRF$  and potentially further confined by the processed Doppler bandwidth  $B_D \leq I_S$ . It should be noted that in the following “power” is used to describe the average energy of the signals, where – regarding the following calculations of azimuth ambiguous energy or *SNR*– it is equivalent to calculate the averaged energy either as a mean value per frequency (and time), or averaging per sample.

To determine the signal power, at first the output signal power of the reconstruction network is determined. Remember that the filters  $P_j(f)$  are chosen such that the equivalent mono-aperture signal,  $U(f)$ , is reconstructed unambiguously. Recall furthermore that the spectral weighting of  $U(f)$  depends only on the joint pattern of the transmitter and a single receiver element. This means that, basically, a signal is obtained, which is not dependent on the reconstruction filters. According to (44), the original signal with respect to a single channel is reconstructed and consequently the power is kept constant compared to the input signal power of a single channel  $p_{s,el}$ . Then, assuming in average an emitted power  $p_{tx,av}$ , the received signal power  $p_s$  is determined by the mean squared value of  $U(f)$  limited to the system bandwidth in azimuth  $I_S = [-N \cdot PRF/2, N \cdot PRF/2]$  (cf. (57)). The possible *PRF* dependency of  $p_{tx,av}$  will be discussed below.

$$p_s = p_{tx,av}(PRF) \cdot \mathbf{E} \left[ \left| U(f) \cdot \text{rect} \left( \frac{f}{I_S} \right) \right|^2 \right] = p_{s,el} \quad (57)$$

The spectral limitation to  $I_S$  is expressed by the rectangular window function  $\text{rect}(f/I_S)$  and the calculation of the mean value is indicated by the operator  $\mathbf{E}[\cdot]$ .<sup>12</sup>

If the signal is focused with a defined bandwidth  $B_D$ , only this part of  $I_S$  is used for the compression. This can be understood as an additional lowpass filtering of the signal that has to be included in (57). One obtains (58), giving  $p_{s,B_D}$  that describes the signal power after focusing with  $B_D$ , where the mean value is calculated on the original interval  $I_S$ . Further, a “white” scene is assumed, i.e.  $|U(f)|$  can be described by the signal envelope  $A(f)$  which corresponds to the two-way antenna pattern in azimuth. The constant  $C_{UA}$  does not affect the power; it just relates  $U(f)$  and  $A(f)$  in a way to ensure the correct unity of  $A(f)$  with respect to  $p_{s,B_D}$ .

<sup>12</sup>For deterministic signals as  $U(f)$  the mathematical operator  $\mathbf{E}[\cdot]$  is identical to an integration over the frequency interval  $I_S$ , normalized by its width  $N \cdot PRF$  or the respective number of samples. For stochastic processes  $\mathbf{E}[\cdot]$  represents the expectation value. As in both cases  $\mathbf{E}[\cdot]$  gives a measure of the power, the same operator symbol is used to provide a consistent notation.



$$P_{s,B_D} = P_{\text{tx,av}}(PRF) \cdot \mathbb{E} \left[ \left| U(f) \cdot \text{rect} \left( \frac{f}{B_D} \right) \right|^2 \right] = C_{UA} \cdot P_{\text{tx,av}}(PRF) \cdot \mathbb{E} \left[ \left| A(f) \cdot \text{rect} \left( \frac{f}{B_D} \right) \right|^2 \right]; \quad B_D \leq I_s \quad (58)$$

In other words, the signal power is obtained by integrating the area corresponding to  $B_D$  under the squared signal envelope as illustrated in Fig. 42 below. In general, azimuth antenna dimensions and processed Doppler bandwidth are adjusted such that most of the energy within the antenna pattern is located within  $B_D$ , allowing for the rather rough approximation as follows:

$$P_s \approx P_{s,B_D} \quad (59)$$

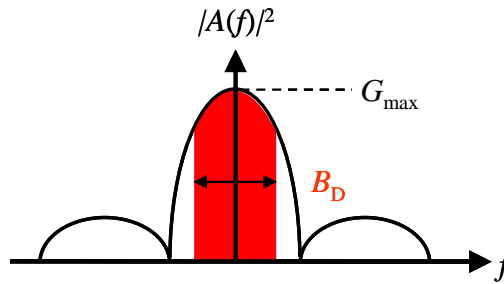


**Fig. 42. Power spectral density (Doppler) of white scene defined by the azimuth signal envelope  $A(f)$ . Signal power is given by the area corresponding to the processed Doppler bandwidth  $B_D$  (red) and the maximum antenna gain  $G_{\text{max}}$ .**

The signal envelope  $A(f)$  can be expanded into  $A_0(f)$ , which represents the normalized weighting of the Doppler spectrum by the joint Tx/Rx azimuth antenna pattern, and the maximum power gain  $G_{\text{max}}$  as follows:

$$A(f) = \sqrt{G_{\text{max}}} \cdot A_0(f) \quad (60)$$

The signal power can then be determined by considering this maximum power gain  $G_{\text{max}}$  and the decay of  $A_0(f)$  which attenuates the recorded signal [78]. Assuming a normalized rectangular filter of bandwidth  $B_D$  for focusing in azimuth, this decay is characterized by the azimuth loss factor  $L_{\text{az}}$  that describes the loss of signal energy compared to a rectangular signal envelope:

$$L_{\text{az}} = \frac{B_D}{\int_{-B_D/2}^{B_D/2} |A_0(f)|^2 df} \quad (61)$$

Note that (61) gives the mean energy within the focused SAR signal and is valid for point-like targets as well as when considering the SAR signal of a “white” scene. In contrast, in the special case when only the peak power of the impulse response of a point-like target is evaluated, the compression of the signal has to be considered which corresponds to an in-phase summation before squaring the result to calculate the power. This means that the above loss changes to an “azimuth compression loss”  $L_{\text{az,co}}$  that is defined by (62).

$$L_{\text{az,co}} = \frac{B_D}{\left( \int_{-B_D/2}^{B_D/2} |A_0(f)| df \right)^2} \quad (62)$$

Finally, the discrete-time character of the azimuth signals has to be taken into account. Basically, this means that the above integrals change to a summation over the samples within the respective interval. Consequently, the azimuth signal power is determined by the number of samples and their power. Regarding the number of pulses, the *PRF* in combination with the azimuth integration time – or the corresponding bandwidth  $B_D$  in Doppler domain – is of importance. In consequence, the larger  $B_D$  or the higher the *PRF*, the more azimuth samples are summed up. The power of each azimuth sample is defined as the peak of the range compressed pulse, which is governed by the transmitted energy and, hence, directly proportional to the transmit pulse's peak power and duration. This means that in a system operated with constant transmit peak power and duty cycle, the average transmit power  $p_{\text{tx,av}}$  is also constant and independent of the *PRF*. Consequently, the resulting power after focusing is also constant, as e.g. the decreasing power of each sample due to a higher *PRF* is compensated by the fact that more samples are gathered within the integration time and then combined during azimuth compression. In contrast, if a constant pulse length is assumed, the transmitted power per sample remains constant, resulting in an increased signal power per time, which is directly proportional to the *PRF*. In this case, strict notation would be  $p_{\text{tx,av}}(\text{PRF})$ . For reasons of succinct notation, the possible dependency of  $p_{\text{tx,av}}$  on the *PRF* will not be given explicitly, but mentioned where necessary. In summary, the transmission “strategy” has to be considered, when evaluating the signal power.

Keeping in mind the above derivation of the signal power, the following Sections 5.6 and 5.7 analyze the azimuth ambiguous energy and the scaling of the noise power, respectively, allowing for a deduction of performance parameters as azimuth ambiguity-to-signal ratio ( $\text{AASR}_N$ ) and signal-to-noise ratio (*SNR*), respectively.

## 5.6 Residual Reconstruction Error and Azimuth Ambiguities: $\text{AASR}_N$

As discussed in Section 5.2 and illustrated in Fig. 40, energy outside the band  $I_S = [-N \cdot \text{PRF}/2, N \cdot \text{PRF}/2]$  of the original signal spectrum is not cancelled by the algorithm and disturbs the unambiguous reconstruction of the multi-channel SAR signal. After focusing, this will give rise to azimuth ambiguities in the SAR image.

This section derives in two steps the residual spectral “error” that remains from these aliased parts after the system of reconstruction filters. The first step deduces the ambiguous contributions of the signal depending on the azimuth antenna patterns and the applied *PRF*. In a second step, the weighting of this ambiguous parts by the reconstruction filter functions  $P_j(f)$  is derived, which are governed by the overall system configuration. As both residual ambiguous power and signal power are directly depending on the emitted signal power, the factor  $p_{\text{tx,av}}$  in (57) will can-

cel out when calculating the ambiguity-to-signal ratio. Hence,  $p_{\text{tx,av}}$  will not be mentioned explicitly in the following derivation.

At the beginning, it is of interest, to which frequency  $f$  the ambiguous parts of  $U(f)$ , i.e. the portions outside the original frequency band  $I_S = [-N \cdot PRF/2, N \cdot PRF/2]$ , are folded back by the sampling. First of all, the sampled signal at receiver  $j$  according to (43) is considered, and focus is turned to the  $k$ -th continuation of the original spectrum given by  $U_j(f+k \cdot PRF) = U_{jk}(f)$ .

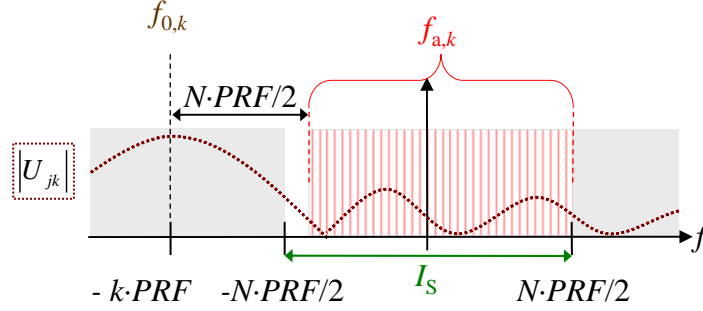


**Fig. 43. Spectrum of  $U_{jk}(f)$  with ambiguous parts marked in red. The relevant contributions are situated within the system band  $I_S$  (green), which is confined by the gray shaded areas.**

As shown in Fig. 43, the spectrum  $U_{jk}(f)$  is located around the center frequency  $f_{0,k} = -k \cdot PRF$ , and consequently the ambiguous contributions are situated at frequencies  $f_{a,k}$  that deviate more than  $\pm N \cdot PRF/2$  from  $f_{0,k}$ , as expressed by the following equation:

$$|f_{a,k} - f_{0,k}| > \frac{N \cdot PRF}{2} \Leftrightarrow |f_{a,k} + k \cdot PRF| > \frac{N \cdot PRF}{2} \quad (63)$$

Further, only contributions situated after sampling within the system band  $I_S$  are relevant, i.e.:

$$|f_{a,k}| < \frac{N \cdot PRF}{2} \quad (64)$$

Combining these two constraints yields the following expressions for the Doppler frequencies where the ambiguous parts are located. The first case, considering  $k > 0$ , is illustrated by the dashed red area in Fig. 43.

$$\frac{N}{2} PRF - k \cdot PRF < f_{a,k} < \frac{N}{2} PRF \quad k > 0 \quad (65)$$

$$-\frac{N}{2} PRF < f_{a,k} < -\frac{N}{2} PRF - k \cdot PRF \quad k < 0 \quad (66)$$

Consequently, depending on  $k$ , spectral sub-bands  $I_m$  containing frequencies according to the above equations are not cancelled by the reconstruction algorithm and have to be considered when determining the remaining ambiguous signals. Assuming a symmetrical pattern, i.e.  $A(f) = A(-f)$ , the problem is symmetrical. Hence, it is sufficient to concentrate only on  $k > 0$ , i.e. the scenario described by (65). In this case, sub-bands  $I_m$  up from index  $m_0 = \max\{N-k+1, 1\}$  contribute to the residual ambiguities.

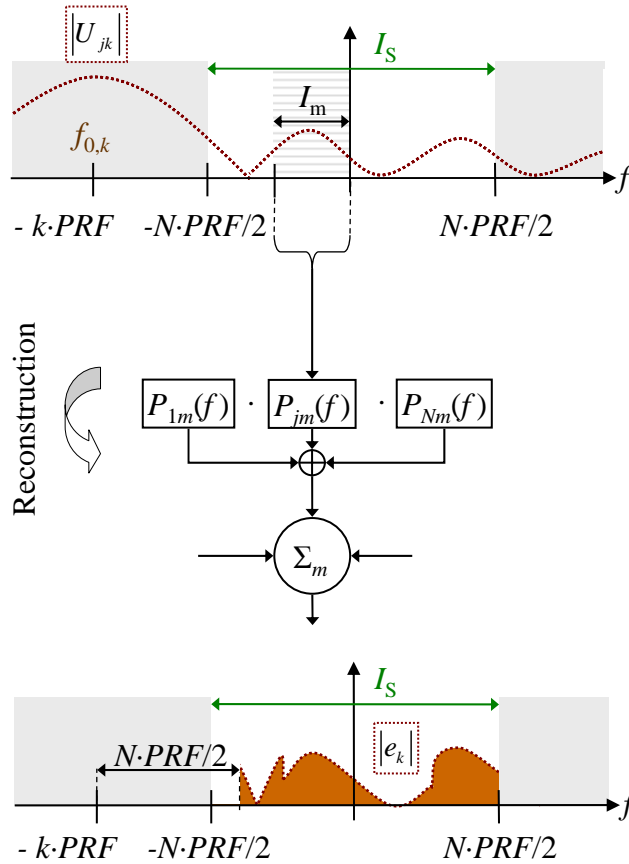


**Fig. 44. Top:** Weighting of ambiguous contributions on each interval  $I_m$  by the respective processing filter  $P_{jm}(f)$ . **Summation over all receiver channels  $j$  and stringing together all intervals  $m$  yields the residual ambiguous energy  $e_k$  (bottom).**

In a next step, the processing of the signal is considered. This means that it is taken into account how the frequency dependent weighting by the filters  $P_j(f)$  affects the ambiguous parts of  $U_{jk}(f)$  (cf. Fig. 44). As discussed before, the system band  $I_S$  is split into  $N$  intervals  $I_m$  on which the filters  $P_{jm}(f)$  are defined, respectively. In order to calculate the residual ambiguities, all sub-bands  $I_m$  where the signal is not properly reconstructed have to be included. One obtains  $e_{k,j}(f)$  that represents the ambiguous error of the  $k$ -th back folded spectrum in channel  $j$ , where  $U_j(f)$  is expressed by the monostatic SAR signal  $U(f)$  multiplied by the respective  $H_j(f)$  (cf. (67)). Again, index  $k$  indicates a shift from  $f$  to  $f + k \cdot PRF$  due to the sampling and the signal is confined to the sub-band  $I_m$  by a rectangular window of width  $PRF$  around the center frequency  $f_{0,m}$  represented by  $\text{rect}((f-f_{0,m})/PRF)$ .

$$e_{k,j}(f) = \sum_{m=m_0}^N \underbrace{U_k(f) \cdot H_{jk}(f)}_{U_{jk}(f)} \cdot \underbrace{P_j(f)}_{P_{jm}(f)} \cdot \text{rect}\left(\frac{f-f_{0,m}}{PRF}\right) = U_k(f) \cdot \sum_{m=m_0}^N H_{jk}(f) \cdot P_{jm}(f) \quad (67)$$

Then, contributions from all receiver channels  $j$  are added. This yields  $e_k(f)$  that describes the spectrum of the remaining output error due to aliasing of the input signal caused by the  $k$ -th back folded spectrum (cf. (68), Fig. 40 bottom right, and Fig. 44). Note that for  $e_k(f)$  choosing the minimum index  $m_0 = 1$  does not lead to wrong results, as it would only consider additionally the

spectral parts located within  $I_S$  and hence the respective contributions would become zero due to the inverse filtering by  $P_{jm}(f)$  and summation over all channels  $j$ .

$$e_k(f) = \sum_{j=1}^N e_{k,j}(f) = U_k(f) \cdot \sum_{m=m_0}^N \sum_{j=1}^N H_{jk}(f) \cdot P_{jm}(f) \quad (68)$$

The complete ambiguous spectrum due to aliasing is obtained by summation of all individual ambiguous contributions after reconstruction,  $e_k$ , yielding  $e_\Sigma(f)$  in (69), where the factor 2 accounts for both signs of  $k$ .

$$e_\Sigma(f) = 2 \cdot \sum_{k=1}^{\infty} e_k(f) = 2 \cdot \sum_{k=1}^{\infty} \left( U_k(f) \cdot \sum_{m=m_0}^N \sum_{j=1}^N H_{jk}(f) \cdot P_{jm}(f) \right) \quad (69)$$

Equation (69) can be divided into the characteristics of the azimuth signal and the overall configuration. The azimuth signal spectrum  $U_k(f)$  is defined by size and tapering of the transmit antenna and the single receive aperture, while the double sum of (69) is defined by the products  $H_{jk}(f) \cdot P_{jm}(f)$  that depend on the relative positions of all apertures and system parameters like sensor velocity and  $PRF$ .

The mean squared amplitude of  $e_\Sigma(f)$  represents the azimuth ambiguous power. Relating it to the signal power  $p_s$  of (57) results in an equivalent azimuth ambiguity-to-signal ratio for multi-channel SAR systems. This parameter is denoted by  $AASR_N$  and – in contrast to the  $AASR$  of conventional systems – it takes into account the weighting and coherent combination of the individual channels by the beamforming network.

$$AASR_N = \frac{E \left[ |e_\Sigma(f)|^2 \right]}{P_s} \quad (70)$$

So far, the  $AASR_N$  was calculated for the complete Doppler bandwidth given by  $N \cdot PRF$ . In a next step, the respective processed Doppler bandwidth  $B_D$  and the associated lowpass filtering are included, yielding an  $AASR_N$  expression for the image. Therefore  $e_\Sigma(f)$  is band-limited to  $B_D$  by a rectangular window function  $\text{rect}(f/B_D)$  before the ambiguous power is calculated, finally yielding the expression for the azimuth ambiguity-to-signal ratio in multi-channel systems:

$$AASR_{N,B_D} = \frac{E \left[ \left| e_\Sigma(f) \cdot \text{rect} \left( \frac{f}{B_D} \right) \right|^2 \right]}{P_{s,B_D}} \quad (71)$$

The numerator of (71) quantifies the ambiguous energy within the focused SAR image, accounting for the applied multi-channel processing.

If one is interested in the ‘‘appearance’’ of the ambiguous energy within the image – i.e. the peak powers of the respective ambiguities – the focusing filter has to be additionally considered. Hence, in order to determine the response of the residual ambiguity of order  $k$  in the image,  $U_{e,k}(f)$ , the respective ambiguous contribution  $e_k(f)$  of (68) has to be focused by the used SAR processor that was defined as  $P_{mf}(f)$  (cf. Fig. 39).

$$U_{e,k}(f) = e_k(f) \cdot P_{mf}(f) \quad (72)$$

Inverse Fourier transformation of  $U_{e,k}(f)$  yields the time domain response of the ambiguity of order  $k$  and allows for evaluating the maximum ambiguous peak power remaining in the image.

## 5.7 SNR Scaling in Digital Beamforming Networks: $\Phi_{bf}$

The reconstruction algorithm aims at recovering the unambiguous Doppler spectrum by suppressing the ambiguous frequency components. In terms of the group antenna characteristic that results from the weighting coefficients of the beamforming algorithm, this corresponds to placing nulls at angles where ambiguous Doppler frequencies are situated. Further, one observes that only for uniform sampling the maximum in the group characteristic is steered at the Doppler frequency that is to be recovered. For increasing non-uniformity, the maximum drifts away from that angle resulting in a decreased gain and, hence, a loss of the signal energy. This is compensated for by a later scaling of the signal which lifts up the noise floor, thus degrading the  $SNR$ .

The present section investigates this influence of the digital beamforming network on signal and noise power and derives a parameter that characterizes the impact of a network of digital filters on the  $SNR$ . As under certain conditions the  $SNR$  is improved by the processing, the term “noise figure” is abandoned and replaced by “ $SNR$  scaling” in beamforming networks which is denoted by  $\Phi_{bf}$  to avoid confusion with existing terminology. According to Fig. 45,  $\Phi_{bf}$  is a measure for the variation of the  $SNR$  in the data due to the processing and considers the full available Doppler bandwidth. In contrast,  $\Phi_{bf,B_D}$  refers to a Doppler bandwidth limited to  $B_D$ , by this taking additionally into account the focusing with this bandwidth. Consequently,  $\Phi_{bf,B_D}$  gives a measure for the image.

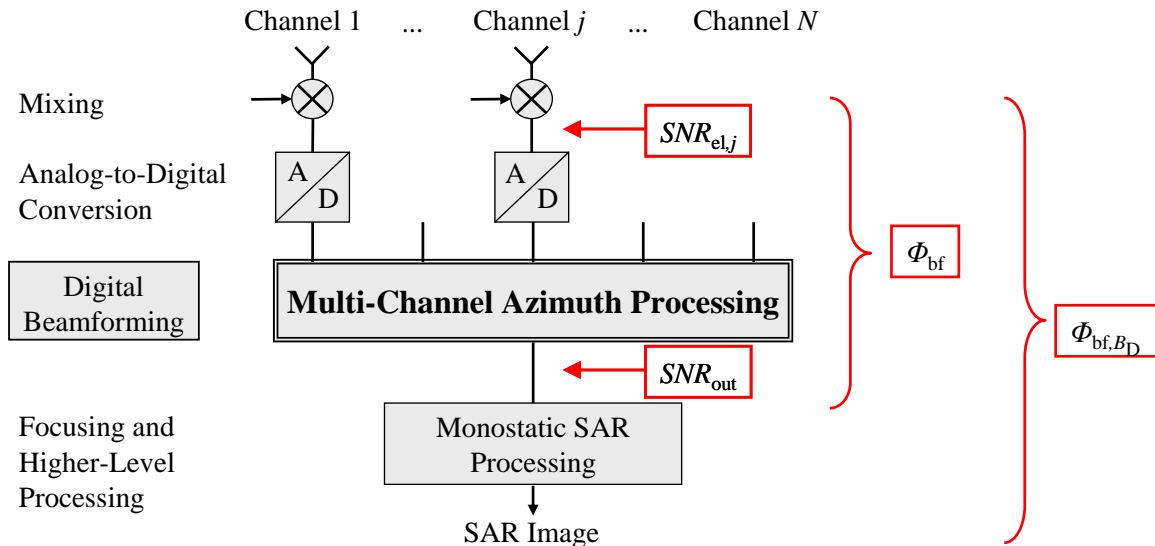


**Fig. 45. Azimuth processing block diagram giving the  $SNR$  scaling factors before ( $\Phi_{bf}$ ) and after focusing ( $\Phi_{bf,B_D}$ ) of the SAR image.**

As depicted in the block diagram of Fig. 45, the multi-channel SAR system is considered as a linear system of  $N$  channels. Fig. 46 shows the system model of channel  $j$  with an input signal

$u_j(t_r, t)$  and additive receiver noise components  $n_{j,B}(t_r, t)$ , where  $t_r$  and  $t$  describe range (fast) and azimuth (slow) time, respectively, and  $m$  and  $k$  represent the corresponding discrete-time variables. Further,  $f_r$  and  $f$  denote the frequency variables in range and azimuth, respectively.

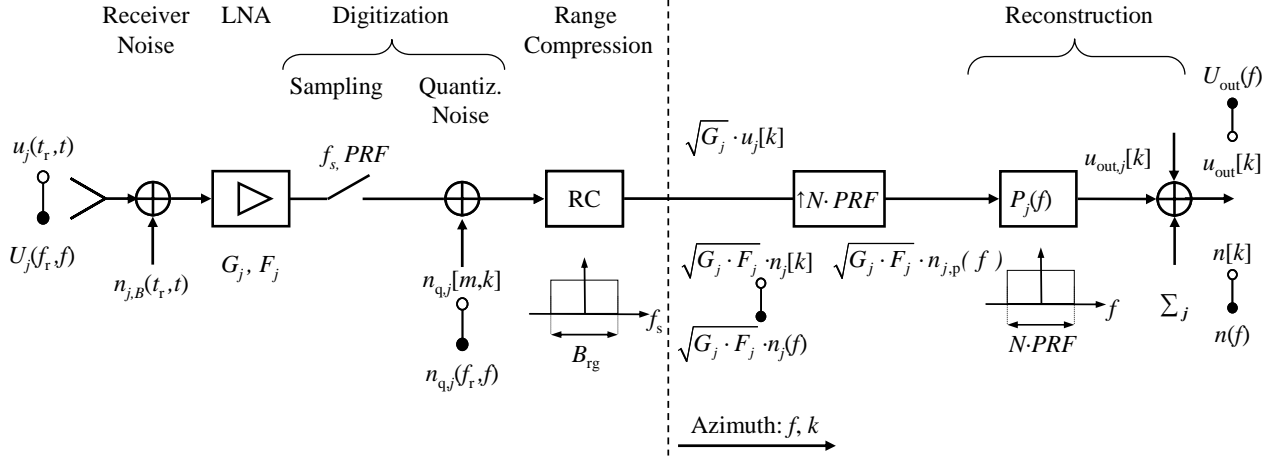


**Fig. 46. System model for a single channel of the multi-channel system. After reception of  $U_j(f_{rx}, f)$ , receiver noise is added. Then the RF signal is amplified, digitized, and range compressed before filtering and coherent combination of all channels.**

The corresponding spectra are given by  $U_j(f_r, f)$  and  $n_{j,B}(f_r, f)$  which define the input signal power,  $p_{s,el,j}$ , and noise power,  $p_{n,el,j}$ , respectively. Relating the two variables results in the input signal-to-noise ratio  $SNR_{el,j}$  (cf. Fig. 45), where  $B$  indicates the analog system bandwidth.<sup>13</sup>

$$SNR_{el,j} = \frac{p_{s,el,j}}{p_{n,el,j}} = \frac{p_{tx,av} \cdot \mathbb{E} \left[ \left| U_j \left( f_r, f \right) \cdot \text{rect} \left( \frac{f_r}{B} \right) \cdot \text{rect} \left( \frac{f}{I_s} \right) \right|^2 \right]}{\mathbb{E} \left[ \left| n_{j,B} \left( f_r, f \right) \cdot \text{rect} \left( \frac{f_r}{B} \right) \right|^2 \right]} \quad (73)$$

The received signal is amplified in the low noise amplifier (LNA) that is characterized by the power gain  $G_j$ , and noise figure,  $F_j$ , which represent equivalent parameters summarizing the complete analog RF chain [79]. In a similar way, all thermal noise is summarized by the equivalent noise sources  $n_{j,B}(f_r, f)$ , which are assumed mutually uncorrelated between the channels. After amplification the signal is sampled in range with a rate of  $f_s$ . In addition, the pulsed operation corresponds to a sampling-rate in azimuth of  $PRF$ , yielding a sub-sampled and consequently aliased time-discrete signal. The quantization error induced by the sampling is modeled as an additive noise source  $n_{q,j}$  and assumed to be uniformly distributed and spectrally white as proposed in [76]. Further, the granular error is assumed dominant and consequently no  $SNR$  loss caused by clipping is encountered.

<sup>13</sup>In this context the expectation/mean value is determined over both dimensions, i.e. a double integral/sum normalized to the respective intervals/pixels is to be performed.

Then, as illustrated by the component ‘‘RC’’ in Fig. 46, range compression and range cell migration correction is carried out, where, for convenience, a chirp bandwidth  $B_{\text{rg}}$  is assumed. For a point-like target, this allows for assuming the complete signal energy to be concentrated in a single pixel in range, by this accounting for pulse length and transmit power. The overall thermal noise power is governed by the system bandwidth  $B$  and possibly reduced by filtering with  $B_{\text{rg}} \leq B$  inherent to range compression. In the end, this results in a noise component with a power according to  $B_{\text{rg}}$  per (fast and also slow) time domain sample. Thus, a one-dimensional consideration limited to only the azimuth signal will not affect the *SNR* and, hence, the following investigations will neglect range dimension, as indicated by the dashed vertical line in Fig. 46. Up from this point, the signal is denoted by  $U_j(f)$  and the noise by  $n_{j,B}(f)$ , allowing to express the respective powers as follows in (74) and (75).<sup>14</sup> As discussed in Section 5.5, the average emitted signal power  $p_{\text{tx,av}}$  includes a possible dependency on the *PRF*. With regard to the noise, its contribution *per sample* does not depend on the *PRF*. This means, within a fixed time interval the noise energy will increase with the *PRF* according to the increased number of samples. As a result, the noise power defined as energy *per time* will vary in direct proportion to the *PRF*.

$$p_{\text{s,el},j} = p_{\text{tx,av}} \cdot \mathbb{E} \left[ \left| U_j(f_r, f) \cdot \text{rect} \left( \frac{f_r}{B_{\text{rg}}} \right) \cdot \text{rect} \left( \frac{f}{I_S} \right) \right|^2 \right] = p_{\text{tx,av}} \cdot \mathbb{E} \left[ \left| U_j(f) \cdot \text{rect} \left( \frac{f}{I_S} \right) \right|^2 \right] \quad (74)$$

$$p_{\text{n,el},j} = \mathbb{E} \left[ \left| n_{j,B}(f_r, f) \cdot \text{rect} \left( \frac{f_r}{B_{\text{rg}}} \right) \right|^2 \right] = \frac{B_{\text{rg}}}{B} \cdot \mathbb{E} \left[ |n_{j,B}(f)|^2 \right] \quad (75)$$

The signal of each channel  $j$  is then digitally filtered by a Doppler frequency dependent filter  $P_j(f)$  that is defined on a bandwidth of  $N \cdot \text{PRF}$ . Finally, the outputs  $u_{\text{out},j}[k]$  of all  $N$  branches are combined coherently yielding the output signal  $u_{\text{out}}[k]$  (cf. Fig. 46). As the system is linear and only additive noise sources are considered, signal and noise power can be analyzed separately, when investigating the influence of the reconstruction network on the *SNR*. For reasons of simplicity, considerations are carried out in frequency domain, designated by  $f$ . After sampling, only Doppler frequency is considered, as reconstruction by the filters  $P_j(f)$  is carried out in Doppler domain.

In the following, it will be derived how the beamforming network affects the input noise power. In a first step, the noise component of a single channel  $j$  is considered directly after sampling. This noise is made up of the sum of thermal noise and noise introduced by quantization, which are given by  $\sqrt{G_j \cdot F_j} \cdot n_j(f)$  and  $n_{q,j}(f)$ , respectively. In a next step, the influence of the periodic continuation of the signals on the noise power has to be regarded. According to Fig. 40, the original noise spectrum of width *PRF* with its original amplitude is continued  $N$  times to cover the Doppler band of  $N \cdot \text{PRF}$ . This means that  $n_j(f)$  is continued to  $n_{j,p}(f)$  and consequently –

<sup>14</sup>The corresponding intervals to determine the expectation/mean value are reduced accordingly to one dimension, yielding the expression for  $p_{\text{s,el},j}$  as already derived in Section 5.5.



as the mean is determined with respect to  $I_S$  – the noise power is increased by a factor of  $N$ .<sup>15</sup> Then, filtering the noise with  $P_j(f)$  and coherent summation of all channels  $j$  results in the overall noise in the reconstructed data that is denoted by  $n(f)$  and given in (76).

$$n(f) = \sum_{j=1}^N P_j(f) \cdot \left( n_{j,p}(f) \cdot \sqrt{G_j \cdot F_j} + n_{q,j}(f) \right) \quad (76)$$

The respective noise power  $p_n$  is then defined by the mean square value of  $n(f)$  given by (77).

$$p_n := \mathbb{E} \left[ |n(f)|^2 \right] = \mathbb{E} \left[ \left| \sum_{j=1}^N P_j(f) \cdot \left( n_{j,p}(f) \cdot \sqrt{G_j \cdot F_j} + n_{q,j}(f) \right) \right|^2 \right] \quad (77)$$

As  $n_{q,j}$  and  $n_j$  are uncorrelated [76], the overall noise power  $p_n$  simplifies to the sum of the noise powers induced by thermal receiver noise components  $p_{n,\text{rx},j}$  and the quantization  $p_{n,q}$ . Further assuming mutually uncorrelated  $n_j$ , the squared sum representing the receiver noise power in (77) simplifies to the sum of squared values:

$$p_n = \underbrace{\sum_{j=1}^N \mathbb{E} \left[ |n_{j,p}(f) \cdot P_j(f)|^2 \right] \cdot G_j \cdot F_j}_{\text{thermal noise: } p_{n,\text{rx}}} + \underbrace{\mathbb{E} \left[ \left| \sum_{j=1}^N P_j(f) \cdot n_{q,j}(f) \right|^2 \right]}_{\text{quantization noise: } p_{n,q}} = p_{n,\text{rx}} + p_{n,q} \quad (78)$$

Equation (78) quantifies the noise power in the multi-channel data after application of a processing network represented by the filter functions  $P_j(f)$ .

In the following, (78) is simplified by making reasonable assumptions and applying mutual relations between the parameters. The power of  $n_j(f)$  can be expressed by the power at the point of reception  $p_{n,\text{el},j}$ , i.e. the power of  $n_{j,B}(f)$  according to (73), as the sampling changes only the power spectral density of the noise without affecting the noise power itself. For convenience,  $B_{\text{rg}} = B$  is chosen. Taking further into account the factor  $N$  that links the powers of  $n_j(f)$  and its periodic continuation  $n_{j,p}(f)$  as explained above, yields the following expression.

$$p_{n,\text{el},j} = \mathbb{E} \left[ |n_{j,B}(f)|^2 \right] = \mathbb{E} \left[ |n_j(f)|^2 \right] = \frac{1}{N} \mathbb{E} \left[ |n_{j,p}(f)|^2 \right] \quad (79)$$

Finally, all sub-aperture elements  $j$  are assumed to be identical, such that for all elements the same characteristics for  $G_j$ ,  $F_j$ , and thermal noise of same power  $p_{n,\text{el},j}$  are expected. Further, the assumption of spectrally white receiver noise, i.e.  $n_j(f) = n_j$ , allows for separating the noise power and its spectral weighting given by the  $P_j(f)$ , yielding the following expression for the system's output noise power  $p_n$  that consists of a thermal component  $p_{n,\text{rx}}$  and the quantization noise power  $p_{n,q}$ .

<sup>15</sup>The signal is affected the same way, but the filters  $P_j(f)$  are chosen to keep the signal power constant (cf. (57)) and hence account for this scaling. Of course, the periodic continuation could just as well be effectuated to keep the signal and noise power constant. As a result the factor  $N$  in (79) would become unnecessary, but the filters  $P_j(f)$  would change with the result that the factor  $N$  would then be included in these new filters. In any case, the value of  $\Phi_{\text{bf}}$  according to (83) remains unaltered.

$$p_n = \underbrace{p_{n,el} \cdot N \cdot G \cdot F \cdot \sum_{j=1}^N \mathbb{E} \left[ |P_j(f)|^2 \right]}_{\text{thermal noise: } p_{n,rx}} + \underbrace{\mathbb{E} \left[ \left| \sum_{j=1}^N P_j(f) \cdot n_{q,j}(f) \right|^2 \right]}_{\text{quantization noise: } p_{n,q}} = p_{n,rx} + p_{n,q} \quad (80)$$

Due to the mutual correlation of the quantization errors in the channels  $j$ , the scaling of the error by the network can be stronger than the amplification of the thermal noise. In the following, the number of bits is expected to be chosen such that the quantization noise in the output signal will be negligible compared to the thermal noise. This means that the overall noise is approximated by  $p_{n,rx}$ , which is defined by the input noise power and an amplification factor determined by the reconstruction filter network according to (80).

In a next step, the influence of the reconstruction network on the signal power is recalled (cf. Section 5.5). Taking into account the power gain  $G$  of the LNA, the signal power after reconstruction,  $p_s$ , is given by the scaled input signal power  $p_{s,el}$  according to (81).

$$p_s = p_{s,el} \cdot G \quad (81)$$

Combining (80) and (81), the scaling of the  $SNR$  is expressed by (82), where Fig. 45 illustrates the  $SNR_{el}$  and  $SNR_{out}$ , respectively. It quantifies the variation of the  $SNR$  induced by the filter functions  $P_j(f)$  of the multi-channel processing network [46].

$$\frac{p_{s,el} / p_{n,el}}{p_s / p_n} = \frac{SNR_{el}}{SNR_{out}} = F \cdot N \cdot \sum_{j=1}^N \mathbb{E} \left[ |P_j(f)|^2 \right] \quad (82)$$

Note that – in addition to the  $PRF$  dependent reconstruction filters – both signal and noise power may also depend on the  $PRF$ . This possible variation of  $SNR_{el}$  with varying  $PRF$  should be kept in mind in the following.

In a next step, the above derived expression for the  $SNR$  scaling is normalized in order to concentrate on the influence of the processing network. This means that (82) is related to the value obtained for the reference scenario, which is represented by a multi-channel system without applying any processing, i.e. a  $PRF$  leading to uniform sampling. In this case the signals of all channels are simply interleaved and the magnitude of the processing filters is constant for all  $j$  and the complete interval  $I_s$ , as  $|P_j(f)| = 1/N$ . Considering the  $SNR$  per sample, this entails a signal-to-noise ratio decreased by  $F$ , while regarding the average sample energy per time, a signal power increased by a factor of  $N$  is obtained while the noise power rises by a factor of  $F \cdot N$ . Altogether, both perceptions yield a  $SNR_{out}$  worsened by  $1/F$  with respect to the input  $SNR_{el}$ , which is confirmed by inserting  $|P_j(f)| = 1/N$  in (82).<sup>16</sup>

<sup>16</sup>It should be noted that  $SNR_{out}$  refers to a signal sampled at an effective sampling rate of  $N$ -fold the sampling of the input signal. Appendix E gives a detailed overview on the  $SNR$  in mono- and multi-channel systems with special focus on the influence of the effective sampling rate.

Consequently, to concentrate on the effect of the beamforming network, (82) is normalized to the value of  $F$  achieved for uniform sampling. One finally obtains  $\Phi_{\text{bf}}$  as a measure for the variation of the  $SNR$  caused by the multi-channel processing (“beamforming”) network:

$$\Phi_{\text{bf}}(PRF) := \frac{SNR_{\text{el}}/SNR_{\text{out}}}{\left( SNR_{\text{el}}/SNR_{\text{out}} \right)_{PRF_{\text{uni}}}} = N \cdot \sum_{j=1}^N \mathbb{E} \left[ |P_j(f)|^2 \right] \quad (83)$$

As a remark, it should be recalled that the reconstruction filter functions depend on the  $PRF$ , and consequently  $\Phi_{\text{bf}}$  also varies with the  $PRF$ . This is stressed by the definition of (83) that explicitly shows this dependency. Again, in order to provide a succinct notation in the following, the notation  $\Phi_{\text{bf}}$  will be used while neglecting the explicit mention of the  $PRF$ . Further, also  $SNR_{\text{el}}$  might vary with the  $PRF$ , be it caused by signal or noise power. Such a variation is *not* included in  $\Phi_{\text{bf}}$ , although it is of importance for the system  $NESZ$  as it will be discussed in the following section. Fig. 45 illustrates the  $SNR$  scaling factors and the respective  $SNR$  values.

Appendix F presents two further ways of calculating the  $SNR$  scaling factor. The first approach is based on matrix theory and derives  $\Phi_{\text{bf}}$  as a sum of eigenvalues by using the Hilbert-Schmidt norm, while the second method expresses the scaling of the noise power by harmonic functions as presented by [80].

In a further step, the focusing of the data is taken into account to describe the noise power in the image denoted by  $p_{n,B_D}$ . Based on the assumption of white receiver noise, the power spectral density of the noise decreases with increasing  $PRF$  while the noise power remains constant [81]. Hence, to derive an expression for the noise power that remains in the image, the noise power spectral density – defined by noise power and  $PRF$  – in combination with a lowpass filter of bandwidth  $B_D$  has to be considered after the signals are filtered by the  $P_j(f)$ . This yields (84) for the noise power after focusing, which is derived from (80) extended by the rectangular window  $\text{rect}(f/B_D)$  limiting the Doppler spectrum.

$$p_{n,B_D} = p_{n,\text{el}} \cdot N \cdot G \cdot F \cdot \sum_{j=1}^N \mathbb{E} \left[ |P_j(f)|^2 \cdot \text{rect} \left( \frac{f}{B_D} \right) \right] \quad (84)$$

The dependency on the  $PRF$  cannot be seen explicitly, but it follows implicitly from the restriction of the filters  $P_j(f)$  to  $B_D$  and the definition of the  $P_j(f)$  on a bandwidth of  $N \cdot PRF$  over which the mean value is calculated. Hence an increasing  $PRF$  in combination with a constant  $B_D$  means a decreasing spectral part – with respect to  $N \cdot PRF$  – that contributes to the noise power in the image. In the following, this will be referred to as gain by oversampling. Relating the noise power given by (84) to the signal power calculated according to (58), one finally obtains the  $SNR$  scaling factor after focusing.  $\Phi_{\text{bf},B_D}$  quantifies the variation of the  $SNR$  in the SAR image induced by the multi-channel processing and allows thus for estimating the performance of a given system configuration.

$$\Phi_{\text{bf},B_D}(PRF) := \frac{\left( \frac{P_{s,\text{el}}/P_{n,\text{el}}}{P_{s,B_D}/P_{n,B_D}} \right)_{PRF}}{\left( \frac{P_{s,\text{el}}/P_{n,\text{el}}}{P_s/P_n} \right)_{PRF_{\text{uni}}}} \quad (85)$$

In contrast to (83), the exact  $SNR$  scaling factor with respect to the image,  $\Phi_{\text{bf},B_D}$ , cannot be given explicitly, as the relation between input and output signal power depends on the shape of  $U(f)$  in combination with  $B_D$  as defined in (58). If the rough approximation of (59) is applicable then (85) can be modified as shown below:

$$\Phi_{\text{bf},B_D} \approx N \cdot \sum_{j=1}^N \text{E} \left[ |P_j(f)|^2 \cdot \text{rect} \left( \frac{f}{B_D} \right) \right] \quad (86)$$

Note that (85) and (86) incorporate the above mentioned “gain” by oversampling, but do not account for a variation of the  $SNR_{\text{el}}$  with the  $PRF$ . In the case of a constant duty cycle, an increased  $PRF$  entails an increased noise power which results from the increased number of samples per time, each with a constant noise component independently of the  $PRF$ . In other words,  $SNR_{\text{el}}$  degrades with  $1/PRF$  while the oversampling for a constant  $B_D$  increases with  $PRF$ . Altogether, the  $SNR_{\text{out}}$  remains constant independently of the  $PRF$ .<sup>17</sup> In contrast, a constant pulse length ensures a constant  $SNR_{\text{el}}$  as the signal power varies with the  $PRF$  equivalently to the noise power. In this case, the  $SNR_{\text{out}}$  is improved for an increasing  $PRF$  according to the effectively higher signal power which is emitted. In conclusion, a derivation of the  $NESZ$  requires not only  $\Phi_{\text{bf},B_D}$  but has additionally to consider  $SNR_{\text{el}}$ .

As a closing remark it should be noted that receiver noise power and ambiguous power (cf. Section 5.6) are mutually independent, and thus the resulting interfering power in the data and the image can be simply determined by addition of the respective expressions.

## 5.8 Noise Equivalent Sigma Zero ( $NESZ$ ) in Multi-Channel SAR

Finally, the well-known expression for the  $NESZ$  in SAR [18], [82] is recalled and adapted to a multi-channel system. To start, consider a transmitted peak power  $P_{\text{tx}}$  which instantaneously illuminates an area defined by the size  $R_0 \cdot \Theta_{\text{az}}$  representing the azimuth extension of the antenna footprint and by  $c_0 \cdot \tau / \sin(\Theta_i)$ , according to the uncompressed pulse length projected on the

<sup>17</sup>As a simple example, consider a monostatic system operated with constant duty cycle at  $PRF_0$  and  $2 \cdot PRF_0$ , respectively, while keeping the processed bandwidth  $B_D$  constant. This means, with increasing  $PRF$  a decreasing energy per emitted pulse is compensated by more pulses per time and vice versa. Thus, the signal power remains constant. Regarding the noise, the doubled  $PRF$  results in filtering twice the amount of input noise power, i.e. an oversampling gain of 3 dB. In turn, the number of samples *per time* has doubled, while the noise component *per sample* remained constant, yielding an input noise power increased by 3 dB. Altogether, the gain by oversampling is directly compensated by the increased noise power and the overall  $SNR$  remains the same, independently of the  $PRF$ .

ground. Further,  $G_{rx,j}(\theta_{az}, \theta_i)$  and  $G_{tx}(\theta_{az}, \theta_i)$  characterize the gain of a single receive aperture and the transmit antenna, respectively, and the ground reflectivity is represented by the normalized radar cross section  $\sigma^0$ . Finally,  $L$  accounts for all power losses (ohmic, system, atmospheric, etc.), yielding  $P_s$  to quantify the received signal power from a single pulse reflected by the instantaneously illuminated area on ground.

$$P_s = P_{tx} \cdot \frac{G_{tx}(\theta_{az}, \theta_i) \cdot G_{rx,j}(\theta_{az}, \theta_i) \cdot \lambda^2}{(4\pi)^3 \cdot R_0(\theta_i)^4 \cdot L} \cdot \sigma^0 \cdot \frac{R_0(\theta_i) \cdot \theta_{az} \cdot c_0 \cdot \tau}{\sin(\theta_i)} \quad (87)$$

Then, the focused number of pulses in azimuth,  $N_{az}$ , and range,  $N_{rg}$ , according to (88) are taken into account. The corresponding resolution cell on ground  $\delta_{az} \cdot \delta_{rg}$  in dependency of sampling rate  $B_{rg}$  and pulse duration  $\tau$  is given in (89), where the factor  $\varepsilon_{bw} \leq 1$  accounts for resolutions in azimuth above the minimum achievable value. Last but not least, a scene of distributed scatterers is assumed, thus imposing the velocity  $v_s$  to relate  $T_{sa}$  and  $L_{sa}$  with regard to the received signal power, while  $v_g$  would be appropriate for point-like targets [83].  $v_s$  is chosen to provide a lower bound for the signal power, i.e. the worse case is considered in the following.

$$N_{az} \cdot N_{rg} = (PRF \cdot N \cdot T_{sa}) \cdot (B_{rg} \cdot \tau) = \left( PRF \cdot N \cdot \frac{R_0(\theta_i) \cdot \lambda}{d_{az,rx} \cdot v_s} \cdot \varepsilon_{bw} \right) \cdot (B_{rg} \cdot \tau) \quad (88)$$

$$\delta_{az} \cdot \delta_{rg} = \frac{d_{az,rx}}{2 \cdot \varepsilon_{bw}} \cdot \frac{c_0}{2 \cdot B_{rg}(\theta_i) \cdot \sin(\theta_i)} \quad (89)$$

In a next step, (87) is multiplied with (88) while adapting the instantaneously illuminated area on ground according to (89). This eliminates the dependency of the gain factors on  $\theta_{az}$ , but requires accounting for the azimuth loss by  $L_{az}$  according to Section 5.5. As a result for the signal power after focusing, one obtains (90), where  $PRF \cdot \tau$  represents the duty cycle.

$$P_s = \frac{P_{tx} \cdot G_{tx}(\theta_i) \cdot G_{rx,j}(\theta_i) \cdot \lambda^3 \cdot PRF \cdot \tau \cdot N \cdot c_0}{4 \cdot (4\pi)^3 \cdot R_0(\theta_i)^3 \cdot L_{az} \cdot L \cdot v_s \cdot \sin(\theta_i)} \cdot \sigma^0 \quad (90)$$

Note that the effective sampling to determine the overall number of focused pulses is given by  $N \cdot PRF$ , while the duty cycle contains only  $PRF \cdot \tau$ . In consequence, an increased signal power by a factor of  $N$  with respect to a mono-aperture system is obtained.<sup>18</sup> This factor could be combined with  $G_{rx,j}(\theta_i)$  to an equivalent receiver gain  $G_{rx}(\theta_i)$ , which shows the same maximum gain as it would be calculated for the complete antenna area instead of a single-aperture area. However, the notation  $N \cdot G_{rx,j}(\theta_i)$  will be used in the following to explicitly express the dependency on the number of effective receiving channels and to keep in mind that the angular dependency is ruled by the pattern of a single receive aperture.

Next, the thermal noise power is taken into account and quantified by  $k \cdot T \cdot B_{rg}(\theta_i)$ , where  $k$  gives Boltzmann's constant and  $T$  the system's equivalent noise temperature. Further, the de-

<sup>18</sup>For a brief overview on the SNR dependency on the effective sampling rate in multi- and mono-aperture systems, refer to Appendix E.

pendency of the chirp bandwidth  $B_{\text{rg}}$  on  $\Theta_i$  is assumed to ensure a constant range resolution for all incident angles. The description of the noise is completed by the receiver noise figure  $F$ .

In a last step, the expression for the  $SNR$  is extended by the  $SNR$  scaling factor of the reconstruction filter network  $\Phi_{\text{bf},B_D}$  (cf. Section 5.7) which comprises a possible gain by oversampling, but does not account for the changed input  $SNR_{\text{el}}$  with the  $PRF$ . As  $\Phi_{\text{bf},B_D}$  is normalized to  $PRF_{\text{uni}}$ , an additional compensation factor  $\Phi_{\text{NESZ}} = PRF/PRF_{\text{uni}}$  is required. Effectively, this considers the noise power at  $PRF$  with respect to  $PRF_{\text{uni}}$  according to the changed number of samples.

Finally, this leads to the following expression for the image  $NESZ$  of a multi-channel SAR system, taking into account the possible effect of a digital processing.

$$NESZ = \frac{256 \cdot \pi^3 \cdot R_0^3(\Theta_i) \cdot v_s \cdot \sin(\Theta_i) \cdot k \cdot T \cdot B_{\text{rg}}(\Theta_i) \cdot \Phi_{\text{bf},B_D} \cdot \Phi_{\text{NESZ}} \cdot L \cdot F \cdot L_{\text{az}}}{P_{\text{tx}} \cdot G_{\text{tx}}(\Theta_i) \cdot N \cdot G_{\text{rx},j}(\Theta_i) \cdot \lambda^3 \cdot c_0 \cdot PRF \cdot \tau} \quad (91)$$

## 6 Demonstration With Airborne Measured Data

After the theoretical derivation and analysis of the multi-channel reconstruction algorithm in Chapter 5, the present chapter verifies the applicability of the algorithm to measured multi-channel SAR data. This proof-of-concept is carried out with C-band data acquired by the E-SAR sensor [84] (cf. Section 6.1) and with X-band data obtained with F-SAR [85] [86] (cf. Section 6.2), both carried by the German Aerospace Center's airplane Do228. In the first case, the multi-channel C-band data were synthesized from originally mono-aperture data and only used for a first demonstration. In contrast, the X-band data are "real" multi-channel data obtained by two parallel channels of the F-SAR system. These data are subject to more detailed investigations in Section 6.2 which successfully demonstrate the unambiguous recovery of aliased channels for point-like targets as well as for distributed targets.

Note that in general in airborne SAR data, the processed Doppler bandwidth is much smaller than the bandwidth resulting from the azimuth beamwidth in order to allow for presumming. As a result the achieved resolution is clearly larger than the antenna's azimuth dimension. Nevertheless, the applied *PRF* is driven by this antenna dimension and is in the range of  $\sim 1\text{-}5$  kHz while a typical geometric resolution in azimuth of  $\sim 0.5$  m requires – depending on the airplane's velocity – a processed Doppler bandwidth in the order of a few hundred Hertz. This means that the relation between *PRF* and processed Doppler bandwidth provides a high oversampling and does not entail noticeable azimuth ambiguities. In order to "generate" data which allow for the suppression of azimuth ambiguities, these have to be artificially introduced before. Thus, the data is 1) bandpass filtered and then 2) decimated in such a way that one obtains two aliased input channels which lead after multi-channel reconstruction to a single output channel which is effectively sampled according to the Shannon-Nyquist sampling theorem.

### 6.1 Reconstruction of E-SAR Measured Data

In a first proof-of-principle, the derived multi-channel reconstruction algorithm is applied to measured SAR data acquired by the E-SAR system [42]. Since there is no simultaneous multi-channel reception possible with E-SAR, monostatic and already range compressed data are used to synthesize multi-channel data in the following example. As mentioned above, bandpass filtering and decimation of the data are accomplished to obtain two appropriately sub-sampled chan-

nels which can then be unambiguously reconstructed and focused, leading to a SAR image #1 as depicted in the block diagram provided in the left part of Fig. 47. As a reference, a single, sub-sampled channel according to the right part of Fig. 47 will be focused and the resulting SAR image #2 compared to the reconstructed SAR image #1. Table 3 summarizes the relevant parameters.

Parameter	Symbol	Value
Carrier wavelength	$\lambda$	0.0565 m (C-Band)
Sensor height above ground	$h_s$	1155 m
Sensor velocity over ground	$v_s$	72 m/s
Synthesized number of channels	$N$	2
Operated transmit $PRF$	$PRF_{op}$	952 Hz
Effective transmit $PRF$ (after decimation)	$PRF$	47.6 Hz
Processed Doppler bandwidth	$B_D$	70 Hz

Table 3. Relevant E-SAR parameters.

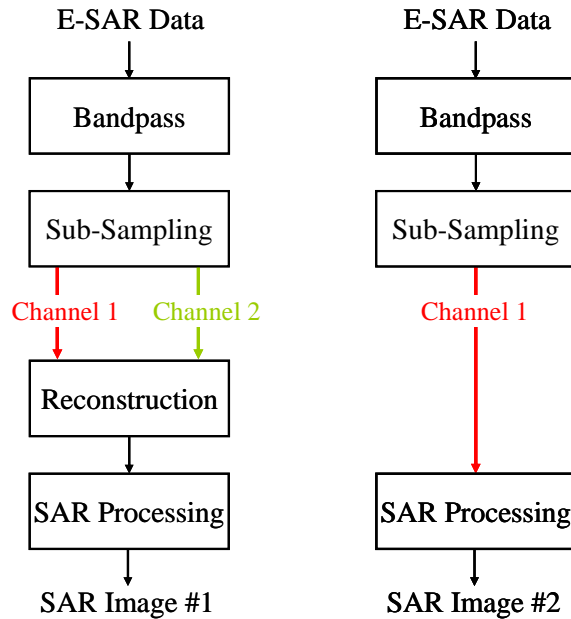
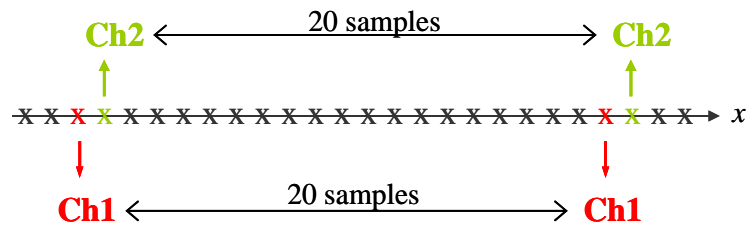


Fig. 47. **Left:** Formation of two ambiguous channels by bandpass filtering, followed by sub-sampling by taking every 20<sup>th</sup> azimuth sample of the original data. **Right:** Single, sub-sampled channel as reference.

Firstly, the data's original Doppler bandwidth of  $PRF_{op}$  is reduced to a bandwidth  $B = PRF_{op}/10$  by an ideal bandpass filter in order to obtain data over-sampled by a factor of 10 (cf. Fig. 47). From these data, two individual channels are “generated” by taking every 20<sup>th</sup> sample of the original data for each channel. This results in two sub-sampled and hence ambiguous inputs, while the combination of both channels yields in average a sufficiently high effective



*PRF* to unambiguously sample the signal bandwidth. To obtain maximum non-uniform sampling, adjacent samples of the original data set were chosen to form the channels while uniform sampling would have required an offset of 10 samples (cf. Fig. 48).



**Fig. 48.** Samples in azimuth dimension  $x$ . The two channels denoted by “Ch1” (red) and “Ch2” (green) are made up by adjacent samples while for each channel every 20<sup>th</sup> sample is taken.

The required reconstruction filters are calculated according to Section 5.1. For the considered case of strong non-uniform sampling, magnitude and phase of the two filter functions  $P_1(f)$  and  $P_2(f)$  are illustrated below:

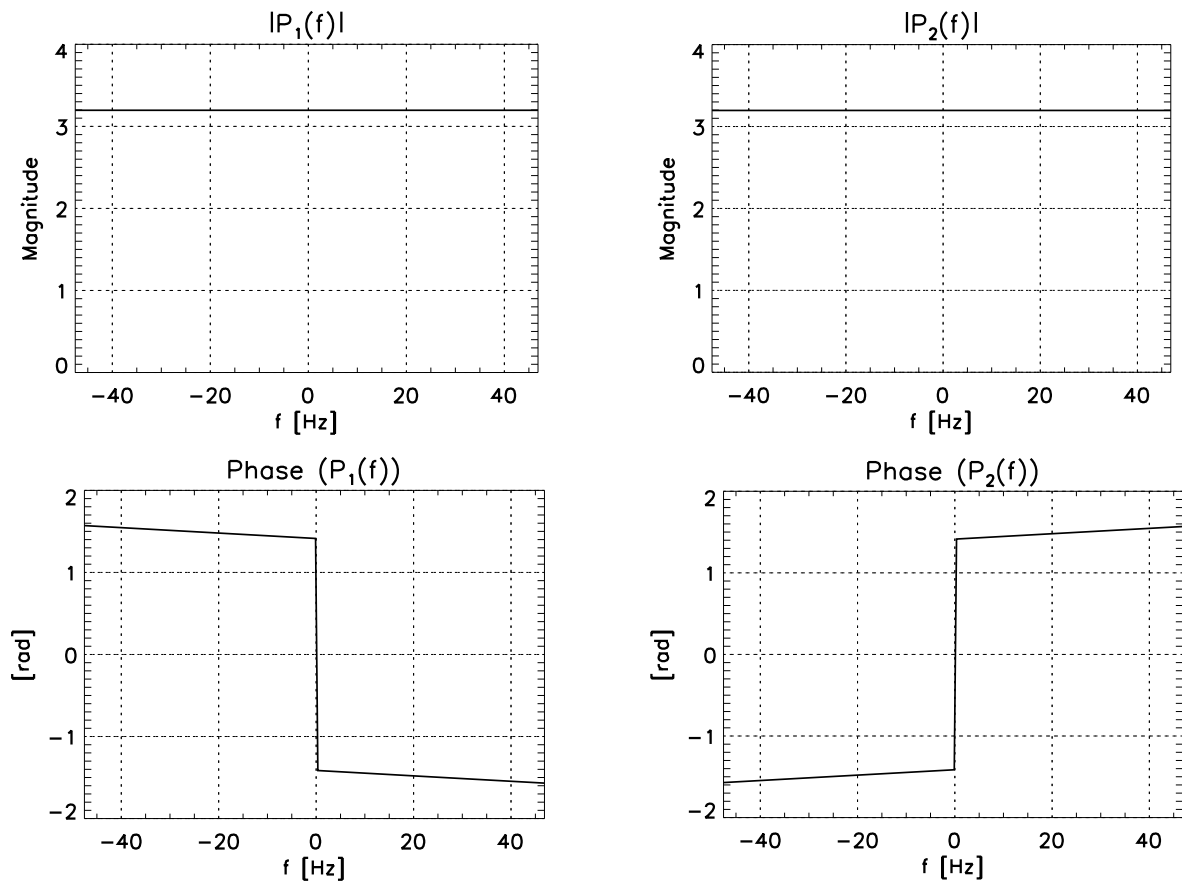


**Fig. 49.** Non-uniform sampling: Magnitude (top) and phase (bottom) of the reconstruction filter functions for channel 1 ( $P_1(f)$ , left) and channel 2 ( $P_2(f)$ , right).

As can be observed, a magnitude of  $\sim 3.2$  is obtained (Fig. 49, top), and the phase (Fig. 49, bottom) shows a linear characteristic within the respective sub-intervals  $I_1$  and  $I_2$ , but a large jump between the intervals. Especially the phase characteristics defined in intervals exemplify that the reconstruction algorithm is more than a mere time shift of the received signals, as this would entail a continuous characteristic of the phase.

In order to demonstrate the effect of the non-uniform sampling, the subsequent Fig. 50 depicts the respective filter functions if the sampling were uniform. As derived, in the optimum case the magnitude of the filter functions is  $1/N=0.5$ . This means that white noise is magnified with a value of 3.2 instead of 0.5 in the optimum case, which illustrates the scaling of the noise power in the case of non-uniform sampling as discussed in Section 5.7. Further, the phase of the filters for optimum sampling show a constant slope, as the reconstruction simplifies to a time shift according to interleaving the samples and – in contrast to the non-optimum case – no jumps between the sub-intervals occur.

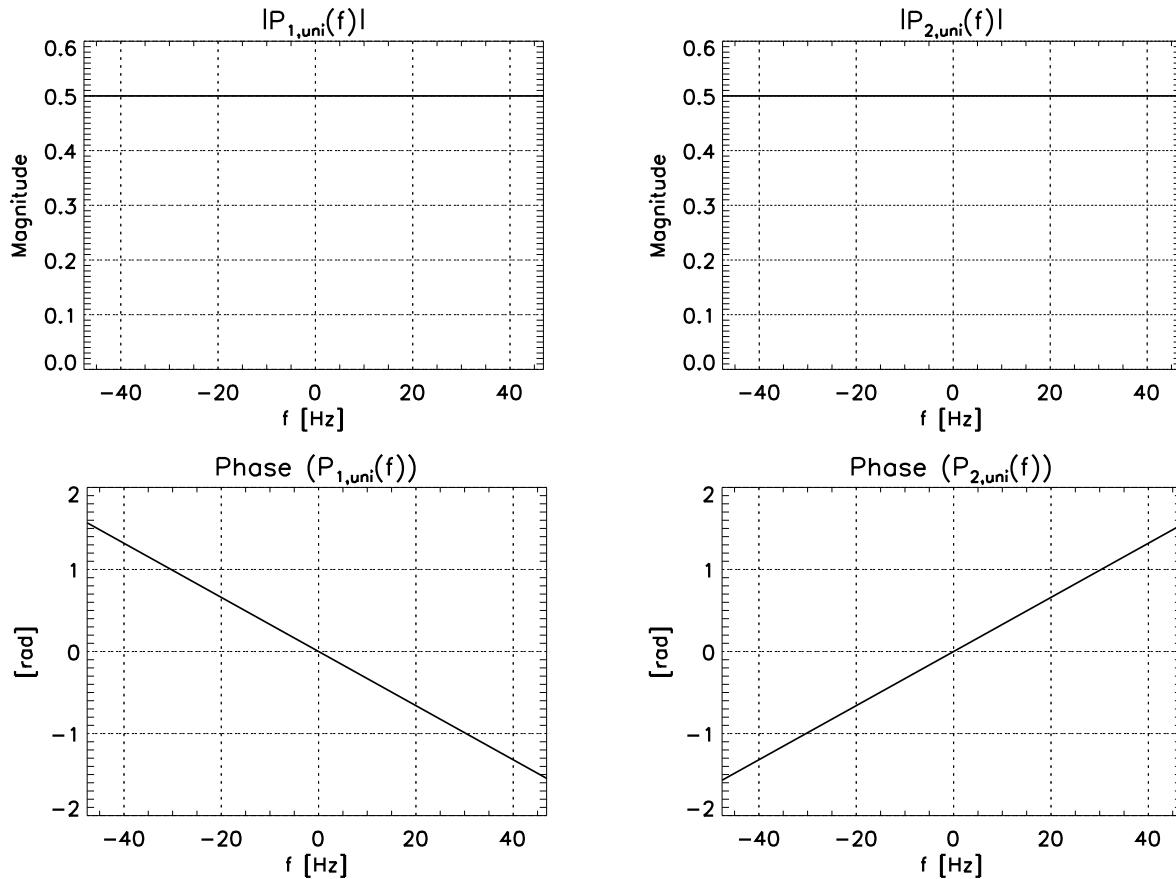


**Fig. 50. Optimum sampling: Magnitude (top) and phase (bottom) of the reconstruction filter functions for channel 1 ( $P_1(f)$ , left) and channel 2 ( $P_2(f)$ , right).**

After multi-channel reconstruction, i.e. the filtering of each channel with its respective  $P_j(f)$  according to Fig. 49 and coherent summation of the resulting output signals, the monostatic SAR processing follows. Fig. 51 compares the obtained SAR image for the reconstruction of two

channels with maximum non-uniform sampling (left,) with the result of a single ambiguous channel (right, SAR image #2). One observes that the non-uniformly sampled signals of the two sub-sampled channels are unambiguously reconstructed and finally lead to a SAR image free of aliasing [42].

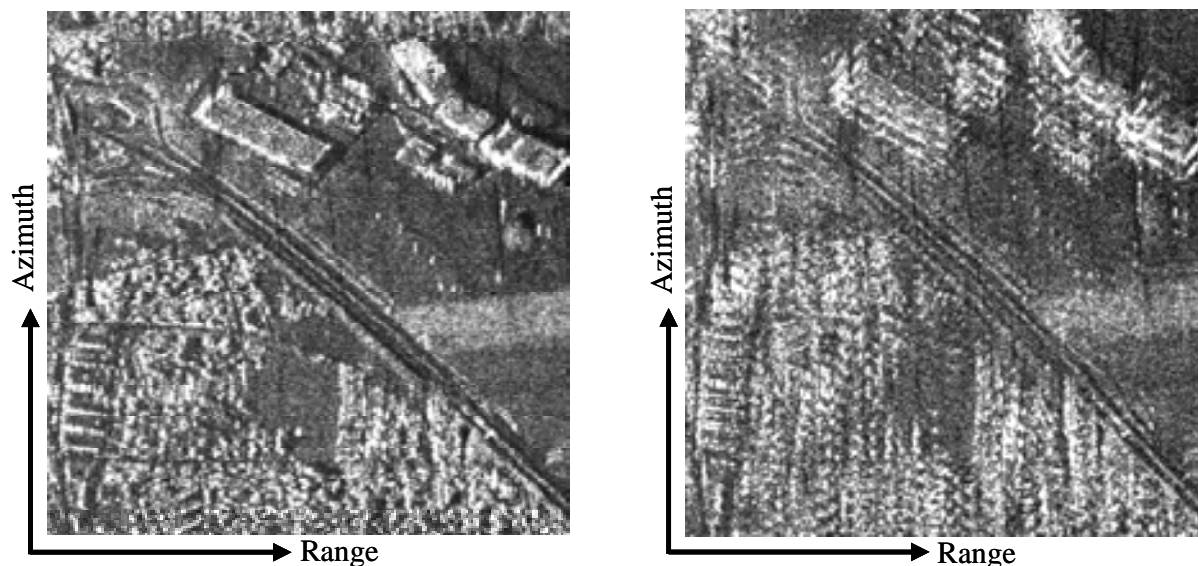


**Fig. 51. SAR image after unambiguous reconstruction of non-uniform sampling (left) and ambiguous image as obtained for a single channel (right).**

In this case the reconstructed image is identical to the reference case given by the monostatic equivalent image, i.e. a uniformly sampled scenario of the same effective *PRF*. Such an optimum performance is achieved, because the data were not real multi-channel data and, consequently, the “two” channels had identical characteristics and no mutually independent noise components were present. The – disturbing – influence of different channel characteristics is demonstrated in the following example, which is based on real multi-channel data.

## 6.2 Reconstruction of F-SAR Measured Data

In contrast to Section 6.1 where a pseudo-multi-channel signal was generated from originally mono-aperture data, the present section deals with a real multi-channel data set obtained by the X-band multi-channel system of the new F-SAR sensor. F-SAR is the successor of E-SAR and is also carried by the Do228 airplane of the German Aerospace Center (DLR). The system had its primal successful flight in November 2006 and the first campaign was conducted in February 2007 over Memmingen in southern Bavaria. At X-band, the F-SAR system allows for the simultaneous reception of two channels which provide the multi-channel data for the following investigations [87]. The relevant key parameters of the acquisition are summarized in Table 4. Detailed information on the F-SAR system can be found on the webpage of the German Aerospace Center [85] and in [86].

Parameter	Symbol	Value
Carrier wavelength	$\lambda$	0.031 m (X-Band)
Sensor velocity	$v_s$	90 m/s
Sensor height above ground	$h_s$	2150 m
Antenna length in azimuth	$d_{az,rx}$	0.2 m
Number of channels	$N$	2
Antenna separation in azimuth	$\Delta x$	0.2 m
Operated transmit $PRF$	$PRF_{op}$	2500 Hz
Effective transmit $PRF$ (after decimation)	$PRF$	312.5 Hz
Optimum transmit $PRF$	$PRF_{uni}$	450 Hz
Processed Doppler bandwidth	$B_D$	365 Hz
Doppler centroid of SAR processor	$f_c$	130 Hz

**Table 4. Relevant F-SAR parameters for demonstration of multi-channel reconstruction using two channels in X-band.**

### 6.2.1 System Setup

In order to demonstrate the applicability of the reconstruction algorithm to real multi-channel data, two simultaneously received X-band channels are taken that were acquired during the Memmingen 2007 campaign.

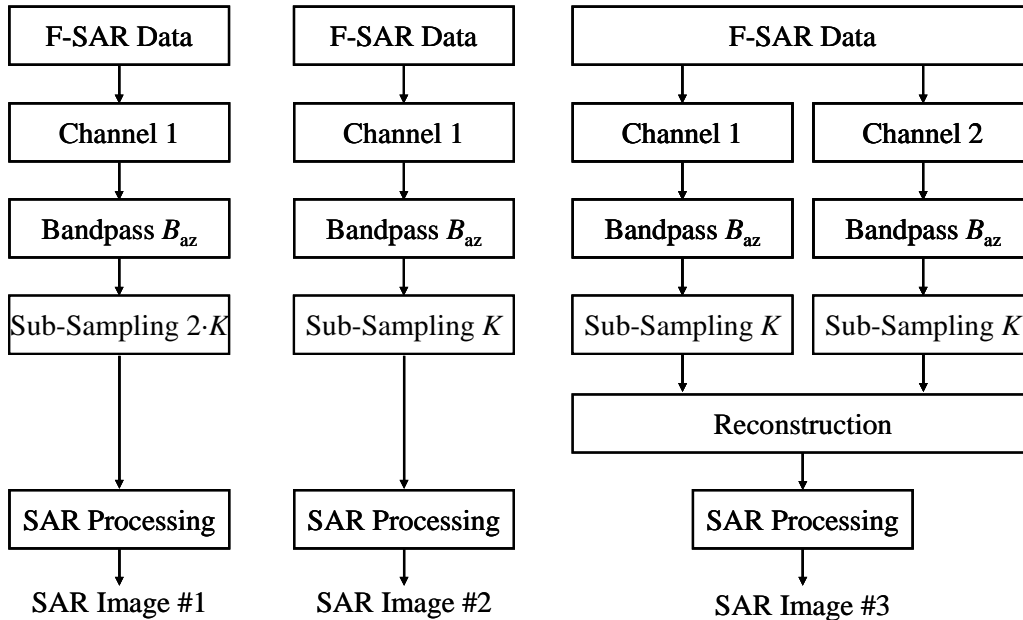


**Fig. 52. F-SAR block diagram for the three investigated scenarios. A Nyquist-sampled monostatic reference (left) and the obtained SAR Image #1 is compared to a sub-sampled single channel (middle) yielding SAR Image #2, and the reconstruction of two aliased channels (right) leading to SAR Image #3.**

In a preliminary processing stage, motion compensation is applied to the range compressed data set of each channel. Further, before multi-channel processing – and similar to the approach presented in Section 6.1 – the data of each channel is bandpass filtered to limit the Doppler frequency to the band  $B_{az} = [-312.5 \text{ Hz}, 312.5 \text{ Hz}]$  (cf. Fig. 52). This is done to allow for a decimation of the data in a next step with the intention to obtain a sampling of the data with a *PRF* in the same order of magnitude as the processed Doppler bandwidth. As explained above, this is necessary to reduce the high oversampling of the data with respect to the processed Doppler bandwidth. In the following, three different data-sets according to Fig. 52 are generated, focused and the resulting SAR images compared.

Firstly, a single channel, which is Nyquist-sampled with a *PRF* of 625 Hz, is generated to provide a unaliased reference signal. Secondly, a single channel is considered, which is sub-sampled by 312.5 Hz, which corresponds to half of the Nyquist frequency. Last but not least, two aliased channels in azimuth dimension are created and reconstructed. According to Fig. 52, this is achieved by decimating each of the channels with a *PRF* of 312.5 Hz, and consequently represents a strong sub-sampling. This means that each of the channels is aliased while the combination of both channels yields in average a sampling that fulfils the Nyquist rate. Considering the spacing of the antennas, one obtains effective phase centers that are separated by  $\Delta x/2 = 0.1 \text{ m}$  while the platform velocity of 90 m/s in combination with the *PRF* yields a distance of  $\sim 0.29 \text{ m}$  between two subsequent samples of the same channel. This means that samples of the two channels are spaced by 0.19 m and 0.1 m, respectively, while a separation of  $\sim 0.15 \text{ m}$  would mean a uniformly sampled data array for the used system *PRF*. Vice versa; a *PRF* of 450 Hz represents the optimum case for uniform sampling. Thus, a clearly non-uniform spatial sampling in azimuth is acquired. The two channels are then processed by the aforementioned multi-channel reconstruction algorithm and combined coherently, yielding a reconstructed SAR signal, which is effectively sampled with a rate of 625 Hz. Note that this corresponds to the same effective sampling in azimuth as the reference scenario mentioned at first.

Then, all signals are focused by a conventional monostatic SAR processor with a Doppler bandwidth of 365 Hz. As the antenna showed a squint angle of  $\sim 1.3^\circ$ , the processed bandwidth is centered on the corresponding Doppler centroid of 130 Hz.

Finally, this allows to compare the obtained SAR images, where the single channel sampled according to Nyquist with 625 Hz data corresponds to the optimum scenario (SAR image #1), while the image of a single channel sub-sampled with 312.5 Hz data represents the worst case (SAR image #2). The image for the reconstructed data (SAR image #3) then allows for demonstrating the performance improvement of the reconstructed image with respect to the worst case, while showing, on the other hand, the further “potential” for improvement defined by the remaining discrepancies to the image quality of the reference signal.

For the given system of two receivers the analytic expression of the reconstruction filter functions can be derived – according to Section 5.1 – as follows, where  $\Delta x_j$  describes the offset of the respective receiver to the transmit aperture. As only the relative distance between the receivers is of importance, one of the  $\Delta x_j$  can in principle be set arbitrarily. According to Table 1,  $\Delta x_1 = 0$  and  $\Delta x_2 = \Delta x$  is chosen.

$$P_1(f) = \begin{cases} \frac{\exp\left(j \frac{\pi \cdot \Delta x_1^2}{2 \cdot \lambda \cdot R_0}\right) \cdot \exp\left(j \frac{\pi \cdot \Delta x_1 \cdot f}{v_s}\right)}{1 - \exp\left(j \pi \cdot \frac{PRF}{v_s} \cdot (\Delta x_2 - \Delta x_1)\right)} & -PRF < f < 0 \\ \frac{\exp\left(j \frac{\pi \cdot \Delta x_1^2}{2 \cdot \lambda \cdot R_0}\right) \cdot \exp\left(j \frac{\pi \cdot \Delta x_1 \cdot f}{v_s}\right)}{1 - \exp\left(j \pi \cdot \frac{PRF}{v_s} \cdot (\Delta x_1 - \Delta x_2)\right)} & 0 < f < PRF \end{cases} \quad (92)$$

$$P_2(f) = \begin{cases} \frac{\exp\left(j \frac{\pi \cdot \Delta x_2^2}{2 \cdot \lambda \cdot R_0}\right) \cdot \exp\left(j \frac{\pi \cdot \Delta x_2 \cdot f}{v_s}\right)}{1 - \exp\left(j \pi \cdot \frac{PRF}{v_s} \cdot (\Delta x_1 - \Delta x_2)\right)} & -PRF < f < 0 \\ \frac{\exp\left(j \frac{\pi \cdot \Delta x_2^2}{2 \cdot \lambda \cdot R_0}\right) \cdot \exp\left(j \frac{\pi \cdot \Delta x_2 \cdot f}{v_s}\right)}{1 - \exp\left(j \pi \cdot \frac{PRF}{v_s} \cdot (\Delta x_2 - \Delta x_1)\right)} & 0 < f < PRF \end{cases} \quad (93)$$

### 6.2.2 Processing Results

The resulting SAR images are given in Fig. 53. They show a small scene around a point-like target represented by a corner reflector on the runway that is marked by a rectangle (middle) and the zoomed slice of the point target's azimuth impulse response (right) for all three scenarios, i.e. the Nyquist-sampled single channel (top), the sub-sampled single channel (middle) and the processed and combined multi-channel data (bottom). The residual ambiguities of the corner reflector are marked with circles in the SAR images and the respective peak values are given in the left column of Fig. 53. Note that the azimuth cut shows a region in the order of the geometric resolution, and consequently the azimuth ambiguities cannot be seen in the given zoom.

The reference scenario does not show any ambiguities and achieves a resolution of 0.31 m (cf. Fig. 53, top). As expected, the sub-sampled channel in the middle of Fig. 53 contains strong azimuth ambiguities and shows much worse image quality. The residual azimuth ambiguities of -12.8 and -14.0 dB, respectively, are highlighted by circles and the azimuth resolution degrades to 0.40 m. Finally, the coherent combination of both sub-sampled channels yields a clearly improved SAR image, as shown in Fig. 53, bottom. Numerically, the peaks of the azimuth ambiguities are reduced from -12.8 dB and -14.0 dB in case of the single channel to -26.3 dB and -25.0 dB, respectively, when applying the multi-channel reconstruction. Besides, the geometric resolution in azimuth is improved from 0.40 m to 0.31 m which is equal to the resolution of the reference scenario, shown on top. Further, it is obvious that the azimuth impulse responses in Fig. 53 do not show the expected  $\sin(x)/x$  behavior due to residual motion errors [88]. These motion errors entail phase errors in the data which lead already to an imperfect focusing of the single channels and increase residual ambiguities in the combination of both channels.

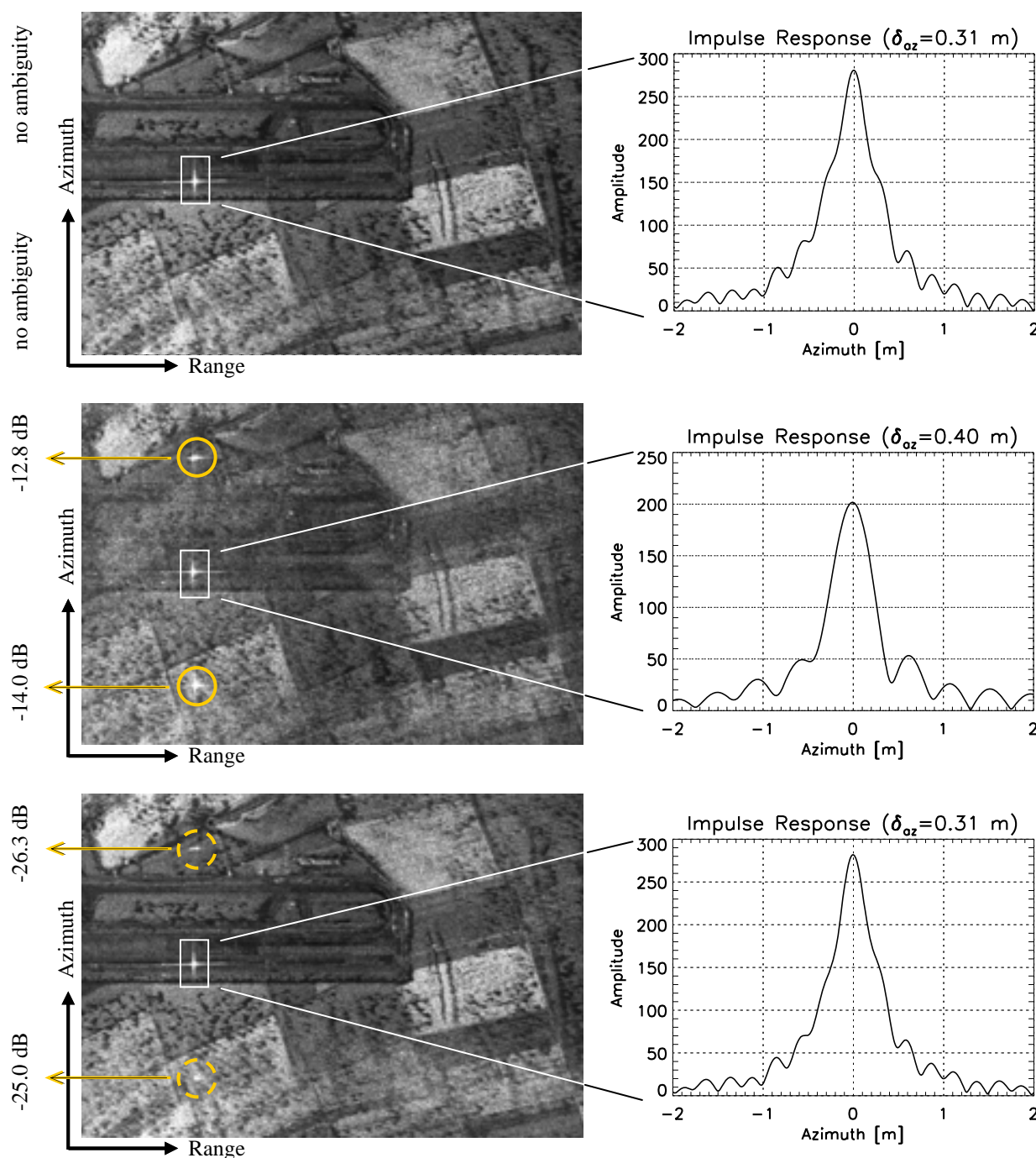


**Fig. 53.** SAR image (left) and zoomed azimuth cut of the point target marked by the rectangle (right). The 1<sup>st</sup> order azimuth ambiguities of the point target are highlighted by the circles and their respective peak values are given on the very left column. **Top:** a Nyquist-sampled single channel as a reference. **Middle:** a single, sub-sampled channel. **Bottom:** the combination of two sub-sampled channels after multi-channel processing.

In a next step, for each of the channels the phase of the mentioned point-like target is analyzed and compared to the expected phase. In this way, the remaining phase error is estimated and a respective correction is applied to the complete data of each channel. Note that this phase

compensation does not only remove residual motion errors but performs also a correction of a possibly misestimated slant range. Fig. 54 shows the results for this “autofocused” SAR data.<sup>19</sup>

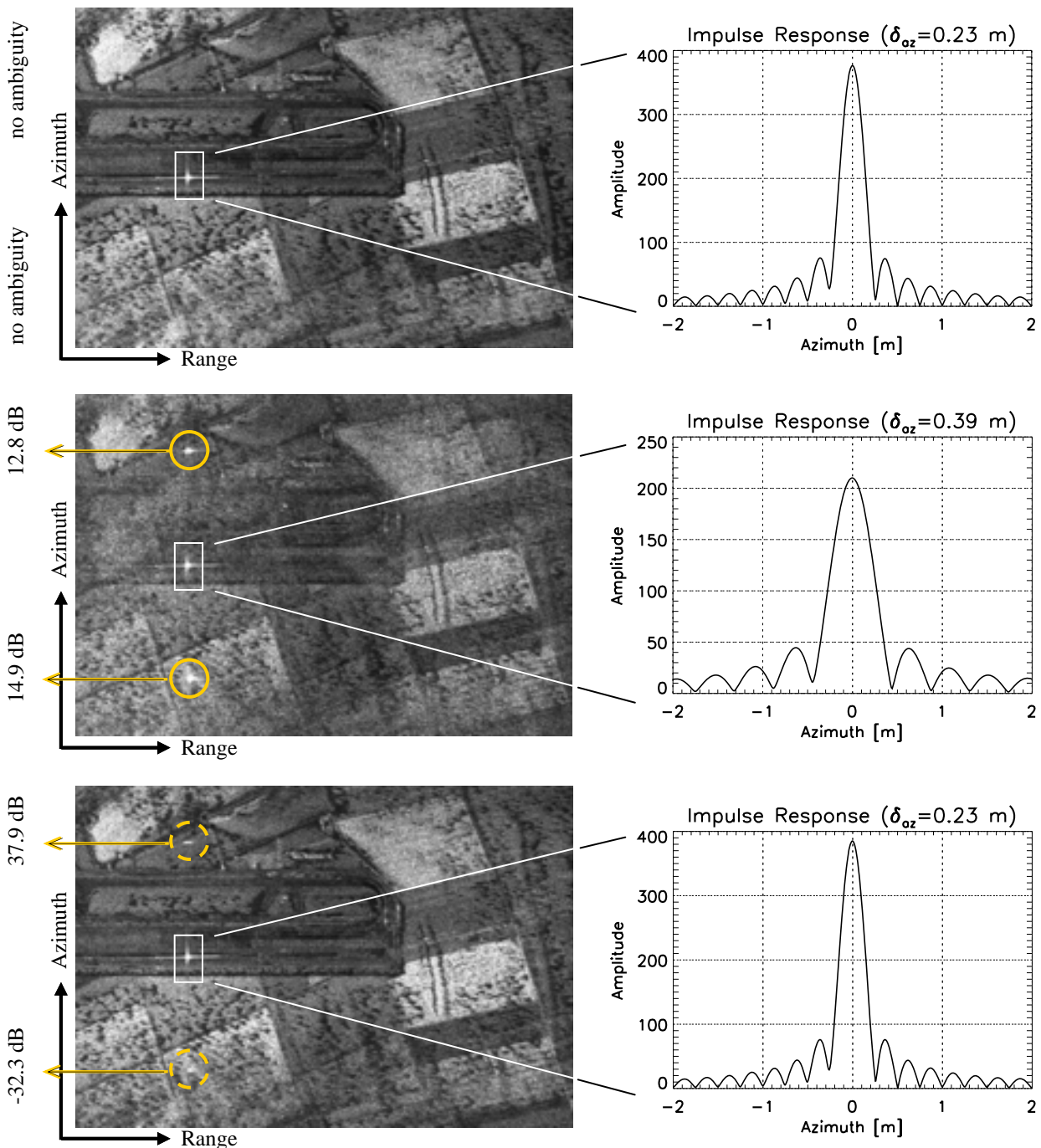


**Fig. 54.** After *autofocus*: SAR image (left) and zoomed azimuth cut of the point target marked by the rectangle (right). The 1<sup>st</sup> order azimuth ambiguities of the point target are highlighted by the circles and their respective peak values are given on the very left column. Top: a Nyquist-sampled single channel as a reference. Middle: a single, sub-sampled channel. Bottom: the combination of two sub-sampled channels after multi-channel processing.

<sup>19</sup>Of course, this corrects only the specific phase errors for the slant range of the point target, but is no valid autofocus for the complete image.



One observes that the impulse responses of all scenarios are now sinc-like shaped entailing a clearly improved azimuth resolution down to 0.23 m in the reference case as well as in the multi-channel scenario. Further, the suppression of the azimuth ambiguities by the multi-channel processing is also clearly improved: While the phase correction does hardly affect the peak ambiguity levels in the case of a single, sub-sampled channel (Fig. 54, middle), the remaining ambiguous returns in the multi-channel case decreased by more than 10 dB and 7 dB down to -37.9 dB and -32.3 dB, respectively (Fig. 54, bottom). For all three scenarios a close-up of the point target and one of its ambiguities marked by a rectangle can be seen in the subsequent Fig. 55.

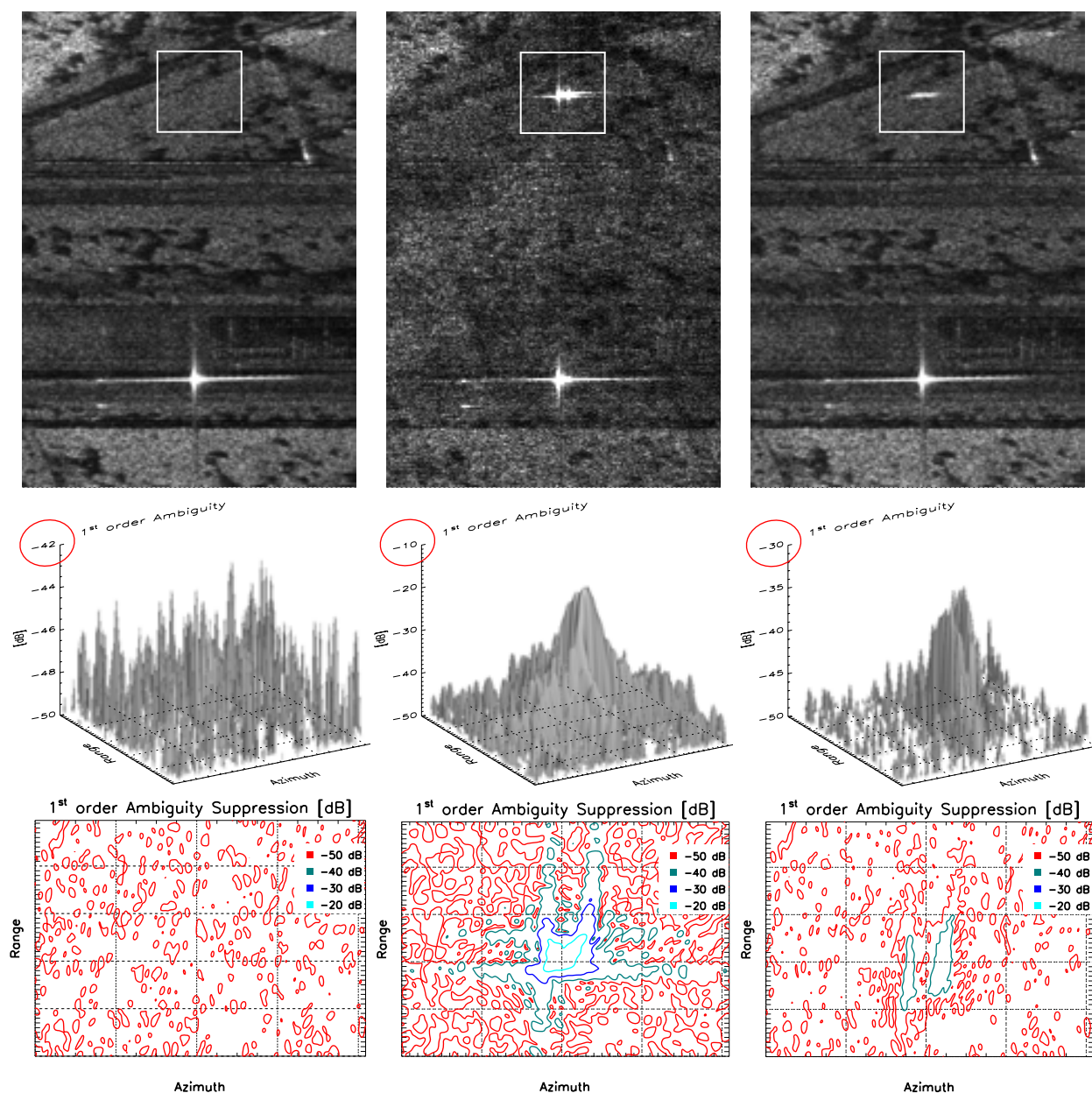


**Fig. 55.** Close-up of Fig. 54: Point target and ambiguity of reference image (left), sub-sampled channel (middle) and multi-channel reconstruction result (right). The surface and contours plots show a zoom (white box) on the respective normalized ambiguity for all scenarios. The improved suppression due to multi-channel reconstruction can be clearly seen.

While the reference image does not show any ambiguity (left column), ambiguities are observed for the single sub-sampled channel (middle column) and the coherent combination of two channels (right column). In order to better illustrate the improvement, a surface (middle row) and a contour (bottom row) plot of the ambiguity are shown for each of the considered scenarios. Compared to the reference image without ambiguity (left), a strong ambiguous return is introduced by the sub-sampling (middle). Application of the multi-channel processing then yields a clearly enhanced suppression as can be observed by comparison of Fig. 55, middle and right.

Regarding range dimension, the clearly larger extension of the point target compared to azimuth can be seen, which results from the different geometric resolutions of  $\sim 1.7$  m and  $\sim 0.3$  m in range and azimuth, respectively. Furthermore, Fig. 55 shows that the point target is not perfectly focused in range dimension. This is caused by the range compression with a reference chirp of linear frequency slope which does not account for higher order terms in the frequency modulation. Due to the experimental status of the multi-channel F-SAR system at the time of the acquisition, no replica was available which could improve the range focusing. As the dissertation concentrates on azimuth, this issue is not further investigated.

To complete this section, a distributed target represented by a vegetated area is investigated. The area is marked by a yellow dotted polygon and is located above the area of low reflectivity which shows the runway (cf. Fig. 56). As can be observed from the sub-sampled channel's image, the ambiguity of the vegetated area is situated on the runway (dashed polygon, Fig. 56, middle). Again, the multi-channel processing yields a clear suppression of the ambiguous energy as illustrated by Fig. 56, right.

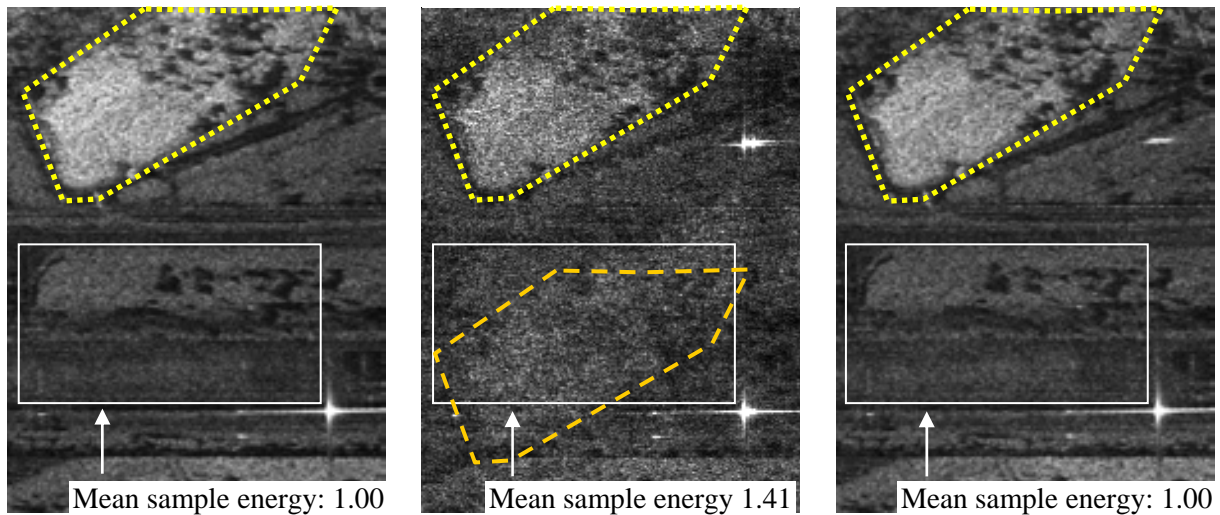


**Fig. 56. Zoom into upper left of Fig. 54. The dotted polygon shows vegetation as an example of a distributed target and its ambiguity in the case of a single sub-sampled channel (middle, dashed polygon). The ambiguity does not show for the reference image (left) and disappears after multi-channel reconstruction (right).**

Quantitatively, a test area is defined which is bounded by the white rectangle and represents the region where the ambiguity is situated (cf. Fig. 56). The mean energy per sample within this

area is then calculated and normalized to the value obtained for the reference image. This analysis reveals – as expected – a value increased by a factor of 1.41 for the sub-sampled image with respect to the reference image where the runway area is not overlaid by the ambiguous energy. In the case of the coherent combination, the value decreases to the reference of 1.00, thus proving the effective cancellation of ambiguous energy within this area.

As a conclusion, it can be stated that the multi-channel reconstruction algorithm provides an effective way to process multi-channel data as it allows for a clearly improved suppression of azimuth ambiguities and for recovering of the unaliased Doppler spectrum also in case of non-optimum *PRF* values entailing strong non-uniform sampling. The recovery of the unaliased Doppler spectrum can be further improved by a correction of the remaining phase errors of the channels, as the application of autofocus leads to a much better suppression of the residual ambiguities. This implies that further calibration and balancing of the two channels bears the potential for additional improvement of the image quality, especially regarding the level of residual ambiguities, which should disappear in the optimum case.



## 7 System Design Example

Chapter 5 derived the multi-channel reconstruction algorithm and Chapter 6 proved its applicability to measured multi-channel data. As a next step, the present chapter turns focus to a complete design example for a multi-channel SAR system that is suited to image a wide swath of 100 km with a high geometric resolution of 1 m. By deriving the system parameters step by step, the design example demonstrates the intricate connection between mission requirements and system parameters in multi-channel SAR systems (cf. Sections 7.1, 7.2). Then the designed system is evaluated by the implemented performance estimator, which enables a point target analysis of multi-channel SAR data. The simulation results demonstrate the capability to perform high-resolution wide-swath imaging (cf. Section 7.4). Within this frame, the theoretically derived expressions regarding azimuth ambiguous energy suppression (cf. Section 5.6) and *SNR* scaling (cf. Section 5.7) are verified by a comparison to the simulated data.

### 7.1 Requirements and Timing

In the following, an X-band high-resolution wide-swath SAR system is designed to image an incident angle range from  $20^\circ$  up to  $55^\circ$  with a swath width of 100 km and a geometric resolution of 1 m. The basic mission performance requirements are summarized in Table 5.

Parameter	Symbol	Value
Carrier wavelength	$\lambda$	0.031 m
Orbit height	$h_s$	500 km – 700 km
Coverage (incident angle)	$\Theta_i$	$20^\circ - 55^\circ$
Swath width on ground	$W_g$	$\geq 100$ km
Geometric resolution in azimuth and range dimension	$\delta_{az}, \delta_{rg}$	$\leq 1$ m

**Table 5. Mission performance requirements.**

Firstly, a detailed timing analysis is performed for a scenario suitable to cover the required incident angle range with six swaths of 100 km each. Based on a duty cycle of 15% and with a variable overlap of adjacent swaths of 10-20 %, an orbit height of 580 km  $\pm$ 10 km proves to be

suitable. The chosen orbit height entails a sensor velocity of 7560 m/s and a footprint velocity on ground of  $\sim 6950$  m/s. The respective timing diagram is shown in Fig. 57 on the left, where the swaths of 100 km each are marked in blue and numbered according to their location from near to far range.<sup>20</sup> In the considered case, the sensor is prevented from receiving by the interference of both the transmit event and the nadir echo. Hence, possible receiving windows which are long enough for a 100 km swath (blue) have to “fit” in between the transmitted pulses (green) and the nadir returns (red). The detailed relation between swaths and incident angles is given in the left columns of Table 6.

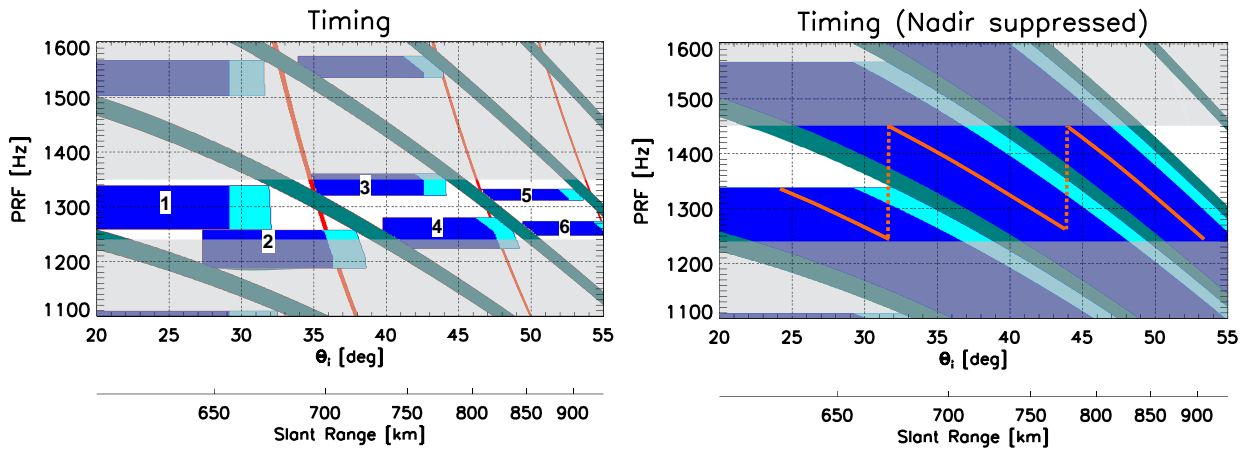


**Fig. 57.** Timing analysis for orbit height of 580 km  $\pm 10$  km and incident angle range from 20-55°. **Left:** Coverage by 6 distinct swaths, each of width 100 km, taking nadir echo (red) and interference of transmit events (green) into account. **Right:** Multi-channel system with nadir echo assumed to be suppressed by digital beamforming in elevation, allowing for swaths centered on arbitrary angles of incidence, which are indicated by the orange line.

Swath	$\theta_i$	$B_{rg}(\theta_{i,min})$	$d_{ev,tx}$	$G_{tx,max}$	PRF	$\Phi_{bf}$
1	20.0° – 29.0°	439 MHz	0.19 m	38.7 dB	1340 Hz	-0.92 dB
2	27.5° – 35.6°	325 MHz	0.22 m	39.4 dB	1250 Hz	0.06 dB
3	34.9° – 41.9°	262 MHz	0.26 m	40.1 dB	1350 Hz	-0.96 dB
4	40.9° – 47.0°	229 MHz	0.30 m	40.7 dB	1260 Hz	-0.12 dB
5	46.4° – 51.7°	207 MHz	0.36 m	41.5 dB	1330 Hz	-0.86 dB
6	50.3° – 55.0°	195 MHz	0.41 m	42.1 dB	1260 Hz	-0.12 dB

**Table 6.** Swaths and respective parameters.

In addition to this, a second system is designed, where the beamforming capability in elevation is assumed to be sufficient for suppressing the nadir echo [89]. Consequently, reception is only restricted by the transmit events, while – in contrast to Fig. 57 on the left – the (red) nadir

<sup>20</sup>The small mutual shift of swaths of same reference number is due to the variable overlap of adjacent swaths.

returns can be neglected, yielding the timing diagram in Fig. 57 on the right. The nadir suppression allows clearly for a more flexible receiving window positioning and thus relaxes the dependency of a specific swath on a certain  $PRF$ . In this case the coverage requirement is modified from distinctly located swaths to swaths centered on an arbitrary angle of incidence.

The timing shows further that for the nominal orbit height a  $PRF$  range from 1250 Hz up to 1350 Hz is sufficient to ensure the coverage of all six swaths (cf. Fig. 57, left). If the height deviates by 10 km, the minimum  $PRF$  decreases to  $\sim 1240$  Hz. In the case where the nadir is suppressed, the same minimum  $PRF$  of 1240 Hz is chosen. To allow for the imaging of an arbitrarily centered swath, the suitable  $PRF$  decreases with increasing incident angle as indicated by the orange line representing the swath's center (cf. Fig. 57, right). When reaching the minimum  $PRF$  of 1250 Hz, a "jump" to a  $PRF$  of 1470 Hz becomes necessary to guarantee continuous coverage (cf. Fig. 57, dotted orange line). Consequently a  $PRF$  range from 1240 Hz up to 1470 Hz has to be covered by the system.

## 7.2 System Parameters

In the following section, the most important system parameters in azimuth as well as in elevation dimension are derived from the mission requirements defined in Section 7.1.

### 7.2.1 Azimuth Parameters

Regarding the geometric resolution in azimuth, a first estimate according to (18) yields a necessary processed Doppler bandwidth in the order of  $\sim 6.25$  kHz to achieve the value of 1 m. As this assumes the optimum rectangular pattern, the obtained value is a lower bound for the required bandwidth which increases for increasing azimuth dimensions of transmit and receive aperture. In combination with the minimum  $PRF$  of the system, this imposes a minimum number of receive apertures, in order to ensure the necessary effective sampling rate on receive. In consequence, the inequality  $N \cdot PRF_{\min} \geq B_D$  has to hold true and requires in the present case a minimum number of 6 receive apertures. Further, the  $PRF$  range of operation and the overall azimuth dimension of the antenna, which determines the optimum  $PRF$ , have to be coordinated. Specifically, the antenna length should lead to an optimum  $PRF$  within the required  $PRF$  range to avoid too large deviations between the optimum and the operated  $PRF$  values. By this, strong non-uniform sampling and the inherent degradation of the  $SNR$  by the digital processing network is prevented. In consequence, an azimuth antenna in the order of 10-12 m is necessary, which defines the sub-aperture size in combination with  $N$ . Finally, the size of the transmit antenna can be chosen more flexible. In general, a larger antenna allows for a better suppression of azimuth ambiguities, but will require a higher processed Doppler bandwidth to ensure the resolution and vice versa.

Hence, within a framework set by the required performance parameters  $W_g$  and  $\delta_{az}$ , the system parameters can be chosen by taking into account the various inter-dependencies illustrated in Fig. 58. In this context, the possible impact on the output performance as  $AASR_N$  and  $NESZ$  has always to be considered. In contrast to conventional systems, no straight-forward design can be

applied, setting one parameter after another, but adaptation of one parameter results in the modification of another, possibly influencing the originally modified parameter. As an example, the azimuth dimensions of transmit ( $d_{az,tx}$ ) and receive ( $d_{az,rx}$ ) aperture affect the required processed bandwidth ( $B_D$ ), which has to be appropriately sampled by  $N \cdot PRF$ . In return, the  $PRF$  is linked to the antenna length ( $l_{az}$ ), which determines in combination with  $N$  the aperture size  $d_{az,rx}$ , closing the “loop” of dependencies.

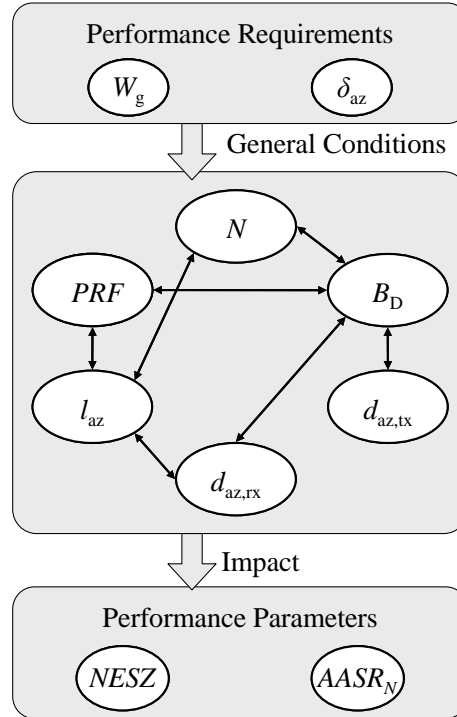


**Fig. 58. Requirements (top) imposing constraints on the system parameters in the middle gray box. Arrows indicate the inter-dependencies of the system parameters which influence the performance parameters shown at the bottom.**

In the present case, fine-tuning of the system with several feedback-loops finally leads to a sensor with an antenna of overall length  $l_{az} = 11.2$  m, corresponding to an optimum  $PRF$  of 1350 Hz (cf. (35)). Regarding the  $SNR$  scaling factor  $\Phi_{bf}$  of the reconstruction network, an acceptable maximum degradation of 0.5 dB is obtained for such a configuration (cf. Fig. 65). For each swath, the specific  $PRF$  determines the respective degradation of the  $SNR$  caused by the recovery of the non-uniform sampling. The values for all swaths are listed in Table 6. Further, the number of receiving channels is increased to  $N=7$ , in order to ensure adequate oversampling. In consequence, a single receive aperture size  $d_{az,rx}$  of 1.6 m is obtained. Based on this size, an analysis of the ambiguous energy shows that a sufficiently high suppression of azimuth ambiguities is achieved with a transmit antenna of length  $d_{az,tx} = 3$  m and without tapering (cf. Fig. 60).<sup>21</sup> For the given antenna dimensions, simulations showed that a processed bandwidth  $B_D$

<sup>21</sup>A detailed analysis of the impact and optimization potential of different antenna lengths and tapering is carried out in Section 8.4.



of 7.6 kHz is needed. Fig. 59 shows an illustration of the system while Table 7 summarizes the system parameters and dimensions.

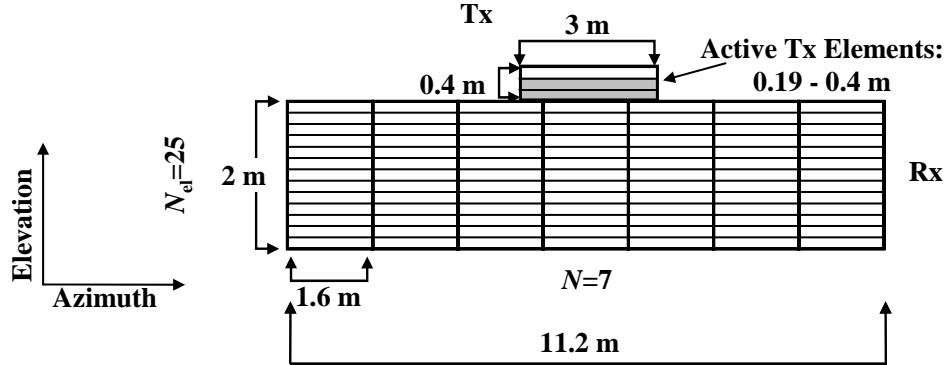


Fig. 59. Illustration of system architecture and antenna dimensions.

Parameter	Symbol	Value
Orbit height	$h_s$	580 km $\pm$ 10 km
Slant range	$R_0$	604 km – 1112 km
Sensor velocity	$v_s$	7560 m/s
Footprint velocity on ground	$v_g$	6950 m/s
PRF range	PRF	1240 Hz – 1470 Hz
Receive aperture size in azimuth	$d_{az,rx}$	1.6 m
Number of Rx apertures in azimuth	$N$	7
Overall receive antenna length in azimuth	$l_{az}$	11.2 m
Transmit antenna size in azimuth	$d_{az,tx}$	3.0 m
Receive aperture size in elevation	$d_{ev,rx}$	0.08 m
Number of Rx apertures in elevation	$N_{el}$	25
Overall receive antenna height in elevation	$h_{ev,rx}$	2 m
Transmit antenna size in elevation	$d_{ev,tx}$	0.19 m – 0.41 m
Maximum transmit antenna gain	$G_{tx}$	38.7 dB – 42.1 dB
Receive antenna gain	$G_{rx}$	54.7 dB
Transmit peak power	$P_{tx}$	5 kW
Duty cycle	$dc$	15 %
System noise temperature	$T$	300 K
Losses (atmospheric, system, receiver noise, 2-way)	$L \cdot F$	5.7 dB
Azimuth loss	$L_{az}$	2.7 dB
SNR scaling factor of digital filter network	$\Phi_{bf}$	$\leq 0.5$ dB

Table 7. System parameters, requirements, and constants.

### 7.2.2 Cross-Track Parameters

To ensure a slant range resolution of 1 m, a chirp bandwidth of 150 MHz is necessary and hence the appropriate bandwidth  $B_{rg}$  for the required ground range resolution of 1 m is given by the projection of the slant range on ground. This means that depending on the incident angle  $\theta_i$  a bandwidth of 150 MHz/sin( $\theta_i$ ) is necessary. Consequently, for each swath the required minimum bandwidth in range depends on the minimum incident angle  $\theta_{i,min}$  of the respective swath, thus yielding for the considered incident angle range values from 195 MHz in far range up to 439 MHz in near range. The respectively necessary chirp bandwidths are summarized in Table 6.

Further, the 3 dB beamwidth of the transmit antenna,  $\theta_{ev}$ , is chosen adaptively to illuminate for all incident angles a swath of 100 km on ground. Depending on the respective slant range, this requires different angles  $\theta_{ev}$ , which are approximated in degrees by  $51 \cdot \lambda / d_{ev,tx}$  according to [90]. Consequently, the effective height  $d_{ev,tx}$  of the transmit antenna is varied to always guarantee the required coverage. The height variation is achieved by assuming an antenna consisting of multiple elements in elevation, which can be individually activated while ensuring constant transmit peak power independent of the antenna area.<sup>22</sup> This results in effective transmit antenna heights from 0.19 m to 0.41 m corresponding to a maximum antenna gain  $G_{tx,max}$  from 38.7 dB to 42.1 dB, respectively (cf. Fig. 59, Table 6). The selection of the respective swath can be either achieved by an electrical steering of the transmit beam or a mechanical steering of the antenna by a roll-maneuver of the satellite. In the following, a mechanical steering is assumed that ensures an optimum pointing of the antenna to the region to be imaged. Table 6 summarizes the respective values for the effective transmit antenna height  $d_{ev,tx}$  and corresponding maximum antenna gain  $G_{tx,max}$ .

On receive, the antenna in elevation consists of a large number of independent elements that allow for beamforming in elevation, which ensures a high gain and a sufficient suppression of range ambiguities. For this, one may apply the scan-on-receive (SCORE) technique suggested in [29] and [31] that uses a real-time beamforming to scan the reflected pulse as it travels over the ground.<sup>23</sup> This allows for assuming an approximately constant gain  $G_{rx}$  with varying incident angle  $\theta_i$  that is defined by the maximum gain of the overall receiving antenna. Problems may occur with this technique by topography and it might be necessary to apply a more sophisticated approach to cope with the problems arising from height variations within the scene [61], [64]. In

<sup>22</sup>Such an assumption requires the “decoupling” of radiated power and effective transmit height which determines the footprint. To achieve this, one could e.g. think of an analog solution enabling to switch the power feeds, thus radiating a higher power per area if the transmit antenna height is reduced. Another possibility would be an appropriate implementation of a frequency multiplex technique on transmit [91]. This method allows for decoupling the overall antenna height and the elevation pattern by dividing the chirp bandwidth into multiple sub-bands and emitting each of these bands by a different part of the transmit antenna. A detailed investigation of this issue is beyond the scope of this work.

<sup>23</sup>It should be noted that a very large antenna height might result in a very narrow footprint which no longer covers the complete pulse on ground resulting in a gain loss for certain frequency components of the chirp. In this case, a frequency dependent steering has to be implemented as addressed in [31] and elaborated in [92].

order to guarantee the steering capability of the elevation beam to cover a swath of 100 km, a scan angle up to  $\pm 4.5^\circ$  with respect to antenna boresight is necessary. The necessary element spacing in elevation to avoid grating lobes is chosen to be 8 cm [51] while a sufficiently high gain on receive – to achieve the required low *NESZ* – is ensured by a receiving antenna height  $h_{\text{ev,rx}}$  of 2 m, entailing a gain  $G_{\text{rx}}$  of 54.7 dB. In combination with the minimum element spacing of 8 cm the receive antenna height results in a number of 25 sub-antenna elements. Fig. 59 gives an illustration of the system and Table 6 and Table 7 summarize the parameters in elevation dimension.

### 7.3 Simulation Environment

In order to evaluate multi-channel SAR signals, a performance estimator was implemented with the programming language IDL. The estimator enables a point-target analysis for arbitrary multi-channel SAR systems in order to derive the performance parameters of the system. This includes the possibility to simulate advanced systems as e.g. cascaded networks or pattern tapering (cf. Chapter 8) or innovative approaches as multi-channel burst mode operation (cf. Chapter 9). This “toolbox” is complemented by further tools which allow for an analytical calculation of the  $AASR_N$  and the *SNR* scaling factor, thus enabling a prediction and/or verification of the simulated results.

Regarding the point-target analysis, the processing flow is as follows: For a given set of parameters, the simulation starts with the generation of SAR data for a point-like target as it is received for each of the receive apertures. Hence a number of  $N$  point target echoes sampled with a rate of *PRF* are generated. These received signals are then weighted according to the respective algorithm and added coherently, yielding a SAR signal with an effective sampling rate of  $N \cdot PRF$ . This signal is then focused by a filter function which corresponds to a band-limited point target echo generated with an effective sampling rate of  $N \cdot PRF$ . The band limitation is chosen according to the processed Doppler bandwidth  $B_D$  and the amplitude of this filter is normalized. The performance parameters are then determined from the obtained time domain impulse response of the point-like target.

This simulation flow is repeated for varying *PRF* values in order to cover the required *PRF* range of operation. The following results are obtained by point-target performance analysis and the respective prediction tools.

### 7.4 System Performance

In this section a point target analysis of the example system is performed to determine key performance figures such as  $AASR_N$ , geometric resolution, signal peak power and *SNR*, or rather *NESZ*. In the case of the azimuth ambiguous energy suppression and the *SNR* scaling, the simulated results are compared to their analytic predictions as derived in Chapter 5.

### 7.4.1 Azimuth-Ambiguity-to-Signal Ratio: $AASR_N$

In a first step, the suppression of azimuth ambiguities of distributed targets ( $AASR_N$ ) is simulated within the relevant  $PRF$  range and compared to its analytic prediction according to (71) derived in Section 5.6. The  $AASR_N$  is calculated by simulating a point target response and integrating the energy of all relevant ambiguous responses. This ambiguous energy is related to the integrated energy of the main response representing the “real” target.

The obtained results for both the simulation (solid red line) and the prediction (dashed blue line) in Fig. 60 show an ambiguous energy suppression of better than -21 dB over the complete  $PRF$  range of operation which is bounded by the gray-shaded areas. This represents a slightly better performance than TerraSAR-X, which achieves a value of -20 dB [93].

Further, one recognizes that the  $AASR_N$  improves with increasing  $PRF$  although an in-depth analysis of (71) reveals an increasing mean squared value of the filter functions  $P_j(f)$  with increasing deviation from the optimum  $PRF$  of 1350 Hz. In consequence, the amplification of the ambiguous energy by the processing network rises. This is mitigated or even compensated by the rising effective sampling rate, which entails decreasing ambiguous contributions in the received signal. According to Fig. 60, the benefit from the increased sampling exceeds the amplification of the ambiguities in the considered case. Note that the special  $PRF$  value entailing coinciding samples is 1575 Hz (cf. Section 4.3.3), which lies outside the covered  $PRF$  range. Such a  $PRF$  results in an infinite amplification as  $\mathbf{P}(f)$  becomes singular.

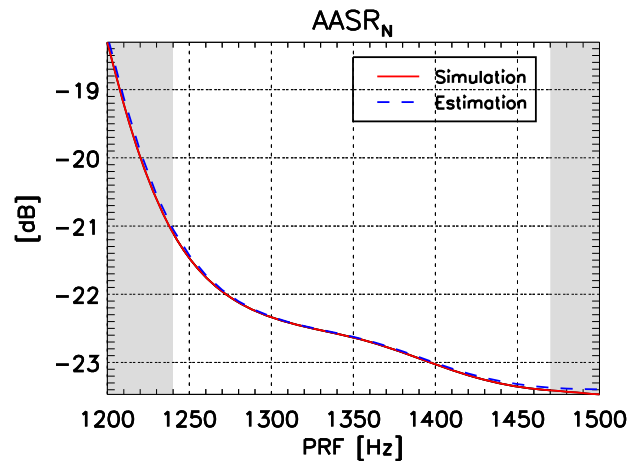


**Fig. 60.** Simulated azimuth ambiguous energy suppression ( $AASR_N$ ) vs.  $PRF$  (solid red) and its prediction (dashed blue).

Fig. 60 already indicates a good agreement between prediction and simulation. The estimation error defined by the ratio between the two curves of Fig. 60 is given in Fig. 61 that reveals a maximum deviation of less than 0.1 dB, which is probably caused by the finite number of ambiguities considered for the estimation. Hence, (71) gives a valid prediction of the residual azimuth ambiguous energy.

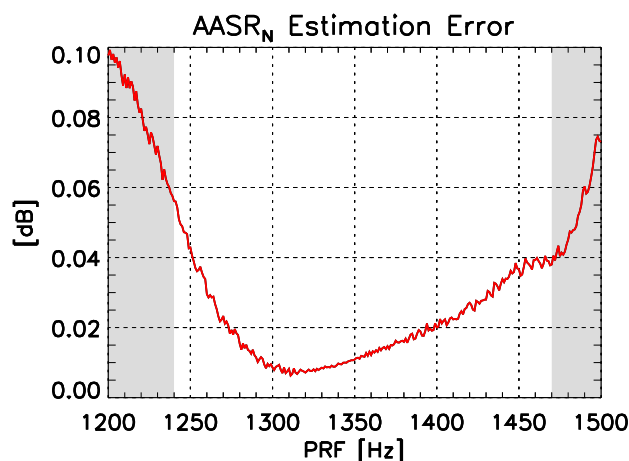


**Fig. 61. Estimation error: Ratio between prediction and simulation of  $AASR_N$  vs.  $PRF$ .**

Next, the multi-channel reconstruction algorithm is compared to alternative algorithms for processing the multi-channel azimuth signal and the results for the azimuth ambiguous energy suppression  $AASR_N$  for the different investigated approaches are presented in Fig. 62.

As a first reference case, the samples of the multiple azimuth channels are simply interleaved yielding the output signal without further processing as proposed in [24] (cf. Section 3.3.2). In a more complex approach, the method of [40] takes the properties of the SAR signal into account. The approach compares the multi-channel signal's phase to the phase of a monostatic and uniformly sampled signal thus yielding a Doppler frequency-dependent phase difference between the actual and the desired signal. This phase difference is corrected by the applied weighting functions (cf. Section 3.4.3). Finally, a space-time approach is evaluated that is based on adaptively adjusting the weighting coefficients of the azimuth channels to steer the nulls in the resulting joint antenna pattern to the angles corresponding to the ambiguous Doppler frequencies. This null-steering corresponds to a spatial filtering of the data to suppress ambiguous frequencies in

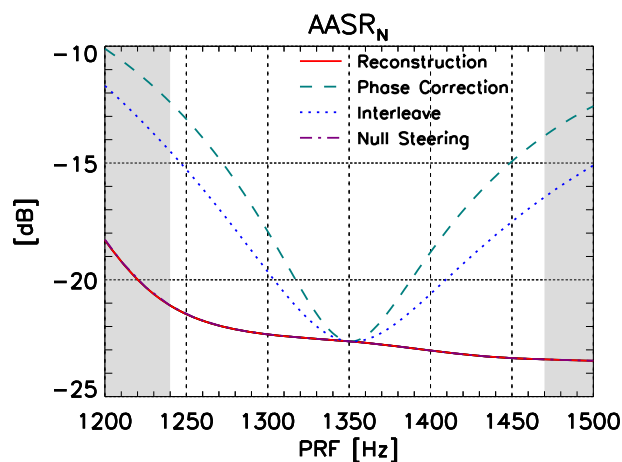


**Fig. 62. Azimuth ambiguity suppression ratio ( $AASR_N$ ) achieved by reconstruction algorithm (solid red) compared to phase correction (dashed green) [40], simple interleaving of samples (dotted blue) [24] and pattern null-steering (dashed light blue) [48]. Null-steering and reconstruction yield nearly identical results. The  $PRF$  region of interest is defined by the shaded areas.**

the azimuth signal [48] (cf. Section 3.4.4). For a more detailed explanation of the different processing methods, refer to Chapter 3 and for a concise overview refer to [52].

The best suppression is achieved by the reconstruction algorithm and the null-steering approach that both provide a sufficient suppression of at least -21 dB over the complete range of  $PRF$ . Note that under certain approximations the null-steering approach is already included in the reconstruction algorithm as shown in Appendix D. In contrast, the phase correction technique and the simple interleaving of channels only yield an acceptable suppression for  $PRF$  values close to the optimum of 1350 Hz but fail with increasing deviation from the uniform sampling case. A suppression of -21 dB or better is only ensured for a  $PRF$  within the interval [1325 Hz, 1380 Hz] for the phase correction technique and [1315 Hz, 1395 Hz] for interleaved channels, respectively. For the boundaries of the considered  $PRF$  interval, unacceptably high values up to -13 dB and -14.5 dB are obtained, respectively.

This leads to the conclusion that an effective cancellation of ambiguities is only provided by “system-based” beamforming concepts, which means that the weighting function of each channel is gained by considering the geometric information of all other channels. In contrast, a “channel-based” processing, where only the information of the single channel with respect to an optimum scenario is taken into account to obtain the respective weighting function, cannot ensure sufficient suppression of ambiguous energy for  $PRF$  values deviating from the optimum  $PRF$ . This is confirmed by the results obtained for several approaches that are all based on the interpolation of the single channels’ signals. Similar to the simple interleaving of samples, this yields an acceptable  $AASR_N$  only close to the optimum  $PRF$  [94].

#### 7.4.2 Geometric Resolution in Azimuth: $\delta_{az}$

The geometric resolution in azimuth is denoted by  $\delta_{az}$  and defined as the 3 dB width of the focused point target impulse response in azimuth dimension.

Fig. 63 shows that all approaches achieve an azimuth resolution below 1 m for the optimum  $PRF$  of 1350 Hz. Over the whole  $PRF$  range, only the multi-channel processing approaches

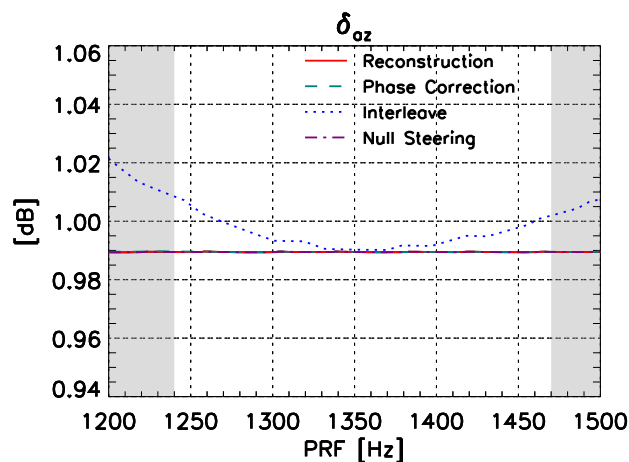


**Fig. 63. Geometric resolution in azimuth,  $\delta_{az}$ , vs.  $PRF$ . While the resolution for the simple interleaving of samples degrades with increasing offset from the optimum  $PRF$ , all other approaches yield – identically – a constant resolution.**

(phase correction, null-steering, reconstruction algorithm) provide a constant resolution of  $\sim 0.99$  m, while the resolution degrades for increasing offset from the optimum  $PRF$  if no dedicated processing is applied and the samples are simply interleaved. Although the degradation is only up to 1.01 m within the considered range of  $PRF$ , it becomes clear that a simple interleaving of samples cannot ensure a constant resolution independent from the respective  $PRF$  value.

### 7.4.3 Signal Peak Power: $p_{s,max}$

The signal peak power describes the normalized maximum power of the point target impulse response as it varies with the  $PRF$ . For each investigated algorithm, the normalization of the peak power characteristic is done by the respective maximum value obtained at the optimum  $PRF$  of 1350 Hz. Fig. 64 presents the results for the example system. Similar to the characteristic of the resolution, all multi-channel approaches, i.e. the phase correction technique, multi-channel reconstruction and null-steering, ensure a constant peak power of the focused point target impulse response, while a simple interleaving of samples results in a drop-off of signal power with increasing deviation from the uniform  $PRF$ . The worst degradation is obtained at the boundaries of the  $PRF$  interval with a decay of -0.2 dB.

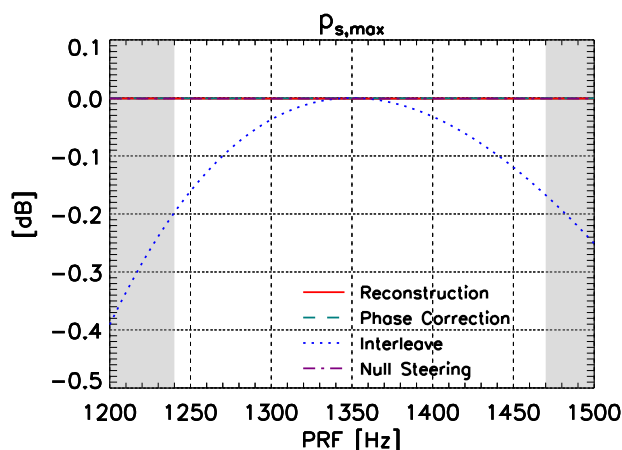


**Fig. 64.** Normalized signal peak power of azimuth impulse response  $p_{s,max}$  vs.  $PRF$ . While the peak power for the simple interleaving of samples reduces with increasing offset from the optimum  $PRF$ , all other approaches ensure – identically – a constant peak power.

### 7.4.4 SNR Scaling – Prediction and Simulation

In a preliminary step to determine the noise equivalent sigma zero ( $NESZ$ ) of the system, the  $SNR$  scaling factor  $\Phi_{bf}$  is measured from simulated data and evaluated theoretically according to the expressions derived in Section 5.7 (cf. Fig. 65).<sup>24</sup>

<sup>24</sup>Keep in mind that  $\Phi_{bf}$  describes the relation between the input and the output  $SNR$  as defined in Section 5.7, but does not include the decreasing  $SNR$  per gathered sample at the input with increasing  $PRF$  as encountered for a constant duty cycle. For the following calculation of the  $NESZ$ , additionally the  $1/PRF$  dependency of the input  $SNR$  will be considered.

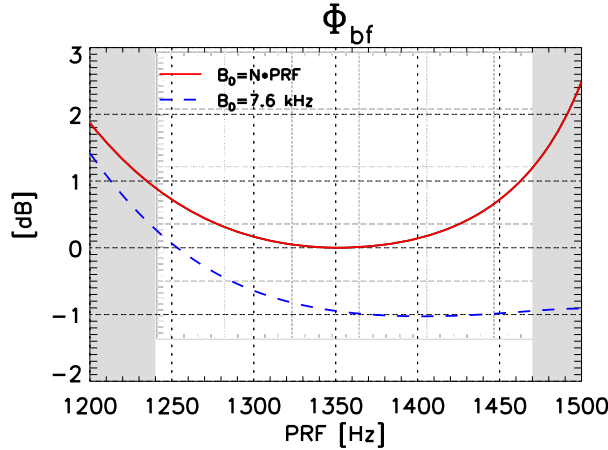


**Fig. 65.** Analytic estimation of the  $SNR$  scaling factor  $\Phi_{bf}$  vs.  $PRF$  due to the signal reconstruction for a constant Doppler bandwidth  $B_D = 7.6$  kHz (dashed blue) and for the whole bandwidth  $N \cdot PRF$  (solid red).

Similar to the  $AASR_N$ ,  $\Phi_{bf}$  worsens with increasing deviation from the optimum  $PRF$  due to the rising mean squared value of the  $P_j(f)$ . Again, the amplification tends to infinity when the  $PRF$  entails spatially coinciding samples and the whole system bandwidth in azimuth is considered (cf. Fig. 65, solid red line). As previously mentioned, for the considered system example this “singularity” is caused by a value of 1575 Hz. This effect is compensated by the increasing oversampling caused by rising  $PRF$  values in combination with a constant processed Doppler bandwidth  $B_D$  (cf. Fig. 65, dashed blue line). This results in an increasingly reduced output noise power compared to the input, while the signal power remains nearly constant. For uniform sampling, the noise spectrum after reconstruction is white and consequently the difference between the two curves is dominated by the reduction of noise power according to the relation between  $B_D$  and effective sampling, i.e.  $N \cdot PRF$ . As a result, the  $SNR_{out}$  is improved by  $B_D / (N \cdot PRF_{uni})$  compared to the  $SNR_{in}$  at this  $PRF$ . In the present case this leads to the offset of 0.95 dB as can be seen from Fig. 65.

An investigation of the spectral properties of  $\Phi_{bf}$  shows that the degradation of the  $SNR$  for strong non-uniform sampling is dominated by the lowest and highest sub-bands within the Doppler band covered by  $P_j(f)$ , i.e. the bandpass filters  $P_{jm}(f)$  defined on the spectral sub-bands  $I_m$  of order  $m = 1$  and  $m = N$ , where  $I_m = [-N \cdot PRF / 2 + (m-1) \cdot PRF, -N \cdot PRF / 2 + m \cdot PRF]$ . Consequently, the singularity of the noise and ambiguity scaling for spatially coinciding samples (cf. Section 7.4.1) is caused by these sub-bands, while the contribution of the other sub-bands to the scaling is not critical.<sup>25</sup> An example is given by Fig. 66 that shows the spectral weighting of the noise spectrum vs. Doppler frequency by the reconstruction filter functions for a nearly uniform  $PRF = 1350$  Hz (left) and a strong non-uniform sampling case with  $PRF = 1520$  Hz (right), which is close to the singular  $PRF$  at 1575 Hz. For the non-uniform  $PRF$  the mean value over the complete bandwidth is much higher while the mean value within the processed Doppler bandwidth, indicated by the

<sup>25</sup>This seems logical from an information theoretical point of view as the samples remaining when skipping the coinciding channels still yield an effective sampling rate which fulfills the Nyquist criterion for these bands.



gray-shaded area, only shows a moderate rise as the strong rise is dominated by the outermost sub-bands that are filtered when focusing (cf. Fig. 66). This explains the rising difference between the two characteristics in Fig. 65 as  $PRF$  values are getting closer to 1575 Hz.

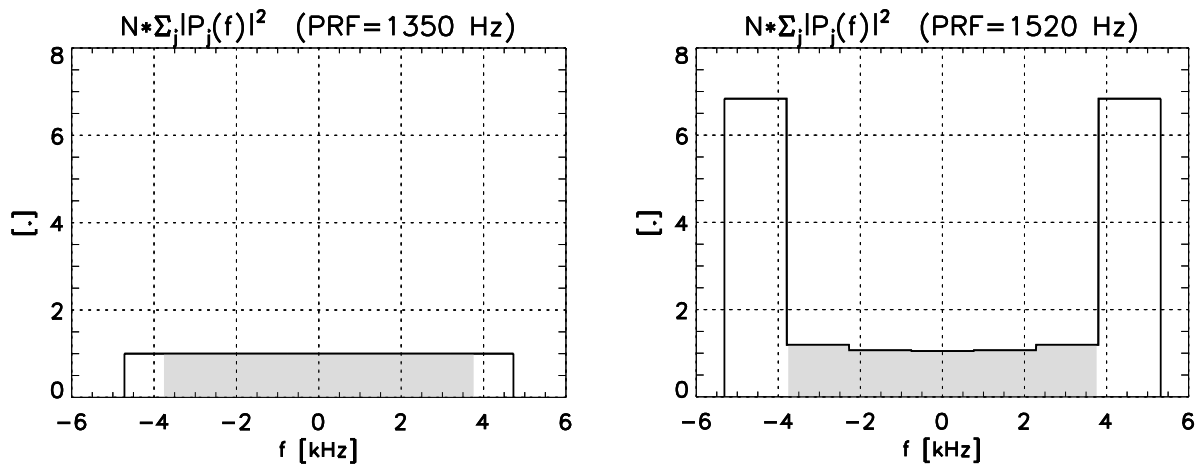


**Fig. 66.** Spectral appearance of noise power scaling defined by the sum over reconstruction filter functions  $\sum_j |P_j(f)|^2$  for the case of nearly uniform sampling at  $PRF = 1350$  Hz (left) and strong non-uniform sampling at  $PRF = 1520$  Hz (right). The contributions when focusing with  $B_D$  are shaded in gray.

Consequently, a strong scaling can be avoided by either selecting favorable  $PRF$  values or by appropriately adjusting the processed Doppler bandwidth to the effective sampling rate, as will be discussed in Section 8.2.

In a next step, the predicted  $SNR$  scaling factor as given by the dashed blue line of Fig. 65 is compared to the simulated ratio of signal to noise power after the digital beamforming network in order to verify the validity of the estimation of  $\Phi_{bf}$  (cf. Fig. 67). One recognizes a very good agreement of the estimation (solid red line) with the simulation (dashed blue line) with an absolute deviation of less than 0.05 dB as it is shown in Fig. 68.

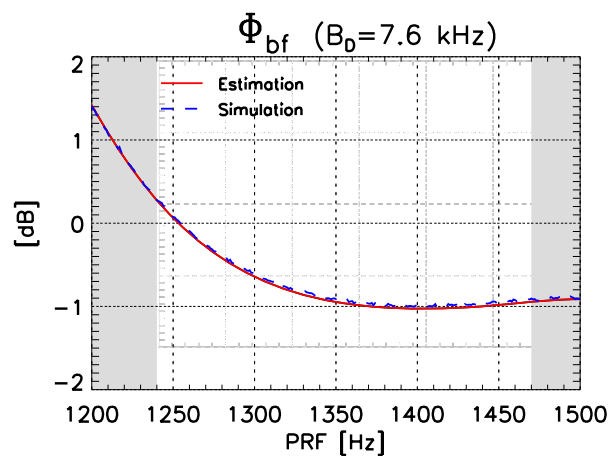


**Fig. 67.** Characteristic of simulated  $\Phi_{bf}$  vs.  $PRF$  (dashed blue) compared to its analytic prediction (solid red) for a processed Doppler bandwidth of 7.6 kHz.

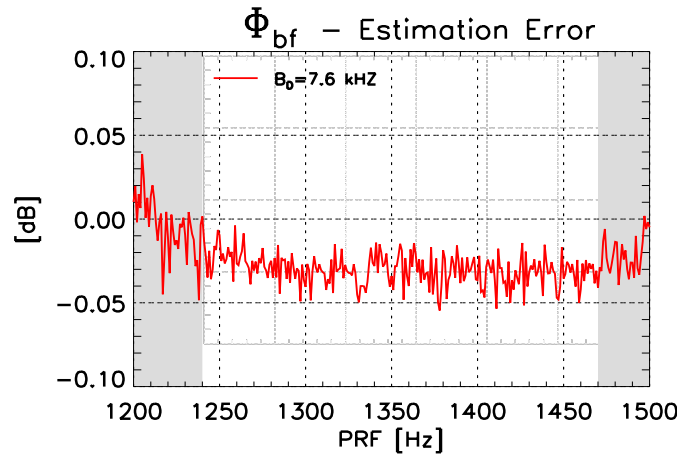


Fig. 68. Estimation error of  $\Phi_{bf}$  vs.  $PRF$  for  $B_D = 7.6$  kHz.

**7.4.5 Azimuth Loss:  $L_{az}$**

In addition to the modified  $SNR$  scaling of the system as derived before, one has to account for the azimuth loss factor  $L_{az}$ . It occurs in any SAR system, be it single- or multi-channel, and considers the decay of the joint Tx/Rx azimuth pattern as a function of the azimuth angle which attenuates the recorded signal while the added noise power remains spectrally white (cf. Section 5.5, [78]). Hence, the  $SNR$  becomes dependent on the Doppler frequency. In the present case, the relevant joint antenna characteristic in azimuth is determined by a transmit antenna of 3 m length and a receiving antenna of 1.6 m length. Fig. 69 gives – in accordance with (61) – the ensuing characteristic of the azimuth loss for a  $B_D$  ranging from 4 kHz to 9 kHz. According to Fig. 69, the investigated system yields a loss of  $L_{az} = 2.7$  dB when focusing the data with a bandwidth of  $B_D = 7.6$  kHz.

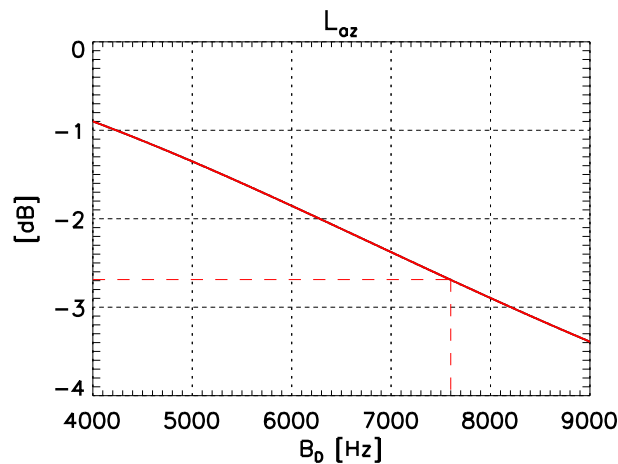
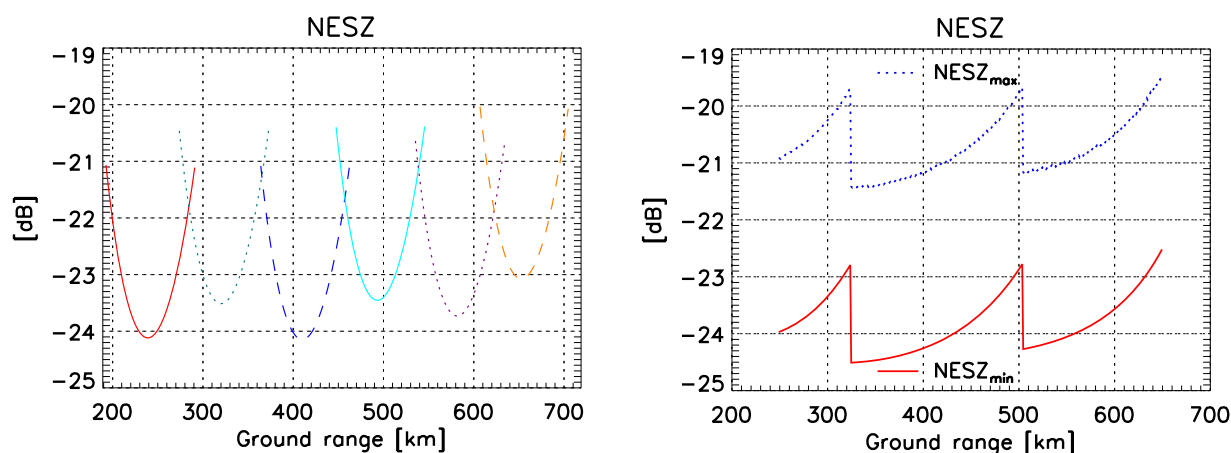


Fig. 69. Azimuth loss  $L_{az}$  vs. processed Doppler bandwidth  $B_D$ .

### 7.4.6 Noise Equivalent Sigma Zero : *NESZ*

Finally, the performance analysis of the system is concluded by the evaluation of the *NESZ*. Under consideration of the parameters  $\Phi_{bf}$  and  $L_{az}$  as derived above, and the respective transmit pattern the following characteristic of the *NESZ* vs. ground range is calculated according to (91). All relevant system parameters necessary for the calculation can be found in Table 7. Note that the receiver gain  $G_{rx,j}(\theta_i)$  as shown in (91) is in the present case assumed to be constant with varying incident angle  $\theta_i$  due to the applied SCORE algorithm in elevation as already discussed in Section 7.2.2. Fig. 70 shows the results obtained for coverage by 6 distinct swaths (left) and swathes centered on arbitrary incident angles (right).



**Fig. 70. Left: *NESZ* vs. ground range for coverage by 6 distinct swaths. Right: Best (solid red) and worst (dotted blue) case *NESZ* for arbitrarily situated swaths. The ground range gives the point on ground where the transmit antenna beam is pointed at.**

In the case where an arbitrary swath of 100 km can be imaged, the variation of the *NESZ* for a swath centered at a certain range is given by the best and worst value within the swath (cf. Fig. 57, right). Note that this takes into account the adaptation of the chirp bandwidth and the effective transmit antenna height with varying ground range. The steps in the curve result from the steps in the *PRF* and the corresponding *SNR* scaling factor of the reconstruction network.

In both cases a maximum *NESZ* of -19.4 dB is obtained, which represents a good value for spaceborne X-band SAR systems, as e.g. TerraSAR-X achieves a *NESZ* of -18 dB [93].



## 8 Optimization Potentials

The results of the system design example in Chapter 7 demonstrated the capability of the multi-channel reconstruction algorithm to enable high-resolution wide-swath imaging with multi-channel SAR systems. Nevertheless, it turned out that the inverse character of the digital processing network restricts the range of application with respect to the *PRF*.

This issue is addressed in the present chapter, where optimization strategies for increasing the flexibility and improving the performance are developed. The first section identifies the main error sources, analyzes their impact on the respective performance parameters and derives general strategies to minimize the errors (cf. Section 8.1). Then, in the following sections, various specific techniques according to those strategies are developed and applied to the system introduced in Chapter 7 and a modified system design derived in Section 8.5, which allows for better exploiting the optimization methods. The presented approaches consider the transmitter as well as the receiver side and range from an adapted processing to advanced hardware configurations. All techniques yield optimized system designs whose increased range of operation and improved performance are verified by simulations. As main parameters to be optimized, focus is turned to the signal-to-noise ratio (*SNR*), suppression of ambiguous energy (*AASR<sub>N</sub>*) and geometric resolution in azimuth ( $\delta_{az}$ ). The optimization aims at improving the *SNR* and the ambiguity suppression while keeping the resolution at a constant level.

### 8.1 Error Sources and Optimization Approaches

In order to optimize *SNR* and *AASR<sub>N</sub>*, the impact of both joint azimuth antenna pattern and digital processing on signal, ambiguities, and noise, has to be considered. Recalling Section 5.5, the **signal power** is only determined by the shape of the azimuth antenna pattern, as the digital processing filters  $P_{jm}(f)$  are chosen such that they do not affect the signal energy. In contrast, the **ambiguous power** in the signal after reconstruction is determined by both aspects (cf. Section 5.6). Firstly, as in any conventional SAR system, the joint azimuth antenna pattern contains ambiguous information from azimuth angles that correspond to Doppler frequencies outside the Nyquist-sampled band  $[-PRF \cdot N/2, PRF \cdot N/2]$ . In addition – and in contrast to the signal power – the ambiguous contributions are weighted and possibly amplified by the filter functions  $P_{jm}(f)$ , leading to the **ambiguous power** in the image. Finally, the thermal receiver **noise power** (cf.

Section 5.7) is only influenced by the processing and possibly amplified by the filters' power spectral densities, i.e. the mean squared amplitude of the  $P_{jm}(f)$ . For both the ambiguities and the noise this amplification by the processing filters is the more severe the stronger the non-uniform sampling is. This is due to the filter system's inverse character, which results in a rising filter amplitude for increasing deviations from the optimum  $PRF$ .

Consequently, one can identify two main areas of possible optimization. Firstly, the maximization of signal energy and the minimization of ambiguous energy in the received signal allows for reducing the ambiguities in the image. This means that **antenna patterns** on transmit and receive are adapted to optimally confine the desired Doppler band, which is the subject of a detailed analysis following in Section 8.4 that introduces the idea of tapering on transmit, while Section 8.7 includes the adaptation of the receive characteristic. Besides, the **azimuth processing** shows potential for improving the performance by minimizing the error amplification caused by the reconstruction filters. In a first simple approach, an optimized parameter choice within the existing processing approach allows for improving the system performance. This can be for example achieved by setting an optimized ratio between  $PRF$  and  $B_D$  as presented in Section 8.2.

Furthermore, one can aim at improving the conditions for the multi-channel processing by adapting the phase centers to the  $PRF$  in order to obtain a data array that is sampled as uniformly as possible. On transmit, this can be either achieved by an adaptive management of the  $PRF$  to adjust the virtual sample positions to obtain an improved sampling (cf. Section 8.3), or the phase centers can be adapted to the  $PRF$  by shifting the transmit antenna phase center from pulse to pulse (cf. Section 8.6). On receive, this adaptation of the system to the  $PRF$  is achieved by adding a reconfigurable pre-processing network to the conventional beamforming obtaining a cascaded network as introduced and elaborated in Section 8.7. The performance analysis of a design example demonstrates the capability of such cascaded networks to flexibly adapt the system to the respective  $PRF$  by varying number and positions of the effective phase centers. In combination with the aforementioned possibility of pattern tapering on receive, this allows for merging the classical ambiguity suppression strategy with a beam steering approach that optimizes the signal power and hence flexibly trades ambiguity suppression and  $SNR$  optimization by accordingly allocating the system resources (cf. Section 8.7).

## 8.2 Optimized Parameter Setup: Adaptation of Processed Doppler Bandwidth

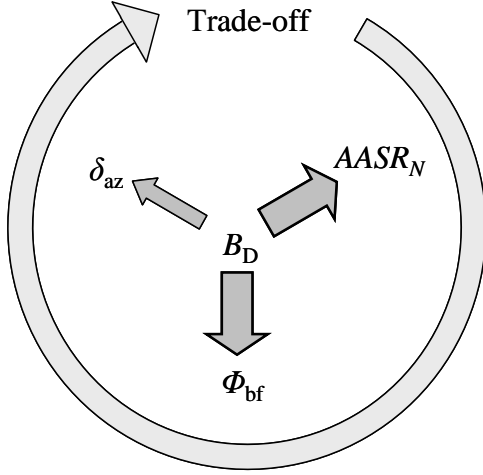


**Fig. 71. Optimized trade-off between performance parameters by exploiting their differing sensitivities on  $B_D$  as visualized by the size of the arrows.**

As mentioned, the processing filter functions have a colored spectrum which scales and possibly amplifies ambiguous and noise power. Consequently, the sensitivity with respect to the interferences varies with Doppler frequency, entailing a rather strong dependency on the processed Doppler bandwidth  $B_D$ , visualized by the big arrows in Fig. 71. On the other hand, signal power and geometric resolution in azimuth,  $\delta_{az}$ , depend on  $B_D$  as in any conventional SAR system (cf. Fig. 71, small arrow). The basic idea is hence to adapt  $B_D$  in a way to benefit from the different sensitivities, i.e. trading a small loss of one parameter against a big improvement of another.

Recalling the explanations given in Section 7.4.4 and illustrated in Fig. 66, the  $P_{jm}(f)$  on the  $n$  outermost bands at the lower and the upper border of the Doppler spectrum, respectively, dominate the strong rise in the amplification of the noise floor and tend to infinity for a singular  $PRF$ . Consequently,  $B_D$  is set in a way to eliminate by the inherent lowpass filtering the frequency bands which primarily cause the degradation of the performance. This allows for achieving acceptably moderate levels of  $SNR$  degradation and  $AASR_N$  even near to singular  $PRF$  values. Quantitatively, the  $n$ -th singular  $PRF_{sgl,n}$  which is defined by  $n$  spatially coinciding channels, requires a filtering of the respective bands  $I_{m,n}$  as given by (94). This allows for completely suppressing the strong rise in noise and ambiguity scaling and thus enables operating the system even at  $PRF_{sgl,n}$ .

$$I_{m,n} = \left[ -\frac{N}{2} \cdot PRF + (m-1) \cdot PRF, -\frac{N}{2} \cdot PRF + m \cdot PRF \right], \quad (94)$$

where  $m \in \{1, 2, \dots, n, N - (n-1), N - n, \dots, N\}$

In other words, the sampling of the signal by  $N \cdot PRF$  has to exceed the processed bandwidth  $B_D$  by a factor of  $N/(N-2 \cdot n)$  to keep the  $SNR$  degradation low, i.e.:

$$B_D \leq (N - 2 \cdot n) \cdot PRF_{sgl,n} \quad (95)$$

Fig. 65 and Fig. 66 give an example for the application of the above principle. The processed Doppler bandwidth  $B_D$  is chosen to be 7.6 kHz, while the first singular  $PRF$  is situated at 1575 Hz. Taking into account the number of  $N=7$  receivers and  $n=1$ , (95) yields a maximum possible  $B_D$  of 7875 Hz which exceeds the actual  $B_D$ . This explains why the  $SNR$  degradation is

acceptably low after focusing with  $B_D$  (cf. Fig. 65, dashed blue line) while it tends to infinity when considering the complete azimuth bandwidth (cf. Fig. 65, solid red line).

Although a very effective way of reducing the  $SNR$  degradation, this requires either a large number of Rx apertures or a relatively high  $PRF$  to guarantee the necessary oversampling with respect to the processed bandwidth  $B_D$ . This entails either high hardware costs or might cause problems with the timing. Ensuring the oversampling by simply decreasing  $B_D$  for a given  $PRF$  represents the easier way, but is at the cost of a deteriorated geometric resolution. Nevertheless, a strongly improved  $SNR$  might be obtained by either a moderately degraded resolution or a slightly increased  $PRF$  leading to a reduced swath. Finally this results in a trade-off between azimuth resolution, coverage and interfering power.

### 8.3 Adaptive $PRF$ Management in Sparse Array Systems

It was mentioned that the conditions for the multi-channel processing can be improved by harmonizing the phase centers with the  $PRF$  to obtain a sampling as uniform as possible. This can be either achieved by adapting the phase centers or, as discussed in this section, more easily by choosing adaptively a  $PRF$  value favorable for the system. Especially in sparse array systems, an adaptive management of the  $PRF$  shows great potential to adjust the virtual sample positions as spatially neighbored samples usually originate from transmit pulses emitted at different times. An example is given by Fig. 72, where the spatial sample distribution in azimuth dimension  $x$  is shown for a system of  $N=3$  receivers. Samples from three temporally different pulses are given by the red dotted, blue dashed, and black solid boxes, respectively.

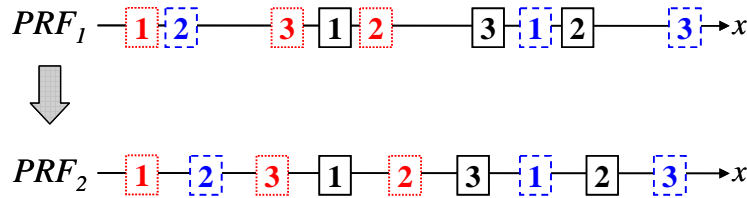


**Fig. 72.** Same system operated with different  $PRFs$ . A switch from  $PRF_1$  to a similar  $PRF_2$  yields a clearly different spatial sample distribution of better uniformity.

According to Chapter 4, the distance between adjacent samples originating from transmit pulse  $p$  at channel  $j$  and transmit pulse  $q$  at channel  $i$  is expressed by (96), where  $\Delta x_j$  denotes the distance of the respective receiver to the transmitter.

$$\Delta x_{j,i} = x_{j,p} - x_{i,q} = \frac{\Delta x_j}{2} - \frac{\Delta x_i}{2} + (p - q) \cdot \frac{v_s}{PRF} ; \text{ with } p, q \in \mathbb{Z} \quad (96)$$

In a conventionally operated single-platform system, adjacent samples originate from the same or subsequent pulses, i.e.  $|p - q| \leq 1$ , and consequently the inter-sample distance is smaller than the inter-pulse distance. Hence, in such a system the potential is limited as small changes in the  $PRF$  entail only small changes in the sample positions thus not allowing for large variations



in the spatial sampling. In contrast to single-platform systems, in sparse arrays the spatial position of adjacent samples is not bound to the same transmitted pulse. Equation (96) reveals that variations in the  $PRF$  result in variations of the position  $\Delta x_{j,i}$  amplified by a factor  $(p-q)$  and hence only small changes in the  $PRF$  might already have a large impact on the spatial distribution of the samples. As shown in Fig. 72, this results in two clearly different sample distributions for two similar  $PRF$  values. This offers wide flexibility to adapt the sampling even if only a small variation of the  $PRF$  is possible and thus allows for compensating for the high sensitivity of the systems'  $SNR$  and  $AASR_N$  regarding  $PRF$  variations.

## 8.4 Pattern Tapering on Transmit

As derived in Section 5.5, all spectral energy outside the band  $[-N \cdot PRF/2, N \cdot PRF/2]$  is not properly cancelled by the multi-channel reconstruction and causes aliasing in the reconstructed signal, finally resulting in ambiguities in the SAR image. This can be mitigated by confining the Doppler bandwidth of the signal to  $N \cdot PRF$  by an appropriate joint antenna pattern. In a very simple approach, one could just enlarge the dimension of the transmit antenna resulting in a narrower pattern, but being at the expense of resolution. A bigger antenna in combination with an adapted tapering is required to provide an improved suppression of the ambiguous frequency bands without degrading the resolution. Furthermore, the better the pattern is limited to the relevant Doppler frequencies, the better the emitted power is used as less power is lost by illuminating unwanted areas. The basic idea of concentrating the transmitted energy in the mainlobe according to the processed Doppler bandwidth  $B_D$  while reducing the emission to directions corresponding to ambiguous returns is visualized in Fig. 73: A minimum gain level of the joint antenna pattern within the interval  $B_D$  ensures sufficient signal energy, while a maximum allowable gain outside the system band restricts the ambiguous energy.

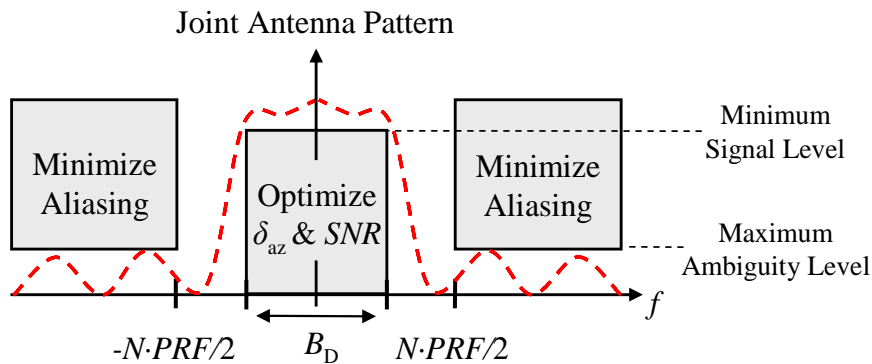


**Fig. 73. Joint Tx-Rx antenna pattern in azimuth (dashed red) illustrating the basic principle of pattern tapering on transmit. Suppression of aliased energy by imposing a maximum allowable ambiguity level in combination with a minimum signal level to optimize the signal energy.**

It should be noted that the presented tapers can be either realized by a separate transmit antenna, or by using an active array based on transmit-receive (T/R) technology. While the first

requires less sophisticated hardware, the latter offers the flexibility to use parts of the receiving antenna for transmit and hence allows for benefiting from its length.

To demonstrate the potential of pattern tapering on transmit, the system presented in Chapter 7 is investigated for different combinations of transmit antenna dimensions and amplitude excitations.<sup>26</sup> The transmit antenna of the example system of length 3 m with a uniform taper entailing a  $\text{sinc}(f_x)/f_x$  pattern characteristic is compared to three different pattern tapering concepts. The respective transmit antenna lengths  $d_{\text{az,tx}}$ , the applied excitation, and the resulting far field pattern are summarized in Table 8, where the notation  $\text{sinc}(x)$  is used to denote the  $\sin(x)/x$  function.

$d_{\text{az,tx}}$	Excitation (Azimuth)	Far Field (Azimuth)	$\delta_{\text{az}}$	Represented by	
3 m	uniform	$\text{sinc}(f_x)$	< 1 m	“Sinc”	—
4 m	$\cos(x)$	$\text{sinc}(f_x - \pi/2) + \text{sinc}(f_x + \pi/2)$	< 1 m	“Cos”	---
4.6 m	triangular	$\text{sinc}^2(f_x)$	< 1 m	“Sinc <sup>2</sup> ”	.....
11.2 m	$\text{sinc}(x)$	$\text{rect}(f_x/B_D)$	< 1 m	“Rect”	-.-

**Table 8. Pattern tapering on transmit: Excitations and resulting pattern characteristics.**

Further, it is well-known that excitation and far field are related by Fourier transform with the variables  $x$  and  $f_x$ , respectively. The variable  $x$  represents azimuth dimension while  $f_x$  describes the spatial frequency given by (97). Recalling the relation between azimuth angle  $\Theta$  and Doppler frequency  $f$  (cf. (98)), one recognizes that  $f_x$  and  $f$  are linked by the sensor velocity.

$$f_x = \frac{\sin(\Theta)}{\lambda} = \frac{f(\Theta)}{2 \cdot v_s} \quad (97)$$

$$f(\Theta) = \frac{2 \cdot v_s}{\lambda} \cdot \sin(\Theta) \quad (98)$$

Fig. 74 shows the resulting patterns with normalized amplitude, which is given in dependency on the Doppler frequency  $f(\Theta)$ . This allows for highlighting the potential of the different tapers to confine the transmitted energy to the desired azimuth region, i.e. the processed Doppler band, which is marked in gray. Consequently, Fig. 74 does not take into account a possible gain loss due to the amplitude taper, which is investigated in the second part of this section. Finally, to give a better overview, two approaches are combined in each of the plots.

<sup>26</sup>Although phase coefficients avoid a tapering loss by attenuation, they cannot be determined straightforwardly like the amplitude coefficients. An exhaustive analysis of both methods is beyond the scope of this work and thus only amplitude tapering is investigated to demonstrate the potential this technique.

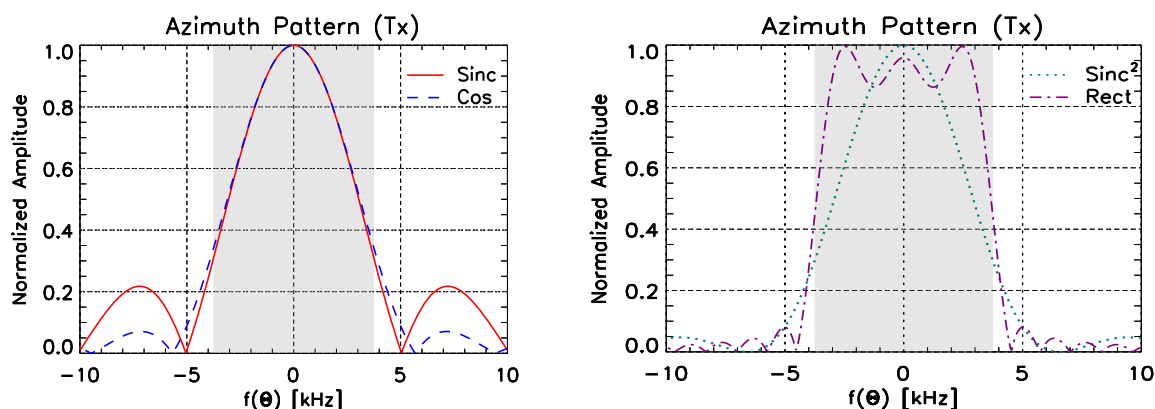


**Fig. 74.** Normalized amplitude of azimuth transmit pattern vs. Doppler frequency  $f(\theta)$  for excitations and antenna dimensions according to Table 8.  $B_D$  is marked by the gray-shaded area. **Left:** 3 m antenna with uniform excitation (“Sinc”, solid red) and 4 m antenna with cosine excitation (“Cos”, dashed blue). **Right:** 4.6 m antenna with triangular excitation (“Sinc<sup>2</sup>”, dotted green) and 11.2 m antenna with  $\sin(x)/x$  excitation (“Rect”, dotted dashed violet).

Regarding the suppression of azimuth ambiguities, Fig. 75 shows the  $AASR_N$  that is achieved for the different antenna patterns, respectively. It is stated that the suppression is already clearly improved for higher  $PRF$  values by applying the 4 m antenna with a  $\cos(x)$ -like excitation (dashed blue). This results from the reduced sidelobes of the modified antenna pattern as can be seen in the left plot of Fig. 74. The suppression becomes even better with a 4.6 m antenna with a triangular tapering which entails a  $\text{sinc}(f_x)^2$  characteristic (dotted green). However, to provide an improvement in suppression also for lower  $PRF$  values, a larger transmit antenna is necessary. An unconventional realization is given by the quasi-optimum – as it approximates a rectangular pattern –  $\text{sinc}(x)$  excitation in combination with a transmit antenna of 11.2 m (dotted dashed violet). This corresponds to the antenna on receive and represents consequently the maximum avail-

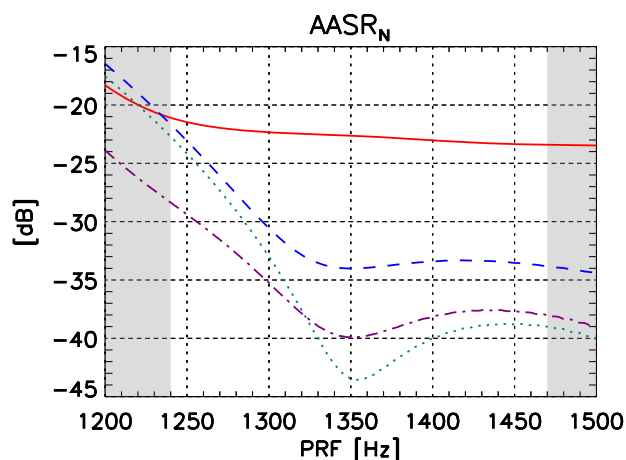


**Fig. 75.** Azimuth ambiguity suppression vs.  $PRF$  for different transmit antenna sizes and patterns according to Table 8: 3 m antenna with  $\text{sinc}(f_x)$  characteristic (solid red) 4 m antenna with  $\cos(x)$  excitation (dashed blue), 4.6 m antenna with  $\text{sinc}^2(f_x)$  characteristic (dotted green) and approximately rectangular pattern (dotted dashed violet) for 11.2 m antenna.

able length if T/R modules are used. In the present simulation, it is realized by 35 elements of 0.32 m length each. Especially this  $\text{sinc}(x)$ -excitation demonstrates the potential of tapering to effectively cancel the spurious spectral components while preserving the resolution. A full exploitation of the benefits of tapering requires a fine adjustment of antenna dimensions,  $PRF$  and  $B_D$ , taking into account the trade-off between resolution and ambiguity suppression.

Further, an analysis of the respective point target impulse response shows, that all scenarios yield an azimuth resolution of better than 1 m for a processed bandwidth  $B_D = 7.6$  kHz.

To conclude this section, the impact of the tapering on the  $NESZ$  is investigated. As mentioned above, the enlarged antenna size in combination with an appropriate tapering improves the distribution of the transmitted energy. This can be quantified by the joint Tx/Rx antenna azimuth loss  $L_{az}$ , which accounts for the spectral shape of the pattern (cf. (60) and (61)). Further, the overall transmitted energy changes with antenna length and amplitude taper. Hence, additionally to  $L_{az}$ , the maximum power gain  $G_{tx}$  of the antenna characteristic has to be considered. Note that the calculation of the modified gain takes into account the new antenna length and is based on the assumption of a constant transmit power per antenna area, i.e. an equal feeding voltage/power of each individual transmit antenna element. The respective values with respect to the original system defined by  $G_{tx,0}$ ,  $L_{az,0}$  and  $NESZ_0$  are summarized in the following Table 9. It gives the resulting improvement (“-”) or degradation (“+”) of the new  $NESZ$  that can be directly applied to Fig. 70 to obtain the  $NESZ$  corresponding to the modified system. Equivalently, Table 9 allows for deducing how the peak transmit power per antenna area can be reduced (“-”) or has to be increased (“+”) to keep the  $NESZ$  constant. Finally, the efficiency of the taper itself is measured by relating the different peak power gains if the antenna lengths were all the same. The results are listed in Table 9 in the very right column.

Excitation	Maximum Transmit Power Gain $G_{tx}/G_{tx,0}$	Azimuth Loss $L_{az}/L_{az,0}$	$NESZ/NESZ_0$	Efficiency
uniform	0 dB	0 dB	0 dB	0 dB
$\cos(x)$	+1.42 dB	-0.03 dB	+1.39 dB	+3.92 dB
triangular	+2.30 dB	+0.18 dB	+2.48 dB	+6.02 dB
$\text{sinc}(x)$	+9.30 dB	-0.97 dB	+8.33 dB	+20.74 dB

**Table 9. Pattern tapering on transmit: Maximum antenna gain  $G_{tx}$ , azimuth loss  $L_{az}$  and resulting  $NESZ$  relative to the original system defined by  $G_{tx,0}$ ,  $L_{az,0}$  and  $NESZ_0$ . Improvement is indicated by “-” while “+” means a degradation.**

As one can see from the change in the  $NESZ$ , particularly the cosine taper seems to be a good choice if a clearly improved azimuth ambiguity suppression is needed while a moderate degradation of the  $NESZ$  can be afforded. Especially for  $PRF$  values above 1300 Hz, an  $AASR_N$  improved by  $\sim 10$  dB is achieved at the cost of a  $SNR$  decreased by only  $\sim 1.4$  dB. The triangular taper yields an even faster drop of the residual ambiguities, but entails a degraded  $NESZ$  by already  $\sim 2.5$  dB. Finally, the approximated rectangular pattern was only evaluated to demonstrate its potential regarding the suppression of azimuth ambiguous energy, as the transmitted signal power decreases too strongly with respect to the original system.

## 8.5 Optimized System Design Example

So far, the performance of the example system of Section 7 has been improved without concentrating on increasing the system flexibility, i.e. extending the range of operation. In the following, focus is turned to techniques allowing for such an improved flexibility. In order to better demonstrate the potential of the proposed optimization methods, a modified design is proposed.

As a first step, the present chapter introduces an adapted example system based on the system presented in Chapter 7, but designed with the goal to extend the applicable *PRF* range from 1150 to 1550 Hz. Hence, the sub-aperture length is increased to 1.75 m resulting in an overall length of 12.25 m and a decreased optimum *PRF* of 1236 Hz, which allows for operating in the lower regions of the required *PRF* range. On transmit, a slightly increased antenna of 3.15 m length is required to ensure a sufficient ambiguity suppression as will be seen later. The modified parameters are summarized in Table 10, while all other system parameters remain unaltered and can be looked up in Table 7.

Parameter	Symbol	Value
<i>PRF</i> range	<i>PRF</i>	1150 Hz – 1550 Hz
Overall receive antenna length in azimuth	$l_{az}$	12.25 m
Receive aperture size in azimuth	$d_{az,rx}$	1.75 m
Number of “virtual” azimuth channels	$N_0$	7
Receive antenna gain	$G_{rx}$	55.1 dB
Transmit antenna size in azimuth	$d_{az,tx}$	3.15 m
Maximum transmit antenna gain	$G_{tx}$	38.9 dB – 42.3 dB
Azimuth loss	$L_{az}$	2.9 dB

**Table 10. System parameters of modified example system.**

In the following, the system performance is analyzed, showing the limits to obtain satisfactory results over the full range of requested *PRF* values. The subsequent sections then introduce innovative techniques for system optimization and give examples how these techniques enable to extend the *PRF* range. This comprises a method based on a sophisticated transmit antenna architecture (cf. Section 8.6) as well as cascaded processing networks, which are presented in Section 8.7. In the case of cascaded structures two examples are given, considering an analog pre-processing (cf. Section 8.7.7) as well as a digital approach (cf. Section 8.7.8).

Starting with the obtained geometric **resolution** in azimuth, the increased sub-aperture length of 1.75 m with respect to the length of 1.6 m in the original system entails a minor degradation to 1.03 m due to the slightly narrowed azimuth antenna pattern.

Next, an analysis of the **SNR scaling factor**  $\Phi_{bf}$  of the reconstruction network is given in Fig. 76 that shows the simulated results before (solid red line) and after focusing with  $B_D = 7.6$  kHz (dashed blue line). The analytic prediction of selected samples is given by the diamond symbols, which show a very good match to the simulations (lines) for the data after reconstruction as well as for the image after focusing.

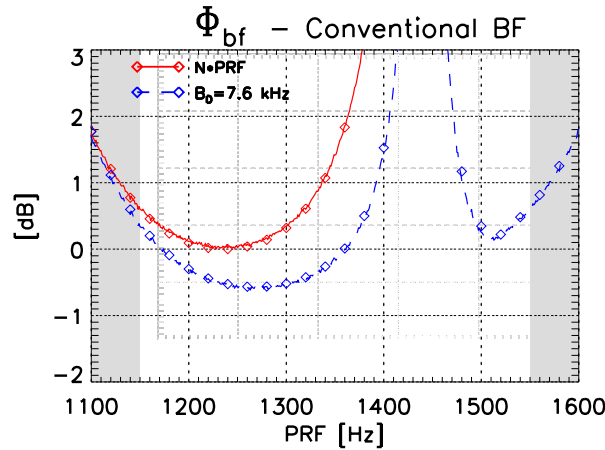


**Fig. 76.** Simulated  $SNR$  scaling factor  $\Phi_{bf}$  of the conventional digital beamforming network before (solid red) and after focusing with  $B_D = 7.6$  kHz (dashed blue). Selected samples of the analytic predictions according to (83) and (84), respectively, are overlaid with the diamond symbols.

$\Phi_{bf}$  shows sufficiently low values from 1150 Hz up to approximately 1370 Hz, but yields unacceptably high values for the  $PRF$  range above 1400 Hz (cf. Fig. 76). The increasing improvement of the curve representing the focused image with rising  $PRF$  results from the increasing oversampling of the signal, as this yields a reduced noise power due to the lowpass filtering inherent to focusing. It was already mentioned in Section 7.4 that for white noise the improvement for uniform sampling is directly linked to the ratio between processed bandwidth  $B_D$  and effective sampling rate. In the present case this results in a “gain” of 0.56 dB after focusing which is consistent with the value obtained in Fig. 76.

In terms of the  $NESZ$ , focus is turned to the differences between the modified conventional system presented before and the system of Chapter 7. As mentioned, the new system shows an enlarged transmit antenna of 3.15 m and an increased receive aperture of 1.75 m compared to 3 m and 1.6 m, respectively, before. Firstly, this gives rise to an overall  $L_{az}$  of 2.9 dB compared to 2.7 dB of the original system and consequently, one can state a degradation of the azimuth loss factor  $L_{az}$  by 0.2 dB. Secondly, the new dimensions entail an increased maximum gain of 0.2 dB on transmit and 0.4 dB on receive, which lead to an overall improvement of the gain by 0.6 dB. For the time neglecting the  $SNR$  scaling factor and assuming an unchanged mapping of swathes and  $PRF$ , the  $NESZ$  of the original system (cf. Fig. 70) is improved by approximately  $-0.2$  dB +  $0.6$  dB =  $0.4$  dB, yielding a value of better than  $-19.8$  dB.

Further, the  $SNR$  degradation encountered for increasing  $PRF$  in combination with a constant duty cycle is given by  $PRF/PRF_{uni}$  and has to be considered (cf. Sections 5.7 and 5.8). For the system example of Chapter 7, the worst  $NESZ$  is obtained at the maximum  $PRF$  of 1470 Hz entailing a loss of 0.37 dB with respect to  $PRF_{uni}$ . In the present case, the worst case is given by the maximum  $PRF = 1550$  Hz compared to a new  $PRF_{uni} = 1236$  Hz, leading to a  $SNR_{cl}$  degraded by 0.98 dB. This means that an additional loss of  $\sim 0.6$  dB is to be considered, and consequently the “reference”  $NESZ$  – still neglecting  $SNR$  scaling factors – modifies to  $-19.2$  dB.

In a final step, the modified  $SNR$  scaling factor (cf. Fig. 76) is considered which will – at least partly – compensate for the degradation discussed above. A valid estimation for the  $NESZ$

is then obtained by taking into account the above reference value and including the differences with respect to the  $SNR$  scaling obtained in Chapter 7. According to Fig. 76, the conventionally operated system cannot provide a low  $SNR$  scaling – and consequently an acceptable  $NESZ$  – over the complete  $PRF$  range. Hence, a reconfiguration of the system is required with the goal to obtain a low  $SNR$  scaling factor for higher  $PRF$ s, thus extending the  $PRF$  range of operation. This can be either achieved by using an advanced Tx antenna concept or by adding a pre-processing stage to the beamforming network, as will be demonstrated in the subsequent sections.

## 8.6 Phase Center Adaptation on Transmit

In the frame of advanced concepts of transmit antenna architectures in azimuth, a next step comprises a more sophisticated antenna structure allowing for the compensation of non-optimum  $PRF$  values. After the introduction of the basic principle in Section 8.6.1, the proposed technique is analyzed analytically in Section 8.6.2, followed by a system example demonstrating the potential of the phase center adaptation (cf. Section 8.6.3).

### 8.6.1 System Architecture and Basic Principle

In contrast to classical transmit antenna concepts (Fig. 77, top) the innovative approach is based on a long transmit antenna, which consists of a large number of individually controllable elements as indicated in Fig. 77, bottom. Especially with T/R technology, this allows for benefiting on transmit from the long receive antenna without increasing the antenna dimensions.

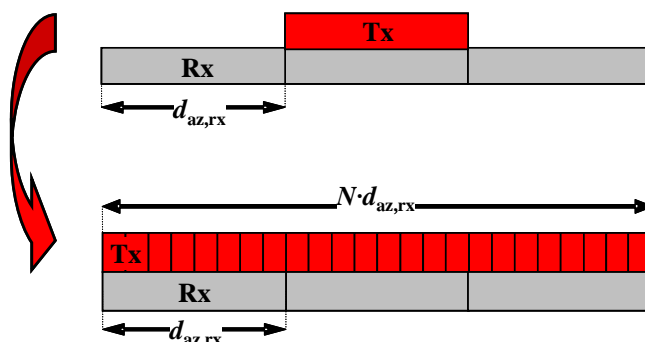


**Fig. 77. Novel transmit antenna architecture with increased length and consisting of multiple individual elements (bottom) compared to classical one-element transmit antenna of small size (top).**

Such an antenna permits to change the size of the aperture and its position on the antenna by activating the respective elements. This patented method allows for adaptively varying the transmit phase center position by using only certain parts of the antenna [56], [57]. Activating different parts of the antenna from pulse to pulse yields a phase center in azimuth that “travels” over the antenna as shown exemplarily for three subsequent pulses in Fig. 78 on the left. Taking further into account the receiver phase centers of a conventional multi-channel antenna, the resulting effective phase centers of the system can be shifted by half of the displacement of the

transmit antenna phase center with respect to its center position. A system with exemplary three receive apertures and a variable transmit phase center position is shown in Fig. 78 on the right.

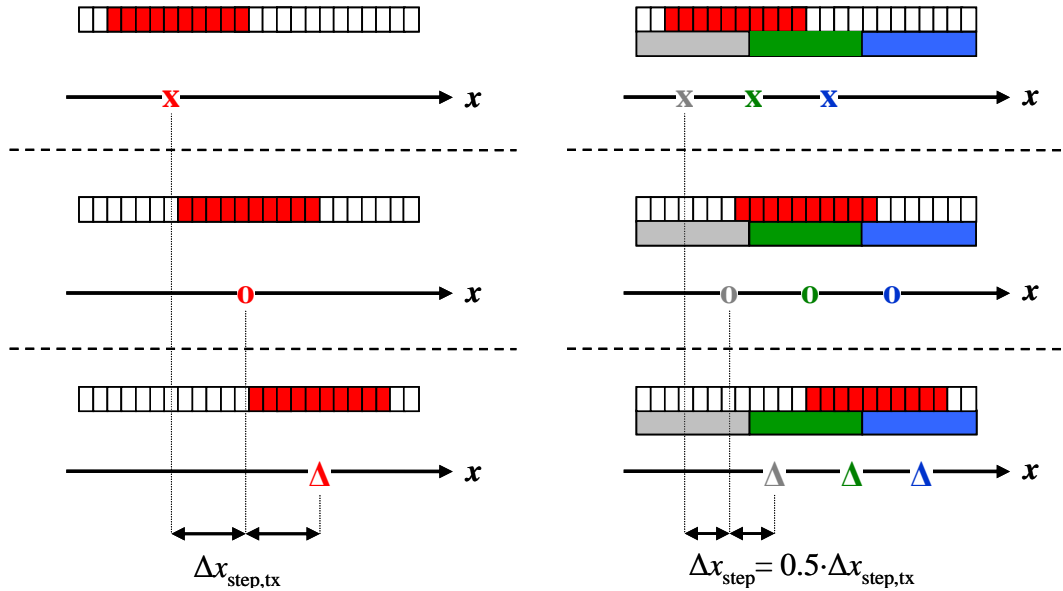


**Fig. 78. Left:** Adaptive shift of transmit antenna phase center according to active elements marked in red. **Right:** Resulting spatial samples for a multi-channel system with varying transmit phase center.

This capability to adjust the spatial samples from pulse to pulse offers the possibility to compensate for non-optimum  $PRF$  values. Thereby the step size of the phase center variation from pulse to pulse can be set flexibly to compensate for the actual  $PRF$  thus yielding uniform sample spacing or at least a mitigated non-uniform sample distribution. A simple example to illustrate the basic principle is given in the following: Fig. 79 shows a conventional multi-channel SAR system operated with a non-optimum  $PRF$ . The azimuth positions of the non-uniformly distributed samples received for four transmit pulses are shown at the bottom where the samples arising from different pulses are coded with different symbols while the samples and the corresponding receive sub-aperture are marked by the same color.

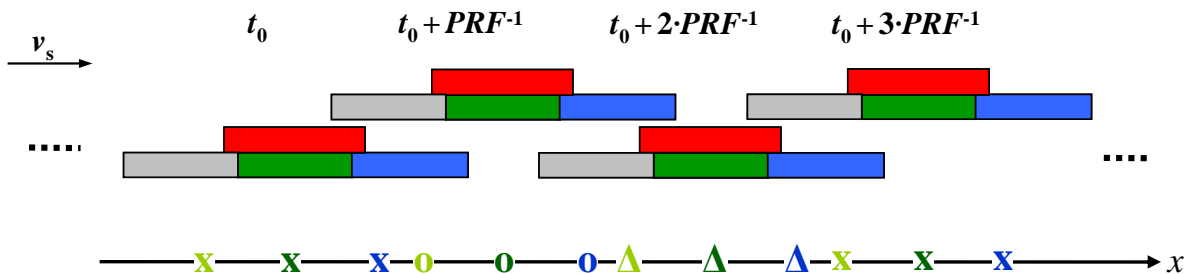


**Fig. 79. Multi-channel system with conventional transmit antenna operated at non-optimum  $PRF$  entailing non-uniformly spaced samples, exemplarily given for four subsequent pulses.**

Fig. 80 demonstrates how an adaptive shift of the transmit aperture from pulse to pulse can compensate for the non-optimum  $PRF$  yielding uniform sampling. In this exemplary case, the



cycle time after which the phase center has reached its outermost position and “jumps” back to the opposite antenna end is chosen to three pulses. Hence, as the non-optimum  $PRF$  is assumed to be too high, every fourth pulse two samples coincide and have to be averaged or skipped.

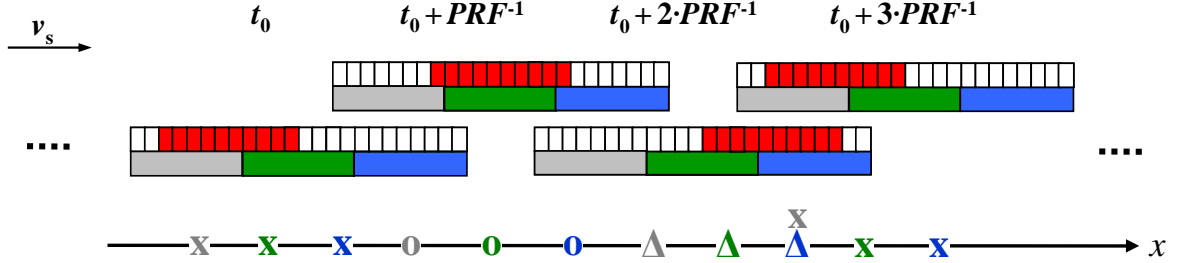


**Fig. 80. Multi-channel system with pulse-to-pulse phase center adaptation on transmit that compensates for the non-optimum  $PRF$  and finally yields uniformly spaced samples.**

Note that Fig. 80 shows a special case, as the transmit phase center starts a new cycle at its original starting position, which is not necessarily the case in a general scenario.

### 8.6.2 Analytic Description

As a next step, the present section carries out an analytic description of the technique. Firstly, (99) quantifies the necessary shift  $\Delta x_{\text{step}}$  of the samples that has to be effectuated from pulse to pulse to compensate for the non-optimum  $PRF$  if the optimum value is given by  $PRF_{\text{uni}} = 2 \cdot v_s / l_{\text{az}}$ .

$$\Delta x_{\text{step}} = \frac{v_s}{PRF_{\text{uni}}} - \frac{v_s}{PRF} = \frac{l_{\text{az}}}{2} - \frac{v_s}{PRF} \quad (99)$$

Taking into account the effective phase centers midway between transmitter and receiver, the necessary shift of the transmit aperture per pulse is given by  $\Delta x_{\text{step,tx}} = 2 \cdot \Delta x_{\text{step}}$  to ensure the necessary shift of the phase centers. To calculate the phase center position from pulse to pulse, the initial position of the transmit phase center is assumed at its outermost position  $x_{\text{tx,max}}$  that is defined by (100), where the “ $\pm$ ” specifies the maximum fore or aft position, respectively, with respect to the flight direction.

$$x_{\text{tx,max}} = \pm \left( \frac{l_{\text{az}}}{2} - \frac{d_{\text{az,tx}}}{2} \right) \quad (100)$$

Then the phase center position  $x_{\text{tx}}(t)$  is shifted by  $\Delta x_{\text{step,tx}}$  between subsequent pulses according to (101) as long as the opposite maximum position on the antenna is not reached yet, i.e. (102) has to be fulfilled.

$$x_{\text{tx}}(t + PRF^{-1}) = x_{\text{tx}}(t) + \Delta x_{\text{step,tx}} \quad (101)$$

$$\mp x_{\text{tx,max}} \pm k \cdot \Delta x_{\text{step,tx}} \leq \pm x_{\text{tx,max}} ; k \in \mathbb{N} \quad (102)$$

When (102) does not hold true any more, the phase center shifts backward or forward, towards the opposite side of the antenna. Performing this shift, it has to be assured that the position

of two subsequent transmit phase centers yields again a phase center distance that corresponds to the uniform  $PRF$ . Consequently, the distance of the transmit phase center has to include the necessary shift  $\Delta x_{\text{step,tx}}$  and an integer multiple of the receive phase center distance  $\Delta x$ . Assuming a transmit antenna phase center  $x_{\text{tx}}(t_0)$  at time  $t_0$ , and a position  $x_{\text{tx}}(t_1)$  at the next pulse at time  $t_1 = t_0 + PRF^{-1}$ , one obtains:

$$x_{\text{tx}}(t_1) - x_{\text{tx}}(t_0) = \Delta x_{\text{step,tx}} - q \cdot \Delta x = m \cdot \Delta x - \frac{2 \cdot v_s}{PRF} ; \quad q, m \in \mathbb{Z} \quad (103)$$

As mentioned, a shift of the phase center back to the opposite side of the antenna is necessary every time it has reached its outermost position. When this happens,  $PRF$  values higher than  $PRF_{\text{uni}}$  entail samples that are obtained for coinciding spatial positions which have to be “reduced” to a single sample, e.g. by averaging the two samples or simply discarding one of them. This yields a uniformly sampled signal independent from the  $PRF$ . If the  $PRF$  is below the optimum value, this results in “missing” samples within the synthetic aperture, as a gap occurs in the spatial sampling every time the phase center is switched. These gaps have to be filled, for example by interpolation techniques.

Finally, before focusing the signal with a filter matched to the uniform  $PRF$ , the impact on the received multi-aperture SAR signal in azimuth has to be considered. Recalling the multi-aperture impulse response in azimuth (cf. (28)), one remembers a constant phase term which is dependent on the distance between transmitter and respective receiver. As the transmitter phase center now varies from pulse to pulse, its distance to the receivers changes continuously and (28) has to be extended by a time dependent phase. This means that depending on the pulse and the respective position of the transmit phase center, a phase  $\gamma_j$  has to be applied to each of the channels  $j$ .

$$\gamma_j(t) = \frac{\pi \cdot (\Delta x_j - x_{\text{tx}}(t))^2}{2 \cdot \lambda \cdot R_0} \quad (104)$$

In a real system, the transmit phase center cannot be adjusted arbitrarily, but is bound to discrete positions that result from the size of the individually controllable antenna elements. Assuming an antenna divided into a number of  $K$  elements, the required shift of the transmit phase center by  $p$  elements from pulse to pulse can be calculated from (105).

$$p = \frac{K}{l_{\text{az}}} \cdot \Delta x_{\text{step,tx}} \quad (105)$$

Further, the fine-tuning ability of the position, i.e. the minimum possible step size of the phase center from pulse to pulse, depends also on the distance between single transmit elements and is given by  $l_{\text{az}}/K$ . Further, the sign of  $p$  – and consequently  $\Delta x_{\text{step,tx}}$  – defines the direction of the movement of the sliding phase center, either along for positive values or against the flight direction for negative values, to adjust the spatial sampling resulting from too high or too low  $PRF$  values, respectively. Rearranging (105), one obtains (106) that can be understood as a generalization of the timing requirement of (35) by replacing the constant overall antenna length  $l_{\text{az}}$

by an effective overall length  $l_{az,eff}$  that can be adapted by the settings for the pulse-to-pulse adaptation.

$$PRF = \frac{2 \cdot v_s}{l_{az} - \Delta x_{step,tx}} = \frac{2 \cdot v_s}{l_{az,eff}} = \frac{2 \cdot v_s}{l_{az} \left(1 - \frac{P}{K}\right)} = \frac{PRF_{uni}}{\left(1 - \frac{P}{K}\right)} \quad (106)$$

The  $PRF$  range that can be compensated is determined by the maximum displacement of the phase center that is defined by the distance between the outermost positions given by (100). Assuming a transmit aperture size  $d_{az,tx}$  equal to a single receive aperture  $d_{az,rx}$ , this entails the maximum step size  $\Delta x_{step,tx,max}$  as follows:

$$\Delta x_{step,tx,max} = \pm (l_{az} - d_{az,tx}) = \pm (N-1) \cdot d_{az,rx} \quad (107)$$

Equation (107) defines, dependent on the direction of the step according to its sign, the maximum and minimum possible  $PRF$  to be compensated in (108) and (109), respectively.

$$PRF_{max} = \frac{1}{\left(1 - \frac{N-1}{N}\right)} \cdot PRF_{uni} = N \cdot PRF_{uni} \quad (108)$$

$$PRF_{min} = \frac{1}{\left(1 + \frac{N-1}{N}\right)} \cdot PRF_{uni} = \frac{1}{\left(2 - \frac{1}{N}\right)} \cdot PRF_{uni} \quad (109)$$

Despite the theoretical possibility to compensate  $PRF$  values up to  $N \cdot PRF_{uni}$  (cf. (108)) it should be noted that for  $N \geq 3$  additional strategies are possible, as e.g. uniform sampling of higher order (cf. Section 4.3.3) could be achieved. This means that in this case the presented technique would be applied up to a maximum  $PRF$  of  $2 \cdot PRF_{uni}$ . Above this value the compensation could be adapted to a uniform  $PRF$  of higher order, i.e. the pulse-to-pulse steps are derived for the closest integer multiple of the  $PRF_{uni}$  that is below the given  $PRF$ .

For the above limits of  $PRF_{min}$  and  $PRF_{max}$ , this results in coinciding samples every second pulse if the maximum  $PRF$  is corrected for, while a gap in the spatial sampling occurs every two pulses if the minimum  $PRF$  shall be compensated. Hence, (109) represents only the theoretical value that can be compensated but does not give information on how frequently gaps in the sampling can be tolerated.

### 8.6.3 Performance Analysis

In order to give an example of the benefits arising from this technique, the system presented in Section 8.5 is extended by a transmit antenna architecture as given in Fig. 77. For reasons of demonstrating the general potential of this technique, the possibility for arbitrarily setting the transmit antenna phase center is assumed. In the presented case the gaps in the sampling grid for  $PRF$  values smaller than  $PRF_{uni}$  were filled by an interpolation method that closely approximates a sinc-interpolation. The resulting  $AASR_N$  is shown in Fig. 81:

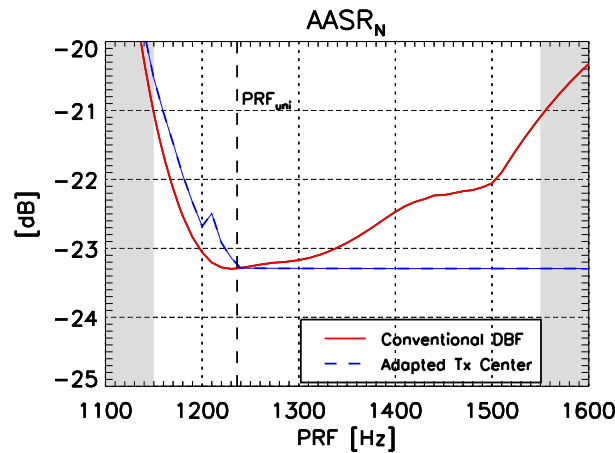


**Fig. 81.** Ambiguous energy suppression,  $AASR_N$ , vs.  $PRF$  for adaptive phase center shift on transmit (dashed blue) compared to conventional DBF (solid red).

For  $PRF$  values below  $PRF_{uni}$ , the  $AASR_N$  slightly decreases with respect to the conventional reference, caused by the missing samples at times when the transmit phase center switches. This problem can possibly be mitigated by special pre-processing – e.g. advanced interpolation techniques – to fill the gaps in the spatial sampling, but the investigation of such techniques shall not be subject of this work. For a  $PRF$  higher than the optimum value, the  $AASR_N$  stays constant at the value corresponding to the optimum  $PRF$ , as in this case the signal is identical to the uniformly sampled signal (cf. Fig. 81). This yields an optimized ambiguity suppression compared to the conventional digital beamforming (DBF) case, resulting in an improvement of up to 2 dB for a  $PRF$  value of 1550 Hz.

Regarding the  $SNR$ , the big advantage of the adaptive phase center technique becomes clear. As uniform sampling is ensured for any  $PRF$ , no degradation of the  $SNR$  is induced by the processing, i.e. a constant  $SNR$  scaling factor is provided independently of the  $PRF$ . The respective constant is defined by the value obtained for uniform sampling (cf. Fig. 82, dashed blue line). Compared to the  $SNR$  scaling of the conventional system (solid red), this results in a clear improvement, especially for higher  $PRF$  values.

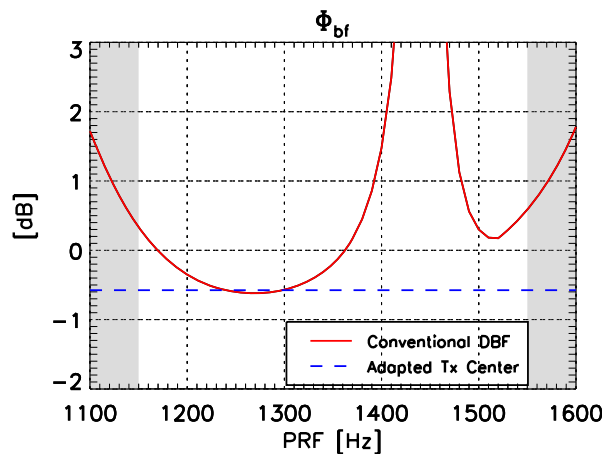


**Fig. 82.**  $SNR$  scaling factor  $\Phi_{bf}$  for conventional DBF approach (solid red) and for adaptive phase center shift on transmit (dashed blue).  $B_D = 7.6$  kHz.

In consequence, the formerly restricted *PRF* range of operation is extended when applying this technique, thus enabling the operation of the system over the complete required range. Nevertheless, it should be kept in mind that the sampling rate does not increase with the *PRF*. On the one hand, this means that even for higher *PRF* values the data volume does not increase. On the other hand, one does not benefit from an increasing effective sampling rate with respect to the *NESZ*, i.e. in the calculation according to (91) always the optimum *PRF* is to be considered. In the worst case, given by the ratio of the maximum *PRF* of 1550 Hz to the optimum one of 1236 Hz, this yields a “loss” of  $\sim 1$  dB. This is caused by the fact that for an increasing *PRF* the reduced signal energy per sample is not compensated by an increased number of samples. In this context it should be noted that this does not take into account the possibly increased signal power of such samples that arose from the combination of two spatially coinciding samples. Taking further into account the constant *SNR* scaling of  $\sim -0.6$  dB (cf. Fig. 82, dashed blue line), the *NESZ* of the optimized reference system (cf. Section 8.5) worsened by not more than  $\sim 0.4$  dB represents a conservative estimation for the obtained *NESZ*.

Regarding the **geometric resolution in azimuth**, both techniques provide a value of  $\sim 1.04$  m above the optimum *PRF*, while below this value the phase center adaptation entails a moderate degradation that increases with increasing offset from the optimum *PRF* value.

In conclusion, the proposed method enables to clearly extend the full performance *PRF* region. The presented advanced antenna architecture can be seen as a further step towards more sophisticated transmit antennas leading to a fully active SAR in the future and enabling new concepts as e.g. digital waveform encoding on transmit which offer various and powerful opportunities to push the system performance even further [63], [64], [95].

## 8.7 Cascaded Beamforming Networks

As a further component for system optimization, more sophisticated beamforming approaches represent powerful tools to adaptively improve the system performance. This section introduces the idea of adding a second processing stage leading to cascaded beamforming networks and investigates the new concept with respect to the network capability to adaptively position the systems’ phase centers. In the following, the impact on signal, ambiguities and noise power are derived in detail. The section is completed by the performance analysis of two different system examples.

The basic idea behind the additional network is to modify the received signal such that it matches the subsequent reconstruction network, primarily by flexibly adjusting the virtual sample positions to the actual system *PRF*. This allows for minimizing the non-uniform sampling thus influencing the *SNR* scaling factor of the processing network, as it will be investigated in the following. In this context, the modified *SNR* scaling factor of cascaded beamforming networks is derived and the potential to improve the *NESZ* is demonstrated.

In addition, such networks enable to implement pattern tapering on receive and thus offer an efficient instrument to further suppress ambiguities or to improve the received signal power. In

the latter case, the pre-processing network is explicitly designed to maximize the signal power, e.g. by implementing a beamsteering in the first processing stage followed by the reconstruction network which effectuates the ambiguity suppression in the second stage. This means – in some respects similar to the STAP approach mentioned in Section 5.3 – that no longer all degrees of freedom are used for ambiguity suppression, but are partly dedicated to optimize the  $SNR$ .

In summary, such reconfigurable networks show flexibility with respect to the receiving pattern, the effective sampling rate given by the number of different reconstructed channels, and the spatial sample positions. The cascaded structure of the networks allows for flexibly allocating the network resources to emphasize a specific system parameter, finally resulting in an adjustable trade-off between  $SNR$ ,  $AASR_N$  and resolution.

### 8.7.1 System Architecture and Extended System Model

As illustrated in Fig. 83, in a cascaded beamforming network the existing system is extended by a second network that is used for analog or digital pre-processing of the multi-channel SAR signals before the reconstruction filter network introduced in Chapter 5 is applied.

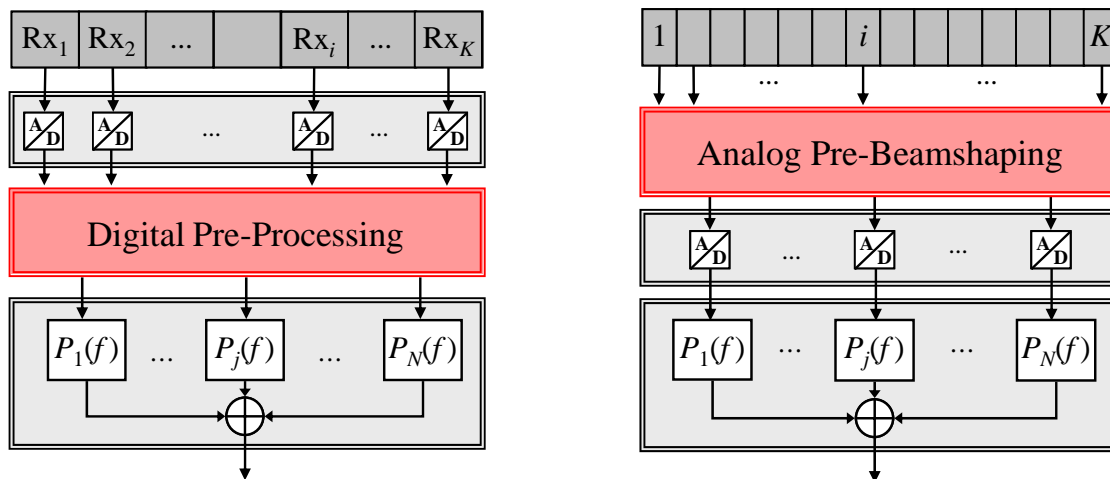


**Fig. 83. Cascaded Beamforming Networks. Left:** Digital pre-processing network with a-posteriori processing after digitization and storage of the signals. **Right:** Analog pre-processing network (“Pre-beamshaping”) applied to the RF signal before digitization.

In the following, the general idea and principles of cascaded networks will be presented, distinguishing between analog and digital pre-processing only where necessary. As specified in Fig. 84, the system is based on an antenna consisting of a number of  $K$  independent elements, each receiving a signal  $U_i(f)$ . Then a pre-processing network follows, allowing for an individual and reconfigurable weighting and combination of the elements’ signals  $U_i(f)$  resulting in  $N$  “virtual” output channels  $U_{c,j}(f)$ . The weights may vary from sub-aperture to sub-aperture and from channel to channel. This allows for “using” the signal of a certain sub-aperture in more than one of the virtual channels resulting in a spatial overlap of the respective elements that form these channels. The contribution of the signal of element  $i$  to the virtual channel  $j$  is described by the complex coefficient  $w_{ij}$  (cf. Fig. 84) that is optionally Doppler frequency dependent and then denoted

by  $w_{ij}(f)$ . Finally, filtering by the reconstruction filter functions  $P_j(f)$  takes place, followed by coherent combination of all  $N$  output branches finally yielding the signal  $U_{out}(f)$ .

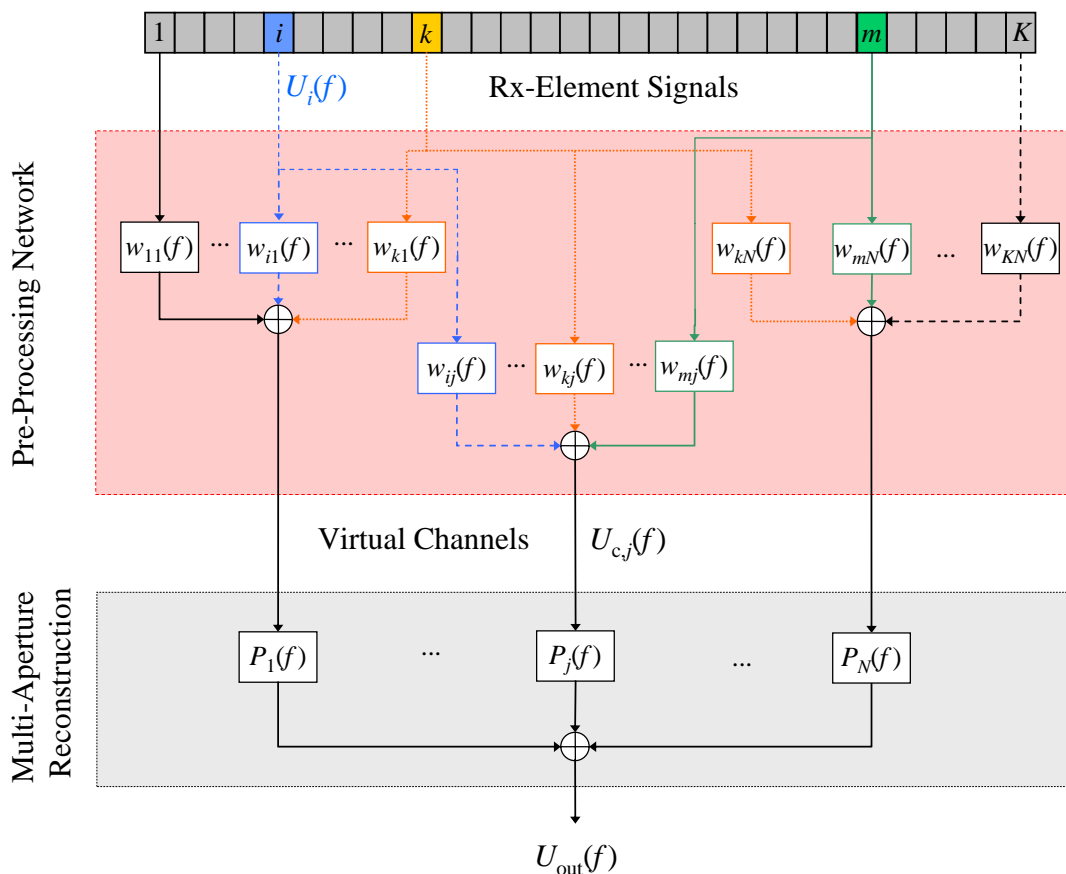


**Fig. 84. Pre-processing network enabling adaptive weighting and combination of signals of various apertures (“Rx-Elements”). This yields  $N$  optimized “virtual” output channels that enter the following digital beamforming network.**

Based on the system model presented in Fig. 46, Section 5.7, and on the above block diagram, new system models for cascaded beamforming networks are obtained:

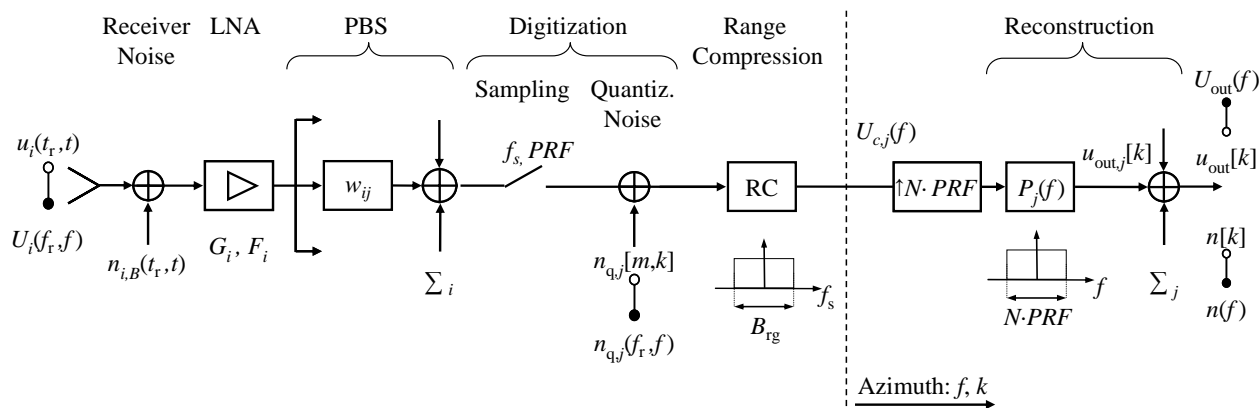


**Fig. 85. Multi-channel system model taking into account a network to perform pre-beamshaping on receive before the signals are sampled and pass through the reconstruction filter network.**

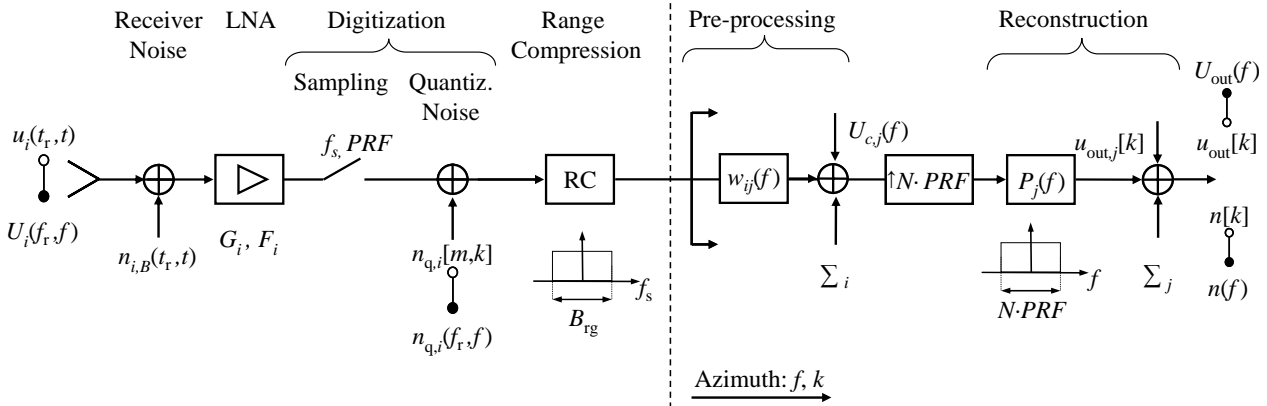


**Fig. 86. Multi-channel system model including cascaded networks to perform pre-processing after the signals are sampled and pass through the reconstruction filter network.**

The previous model is extended by a block representing the additional processing steps, either a pre-beamshaping (PBS) network situated before the analog-to-digital converter (ADC) (cf. Fig. 85) or a network processing the already digitized data as shown in Fig. 86. In the case where the pre-processing network is located behind the ADC, the order of the applied filters can of course be exchanged as long as the overall transfer function of each branch remains the same. This means that the digital pre-processing can in principle also be applied before the range compression, as well as afterwards, as depicted exemplarily in Fig. 86.

As discussed in detail in Section 5.7, the complete signal energy of a point-like target after range focusing is assumed being concentrated in a single pixel in range, by this accounting for pulse length and transmit power. In addition, the noise component does not depend on the sampling rate, i.e. an arbitrary resampling of the signal does not affect the *SNR*. Thus, a one-dimensional consideration limited to only the azimuth signal will not affect the *SNR* and, hence, the following investigations will neglect range dimension, and the above system models can be simplified to the subsequent Fig. 87 and Fig. 88, respectively.

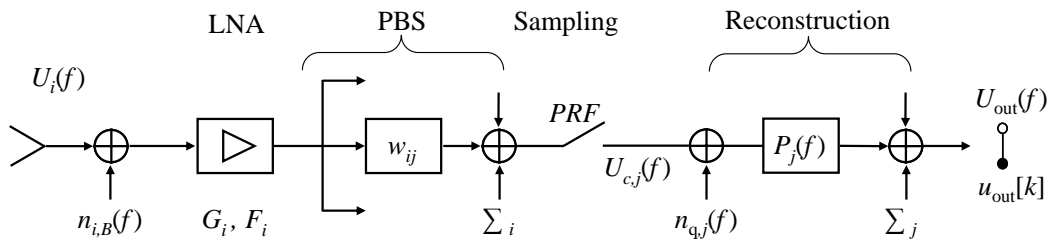


**Fig. 87. Simplified multi-channel system model considering analog pre-beamshaping on receive.**

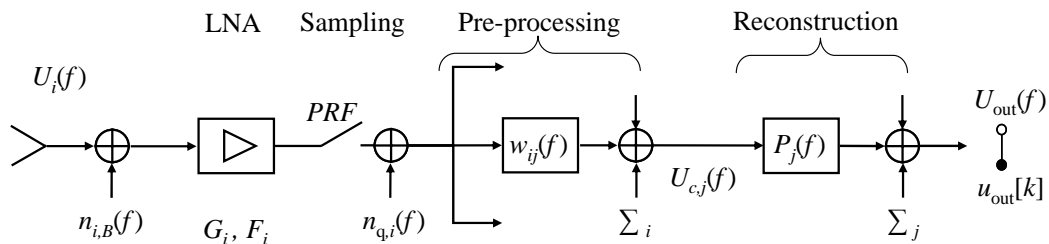


**Fig. 88. Simplified multi-channel system model considering a digital pre-processing stage.**



As defined above, the weight functions are given by  $w_{ij}(f)$  while  $U_i(f)$  denotes the elements' input signals. Further, a receiver noise component  $n_i(f)$  is introduced and the corresponding signal-to-noise ratio is described by  $SNR_{el,i}$ . As discussed in 5.7, receiver noise is considered to be the dominant thermal noise source and is assumed to be additive, white, and mutually uncorrelated between the channels. After reception, the input signals are weighted and combined to form intermediate channels which enter the reconstruction filter network. These channels are then – either before or after the pre-processing – sub-sampled in azimuth with a sampling rate of  $PRF$  inducing quantization errors which are modeled as additive noise sources  $n_{q,j}(f)$  and  $n_{q,i}(f)$ , respectively (cf. Fig. 87, Fig. 88).

### 8.7.2 Phase Center Adaptation

In this section, the basic relations regarding the formation of virtual channels are presented to demonstrate the idea and potential of the cascaded networks concept. Consider a multi-channel antenna of overall length  $l_{az}$  in azimuth, consisting of  $K$  individual elements of length  $d_{el}$  each, as illustrated in Fig. 89. It shows the well-known multi-channel antenna, which is subdivided into  $N_0$  apertures of length  $d_0$  each. Index “0” indicates the conventional architecture where the sub-apertures do not overlap, i.e.  $l_{az} = N_0 \cdot d_0$ . In this case, the spacing between the phase centers, which determines the optimum  $PRF$  (cf. Section 4.3.2), is equal to the length of the sub-apertures and hence also given by  $d_0$ .

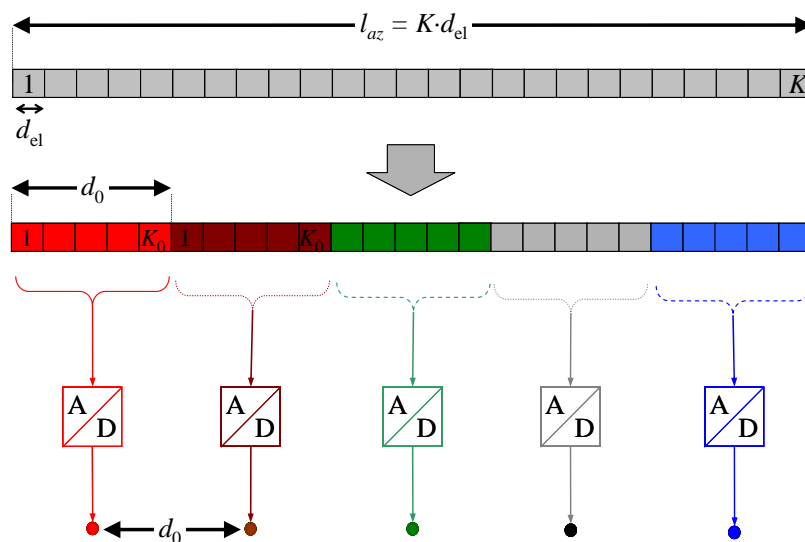


**Fig. 89. Conventional multi-channel system where sub-aperture size  $d_0$  defines the phase center distance between adjacent sub-apertures.**

In contrast, Fig. 90 shows a simple realization of a cascaded network, where some of the receiving elements are part of multiple virtual channels yielding  $N$  mutually overlapping sub-apertures of length  $d'_1 > d_0$ . Note that the number of virtual channels that are formed,  $N$ , may be different from the number of original channels,  $N_0$ , or independent elements,  $K$ . Due to the overlap of the adjacent apertures, the resulting phase center spacing  $d_1$  decreases with respect to the reference case shown on the top, where no cascaded structure is used, i.e.  $d_1 < d_0$ .

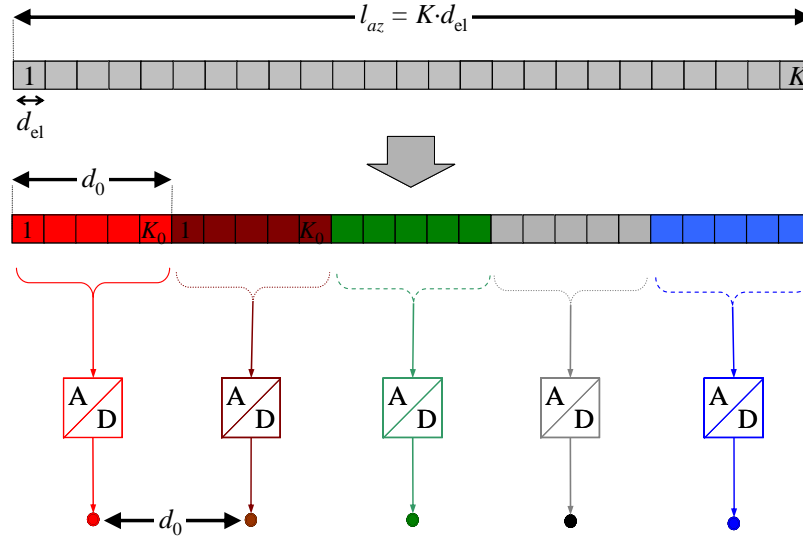


**Fig. 90. System with pre-processing network. Multiple use of certain elements yields mutually overlapping sub-apertures of increased length  $d'_1$ , but decreased phase center spacing  $d_1$ .**

The relation between the enlarged sub-aperture length  $d'_1$  and the resulting modified phase center distance  $d_1$  is given as follows:

$$d_1 = \frac{l_{az} - d'_1}{N - 1} = \frac{N_0 \cdot d_0 - d'_1}{N - 1} \quad (110)$$

In combination with the number of virtual channels,  $N$ , the modified phase center spacing  $d_1$  defines the new optimum  $PRF_{uni,c}$  as quantified below.

$$PRF_{uni,c} = \frac{2 \cdot v_s}{N \cdot d_1} = \frac{N_0 \cdot (N - 1)}{N \cdot \left( N_0 - \frac{d'_1}{d_0} \right)} \cdot PRF_{uni} \quad (111)$$

Consequently – although the overall length of the antenna remains constant – the phase center distances of the system can be adjusted by choosing  $N$  and  $d_1$ . This means that one obtains a system that allows for flexibly modifying the spatial sampling, thus adapting the optimum system  $PRF$  to the respective operating  $PRF$ . In addition, a larger sub-aperture length  $d'_1$  is available enabling pattern tapering of the receiving apertures by adjusting the weighting coefficients of the network.

In order to obtain an equal spacing between the phase centers of the antennas' virtual channels, the length of the reformed sub-apertures may not be chosen arbitrarily. Assuming a total number of  $K$  elements of length  $d_{el}$  each, and  $N$  required output channels made up of  $K_1$  elements each, the possible values  $K_1$  are given by (112). It is obtained by rearranging (110) and the fact that sub-apertures made up of integer multiples of  $d_{el}$  can only result in adjacent phase centers that are separated by an integer multiple of  $d_{el}$ .  $K_0$  represents the number of individual antenna elements that form the “original” aperture of size  $d_0$ .

$$\frac{d_1}{d_{el}} = \frac{K - K_1}{N - 1} \in \mathbb{N} \Leftrightarrow K_1 = K_0 \cdot N_0 - n \cdot (N - 1), \quad n \in \mathbb{N} \quad (112)$$

As only  $K_1 > K/N_0$  makes sense, the minimum length of the pre-beamshaping sub-apertures is defined by (113) where  $n_{\max}$  represents the maximum integer that ensures  $K_1 > K/N_0$ .

$$\frac{d'_{1,\min}}{d_{\text{el}}} = K_{1,\min} = K_0 \cdot N_0 - n_{\max} \cdot (N - 1) \quad (113)$$

Inserting the obtained  $d'_{1,\min}$  into (111) results in the next higher optimum  $PRF$  that can be adjusted by the network. Or, in other words, based on the timing and the consequential  $PRF_{\text{uni}}$  and  $PRF_{\text{uni,c}}$ , (113) allows for determining the overall number of elements  $K$  that are needed to enable the adjustment by the pre-processing network. Once  $K$  is fixed,  $d'_1$  can be deduced from the above equations.

One recognizes that the way of combining the two stages offers a wide range of flexibility, as for example a closer spacing of the resulting phase centers can be achieved by sub-apertures that are no longer formed by adjacent but distributed elements. Assume identical weighting for each group of elements forming the sub-apertures. Then, the minimum possible phase center spacing is given by the distance between adjacent elements. It can be achieved if sub-apertures are made up of  $N$  elements while overlapping by  $N-1$  elements with their neighbored sub-apertures, or if distributed elements are chosen to form the sub-apertures (cf. Fig. 91). In this case the elements forming a specific virtual channel are no longer neighbored, but distributed over the antenna. The resulting channels are then mutually shifted by a single receiving element, leading to a phase center spacing  $d_1 = d_{\text{el}}$  as indicated in Fig. 91.

Under the assumption that all elements are used, the maximum spacing is obtained in the conventional case where adjacent sub-apertures do not overlap. In combination with the number of channels that are formed, this offers a wide range of adaptation regarding the  $PRF$ . Note that in a digital cascaded network all processing is applied a-posteriori and consequently the system setting can be reconfigured arbitrarily to focus on the respective performance parameter of interest, be it ambiguity suppression, resolution or  $NESZ$ .

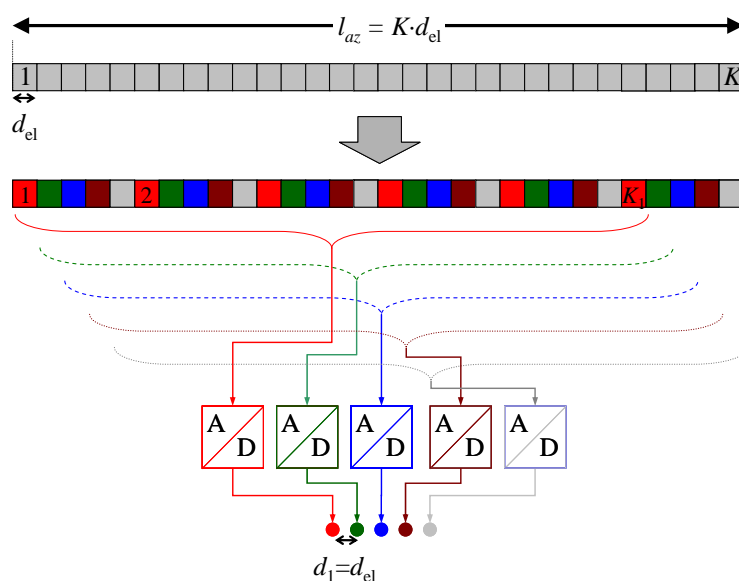


**Fig. 91. System with pre-processing network forming channels from distributed elements, yielding the minimum possible phase center spacing  $d_1 = d_{\text{el}}$ .**

### 8.7.3 Compensation for Power Loss in Analog Networks

In the analog representation of a pre-processing network, amplitude imbalances might occur as not all elements' signals are to be split equally. Hence, depending on the necessary branching of the respective signal, the gain loss is different and has to be compensated to ensure uniform amplitudes of all signals when entering the first processing network. This can be achieved by including the compensation in the weighting functions of this first stage by replacing the amplitude gain  $|w_{ij}|$  by the new factor  $|w'_{ij}|$  according to (114), where  $N_{\text{ch},i}$  represents the number of signals in which the original signal of element  $i$  is split. By this, the amplitude of the signal after being split is recovered as given in (115), where  $U_{i,\text{split}}(f)$  gives the signal after splitting while  $U_i(f)$  denotes the original signal of channel  $i$ . With these adapted weighting functions and considering the same for the noise contributions in the respective channels, all following equations remain valid.

$$|w'_{ij}| = |w_{ij}| \cdot \sqrt{N_{\text{ch},i}} \quad (114)$$

$$U_{i,\text{split}}(f) \cdot w'_{ij}(f) = \frac{U_i(f)}{\sqrt{N_{\text{ch},i}}} \cdot w'_{ij}(f) = U_i(f) \cdot w_{ij}(f) \quad (115)$$

### 8.7.4 Signal Power

According to Section 5.5, the signal that is relevant for the output signal power is determined by the input signal of the reconstruction network which is equivalent to the output signals  $U_{c,j}(f)$  of the pre-processing stage. These signals are defined by the weighted sum of signals received by the single elements and denoted by  $U_i(f)$ . The respective weighting in the pre-processing stage is given by the coefficients  $w_{ij}(f)$  (cf. (116)). Note that this – unaliased – signal does not depend on the location of the ADC and hence the following considerations are valid for both representations of pre-processing networks.

$$U_{c,j}(f) = \sum_{i=1}^K \sqrt{G_i} \cdot U_i(f) \cdot w_{ij}(f) \quad (116)$$

Recall the reference functions  $H_j(f)$ , which relate the signal  $U_j(f)$  to  $U(f)$  representing the signal received by a single element at the same position as the transmit aperture (cf. Section 4.2). Equivalently,  $U_i(f)$  can be related to the monostatic reference function  $U(f)$  by a function  $M_i(f)$ :

$$U_i(f) = M_i(f) \cdot U(f) \quad (117)$$

Basically, the functions  $M_i(f)$  correspond to a time shift and the addition of a constant phase as already derived for the functions  $H_j(f)$ . Nevertheless, they are denominated by  $M_j(f)$  to avoid confusion with the reference functions.

Again assuming identical gain  $G$  of all LNAs and inserting (117) in (116), the following equation is obtained.

$$U_{c,j}(f) = \sum_{i=1}^K \sqrt{G_i} \cdot U_i(f) \cdot w_{ij}(f) = \sqrt{G} \cdot U(f) \cdot \sum_{i=1}^K M_i(f) \cdot w_{ij}(f) \quad (118)$$

In a next step,  $w_{ij}(f)$  is assumed being the same for every virtual channel  $j$ . Consequently, all resulting virtual channels  $j$  are identical in terms of their envelope and only shifted relative to each other with respect to their phase centers. This interpretation allows for expressing the signals by an equivalent monostatic signal  $U_c(f)$  and functions  $H_j(f)$  characterizing the virtual channels  $j$  as done in (30). Hence, (118) can be rearranged to (119), where  $U_c(f)$  corresponds to the signal that would arise by the weighted sum of the single elements, if the resulting phase center was situated at the same position as the transmitter. The power gain  $G$  is mentioned separately as it will cancel later. The relation between the envelopes of all channels' signals and the equivalent monostatic signal is expressed in (120).

$$U_{c,j}(f) = \sqrt{G} \cdot U_c(f) \cdot H_j(f) \quad (119)$$

$$|U_{c,j}(f)| = |\sqrt{G} \cdot U_c(f)| \quad (120)$$

Note that only the pre-processing changes the characteristic of  $U_c(f)$  while the digital beamforming network that reconstructs the signal does not affect the pattern of  $U_c(f)$ . Hence, the signal power is determined by the spectral appearance of  $U_c(f)$  given by the resulting azimuth pattern characteristic of the combined sub-apertures,  $A(f)$ . Using (121), one obtains the following output signal after reconstruction in the data (cf. (122)) and in the image after focusing with a Doppler bandwidth of  $B_D$  (cf. (123)), respectively. Again,  $p_{\text{tx,av}}$  represents the average emitted signal power and the constant  $C_{UA}$  does not affect the power; it just relates  $U_c(f)$  and  $A(f)$  to ensure the correct unity of  $A(f)$  with respect to  $p_{\text{s,c},B_D}$ .

$$|U_c(f)| = \left| U(f) \cdot \sum_{i=1}^K M_i(f) \cdot w_{ij}(f) \right| = C_{UA} \cdot A(f) \cdot \left| \sum_{i=1}^K M_i(f) \cdot w_{ij}(f) \right| \quad (121)$$

$$p_{\text{s,c}} = p_{\text{tx,av}} \cdot G \cdot \mathbb{E} \left[ \left| U_c(f) \cdot \text{rect} \left( \frac{f}{I_S} \right) \right|^2 \right] = p_{\text{s,el}} \cdot G \cdot \mathbb{E} \left[ \left| \sum_{i=1}^K (M_i(f) \cdot w_{ij}(f)) \right|^2 \right] \quad (122)$$

$$p_{\text{s,c},B_D} = p_{\text{tx,av}} \cdot G \cdot \mathbb{E} \left[ C_{UA}^2 \cdot A(f)^2 \cdot \left| \sum_{i=1}^K M_i(f) \cdot w_{ij}(f) \cdot \text{rect} \left( \frac{f}{B_D} \right) \right|^2 \right] \quad (123)$$

The different signal powers for a system with and without pre-processing are quantified by (58) and (123), respectively. The difference is governed by the weighted sum which basically entails a modified azimuth pattern. This can be quantified by the modified power gain of the cascaded network,  $G_{\text{rx,c}}$ , in combination with the influence of the changed spectral shape on the signal power, which is considered in the azimuth loss factor  $L_{\text{az}}$ . This loss factor is defined in (61) in Section 5.5 and takes into account the loss of energy due to the drop-off of the azimuth antenna pattern after the pre-processing, which depends on the size and tapering of the used apertures.

The maximum gain corresponds to the evaluation of (122) and (123), respectively, in bore-sight, i.e.  $f=0$ . Hence,  $G_{\text{rx,c}}$  is determined by the number of used elements and the applied weighting coefficients that might entail a taper loss if amplitude tapering is applied. Assuming a number of  $K_1$  elements forming a single channel, the summation over all elements taking into account the respective weighting defines  $G_{\text{rx,c}}$ :

$$G_{\text{rx,c}} = \left( \sum_{i=1}^{K_1} w_{ij}(f=0) \right)^2 \quad (124)$$

For comparison, a conventionally operated system, where  $K_0$  elements without taper form a single aperture, yields a reference gain  $G_{\text{rx,0}}$  as follows:

$$G_{\text{rx,0}} = K_0^2 \quad (125)$$

Note that for an evaluation of the resulting *NESZ*, the changed number of  $N$  virtual channels with respect to the conventional system with  $N_0$  channels has to be taken into account as it results in a different effective sampling rate of  $N \cdot \text{PRF}$  compared to  $N_0 \cdot \text{PRF}$  before. As mentioned in Section 5.8, this affects the energy “gathered” by the system. This dependency on  $N$  is implicitly included in the *NESZ* definition of (91) which considers the effective number of channels.

### 8.7.5 Residual Reconstruction Error and Azimuth Ambiguities: $AASR_{N,B_D}$

The extension of the multi-channel reconstruction processing by a pre-processing network influences the signal power as well as the azimuth ambiguous energy. This requires that all expressions derived in Sections 5.5 and 5.6 for the conventional beamforming case are adapted to the cascaded beamforming networks. In the case of the residual ambiguities this can be achieved by taking into account the gain factor  $G$  and replacing  $U(f)$  in the equations of Section 5.5 by the resulting output signal of the pre-processing network  $U_c(f)$  described in (119), that represents the spectral appearance of the signal before the reconstruction network, but takes into account the pre-processing, both analog or digital. Again, (119) assumes that all virtual channels  $j$  that enter the reconstruction filter network are identical in terms of weighting of the respective elements  $i$  that form the channel and are hence identical in terms of their envelope. Furthermore, as both residual ambiguous power and signal power are directly depending on the emitted signal power, the factor  $p_{\text{tx,av}}$  in (122) will cancel out when calculating the ambiguity-to-signal ratio. Hence,  $p_{\text{tx,av}}$  is neglected in the following derivation.

Analog to (68) for the conventional beamforming case,  $e_{c,k}$  in (126) expresses the residual ambiguous contribution of order  $k$  in the signal after reconstruction if a pre-processing network is applied. Again, the more convenient notation  $U_{c,k}(f) = U_c(f+k \cdot \text{PRF})$  is used to denote the shifted spectra while  $I_m$  denotes the sub-band  $m$  of the Doppler spectrum and  $m_0$  gives the first sub-band that contains ambiguous contributions.

$$e_{c,k}(f) = U_{c,k}(f) \cdot \sum_{m=m_0}^N \sum_{j=1}^N H_{jk}(f) \cdot P_{jm}(f) \cdot \text{rect}\left(\frac{f}{I_m}\right) \quad (126)$$

Then, the respective ambiguous power in a cascaded network,  $p_{a,c}$ , is determined by the mean squared amplitude of all residual ambiguities, i.e. the squared sum over all ambiguities  $e_{c,k}$  as described in (127). In combination with the signal power of (122) this yields the ambiguous energy suppression  $AASR_N$  of cascaded networks (cf. (128)).

$$p_{a,c} = \mathbb{E} \left[ \left| 2 \cdot G \cdot \sum_{k=1}^{\infty} e_{c,k}(f) \right|^2 \right] \quad (127)$$

$$AASR_N = \frac{p_{a,c}}{p_{s,c}} \quad (128)$$

To obtain the respective expressions after focusing, the bandwidth  $B_D$  of the focusing filter has to be taken into account to derive  $e_{c,k,B_D}$  that gives the ambiguous error of order  $k$  after focusing (cf. (129)). Then the squared sum over all contributions  $k$  normalized to the signal power expressed by (123) yields the azimuth ambiguous energy suppression in the image denoted by  $AASR_{N,B_D}$  (cf. (130)).

$$e_{c,k,B_D}(f) = U_{c,k}(f) \cdot \sum_{m=m_0}^N \sum_{j=1}^N H_{jk}(f) \cdot P_{jm}(f) \cdot \text{rect} \left( \frac{f}{B_D} \right) \quad (129)$$

$$AASR_{N,B_D} = \frac{p_{a,c,B_D}}{p_{s,c,B_D}} = \frac{\mathbb{E} \left[ \left| 2 \cdot G \cdot \sum_{k=1}^{\infty} e_{c,k,B_D}(f) \right|^2 \right]}{G \cdot \mathbb{E} \left[ A(f)^2 \cdot \left| \sum_{i=1}^K M_i(f) \cdot w_{ij}(f) \cdot \text{rect} \left( \frac{f}{B_D} \right) \right|^2 \right]} \quad (130)$$

In order to obtain the response of the residual ambiguity of order  $k$  in the image, the respective ambiguous contribution  $e_{c,k}$  defined by (126) has to be focused by the used SAR processor.

### 8.7.6 SNR Scaling in Cascaded Beamforming Networks: $\Phi_{bf,c}$

Recalling the definitions and assumptions given in Section 5.7 and taking into account the extended system models of Fig. 87 and Fig. 88, respectively, the influence of the pre-processing network on the noise power is investigated. Firstly, the weighting elements  $w_{ij}(f)$  are assumed to be noise-free, i.e. the noise figure of the pre-processing network is equal to 1. The receiver noise is assumed to be mutually uncorrelated additive white Gaussian noise  $n_{i,B}(f)$  with a power spectral density of  $N_{0,B}$  with respect to the system bandwidth  $B$ . Further, quantization noise is assumed to be uniformly distributed and spectrally white as proposed in [76] and the noise before and after sampling in azimuth will be distinguished by the index  $B$ . Again identical elements  $i$ , implying the same characteristics for  $G_i$  and  $F_i$  for all  $i$  are assumed, yielding the following output noise power  $p_{n,c}$  of the system made up of thermal receiver noise contributions  $p_{n,c,rx}$  and quantization noise  $p_{n,q}$ .

$$p_{n,c} = \underbrace{p_{n,el} \cdot N \cdot G \cdot F \cdot \sum_{i=1}^K \mathbb{E} \left[ \left| \sum_{j=1}^N P_j(f) \cdot w_{ij}(f) \right|^2 \right]}_{\text{receiver noise: } p_{n,c,rx}} + \underbrace{p_{n,q}}_{\text{quantization noise}} = p_{n,c,rx} + p_{n,q} \quad (131)$$

This means that the input noise power is amplified by the pre-processing network as well as by the reconstruction filters. Further, weighted quantization noise is added. The amplification of the receiver noise is independent of the chosen type of pre-processing network, while the quantization error depends on the location of the ADC. If the pre-processing is applied before digitization, i.e. an analog network is added, then the quantization noise at the output is given by  $p_{n,q,an}$  in (132) where the additional index “an” indicates the analog processing. In contrast, (133) is valid if a digital processing stage is implemented and hence the quantization error is introduced in the signal before the additional network is passed. The respective error power is denoted by  $p_{n,q,d}$  where the index “d” refers to the digital pre-processing.

$$p_{n,q,an} = \mathbb{E} \left[ \left| \sum_{j=1}^N P_j(f) \cdot n_{q,j}(f) \right|^2 \right] \quad (132)$$

$$p_{n,q,d} = \sum_{i=1}^K \mathbb{E} \left[ \left| \sum_{j=1}^N P_j(f) \cdot w_{ij}(f) \cdot n_{q,i}(f) \right|^2 \right] \quad (133)$$

A comparison of (132) and (133) shows that sampling after the pre-processing avoids the summation over all elements  $i$  which represents the mutual correlations of the quantization error introduced by the pre-processing network. This implies that sampling as late as possible is more favorable in terms of quantization error.

Again, the number of bits is assumed to be chosen such that the quantization error in the output signal will be negligible compared to the (thermal) receiver noise. In consequence, the overall noise is approximated by  $p_{n,c,rx}$ . This results in (134) to quantify the scaling of the noise power by the pre-processing network and the following reconstruction. In contrast to the mere digital beamforming network discussed in Section 5.7, the pre-processing introduces a coupling between the virtual channels’ signals as the signal from the same receiving element might be part of different virtual channels. Hence, mutual correlations arise that do no longer allow for “separating” the noise contributions from the individual channels. From a mathematical point of view, this means that the squared sum in (134) can no longer be simplified to a sum of squares.

$$\frac{p_{n,c}}{p_{n,el}} = N \cdot G \cdot F \cdot \sum_{i=1}^K \mathbb{E} \left[ \left| \sum_{j=1}^N P_j(f) \cdot w_{ij}(f) \right|^2 \right] \quad (134)$$

Analogously to (82) that gives the  $SNR$  scaling factor of conventional beamforming networks, the  $SNR$  scaling factor of the cascaded network with respect to the data,  $\Phi_{bf,c}$ , is determined by the combination of (122) – that gives the output signal power – and (134) that approximates the noise power (cf. (135)). Analogously to (83), the  $SNR_{el}/SNR_{out}$  value at the optimum  $PRF$  is given by the inverse of the LNA’s noise figure  $F$ .



$$\Phi_{\text{bf,c}} = \frac{p_{\text{n,c}}/p_{\text{n,el}}}{p_{\text{s,c}}/p_{\text{s,el}}} \cdot \frac{1}{F} = \frac{N \cdot \sum_{i=1}^K \mathbb{E} \left[ \left| \sum_{j=1}^N P_j(f) \cdot w_{ij}(f) \cdot \text{rect} \left( \frac{f}{I_s} \right) \right|^2 \right]}{\mathbb{E} \left[ \left| \sum_{i=1}^K \left( M_i(f) \cdot w_{ij}(f) \cdot \text{rect} \left( \frac{f}{I_s} \right) \right) \right|^2 \right]} \quad (135)$$

As before, the *SNR* scaling factor for the focused image cannot be given explicitly, as the relation between the input and output signal power depends on the shape of  $U(f)$  and other parameters as defined in (123). Of course,  $\Phi_{\text{bf,c}}$  can be calculated by using (123) for determining the signal power, and expression (136) giving the remaining noise power after focusing.

$$p_{\text{n,c},B_D} = p_{\text{n,el}} \cdot N \cdot G \cdot F \cdot \sum_{i=1}^K \mathbb{E} \left[ \left| \sum_{j=1}^N P_j(f) \cdot w_{ij}(f) \cdot \text{rect} \left( \frac{f}{B_D} \right) \right|^2 \right] \quad (136)$$

### 8.7.7 Performance Analysis I - Analog Pre-Beamshaping on Receive

In the following, the first example for a cascaded beamforming network is given to demonstrate the potential of the technique. In the present section, an analog pre-processing technique of the multi-channel RF signals is chosen as a representation of such a cascaded structure. The method is referred to as “pre-beamshaping on receive” and it requires a more complex Rx antenna architecture, as multiple independent receiving elements are needed to enable the pre-processing. Thus, in the following,  $K = 168$  receiving elements are assumed, each allowing for a tapering in amplitude and phase. This means that in the reference case – given by the “conventional” system according to Section 8.5 –  $K_0 = 24$  receiving elements are grouped to a single virtual channel to obtain  $N_0 = 7$  channels without mutual overlap. In the cascaded case, the pre-processing network is configured such that mutually overlapping sub-apertures of 2.625 m length each are formed; i.e. each channel consists of  $K_1 = 36$  single elements. This yields a decreased phase center spacing entailing a new optimum *PRF* of 1346 Hz according to (111). In order to keep the beamwidth of the receiving pattern constant and to suppress its sidelobes, a cosine taper is applied to each of the sub-apertures, leading to different impacts on signal and noise power as will be discussed in the following. In detail, the chosen weighting functions are as follows:

$$w_{ij}(f) = w_{ij} = \cos \left( \pi \frac{i \cdot d_{\text{az,el}}}{d_1} \right) = \cos \left( \pi \frac{i}{K_1} \right); \text{ where } i \in \left[ -\frac{K_1}{2}, \frac{K_1}{2} \right] \quad (137)$$

Concerning the **signal power** in the pre-beamshaping case, the new antenna dimensions and the pre-processing network entail for the considered bandwidth of  $B_D = 7.6$  kHz an increased azimuth loss  $L_{\text{az}}$  of 3.05 dB compared to  $L_{\text{az}} = 2.9$  dB in the conventional case (cf. (61)). This loss of 0.15 dB is increased by a new maximum gain on receive in the pre-beamshaping case that is worsened by ~0.55 dB compared to the maximum gain in the conventional case. It results from the applied tapering and takes into account the increased sub-aperture length. This maximum gain is calculated accordingly to (125), where  $K_0 = 24$ ,  $K_1 = 36$ , and the tapering coefficients as

given by (137) are considered. Note that the loss of 0.55 dB not only depends on the applied tapering but also on the number of elements. In the limit given by continuous amplitude tapering of the antenna, i.e.  $K_1 \rightarrow \infty$  and  $d_{el} \rightarrow 0$ , the loss reduces to 0.4 dB. Regarding the **noise power scaling**, the amplitude tapering of the pre-processing network attenuates the noise power in a similar way as the signal power. Due to the large number of elements that are combined and due to the applied amplitude taper, the ratio of the noise powers for the respective uniform *PRF* values of the two investigated systems cannot be derived illustratively as the signal power above. Nevertheless, the simulation of the *SNR* scaling factor for the pre-beamshaping scenario and its estimation according to (135) and (136), respectively, show very good coincidence and prove the validity of the derived equations (cf. Fig. 92).

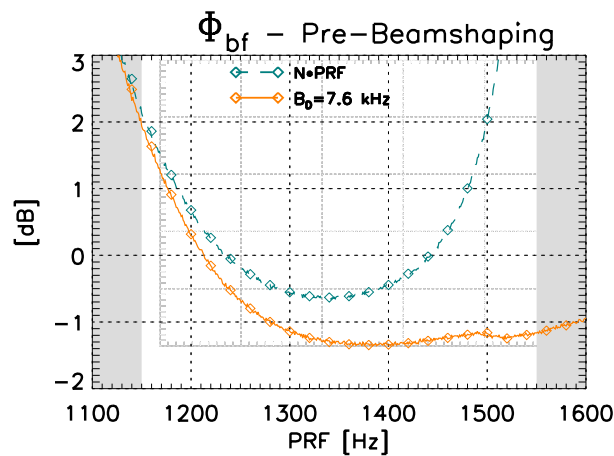


**Fig. 92.** Simulated *SNR* scaling factor  $\Phi_{bf}$  of the pre-beamshaping scenario normalized to the uniform value of the conventional case. Results before (dashed green) and after focusing with  $B_D = 7.6$  kHz (solid orange). Selected samples of the respective analytic predictions according to Section 8.7.6 are overlaid with the diamond symbols.

According to the decreased phase center spacing, the optimum *PRF* and consequently the optimum *SNR* scaling factor moved towards higher *PRF* values and provides good results for the higher *PRF* region. The shown *SNR* scaling factor of the cascaded network is normalized to  $\Phi_{bf}$  obtained for uniform sampling of the conventional network.<sup>27</sup> It already incorporates the impact of the sub-aperture dimension and taper coefficients on noise and signal power and allows hence for a direct comparison to the conventional beamforming approach. This comparison of the two characteristics regarding the ***SNR* scaling** in the focused image is given in Fig. 93. Again, both curves are normalized to the uniform value of the conventional case.

Fig. 93 shows that an improved *SNR* scaling factor is obtained for the pre-beamshaping scenario for *PRF* values above 1240 Hz (solid orange line) while the conventionally operated system is favorable for *PRF* values below 1240 Hz (dashed blue line). Further, the combination of both operational modes guarantees a sufficiently low *SNR* scaling over the complete range of

<sup>27</sup>It should be noted that in Fig. 92 the normalization of the *SNR* scaling is not (and in the following will not be) done to the single-element *SNR*, but to the *SNR* of a single virtual aperture in the conventional beamforming case, i.e. the combination of  $K_0$  individual elements.

*PRF*. Compared to the example system of Chapter 7, a better *SNR* scaling is obtained for all operated *PRF* values, thus ensuring a *NESZ* below -19.2 dB.

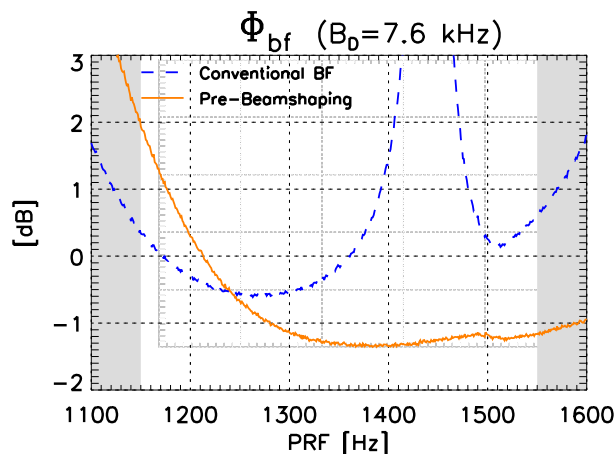


**Fig. 93.** Simulated *SNR* scaling factor  $\Phi_{bf}$  of the conventional digital beamforming network (dashed blue) compared to the case where a pre-beamshaping network is added (solid orange) ( $B_D = 7.6$  kHz).

In a next step, an analysis of the **geometric resolution in azimuth** yields a value of 1.03 m for both conventional and pre-beamshaping operation.

Finally, the **ambiguous energy suppression** of the modified system is investigated. As mentioned above, the transmit antenna was slightly increased to 3.15 m to guarantee a minimum ambiguity suppression of -21 dB in conventional operation of the system (cf. Fig. 94, dashed blue line). When the pre-processing network is applied, the suppression becomes better for *PRF* values above ~1210 Hz and is clearly improved for higher *PRF* values due to reduced sidelobes of the receive pattern and minimized amplification of the ambiguous energy caused by the adapted phase centers (cf. Fig. 94, solid orange line).

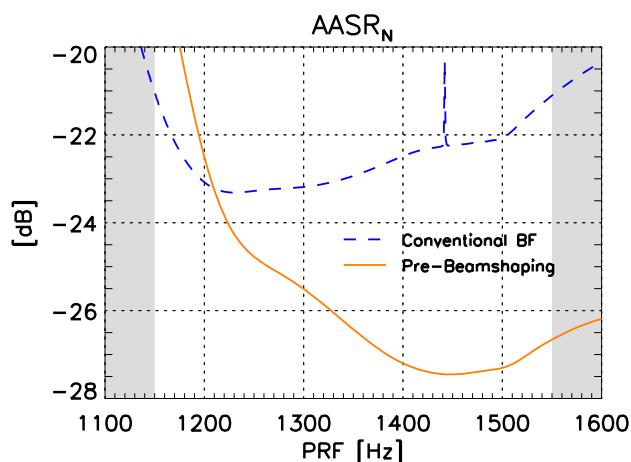


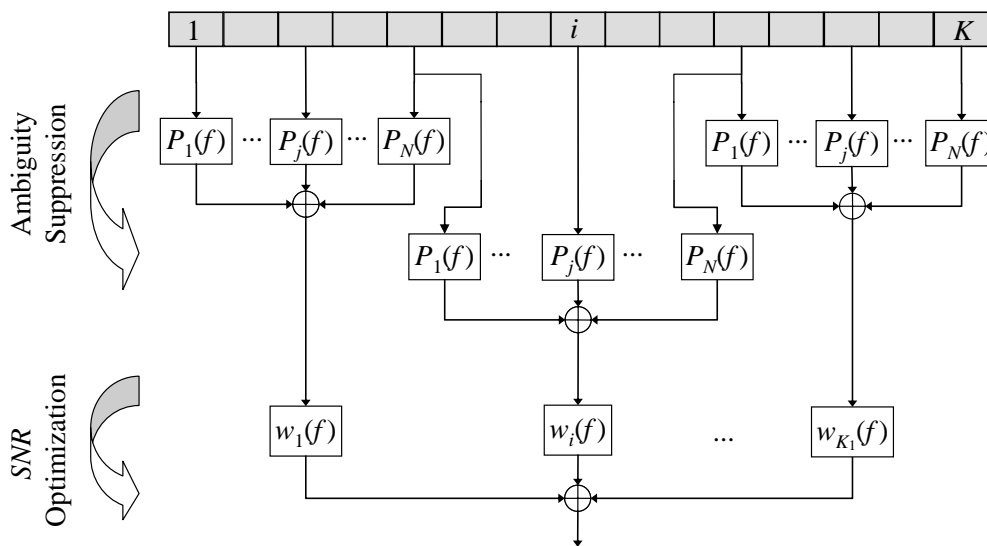
**Fig. 94.**  $AASR_N$  vs. *PRF* with pre-beamshaping network (solid orange) compared to conventional digital beamforming (dashed blue) ( $B_D = 7.6$  kHz). The peak in the conventional approach occurs at the “singular” *PRF* = 1440 Hz (cf. Section 4.3.3).

In conclusion, it can be stated that the application of an appropriate analog pre-processing network clearly extends the full performance range with respect to the operating *PRF*. In combination, the results for  $AASR_N$ , resolution, and the *SNR* scaling factor  $\Phi_{bf}$  show that it is favorable to use the conventional configuration below a *PRF* of 1210 Hz and apply the pre-beamshaping for *PRF* values higher than 1240 Hz. In between, the focus can be either turned to the *NESZ* by choosing the conventional approach or the pre-processing is applied to concentrate on the optimization of the  $AASR_N$ .

### 8.7.8 Performance Analysis II - Adapted Digital Beamforming

Similar to the pre-beamshaping network presented before, this approach is based on subsequent processing networks. But in contrast to the analog pre-beamshaping, all signals are sampled, digitized and stored before processing. Hence, the amount of data to be handled does not allow for a large number of individual elements, but such an architecture enables to perform all processing a-posteriori and thus offers wide flexibility and reconfigurability in terms of order and structure of the networks. Different from the analog system of Section 8.7.7, an Rx antenna of only  $K=7$  independent receiving elements is assumed for the following investigations. This means that in the reference case each channel is formed by a single receiving element, i.e.  $N_0 = K$ , and no special architecture is necessary.

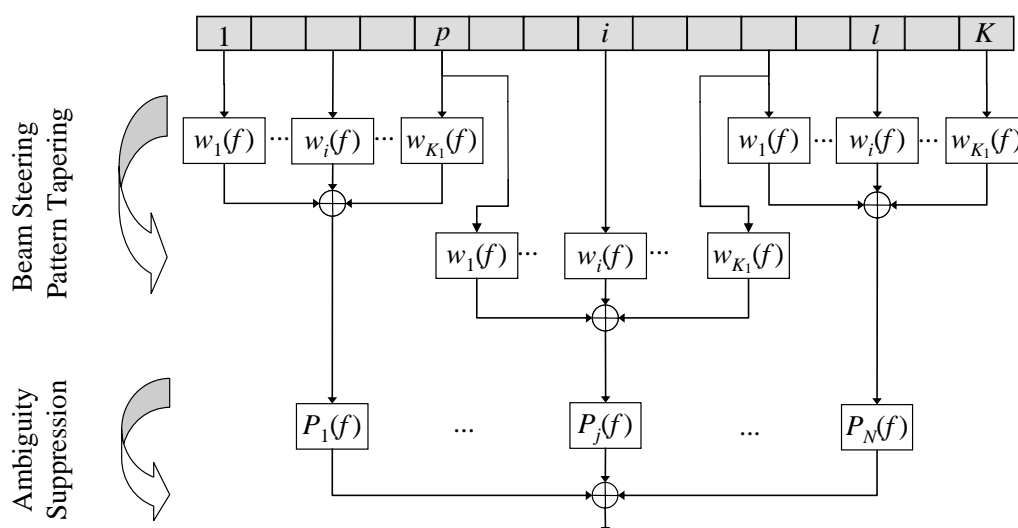
A possible realization of such a digital cascaded network is given by Fig. 95, where the multi-channel reconstruction is followed by a beam-steering with weights  $w_i(f)$ . The structure incorporates the idea of trading one or more degrees of freedom used for ambiguity suppression against an optimization of the *SNR*. The antenna consists of  $K$  receiving elements, but only  $N$  channels are processed by the multi-channel reconstruction algorithm, respectively, to form  $K_1$  output channels that may mutually overlap or not. The resulting  $K_1$  channels are then weighted and combined by the weighting functions  $w_i(f)$  with the goal to increase the signal power. As the



**Fig. 95.** Cascaded networks for ambiguity suppression followed by beam-steering with mutual overlap of adjacent filter groups of the first stage.

multi-channel reconstruction processing does not affect the signal envelope, the beamwidth of the output signal is still defined by the single-element length and the weighting, while the gain is determined by the number of channels that are combined in the second stage. This means that the signal amplitude gain can be increased up to a factor of  $K_1$  at the cost of an effective sampling rate that is decreased by a factor of  $K/N$  and an increased noise floor. The latter is due to partly overlapping channels which introduce mutual correlations between the noise components in the resulting output channels.

The commutativity of the system allows for changing the different stages as long as the resulting processing of each element's branch remains unaltered. Consequently, the system of Fig. 95 can be equivalently represented by a structure where the networks are ordered inversely and the steering of the beam in combination with a possible tapering precedes the multi-channel reconstruction. As depicted in Fig. 96 one obtains a structure similar to the basic block diagram introduced in Fig. 84. Note that Fig. 95 and Fig. 96 give equivalent representations for cascaded digital networks, but do not show identical systems in terms of the overall transfer function.

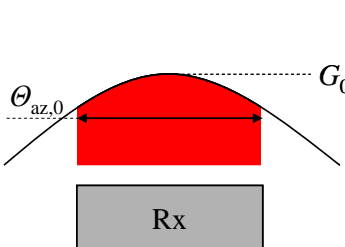
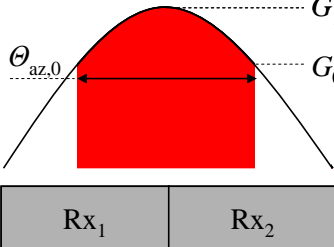
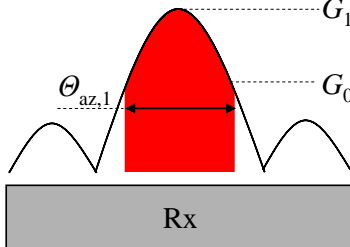


**Fig. 96. Cascaded networks: Beam-steering for SNR optimization followed by reconstruction of  $N$  channels with mutual overlap of adjacent beam-steering groups. This representation is similar to a pre-beamshaping network but with less elements and A/D conversion carried out before processing.**

In the subsequent section, the potential of the adapted beamforming approach is demonstrated with the system example of Section 8.7. The Rx antenna consists of 7 sub-apertures of length 1.75 m each, and the applied  $PRF$  values range from 1150 Hz to 1550 Hz. As already derived in Section 8.7, the  $SNR$  scaling factor of the reconstruction network shows sufficiently low values for the  $PRF$  range from 1150 Hz to 1350 Hz, but yields unacceptably high values for  $PRF$  values higher than 1350 Hz (cf. Fig. 76). To operate the system in these  $PRF$  ranges, the gathered data are processed in a different way. According to the basic structure given in Fig. 95 and Fig. 96, respectively, the signals of six adjacent sub-apertures, respectively, are processed by the multi-channel reconstruction algorithm, yielding two output channels that are weighted and combined to maximize the signal power. Changing the order of the processing networks, this is

equivalent to combining two adjacent receiving elements, respectively, yielding six channels that are reconstructed unambiguously in the second stage. Due to this adapted processing the number of phase centers is reduced and consequently the optimum *PRF* is shifted to 1440 Hz.

In the following, two different weighting approaches for combining two adjacent sub-apertures, respectively, are evaluated and compared to the conventional case, where no pre-processing is applied (cf. Fig. 97, left). All approaches are summarized in Fig. 97.

Conventional Case	Scenario 1	Scenario 2
		
<ul style="list-style-type: none"> <li>▪ Effective channels <math>N_{\text{eff}} = 7</math></li> <li>▪ Power gain <math>G_0</math></li> <li>▪ HPBW <math>\theta_{\text{az},0}</math></li> <li>▪ Azimuth Loss <math>L_{\text{az},0}</math></li> </ul>	<ul style="list-style-type: none"> <li>▪ <math>N_{\text{eff}} = 6</math></li> <li>▪ <math>G_1 = G_0 + 6 \text{ dB}</math></li> <li>▪ <math>\theta_{\text{az},0}</math></li> <li>▪ <math>L_{\text{az},0}</math></li> </ul>	<ul style="list-style-type: none"> <li>▪ <math>N_{\text{eff}} = 6</math></li> <li>▪ <math>G_1 = G_0 + 6 \text{ dB}</math></li> <li>▪ <math>\theta_{\text{az},1} = 0.5 \cdot \theta_{\text{az},0}</math></li> <li>▪ <math>L_{\text{az},1} = L_{\text{az},0} + 1.1 \text{ dB}</math></li> </ul>

**Fig. 97. Conventional case (left) compared to two different pre-processing scenarios with respect to effective number of channels  $N_{\text{eff}}$  and receiving pattern with power gain  $G_i$ , half power beamwidth (HPBW)  $\theta_{\text{az},i}$ , and azimuth loss  $L_{\text{az},i}$ . In Scenario 1 a Doppler frequency dependent weighting is applied (middle); in Scenario 2 (right) the respective signals are simply added.**

▪ *Adapted Beamforming Scenario 1:* In a first scenario, the two signals are combined by a Doppler frequency dependent weighting where the respective functions  $w_{ij}(f)$  are chosen to steer the maximum of the joint antenna characteristic for every  $f \in [-B_D/2, B_D/2]$  in the direction corresponding to that frequency  $f$ :

$$w_{ij}(f) = w_{2j}^*(f) = \exp \left[ j \cdot \frac{\pi \cdot \Delta x}{2 \cdot v_s} \cdot f \right] \quad (138)$$

Regarding the output signal of the pre-processing step, this yields a signal envelope whose beamwidth is still defined by the single-element length, while its gain is determined by the number of channels that are combined in the second stage. This means that the signal amplitude doubles and the respective power gain  $G_1$  rises by 6 dB (cf. Fig. 97, middle) at the cost of an effective sampling rate that is decreased by a factor of 6/7 according to the reduced number of virtual channels. Further, an increased noise floor occurs due to mutual correlations between the noise components in the resulting output channels that are caused by the partly overlapping channels. Note that the new effective number of channels requires a minimum *PRF* of  $B_D/6 = 1267$  Hz to ensure a sampling according to Nyquist. Consequently the respective curves characterizing this scenario are only defined starting from a *PRF* of  $\sim 1300$  Hz, while the region below this value is stressed by the area shaded in light gray.

▪ *Adapted Beamforming Scenario 2*: Secondly, the signals of two adjacent sub-apertures are simply added without any frequency dependent weighting, i.e. the respective  $w_{1j}$  and  $w_{2j}$  are equal to 1. As in scenario 1, this results in an increased maximum gain  $G_1 = G_0 + 6$  dB which is at the cost of an effective sampling rate decreased by a factor of 6/7. Further, and in contrast to scenario 1, a receiving pattern of half the 3 dB-beamwidth is obtained (cf. Fig. 97, right), entailing an azimuth loss  $L_{az,1}$  risen by 1.1 dB and a coarsened resolution, as it will be shown later. Like before, mutually correlated noise components occur in different channels entailing a rise of the noise level. Again, the effective number of channels requires a minimum *PRF* of 1267 Hz and consequently the respective curves are shown for *PRF* values higher than  $\sim 1300$  Hz.

The influence of the adapted processing on the azimuth antenna pattern on receive is summarized in Fig. 97. This comprises changes of peak power gain  $G$  and the half power beamwidth  $\Theta_{az}$  which affects directly the azimuth loss  $L_{az}$ . Taking further into account the resulting effective number of channels  $N_{eff}$  and the – accordingly adapted – reconstruction filter network and effective sampling rate, allows for determining the impact of the pre-processing network on the signal and noise power, respectively.

Firstly, the derived analytic expressions for the **SNR scaling factor**  $\Phi_{bf}$  as given in (83) and (135) are compared to the values obtained by simulation. For a better overview, the results for the *SNR* scaling before and after focusing for each approach are given in separate plots. Fig. 98, top, shows the comparison of simulation and estimation for the conventional scenario while Fig. 98, middle and bottom, give the *SNR* scaling for the frequency dependent pre-processing and the combination of two adjacent apertures without weighting, respectively. Note the different scales on the respective ordinates. A very good match between simulations (solid lines) and prediction (dashed lines) is observed for the data after reconstruction (solid red and dashed blue lines) as well as for the image after focusing (solid orange and dashed green lines) and proves again the validity of the analytic expressions. As it was previously mentioned, the improvement of the characteristics for the focused image with rising *PRF* results from the increasing oversampling of the signal. This entails a reduced noise power due to the lowpass filtering inherent to focusing.

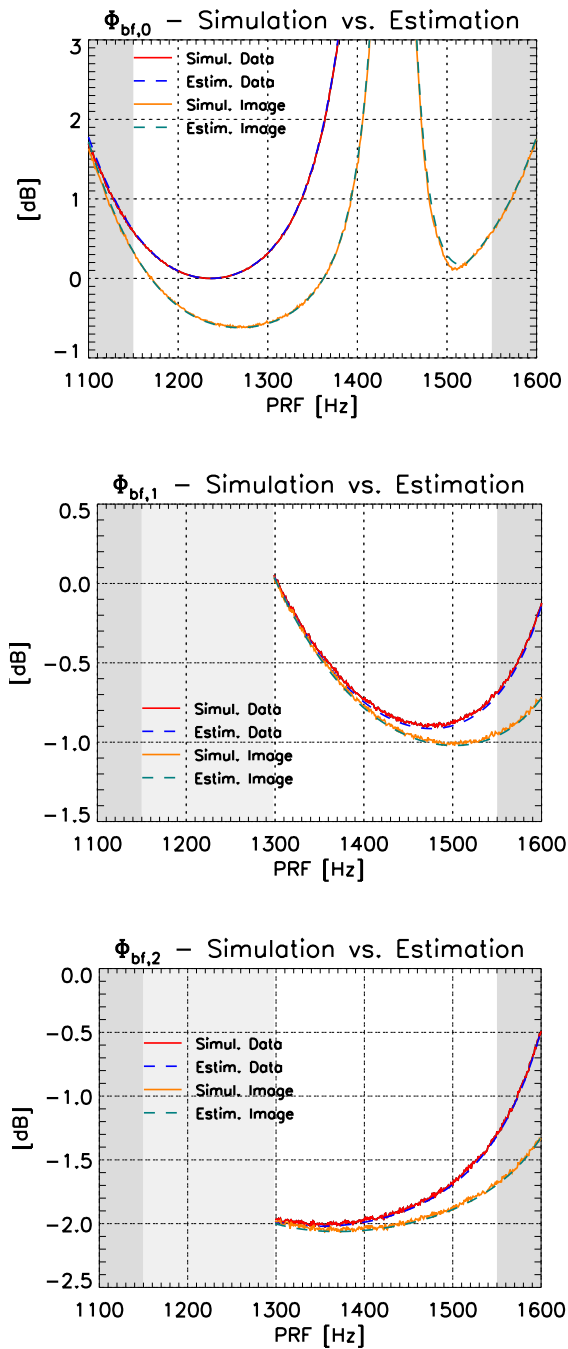


**Fig. 98.** Simulated (solid lines) and predicted (dashed lines) values for the SNR scaling factors  $\Phi_{bf,i}$  before (solid red and dashed blue) and after focusing (solid orange and dashed green) of the data. The conventional case is represented by  $\Phi_{bf,0}$  (top), while the frequency dependent pre-processing is related to  $\Phi_{bf,1}$  (middle) and the addition of adjacent signals without weighting is given by  $\Phi_{bf,2}$  on the bottom.

When considering the different noise powers after reconstruction of the conventional approach and the adapted beamforming scenario 2 at their respective uniform PRF values of 1236 Hz and 1440 Hz, one obtains a ratio that does only depend on the number of used elements. While the input noise power in the conventional case is scaled by a factor of  $K_0$ , this scaling is given by  $K_1$  in the adapted beamforming scenario. The factor  $K_1$  accounts for the noise power



which has risen due to mutual correlations in the pre-processing stage. In the present case for a simple addition of individual elements, one obtains  $K_1/K_0=2$  and consequently a  $SNR$  degradation of 3 dB. Note that this simple and illustrative explanation is no longer valid if a more complex tapering is applied. This is compensated by the increased signal power of 4.9 dB which results from an increased gain  $G_1$  by 6 dB due to the doubled signal amplitude after summation of two sub-apertures' discrete-time signals, each, in combination with an azimuth loss that has risen by  $\sim 1.1$  dB as the antenna pattern narrows. Consequently, the respective values for uniform sampling show a deviation of  $\sim 1.9$  dB in favor of the pre-beamshaping case.

Combining the simulated results for the reconstructed SAR data for all three scenarios gives the  $SNR$  scaling factor  $\Phi_{bf}$  in Fig. 99. The offset between the solid red line for the conventional case and the dashed blue line for the adapted beamforming at their respective uniform  $PRFs$  of 1236 Hz and 1442 Hz, respectively, is validated with the expected value of  $\sim 1.9$  dB.

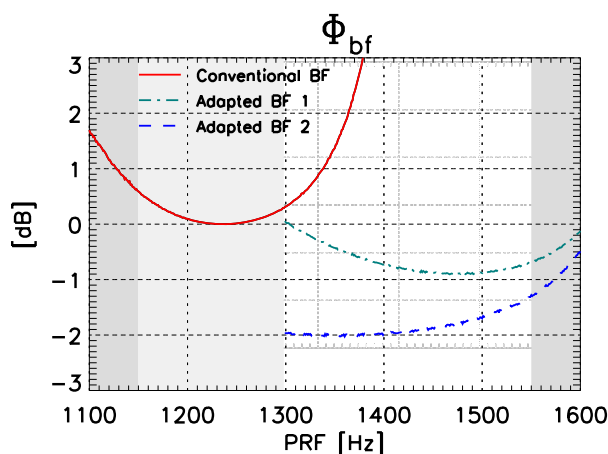


**Fig. 99.** Simulated  $SNR$  scaling factors  $\Phi_{bf}$  after reconstruction of the signal for adapted beamforming with frequency dependent pre-processing (“Adapted BF 1”, dotted dashed green) and simple addition of two adjacent apertures (“Adapted BF 2”, dashed blue) compared to conventional DBF (solid red).

In a next step, the focusing of the signal is taken into account. To concentrate on the effect of the pre-processing network, the signal power is defined as the unaliased contribution within the processed bandwidth  $B_D$ . In consequence, the signal power remains the same after focusing but one benefits from the oversampling of the signal in azimuth as parts of the noise spectrum are filtered. Hence, the noise power is reduced and the characteristics of Fig. 99 improve with increasing  $PRF$ . This yields Fig. 100 that quantifies the degradation or the improvement of the  $SNR$ , respectively, that is caused by the (cascaded) digital processing network. As discussed before, in conventional beamforming the improvement for uniform sampling is defined by  $B_D/PRF_{eff}$ . In the present case this results in a “gain” of 0.56 dB which is consistent with the value obtained (cf. Fig. 100, solid red line). However, this does not hold true for cascaded networks, due to the fact that the noise power is scaled by squared sums of filter functions  $P_j(f)$ . Even for uniform sampling, the sum of squares does not correspond to the squared sum and consequently the variation of the respective  $SNR$  scaling factor cannot be derived as easily as for conventional beamforming.

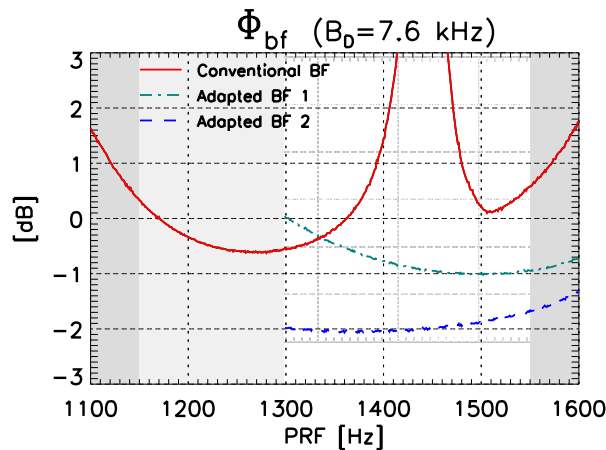


**Fig. 100.** Simulated  $SNR$  scaling factors  $\Phi_{bf}$  after focusing, normalized to the uniform sampling case of conventional beamforming. Results for adapted beamforming with frequency dependent pre-processing (“Adapted BF 1”, dotted dashed green) and simple addition of two adjacent apertures (“Adapted BF 2”, dashed blue) compared to conventional DBF (solid red).

The  $NESZ$  of this system can then be deduced based on the  $NESZ$  derived in Section 8.5 but taking into account the respective modified  $\Phi_{bf}$  of Fig. 100. It was mentioned that the noise scaling factors are derived with respect to the conventional scenario and incorporate the changes on signal and noise power introduced by the pre-processing stage. Further, the modified number of effective channels has to be taken into account, as it affects the effective sampling and thus the number of focused pulses. Consequently,  $N$  in (91) has to be adapted to the effective number of virtual channels  $N_0$  according to the applied pre-processing. This means that regarding the  $NESZ$  an additional scaling factor of  $N_0/N$  is to be considered to enable a fair comparison of the different systems. In the present case this entails a “loss” of 0.67 dB for the adapted scenarios which is added to the result of Fig. 100 and finally yields  $\Phi_{bf,NESZ}$  in Fig. 101.

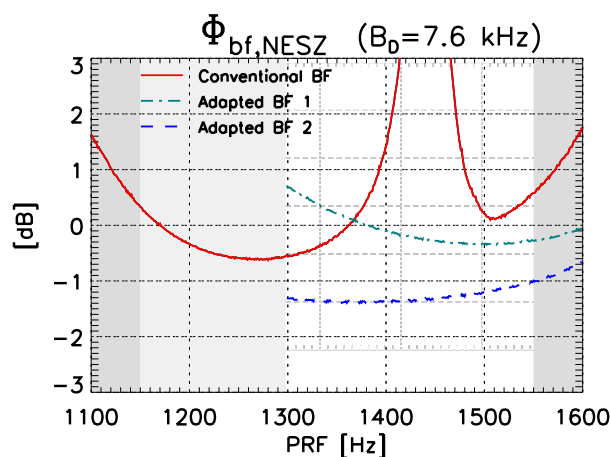


**Fig. 101.** Simulated  $SNR$  scaling factors  $\Phi_{bf}$  after focusing, normalized to the uniform sampling case and including a loss in  $NESZ$  due to a reduced effective sampling. Results for adapted beamforming with frequency dependent pre-processing (“Adapted BF 1”, dotted dashed green) and simple addition of two adjacent apertures (“Adapted BF 2”, dashed blue) compared to conventional DBF (solid red).

Section 8.5 derived a reference  $NESZ$  value of better than  $-19.2$  dB when neglecting the  $SNR$  scaling. Recalling the  $SNR$  scaling of the example system (cf. Fig. 67), a comparison to the above results in Fig. 101 shows a  $SNR$  scaling which is always better. In consequence, the minimum  $NESZ$  of the system remains better than  $-19.2$  dB.

The analysis of the **ambiguous energy suppression** of the system yields the results presented in Fig. 102. The red line shows the suppression of the original system that is improved by the frequency dependent adapted beamforming above  $1340$  Hz (dotted dashed green line), while the pre-processing approach that simply adds the signal of two adjacent apertures yields a clearly improved ambiguity suppression over the whole considered range of  $PRF$  (dashed blue line).

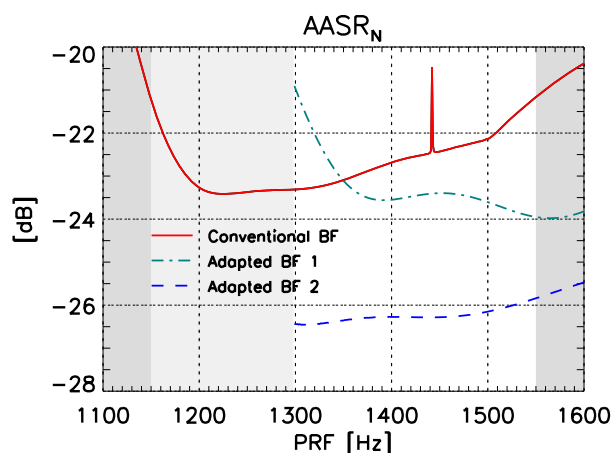


**Fig. 102.**  $AASR_N$  for adapted beamforming with frequency dependent pre-processing (“Adapted BF 1”, dotted dashed green) and simple addition of two adjacent apertures (“Adapted BF 2”, dashed blue) compared to conventional DBF (solid) ( $B_D = 7.6$  kHz). The peak in the conventional approach occurs at the “singular”  $PRF$  of  $1440$  Hz (cf. Section 4.3.3).

Regarding the **geometric resolution in azimuth**, the frequency dependent adapted beamforming approach yields a value of  $1.04$  m (cf. Fig. 103, dotted dashed green line), which is almost identical to the conventional case (cf. Fig. 103, solid red line). The dashed blue line in Fig.

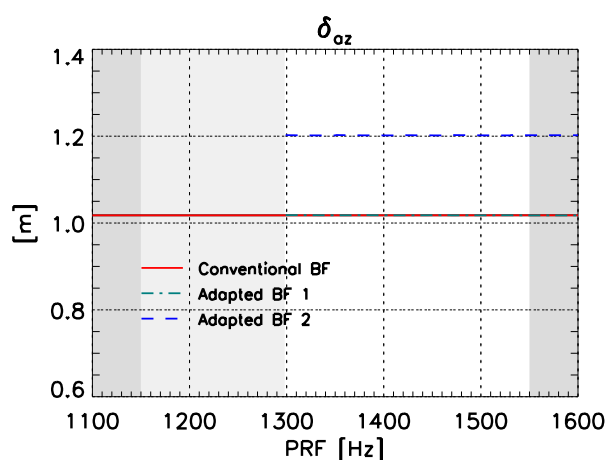


**Fig. 103.** Geometric resolution in azimuth ( $\delta_{az}$ ) for adapted beamforming with frequency dependent pre-processing (“Adapted BF 1”, dotted dashed green) and simple addition of two adjacent apertures (“Adapted BF 2”, dashed blue) compared to conventional DBF (solid) ( $B_D = 7.6$  kHz).

103 finally reveals the drawback of the second adapted beamforming scenario as it yields a resolution which degraded to a value of 1.20 m.

The obtained results for the variation of the *NESZ* (Fig. 101) and the suppression of azimuth ambiguities (Fig. 102) in combination with Fig. 103 giving the resolution allows for the following conclusions. If a geometric resolution of  $\sim 1$  m is necessary, the conventional approach is suitable for *PRF* values below 1345 Hz, while the frequency dependent adapted beamforming method is favorable for a *PRF* above 1365 Hz, regarding both the *AASR<sub>N</sub>* and the *NESZ*. In between, the focus can be either turned to the *NESZ* by choosing the conventional approach or the pre-processing is applied to concentrate on the optimization of the *AASR<sub>N</sub>*. In contrast, the adapted beamforming that combines two adjacent apertures without weighting achieves only a resolution of 1.20 m but yields the best *AASR<sub>N</sub>* and *NESZ* for all possible *PRFs*, i.e. *PRF* values above 1300 Hz. Consequently, for scenes of low *SNR* that do not require the best resolution, this represents the best solution for processing the data.

It should be noted that for the digital a-posteriori processing, the whole image can be processed by each of the different strategies. Then, afterwards, the image could be sub-divided into local areas whose quality is evaluated separately for each processing approach. The final image would then be obtained by an optimum fusion of the respectively obtained local areas. Such a data adaptive processing would allow for applying the locally optimum processing strategy, e.g. the adapted beamforming 2 for homogenous areas with low *SNR* and the conventional beamforming in regions with strong scatterers such as urban areas.

## 9 Multi-Channel Reconstruction in Burst Mode Operation

So far, this work only considered systems in stripmap operation. However, stripmap mode does not allow for the imaging of ultra-wide swaths which are requested by future SAR missions. Consequently, new approaches become necessary as e.g. the operation of multi-channel SAR in burst modes which is introduced and investigated in the present chapter.

In this context, the first section highlights the needs for ultra-wide-swath imaging and shows the limitations of stripmap systems to fulfill them, leading to the idea of multi-channel burst mode systems as a possible solution to overcome these limitations (cf. Section 9.1). Then the basic relationships of burst mode operation are recalled in Section 9.2 before the applicability of the multi-channel reconstruction algorithm to burst modes is analyzed in the following. In this context especially the impact of the variable target position within the burst that results in a variable Doppler band of the reflected signal will be investigated with respect to the Doppler frequency dependent multi-channel processing network yielding an extension of the analytic descriptions for both azimuth ambiguous energy suppression (cf. Section 9.4) and *SNR* scaling factor (cf. Section 9.5). These considerations are embedded in a multi-channel ScanSAR system design example to demonstrate its capability to image an ultra-wide swath with good resolution (cf. Section 9.6). In this context, the intricate connection between multi-channel system design and the various parameters becomes clear. In a next step, the TOPS mode is applied straightforward to the ScanSAR system in order to provide an indication of the achievable performance and possible limitations of a multi-channel TOPS system (cf. Section 9.7). Based on this analysis, the chapter is closed with the description and implementation of an optimized multi-channel processing that is adapted to the TOPS mode by introducing a “squinted” reconstruction.

### 9.1 Motivation of Multi-Channel Burst Mode Systems

When investigating the needs of future SAR missions, especially a complete and frequent coverage of the Earth with a reasonably high resolution is mentioned very often. To enable such a “mapping machine”, a resolution of well below 10 m is required in combination with a swath of several hundreds of kilometers. As an example, a complete imaging of the Earth with a

weekly revisit time requires a swath width of 400 km. A timing analysis of such a case reveals a maximum applicable *PRF* around  $\sim 400$  Hz, which is driven by the required swath width. According to the timing requirement for uniform sampling, this imposes a certain antenna length in azimuth in order to ensure a spatial sampling that deviates not too strongly from the uniform distribution. In the given case, a suitable length for stripmap operation would be in the order of  $\sim 35$ - $40$  m, which is of course far too long to be realized.<sup>28</sup> Consequently, conventionally operated multi-channel SAR systems provide a high resolution, but the antenna length limits the achievable swath width (cf. Fig. 104, left).

On the other hand, burst modes as e.g. ScanSAR, TOPS [13]-[15], or the multi-beam burst mode (MBBM) [60] allow for a very wide swath, which is achieved by continuously switching the antenna footprint between several sub-swaths. One solution is represented by the ScanSAR mode (cf. Fig. 104, middle left, [13]) where the footprint is steered only in range dimension to cover all sub-swaths subsequently. A more sophisticated burst mode is TOPS (cf. Fig. 104, middle right, [15]), where additionally to the switching in range a steering of the footprint in azimuth dimension is done. Both modes provide an overall swath width that consists of all sub-swaths. Unfortunately, this is at the cost of a reduced illumination time per sub-swath entailing a coarsened azimuth resolution thus excluding the capability of high resolution imaging.

Consequently, advanced concepts are needed for the imaging of an ultra-wide swath of several hundreds of kilometers with high azimuth resolution well below 10 m. In this regard, the innovative operation of multi-channel SAR systems in burst modes is suggested [58]-[60], [65] as illustrated in Fig. 104 on the right. A detailed investigation of the multi-channel burst modes with focus on ScanSAR will be given in the following sections.

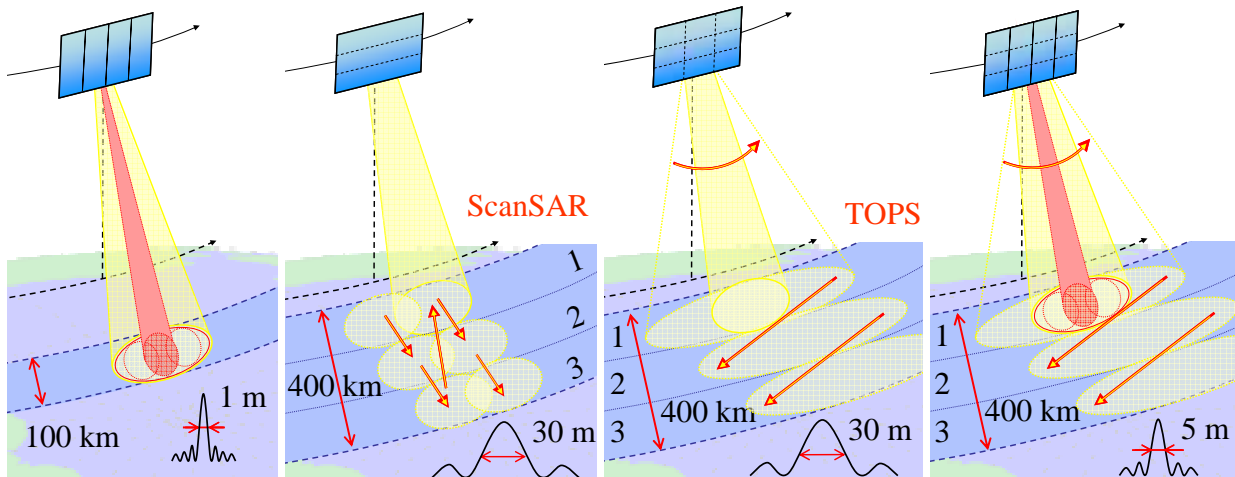


**Fig. 104. Multi-channel system in burst mode operation (exemplarily multi-channel TOPS, right) combining the high performance of multi-channel reception (left) with the ultra-wide swaths enabled by burst mode systems as ScanSAR or TOPS (middle left, middle right).**

<sup>28</sup>For comparison, the multi-channel SAR system of Chapter 7 enables a swath of 100 km with 1 m resolution in stripmap mode. This allowed for a maximum *PRF* of  $\sim 1.4$  kHz leading to a reasonable antenna length of 11.2 m.

## 9.2 Burst Mode Operation

### 9.2.1 ScanSAR Timing

In order to achieve a required azimuth resolution  $\delta_{az}$  the necessary illumination time,  $T_{B,i}$ , or corresponding Doppler bandwidth,  $B_B$ , respectively, of a single burst is given as follows, where  $R_0$  gives the mean slant range distance,  $v_s$  the sensor velocity,  $v_g$  the beam velocity on ground and  $\lambda$  the carrier wavelength. The index “ $i$ ” accounts for the varying mean slant range of the respective sub-swath and the consequentially varying illumination time for a constant  $B_B$ .

$$T_{B,i} = \frac{\lambda \cdot R_{0,i} \cdot B_B}{2 \cdot v_s \cdot v_g} \approx \frac{\lambda \cdot R_{0,i} \cdot 0.89}{2 \cdot v_s \cdot \delta_{az}} \quad (139)$$

The cycle time  $T_C$  that defines the time between two subsequent illuminations of the same sub-swath is simply determined by the sum of all burst times (cf. (140)).  $T_C$  can be approximated by a mean burst time  $T_B$  and  $N_B$  representing the number of bursts. In the following, the mean burst time  $T_B$  will be used, neglecting the index  $i$ , but keeping in mind the dependency on the respective sub-swath.

$$T_C = \sum_{i=1}^{N_B} T_{B,i} \approx N_B \cdot T_B \quad (140)$$

In addition, the timing has to ensure that every single target is continuously illuminated for the time  $T_B$  while located within the antenna footprint defined by the angle  $\Theta_{az}$  (cf. Section 2.1), as expressed by (141). In other words,  $\Theta_{az}$  of (141) gives the maximum angle under which signals are received and consequently  $\Theta_{az}$  corresponds to the system bandwidth in azimuth.

$$T_C = \frac{R_0 \cdot \Theta_{az}}{v_g} - T_B \quad (141)$$

Combining (140) and (141) and replacing  $\Theta_{az}$  by the corresponding bandwidth  $B_D$  allows for relating the overall system bandwidth in azimuth,  $B_D$ , with the burst bandwidth.

$$B_D = (N_B + 1) \cdot B_B \quad (142)$$

Note that  $B_D$  and  $B_B$  are connected by a factor  $N_B + 1$  although the system bandwidth is distributed to only  $N_B$  bursts, i.e. the overall swath compared to a stripmap system will be increased by a factor of  $N_B$  while the resulting coarsening of the azimuth resolution will be in the order of  $N_B + 1$ .

### 9.2.2 Burst Mode Target Signal Spectrum

It is well-known that the target signal spectrum depends on the target’s position as this defines the angle under which the target is illuminated by the antenna (cf. Fig. 105). In consequence, targets at different positions yield echoes with different Doppler characteristics, both for ScanSAR and TOPS. This means that the target position within the burst can be “translated” to a “target center frequency” denoted by  $f_{0,t}$  that represents the mean frequency of the Doppler spec-

trum of width  $B_B$  reflected by the target during a burst. To provide a consistent notation in the following,  $f_{0,t}$  will be used when referring to the position dependent characteristics in burst mode operation.

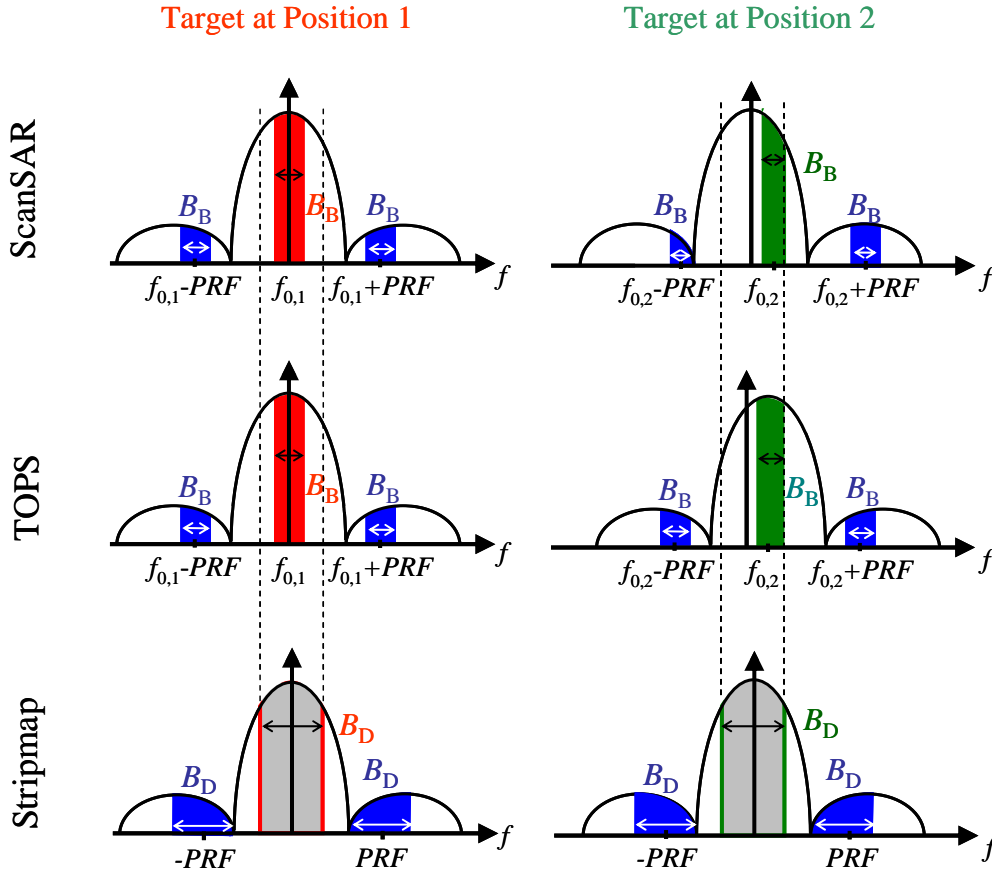


**Fig. 105.** Target signal spectrum (Doppler domain) in ScanSAR (top) and TOPS (middle) mode for two targets at different positions. The respective band of a specific target depends on its position that entails a center frequency  $f_{0,t}$ . Respective ambiguous bands are marked in blue. For comparison, the spectrum for stripmap mode is shown (bottom).

The maximum  $f_{0,t}$  is obtained for targets at the outermost position within the antenna main beam. Taking into account the signal bandwidth  $B_B$  and the overall system bandwidth  $B_D$ , the maximum  $f_{0,t}$  is expressed by (143).

$$\pm f_{0,t,\max} = \pm \frac{B_D}{2} \mp \frac{B_B}{2} = \pm \frac{B_B \cdot N_B}{2} \quad (143)$$

In a further step, the multi-channel processing of the burst mode data is investigated. Recalling the Doppler spectrum of the reconstruction filter functions – exemplarily for a non-optimum  $PRF$  – the colored shape given in Fig. 106 is obtained. Considering the target signal spectra derived above, it becomes obvious that – in contrast to stripmap operation – targets at different positions are “weighted” differently by the multi-channel reconstruction. In consequence, the performance figures become dependent on the target position.



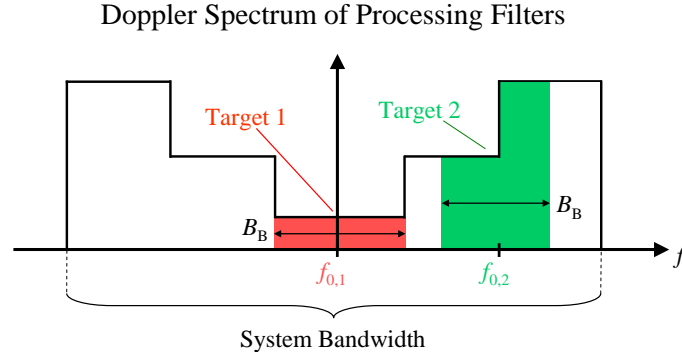


**Fig. 106.** Power spectral density of multi-channel processing functions and spectral bands covered by targets at two different positions “1” (red) and “2” (green), respectively.

### 9.3 Burst Mode Signal Power

The signal power in ScanSAR operation depends on several factors. Firstly, it is governed by the illumination time resulting in a bandwidth  $B_B$ . In addition, the signal power varies with the target position represented by the target center frequency  $f_{0,t}$  (“scalloping”) according to the respective illumination intensity as can be seen from Fig. 105, top. Furthermore, the timing of the burst mode has to be considered. According to Section 9.2, the switching of the antenna footprint is timed in a way to ensure any target being continuously illuminated by the mainlobe for a time  $T_B$ . This means that the same target can be located within the antenna mainlobe in two subsequent bursts, but it will be only partly illuminated in one of these bursts and hence only contribute with reduced bandwidth in this case. Nevertheless, this represents additional signal energy which could be used. Starting with the first burst, the received spectrum of a point-like target is characterized by a bandwidth  $B_B$  around a varying center frequency  $f_{0,t}$  corresponding to the target position. This target spectrum is denoted by  $B_{s,1}$  and given in (144).

$$B_{s,1} = \left[ f_{0,t} - \frac{B_B}{2}, f_{0,t} + \frac{B_B}{2} \right] \quad (144)$$

In order to provide succinct notation, the rectangular window function confining the Doppler spectrum  $B_{s,1}$  will be defined by  $W(B_{s,1})$ , i.e.:

$$W(B_{s,1}) = \text{rect} \left( \frac{f - f_{0,t}}{B_B} \right) \quad (145)$$

Additionally to  $B_{s,1}$ , a second burst situated – partly – within the system band  $B_D$  contributes to the signal of a specific target. The respective signal band is denoted by  $B_{s,2}$  and can be obtained from the “main” burst  $B_{s,1}$  shifted by a frequency  $f_{\text{off},B}$  corresponding to the time  $T_C$  between the two bursts (cf. (146)). The limitation to components within the interval  $[-B_D/2, B_D/2]$  is expressed by the operator “ $\cap$ ”.

$$B_{s,2} = \left[ f_{0,t} - \frac{B_B}{2} - f_{\text{off},B}, f_{0,t} + \frac{B_B}{2} - f_{\text{off},B} \right] \cap B_D = (B_{s,1} - f_{\text{off},B}) \cap B_D \quad (146)$$

According to “standard” burst mode SAR processing only the full-bandwidth burst will be focused. Nevertheless, in principle also the second contribution can be focused and the respective results later added incoherently. Equivalently to (145), the respective window function for this band is defined by  $W(B_{s,2})$ .

Finally, the signal power  $p_{s,B_{s,i}}$  resulting from the respective band  $B_{s,i}$  can be expressed by (147). For the case where both  $B_{s,i}$  are considered, the respective powers are simply to be added to obtain the overall signal power.

$$p_{s,B_{s,i}} = \mathbb{E} \left[ \left| U(f) \cdot W(B_{s,i}) \right|^2 \right] \quad (147)$$

In the following, basically all relations derived for stripmap imaging can be directly transferred to ScanSAR mode by replacing the dependency on  $B_D$  by the respective band(s)  $B_{s,i}$ . In this context, it should be kept in mind that this introduces an additional dependency on the target position, which is represented by  $f_{0,t}$ .

Furthermore, it should be noted that the above considerations are valid for the ScanSAR mode. Regarding the TOPS mode, the scalloping is mitigated as only the antenna characteristics of the single elements used to effectuate the steering have to be considered when evaluating the loss of peak power with varying target position [96]. In addition, the effectively shrunk pattern caused by the steering will affect the signal power.

## 9.4 Azimuth Ambiguities in Burst Mode Operation: $AASR_{N,B}$

As derived in detail in Section 5.6, the residual azimuth ambiguities in the SAR image are governed by the aliasing contributions in the originally received signal in combination with a possible amplification due to the weighting by the reconstruction filter functions  $P_j(f)$  of the digital beamforming network (cf. Section 5.6). Consequently, (71) is modified replacing the dependency on  $B_D$  by  $W(B_{s,i})$ , which restricts the spectrum to the burst mode signal. One obtains (148) for the azimuth ambiguous power  $p_{a,B_{s,i}}$  resulting from the band  $B_{s,i}$ . Equivalently to the signal power, the respective ambiguous contributions for  $i=1$  and  $i=2$  are simply to be added if both  $B_{s,i}$  are considered.

$$p_{a,B_{s,i}} = \mathbb{E} \left[ \left| 2 \cdot \sum_{k=1}^{\infty} \left( U_k(f) \cdot \sum_{m=1}^N \sum_{j=1}^N H_{jk}(f) \cdot P_{jm}(f) \right) \cdot W(B_{s,i}) \right|^2 \right] \quad (148)$$

The ratio of the sums of the respectively considered signal and noise powers then yields the azimuth ambiguity-to-signal ratio in burst mode,  $AASR_{N,B}$ , according to (149) where  $i_{\max}$  represents the number of bursts for focusing.

$$AASR_{N,B} = \frac{\sum_{i=1}^{i_{\max}} p_{a,B_{s,i}}}{\sum_{i=1}^{i_{\max}} p_{s,B_{s,i}}} \quad (149)$$

Hence, besides the well-known varying signal power (scalping), the use of different sub-spectra corresponding to different target positions within the burst will result in a variation of the residual azimuth ambiguities of these targets thus yielding a scalping-like effect for the  $AASR_{N,B}$  as it varies with  $f_{0,t}$  as can be seen by the dependency of the ambiguous power on  $B_{s,i}$  (cf. (148)). Although (148) is not valid for TOPS, also this mode will suffer a scaling depending on the target position due to the frequency dependency of the filters  $P_{jm}(f)$ .

## 9.5 SNR Scaling in Burst Mode Operation: $\Phi_{\text{bf,B}}$

Equivalently to the  $AASR_{N,B}$ , the resulting SNR is governed by the considered parts of the Doppler spectrum given by the bands  $B_{s,i}$  that determine the signal power  $p_{s,B_{s,i}}$  according to (147) and Section 9.3. Besides, the noise power also depends strongly on the applied focusing method. If the complete system bandwidth  $B_D$  is focused at once, all spectral noise components within  $B_D$  are considered and consequently the possible rise of the noise power due to the beam-forming network is not affected by the Doppler band of the respective target but only by  $B_D$ . In this case the numerator of (82) is valid and the noise scaling is expressed by (150) where the output noise power is denoted by  $p_{n,B_D}$  while  $p_{n,\text{el}}$  describes the input noise power.

$$\frac{p_{n,B_D}}{p_{n,\text{el}}} = N \cdot F \cdot \sum_{j=1}^N \mathbb{E} \left[ \left| P_j(f) \right|^2 \cdot \text{rect} \left( \frac{f}{B_D} \right) \right] \quad (150)$$

In contrast, if multiple sub-bands of the Doppler band are focused separately and the image is obtained by combining the respective results, only noise and signal power within the respective sub-band are taken into account. In this case (151) describes the noise power scaling for a specific sub-band  $B_{s,i}$ . Again, if multiple bursts are considered, the respective signal and noise powers have to be added before the sums are related to obtain the signal-to-noise ratio.

$$\frac{p_{n,B_{s,i}}}{p_{n,\text{el}}} = N \cdot F \cdot \sum_{j=1}^N \mathbb{E} \left[ \left| P_j(f) \right|^2 \cdot \mathbb{W}(B_{s,i}) \right] \quad (151)$$

Note that the above expressions for the noise scaling characterize both ScanSAR and TOPS.

## 9.6 System Design Example – Multi-Channel ScanSAR

This section gives a ScanSAR system design example to demonstrate the applicability and potentials of multi-channel signal processing in burst mode operation for ultra-wide-swath imaging with high geometric resolution [58]. Note that the design was chosen exemplarily and the derived results can be transferred to any burst mode system as e.g. TOPS (cf. Section 9.7) or the innovative multi-beam burst mode concept (MBBM), which is based on multiple transmit beams enabling the simultaneous acquisition of multiple sub-swaths within the same burst [60].

### 9.6.1 Timing and System Parameters

In the following, an X-band system is designed to image a swath of 400 km with an azimuth resolution below 5 m. All requirements and system constraints are summarized by Table 11.

Parameter	Symbol	Value
Carrier wavelength	$\lambda$	3.1 cm
Swath-width on ground	$W_g$	$\geq 400$ km
Geometric resolution in azimuth	$\delta_{az}$	$\leq 5$ m
Azimuth ambiguity-to-signal ratio (distributed targets)	$AASR_{N,B}$	$\leq -20$ dB
Covered incident angle range	$\Theta_i$	$19^\circ - 47^\circ$
Transmit duty cycle	$dc$	15 %

**Table 11. Requirements and constraints for a multi-channel ScanSAR system.**

In a first step, a timing analysis is performed yielding the following result to cover the swath of 400 km by 4 sub-swaths of length 105 km each with an orbit height of 630 km (cf. Fig. 107). The necessary  $PRF$  values vary only from 1150 Hz up to 1240 Hz, representing a quite good-natured case. If a larger  $PRF$  range is needed, e.g. caused by orbit height variations resulting in a modified timing, optimization strategies as presented in Chapter 8 will become necessary.

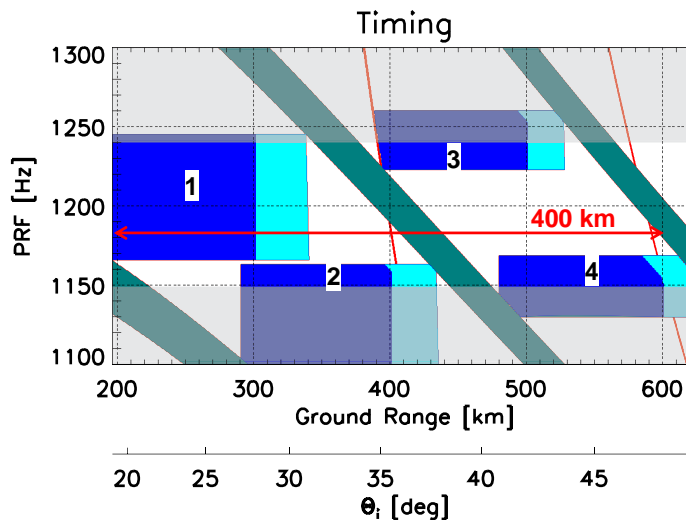


**Fig. 107. Timing diagram considering transmit events (green) and nadir returns (red). 4 swaths of length 105 km each cover a ground range of 400 km.**

In order to ensure an optimum  $PRF_{uni}$  situated within the  $PRF$  range of operation, the overall length of the antenna has to be adapted. A length of 12.8 m is chosen, yielding a  $PRF_{uni}$  of  $\sim 1180$  Hz. Further, a Doppler bandwidth of 1.2 kHz for a single burst ensures a resolution of 5 m for single-look processing. In combination with  $N_B = 4$  bursts, this yields an overall system bandwidth  $B_D = 6$  kHz (cf. (142)). Note that the fixed burst bandwidth in combination with the varying slant ranges of the sub-swaths entails an illumination time that varies from 0.25 s to 0.31 s, respective to the slant range (cf. Table 12).

Parameter	Symbol	Value			
		Sub-Swath 1	Sub-Swath 2	Sub-Swath 3	Sub-Swath 4
Pulse repetition frequency	$PRF$	1180 Hz	1160 Hz	1240 Hz	1150 Hz
Mean incident angle	$\theta_{i,\text{mean}}$	23.5°	31.2°	38.0°	43.9°
Mean swath slant range	$R_{0,\text{mean}}$	681 km	725 km	778 km	840 km
Burst duration	$T_B$	0.25 s	0.26 s	0.28 s	0.31 s

**Table 12. Parameters of different sub-swaths.**

In combination with the minimum  $PRF$ , an overall system bandwidth of 6 kHz requires a minimum number of 6 receive apertures to fulfill the Nyquist criterion according to (152).

$$N \geq \frac{B_D}{PRF_{\min}} \quad (152)$$

In the case of a ScanSAR system, it was observed that a low oversampling might introduce a trade-off between scalloping and azimuth ambiguity suppression, as one parameter can only be improved by degrading the other according to the chosen antenna size. This conflict can be re-

Parameter	Symbol	Value
Orbit height	$h_s$	630 km
Sensor velocity	$v_s$	7545 m/s
$PRF$ range of operation	$PRF$	1150 Hz – 1240 Hz
Sub-swath width on ground	$W_{g,\text{sub}}$	105 km
Number of sub-swaths/bursts	$N_B$	4
Rx sub-apertures in azimuth	$N$	8
Rx sub-aperture length in azimuth	$d_{\text{az},\text{rx}}$	1.6 m
Tx antenna length in azimuth	$d_{\text{az},\text{tx}}$	2.1 m
Cycle time	$T_C$	1.1 s
Burst bandwidth	$B_B$	1.2 kHz
Processed azimuth bandwidth	$B_D$	6 kHz
Transmit antenna size in elevation	$d_{\text{ev},\text{tx}}$	0.19 m – 0.31 m
Overall receive antenna height in elevation	$h_{\text{ev},\text{rx}}$	2 m
Transmit antenna gain	$G_{\text{tx}}$	37.3 dB – 39.3 dB
Receive antenna gain	$G_{\text{rx}}$	55.3 dB
Transmit peak power	$P_{\text{tx}}$	4 kW
Duty cycle	$dc$	15 %
System temperature	$T$	300 K
Losses (atmospheric, system, receiver noise, 2-way)	$L \cdot F$	5.7 dB
Azimuth loss	$L_{\text{az}}$	0.2 dB

**Table 13. Multi-channel ScanSAR system parameters.**

laxed by ensuring sufficiently high oversampling, as this allows for smaller antennas in order to improve scalloping while the ambiguous energy suppression is mainly achieved by the oversampling. The drawbacks of such a solution are, of course, increased hardware costs and complexity, and a higher data rate, as more independent receiving channels are required. In the following,  $N=8$  is chosen to adapt the single receive aperture size to  $B_D$  and to guarantee oversampling in Doppler domain. Finally, the transmit antenna length in azimuth is set to 2.1 m, as this is large enough to ensure sufficient ambiguity suppression but small enough to obtain a resolution of 5 m. All system parameters are summarized in Table 13.

### 9.6.2 Performance Analysis

In the present section, a point target analysis is carried out for the above introduced ScanSAR system, allowing for the derivation of key performance figures such as  $\delta_{az}$ ,  $AASR_N$ , and  $NESZ$ . This performance analysis includes the dependency on the target position represented by the center frequency  $f_{0,t}$ , thus showing possible performance variations depending on the target's location within the antenna footprint. The simulated data are focused with a standard stripmap processor, where the most common approach to process only a single burst for each target is chosen. This means that for a specific target a sub-band of width  $B_B$  around the target's center frequency  $f_{0,t}$  is considered.

The evaluation of the **geometric resolution in azimuth**  $\delta_{az}$  according to Fig. 108 shows a constant value over the  $PRF$  but varies slightly depending on  $f_{0,t}$ . For all sub-swaths, the same resolution better than 5 m is achieved, where a slight decrease for increasing  $f_{0,t}$  is observed (solid red line). This – negligible – degradation is caused by the drop-off of the azimuth antenna characteristic with increasing angles.

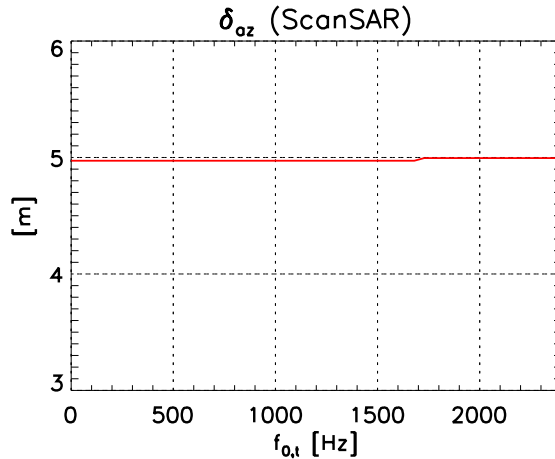
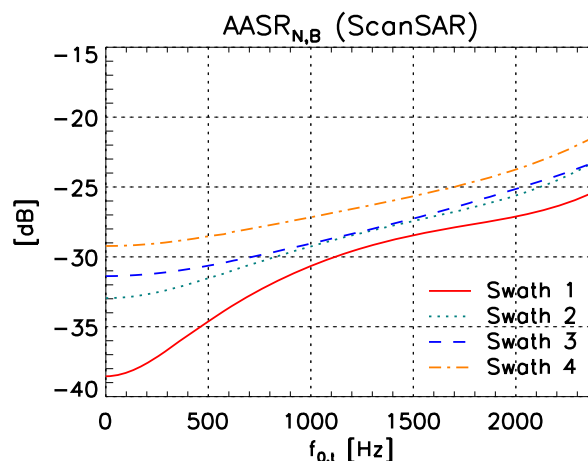


Fig. 108. Geometric resolution in azimuth ( $\delta_{az}$ ) vs.  $f_{0,t}$  for all sub-swaths.

Fig. 109 shows the **Azimuth Ambiguity-to-Signal Ratio** ( $AASR_{N,B}$ ) vs.  $f_{0,t}$  for the different sub-swaths, respectively. As expected, the worst case regarding the azimuth ambiguities is encountered for the combination of minimum  $PRF$  – used to image sub-swath 4 – and maximum

$f_{0,t}$ , i.e. targets situated at the very edge of the burst. In any case, the  $AASR_{N,B}$  is always below a value of -21 dB.



**Fig. 109.** Ambiguous Energy Suppression ( $AASR_{N,B}$ ) vs.  $f_{0,t}$  for all four sub-swaths.

In order to derive the *NESZ* of the system, signal as well as noise power have to be taken into account. Firstly, the ScanSAR-inherent loss of the signal power in dependency on the target position is determined for each of the sub-swaths and shown in Fig. 110. To concentrate only on the variation, the values are normalized to the optimum at  $f_{0,t}=0$ . The obtained “scalloping” is identical for all sub-swaths and shows a maximum decrease of the signal power by nearly  $\sim 2.65$  dB.

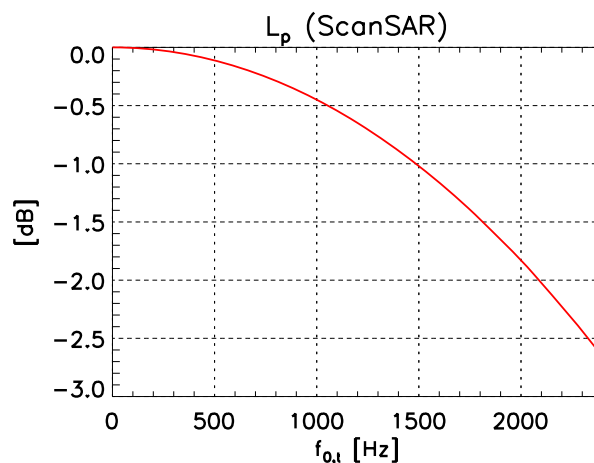


**Fig. 110.** Normalized signal powers  $L_p$  vs.  $f_{0,t}$  for all four sub-swaths.

In addition, the **noise power scaling**  $\Phi_{bf,B}$  induced by the digital processing network is investigated. It is quantified by (151) and depends on the *PRF* of the respective sub-swath. Furthermore, a dependency on the target center frequency  $f_{0,t}$  is observed, entailing a scalloping-like effect. Similar to the scalloping, the worst case is represented by the maximum  $f_{0,t}$ , yielding for the given scenario an uncritical maximum increase of noise power by  $\sim 0.2$  dB induced by the beamforming network (cf. Fig. 111, dotted dashed orange line).

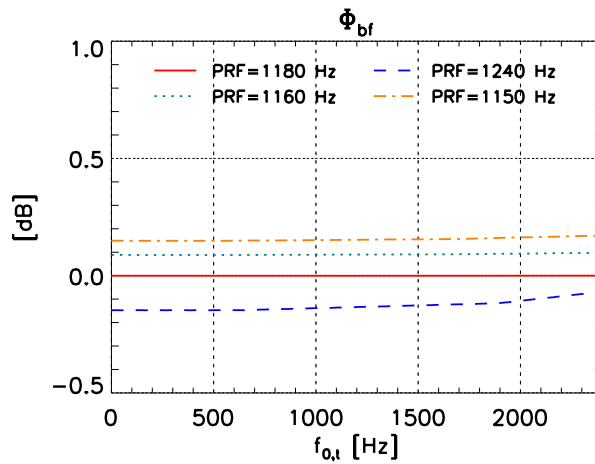


**Fig. 111.** SNR scaling factor of the digital processing network ( $\Phi_{bf}$ ) vs.  $f_{0,t}$ . Results for all four sub-swaths taking into account the respective PRF.

Including the above results for signal and noise power scalloping and taking into account the sensor dimensions and system parameters according to Table 12 and Table 13, the NESZ can be calculated. For each of the sub-swaths this yields two characteristics which are shown in Fig. 112. The solid lines give the best case achieved for a target centered within the antenna footprint, i.e.  $f_{0,t} = 0$ , while the dashed lines represent the worst case which is obtained for targets located at the outermost possible position. In any case a NESZ of nearly -24 dB is achieved.

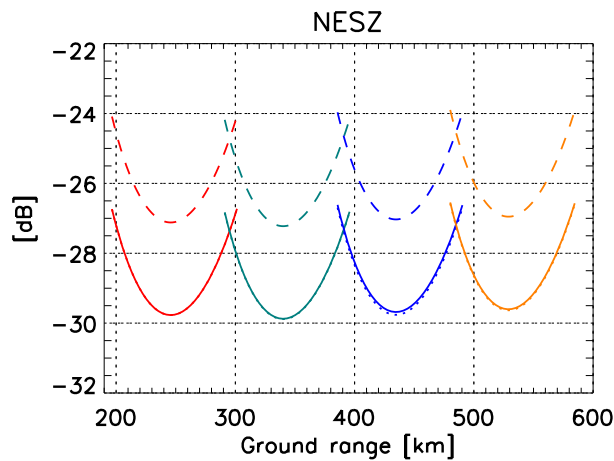


**Fig. 112.** NESZ vs. ground range for the case where a bandwidth of  $B_B$  around a varying  $f_{0,t}$  is processed. The solid lines represent the best case for  $f_{0,t} = 0$  while dashed lines show the worst case obtained for maximum  $f_{0,t}$ .

## 9.7 Multi-Channel TOPS Mode

In a next step, the operation of multi-channel systems in TOPS mode is investigated. Therefore, TOPS is applied straightforward to the ScanSAR system introduced above and a perform-



ance analysis is carried out. In a further step, an optimized processing approach for multi-channel TOPS systems is introduced and the improved performance is demonstrated.

As presented in the preceding section, a large scalloping of the signal power up to 2.65 dB occurred in ScanSAR operation. This unwanted effect can be compensated by applying the TOPS mode, as the steering of the azimuth antenna footprint during signal acquisition ensures a constant signal power independently on the target position. In order to demonstrate the potential, the TOPS mode is applied to the above ScanSAR system design and, consequently, all system parameters can be looked up in Table 13. In addition, the TOPS steering coefficient has to be chosen high enough to ensure the coverage of all sub-swaths. This is driven by the number of bursts and some additional margin, imposing a minimum value exceeding the number of bursts, i.e.  $N_B < \alpha$ . Thus,  $\alpha = 5$  is chosen.

Regarding the subsequent performance analysis, it should be noted that the original system was designed for ScanSAR. Thus the results obtained for TOPS do not represent the full performance possible by TOPS, and a comparison to the ScanSAR results is not fair. Nevertheless, the results give some indication about the potentials and challenges for the operation of multi-channel systems in TOPS mode. In this context, the additional hardware costs which are necessary to enable the beamsteering in TOPS mode have to be kept in mind.

### 9.7.1 Performance Analysis

In the following, the key performance figures  $\delta_{az}$ ,  $AASR_N$ , and  $NESZ$  of the TOPS mode are determined by a point-target analysis. The respective simulations are carried out assuming an ideally steered pattern, thus neglecting effects like grating lobes and the single-element pattern.

As can be seen from Fig. 113, the TOPS mode yields – compared to the ScanSAR system – a slightly increased **azimuth resolution**  $\delta_{az}$  of  $\sim 5.5$  m (cf. Fig. 113). This degradation is caused by the effectively shrunk pattern of the TOPS mode and can be avoided by a specific system design for TOPS. As the single-element characteristic is not considered, the resolution in TOPS is constant for any target position. The variations in the plot of Fig. 113 on the left are caused by numerics, as the number of discrete-time samples within the 3-dB width of the impulse response varies slightly.

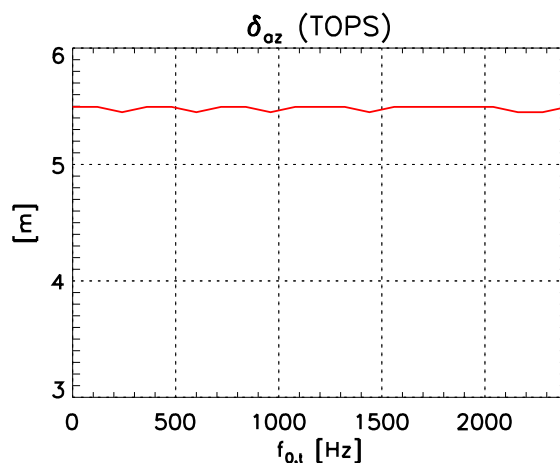
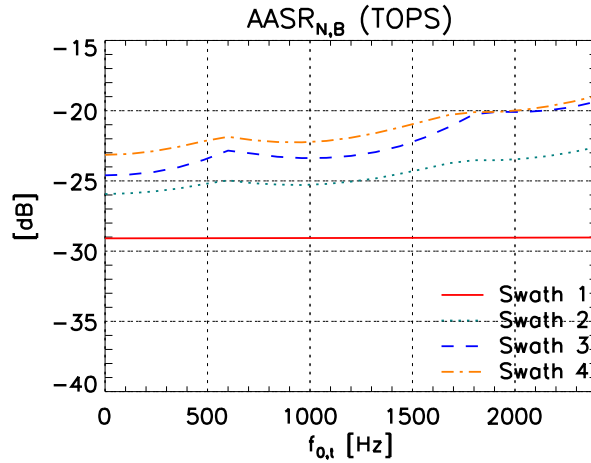


Fig. 113. Geometric resolution in azimuth ( $\delta_{az}$ ) vs.  $f_{0,t}$  for TOPS mode operation.

The suppression of **azimuth ambiguous energy** ( $AASR_{N,B}$ ) by TOPS is shown in Fig. 114 for all four sub-swaths.



**Fig. 114. Azimuth ambiguous energy suppression ( $AASR_{N,B}$ ) vs.  $f_{0,t}$  for TOPS mode operation.**

In the TOPS system the suppression worsens with increasing target center frequency  $f_{0,t}$ . As the beamsteering ensures the same pattern independently on the target position, the different performance is only caused by the respective multi-channel processing of the signal, which is governed by the different  $PRF$  values of the respective swaths. Hence, in contrast to ScanSAR, the influence of the antenna pattern is eliminated. This can be seen from the solid red line in Fig. 114 which corresponds to the optimum  $PRF$  and shows a constant value for all target positions as the sampling is uniform in this case and no multi-channel processing is applied. In reverse, the other characteristics of Fig. 114 (dotted, dashed, dotted dashed), show the scalloping introduced by the multi-channel processing for the respective  $PRF$ . Especially for large values of  $f_{0,t}$  the processing network introduces a clear degradation of the  $AASR_{N,B}$  yielding values up to -19 dB. In comparison to the results for the ScanSAR scenario, the degradation is worse for TOPS thus implying that the steered pattern is more sensitive to the multi-channel processing in terms of azimuth ambiguities. This is possibly caused by the shifted pattern which results in more spectral energy outside the system band  $[-N \cdot PRF/2, N \cdot PRF/2]$  and gives rise to ambiguities (cf. Section 5.6). In consequence, the reduced scalloping of signal power (cf. Section 3) is obtained at the expense of a worsened ambiguity suppression if the processing is not adapted to TOPS. A possible approach to improve the performance by an adaptation of the reconstruction algorithm follows in Section 9.7.2.

In order to derive the  $NESZ$  of the system, the loss of signal power is determined and shown in Fig. 115. As expected, no scalloping is encountered as an optimum TOPS pattern is assumed. In reality, the single-element characteristic of the array antenna is to be considered, entailing a small scalloping effect, but still yielding a clearly better result than in ScanSAR operation.

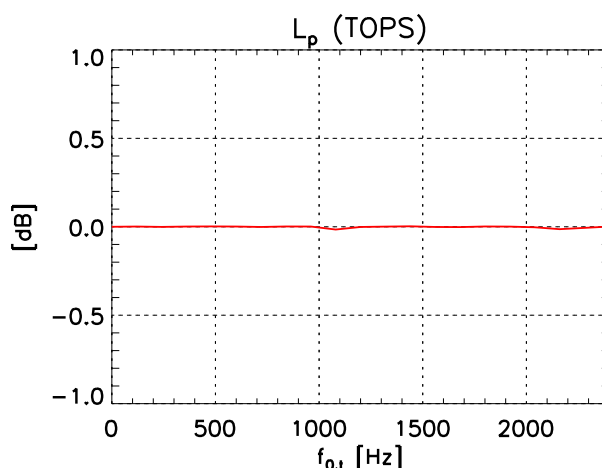


**Fig. 115. Peak power loss normalized to optimum value at  $f_{0,t} = 0$  ( $L_p$ ) vs.  $f_{0,t}$  for TOPS mode operation.**

Further, the **noise scaling** introduced by the digital processing network does not depend on the acquired signal, but only on the processing. Consequently, this scalloping is the same, both for TOPS and ScanSAR operation and Fig. 111 is valid. This means that the *NESZ* for the TOPS mode is simply given by the optimum value for ScanSAR, which is represented by the solid line of Fig. 112. In consequence, TOPS mode ensures for any target a value better than  $\sim -26.5$  dB.

### 9.7.2 Adaptively Squinted Multi-Channel Processing for TOPS

In conventional operation, the burst length in TOPS is chosen to ensure an overall Doppler bandwidth not bigger than the bandwidth covered by the reconstruction filter functions, i.e. the burst bandwidth is limited by the azimuth system bandwidth  $N \cdot PRF$  (cf. Fig. 116). As shown in the preceding chapter, this entails a strong degradation of the ambiguity suppression especially for Doppler frequencies in the outermost regions of the system bandwidth. Further, this entails an unwanted limitation of the burst length in TOPS.

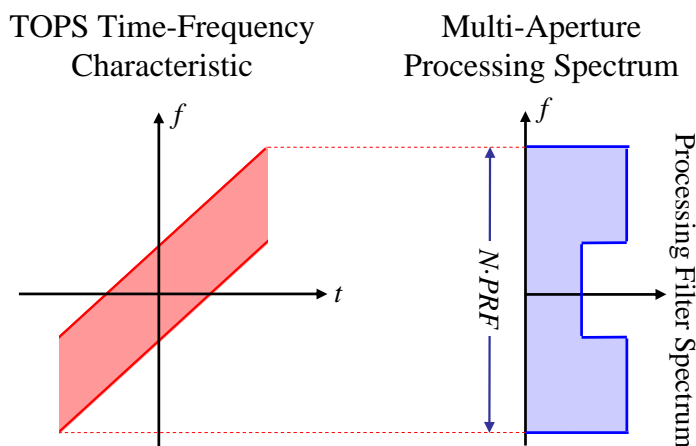


**Fig. 116. TOPS time-frequency characteristic and Doppler spectrum of conventional multi-channel processing functions.**

The basic principle to solve these inconveniences is sketched in Fig. 117. The idea is to center the reconstructed band around a center frequency  $f_0(t)$  which is varied adaptively according to the instantaneous bandwidth of the TOPS signal (“ramping”).<sup>29</sup> In the optimum case, this adaptation is continuous and the bandwidth is adapted to the illumination time of a single target. Consequently, in contrast to the conventional straightforward approach, longer bursts are now possible as spectral components from higher squint angles can be reconstructed.

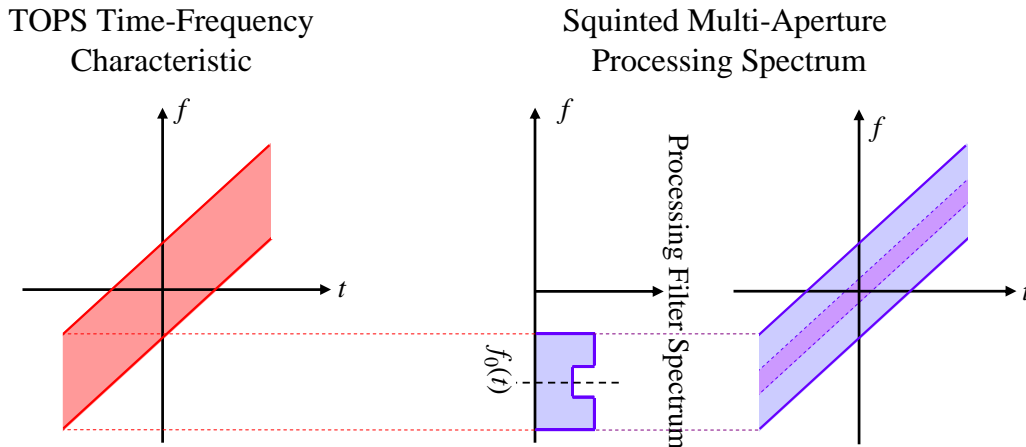


**Fig. 117. Doppler spectrum of multi-channel processing adapted to TOPS: In the optimum case the reconstructed band is centered adaptively around a varying frequency  $f_0(t)$  to ideally cover the TOPS spectrum.**

In reality, only a step-size of  $PRF$  is possible to adapt the center frequency of the processing filters. This means that a center frequency of  $k \cdot PRF$ ,  $k$  integer, is chosen to minimize the offset of the actual target center frequency to the processing center frequency. Hence, the bandwidth is kept constant, i.e. no adaptation to the instantaneous bandwidth is done (cf. Fig. 118).

#### “Staircase” Multi-Aperture Processing

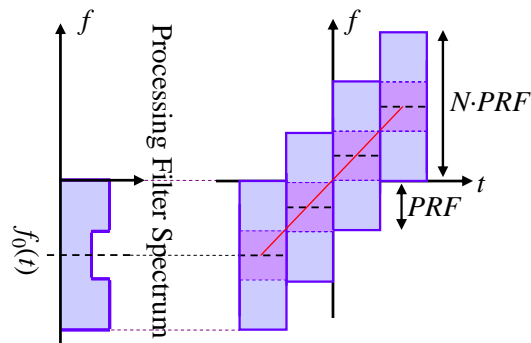


**Fig. 118. Applied squinted multi-channel processing. The reconstructed bandwidth is kept constant and centered adaptively in a staircase-like manner on the target center frequency, which is given by the red line.**

<sup>29</sup>Equivalently to “ramping” the processing filter spectrum, the TOPS signal spectrum can be deramped as proposed in [97] before “regular” processing filter functions – i.e.  $f_0(t) = 0$  – are applied.

Regarding the results, one obtains a clearly improved suppression of azimuth ambiguous energy as shown in Fig. 119, where the scalloping occurs only with a period of  $PRF$  before “switching” to the new center frequency. The four plots show the improved  $AASR_{N,B}$  for all sub-swaths (dashed lines) compared to the results obtained for “conventional” processing (solid lines). The “conventional” straightforward approach yields identical results within the first interval  $[-PRF/2, PRF/2]$  but deviates for target center frequencies higher than  $PRF/2$ . The results of the optimized approach show a suppression of better than  $-22$  dB compared to a minimum suppression of  $-19$  dB without adaptation of the processing.

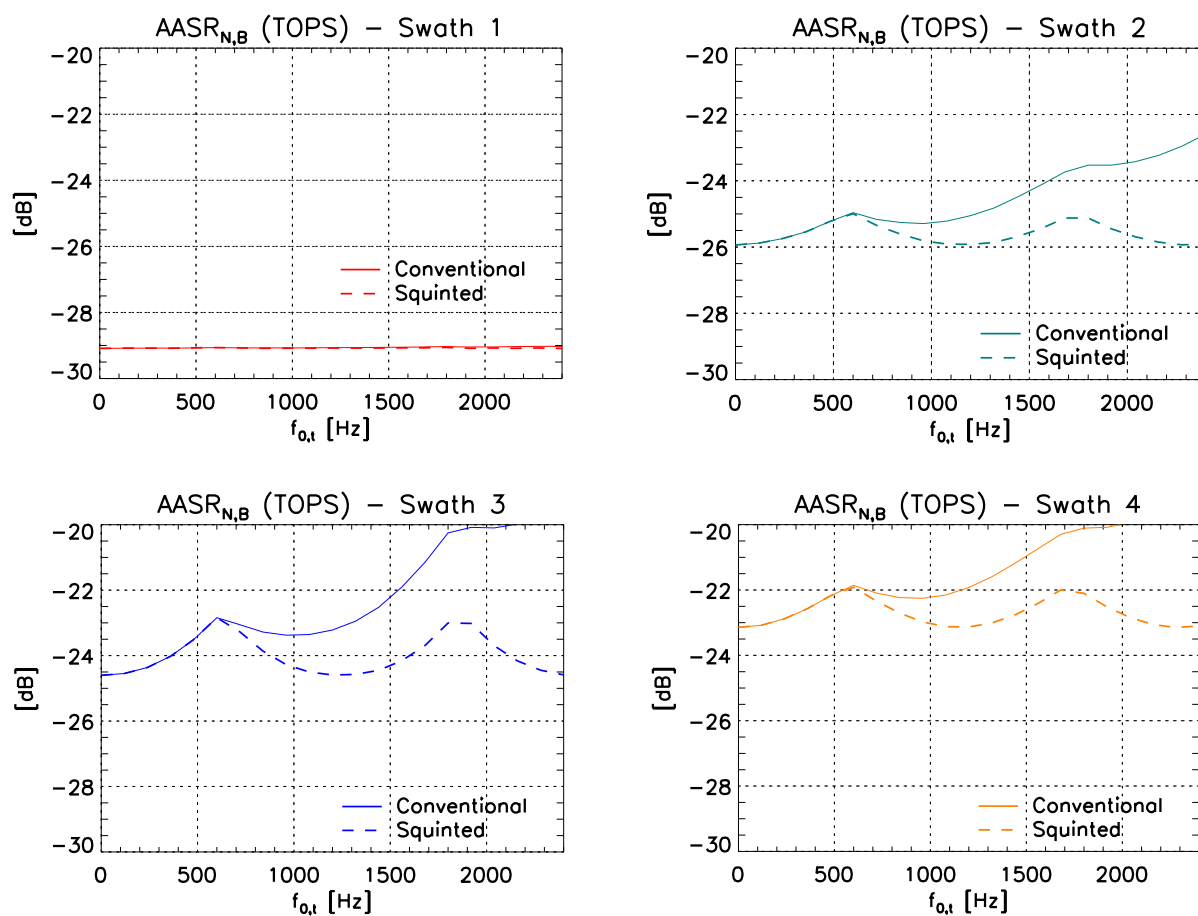


**Fig. 119.** TOPS mode  $AASR_{N,B}$  vs.  $f_{0,t}$  for “conventional” (solid lines) and “squinted” (dashed lines) multi-channel reconstruction for each of the four sub-swaths.

As a final remark, it should be noted that further optimization potential is given by the combination of an adapted center frequency with a reduction of the reconstructed bandwidth to oversample only the Doppler spectrum received during the illumination of a specific target. Such an adaptation of the system bandwidth in azimuth would allow either for lower  $PRF$  values or less receiving channels or an increased bandwidth enabling a better resolution.



## 10 Discussion

This chapter revises the achieved objectives of this work in Section 10.1, followed by a detailed summary of the obtained results (cf. Section 10.2). Finally, an outlook on future issues and potentials is given in Section 10.3.

### 10.1 Conclusion – Achieved Objectives of the Work

Future remote sensing applications demand increasingly detailed imagery with frequent revisit times, i.e. wide area coverage. Due to inherent system limitations, conventional single-aperture SAR systems do not enable wide-swath imaging with high geometric resolution. As a consequence, innovative SAR system concepts are required.

Several novel approaches based on multi-channel systems, such as systems with multiple receive apertures in azimuth, were proposed (Chapter 3) and promise to overcome the restrictions of conventional SAR. As the analysis revealed, the performance of such systems was sensitive to the positions of the gathered samples which were governed by the relation between fixed antenna dimension in azimuth and variable *PRF*. Thus, these systems imperatively required sophisticated digital processing of the received signals in order to guarantee full performance independently of the spatial sample distribution imposed by the applied *PRF*.

Starting from the generalization of the sampling theorem, the present work introduced, analyzed, and evaluated an algorithm suitable to process multi-channel SAR azimuth data, which could be directly integrated into a “regular” two-dimensional SAR processing scheme. As a key characteristic, this “multi-channel reconstruction algorithm” compensated for non-uniform sample distributions in azimuth resulting from variable *PRF* values, thus enabling high-resolution wide-swath imaging. The presented example system showed a geometric resolution below 1 m in combination with 100 km swath width. To allow for the evaluation of multi-channel SAR systems, a versatile performance estimator was developed to provide an innovative “toolbox” to assess and verify multi-channel processing techniques with respect to the azimuth dimension. The obtained simulation results demonstrated that the reconstruction algorithm ensures constant geometric resolution and good suppression of azimuth ambiguous energy independently of the *PRF*. As a drawback, the inverse character of the applied digital processing network entailed a degradation of the *SNR* for non-optimum *PRF* values, thus restricting the *PRF* range of opera-

tion. In this context, the intricate relationship between system design and multi-channel processing became clear. Evidently, system parameters are more closely linked to the performance than in conventional SAR systems.

Based on the obtained results, various optimization strategies for the system and processing algorithm were developed and the performance estimator was extended accordingly. In this context, special focus was turned to mitigating the *SNR* degradation by the processing network and several techniques were presented that extended the *PRF* range of operation. The optimized system approaches were extensively analyzed, demonstrating increased flexibility and improved performance.

Finally, multi-channel SAR systems operating in stripmap mode were shown to be unsuitable for ultra-wide swaths of several hundred kilometers as this would require antennas with an unreasonable length. Thus, the operation of multi-channel SAR systems in burst modes, such as ScanSAR and TOPS, was presented as a possible solution. The performance analysis was extended accordingly to account for the impact of the target position on the SAR signal. Simulations for both ScanSAR and TOPS mode yielded a geometric resolution of 5 m in combination with 400 km swath width, which means that this new class of multi-channel systems enables frequent mapping on a global scale with unprecedented detail.

In summary, the present work introduced, analyzed, and verified various innovative multi-channel processing techniques, system architectures and novel modes of operation, including system design considerations with special focus on the demands of SAR systems with multiple azimuth channels. As demonstrated by the results of the performance estimator, the multi-channel azimuth processing enables SAR systems to be operated with high flexibility and reconfigurability, thus ensuring previously unprecedented performance and a greater range of applications. In conclusion, such systems open up an entirely new field of SAR operation and are ideally suited to answer the needs of future remote sensing missions. Furthermore, the investigated azimuth processing methods have the potential to be an essential component of the next generation's SAR imaging concepts.

## 10.2 Summary of Results

After having recalled the basic properties of multi-channel SAR signals regarding the spatial sampling in Chapter 4, the innovative contributions of the work started with Chapter 5, which introduced an algorithm for processing multi-channel SAR data (“digital beamforming on receive”). This **multi-channel reconstruction algorithm** achieved the unambiguous recovery of the azimuth signal despite a non-uniformly sampled synthetic aperture, thereby avoiding any stringent *PRF* restriction. The method combined the individual receiver signals in a linear space-time processing approach and could be interpreted as solving a linear system of equations in a way that ambiguous parts in the azimuth signal were canceled. In simple words, the algorithm allowed for combining a number of  $N$  sub-sampled input signals to a single output signal of  $N$ -fold the sampling rate and free of aliasing.



In a first step, the algorithm was investigated in detail with respect to the influence of the digital processing network on signal power, ambiguities and noise. This yielded **analytical expressions** for the estimation of residual ambiguities and the determination of the beamforming network's *SNR* scaling factor  $\Phi_{\text{bf}}$  which quantified the degradation of the *SNR* – or equivalently the system *NESZ* – due to the digital processing. The analysis showed that especially strong non-uniform sampling of the azimuth signal may lead to a degraded *SNR* due to an increased network *SNR* scaling factor and an amplification of residual azimuth ambiguities which were both caused by the inverse character of the processing network.

A first **proof of concept** was presented in Chapter 6, where the multi-channel reconstruction algorithm was applied to measured multi-channel data acquired by DLR's airborne systems E-SAR and F-SAR, respectively. In this context the derived algorithm demonstrated its capability to unambiguously recover sub-sampled data and provide efficient ambiguity suppression also for non-optimum *PRF* values.

Chapter 7 tied in with the theoretical analysis of Chapter 5 and verified the derived expressions in simulations when evaluating an **example system** that was designed to image a swath of 100 km with a geometric resolution of 1 m. In order to determine the system **performance** and to compare the reconstruction algorithm to alternative methods of processing the azimuth signal, an estimator was implemented, which enabled a point-target analysis for arbitrary multi-channel SAR systems. This simulation "toolbox" included the possibility of an analytical calculation of the azimuth ambiguity-to-signal ratio ( $AASR_N$ ) and the *SNR* scaling factor, thus enabling a prediction and/or verification of the simulated performance.

The obtained results showed that only the reconstruction algorithm and the very similar null-steering technique provided high resolution in combination with efficient ambiguity suppression over a varying range of *PRF* values. Nevertheless, the applicable *PRF* range was restricted by the maximum tolerable *SNR* scaling factor  $\Phi_{\text{bf}}$ .

In a next step, **system optimization** was performed in Chapter 8 in order to increase system flexibility and improve its performance. Firstly, the main disturbing sources were identified to be aliasing in the received signal and the amplification of ambiguous energy and noise due to the processing in the case of non-uniformly sampled data. Consequently, optimization strategies were derived in order to minimize the received **ambiguous energy** and to ensure a **spatial sample distribution** as uniform as possible.

**On receive**, optimization started with an **optimized parameter setting** (cf. Section 8.2) in order to limit the amplification of ambiguities and noise by benefiting from the "colored" spectral appearance of the processing filters. In this way, the performance of one parameter could be clearly improved at the cost of only a moderate degradation of another.

Further, an **adaptive *PRF* management** was introduced in Section 8.3 as a first simple solution to adjust the spatial sampling. This technique showed large potential for application to sparse array SAR systems but had only limited impact in multi-channel systems on a single platform.

A more sophisticated approach was given by processing methods extended by an additional stage thus yielding **cascaded beamforming networks** (cf. Section 8.7). This allowed for a limi-

tation of the Doppler spectrum by tapering the receive pattern. Further, number and positions of the effective phase centers could be adapted flexibly and reconfigurably to the respective *PRF*, thus optimizing the spatial sampling and allowing for a wider *PRF* range of operation. Furthermore, the cascaded structure allowed for a flexible allocation of system resources enabling a trade-off between *SNR* and ambiguity suppression.

Regarding the optimization **on transmit**, firstly, a simple **pattern tapering** yielded an efficient suppression of ambiguous energy by limiting the aliased part in the signal while concentrating the signal power better on the imaged area (cf. Section 8.4). Since this technique requires large transmit antenna lengths, T/R technology is an appealing solution to directly benefit on transmit from the large receiving antenna. Secondly, a patented technique based on an **advanced transmit architecture** was suggested, which enabled an adaptive cyclic adjustment of the transmit phase center from pulse to pulse thus controlling the spatial sample positions of the multi-channel system (cf. Section 8.6) [56], [57].

Finally, in Chapter 9 attention was concentrated on **ultra-wide-swath imaging** which required an innovative approach, since multi-channel stripmap imaging would need an antenna length of 35-40 m in azimuth for a swath width of 400 km. It was shown that this problem can be solved by the application of **burst modes** like **ScanSAR** or **TOPS in multi-channel systems**. In this context the impact of the Doppler frequency dependent multi-channel processing was investigated with respect to the particular properties of burst mode data. As the target position determined the spectral band of its echo, different targets were processed with different sub-bands of the processing filter's colored spectrum. This resulted in a variation of the performance depending on the target position, introducing a scalloping-like effect both for TOPS and ScanSAR. Simulation results for a multi-channel ScanSAR system and a first straightforward application to TOPS illustrated the introduced scalloping of residual azimuth ambiguities and the *SNR* scaling and demonstrated the possibility to image a swath of 400 km with a resolution of 5 m. In a final step, a first optimized approach for processing multi-channel TOPS data was presented by introducing in the multi-channel reconstruction algorithm an adaptive "squint" according to the time-frequency characteristic of the TOPS mode.

### 10.3 Outlook

Beside multi-channel systems on a single platform, **sparse array SAR systems** formed by a single transmitter and multiple independent receiver satellites are becoming more and more important as they allow for small, passive, and thus cost-effective receive sensors. While the successful application of multi-channel azimuth processing to single platform systems was demonstrated in this thesis, the great potential of the presented algorithm with respect to the latter systems is an important part of future work. As it was shown when deriving the two-dimensional processing scheme, the reconstruction algorithm is directly applicable to such systems, but specific aspects become more important in sparse array geometries. Hence, in a next step, the application of the multi-channel processing to such **distributed SAR configurations** should be analyzed, with special attention to the characteristics described in the following.

Firstly, the increased along-track separations of the receiving apertures entail a high sensitivity of the sampling against *PRF* variations due to modulo influence on the effective sample position. On the one hand, this might cause problems, as small *PRF* changes have a large impact on the sampling scenario, but on the other hand this offers an opportunity to optimize the spatial sampling by adapting the *PRF* as mentioned in Section 8.3. Further, large along-track displacements might require a steering of the antenna footprints to illuminate a joint area on the ground resulting in a different squint of the satellites and thus the reception of mutually shifted Doppler spectra in the receivers. This might lead to sub-sampling and require for new processing approaches, e.g. the combination of multi-channel reconstruction and super-resolution techniques [54]. In this context, the investigation of channel imbalances in gain and phase vs. Doppler frequency and its impact on the processing will also be of interest.

Secondly, any cross-track separation of the receivers will introduce an additional phase in the received signals, which has to be compensated, e.g. via the simultaneous acquisition of a digital elevation model in the case of multiple satellites.

Regarding **multi-channel burst mode systems**, their unprecedented combination of coverage and detailed imagery encourages the further investigation of **advanced concepts for ultra-wide-swath imaging**. Based on the analysis of multi-channel burst mode operation, the adaptation of the multi-channel processing to TOPS mode should be further developed. In this context, more sophisticated burst modes allowing for even higher resolutions and swath widths deserve special interest [60].

Another promising concept to be further investigated is the combination of **large reflector antennas** with a **feed array** enabling digital beamforming both in azimuth and range dimension. The large reflector dimensions ensure a high antenna gain in combination with a narrow beam whose steering angle – and consequently the illuminated footprint on ground – is directly linked to a specific feed element (or a sub-group of them). This makes such systems ideally suited for multi-beam applications, be it to enable effective range ambiguity suppression or to apply super-resolution techniques in azimuth [61], [62].

Finally, one has to be prepared for future SAR following the generation of multi-receiver systems currently discussed. Consequently, the investigation of more sophisticated techniques for signal transmission leading to **fully active radars** should be followed. In this context the **waveform encoding on transmit** technique deserves further analysis and development with special attention to the combination and mutual adaptation of advanced transmit and receive architectures and modes [64], [95].



# Bibliography

- [1] C. Hülsmeier, Verfahren, um entfernte metallische Gegenstände mittels elektrischer Wellen einem Beobachter zu melden, German Patent No. DE 165546A, filed 1904, published 1905.
- [2] C.A. Wiley, Pulsed Doppler radar methods and apparatus, US Patent No. US 3196436, filed 1954, published 1965.
- [3] C.A. Wiley, Synthetic aperture radars, *IEEE Transactions on Aerospace and Electronic Systems*, vol. 21 (3), pp. 440-443, 1985.
- [4] (2008, June) NASA, Jet Propulsion Laboratory (JPL), SEASAT 1978, [Online], Available: <http://southport.jpl.nasa.gov/scienceapps/seasat.html>
- [5] (2008, June), Natural Resources Canada, Canada Center of Remote Sensing, [Online], Available: [http://www.ccrs.nrcan.gc.ca/resource/tutor/iquiz/q03\\_e.php](http://www.ccrs.nrcan.gc.ca/resource/tutor/iquiz/q03_e.php)
- [6] (2008, June), W. Holpp, The century of radar, [Online], Available: [http://www.100-jahre-radar.de/vortraege/Holpp-The\\_Century\\_of\\_Radar.pdf](http://www.100-jahre-radar.de/vortraege/Holpp-The_Century_of_Radar.pdf)
- [7] (2009, April) German Aerospace Center (DLR), TerraSAR-X, [Online], Available: <http://www.dlr.de/TerraSAR-X/>
- [8] (2009, January), Telespazio, COSMO-Skymed, [Online], Available: <http://www.telespazio.it/cosmo.html>
- [9] (2008, June), Radarsat-2, [Online], Available: <http://www.radarsat2.info/>
- [10] (2009, January), Japanese Aerospace Exploration Agency (JAXA), Earth Observation Research Center (EORC), ALOS, [Online], Available: <http://www.eorc.jaxa.jp/ALOS/>
- [11] (2009, January), e-Geos, COSMO-Skymed Products, [Online], Available: [http://www.e-geos.it/cosmo\\_prog.htm](http://www.e-geos.it/cosmo_prog.htm)
- [12] W. Carrara, R. Goodman, and R. Majewski, *Spotlight Synthetic Aperture Radar: Signal Processing Algorithm*, Boston: Artech House, 1995.
- [13] K. Tomiyasu, Conceptual performance of a satellite borne, wide swath synthetic aperture radar, *IEEE Transactions on Geoscience and Remote Sensing*, vol. 19 (2), pp. 108-116, 1981.
- [14] R. K. Moore, J. P. Claassen, and Y. H. Lin, A scanning spaceborne synthetic aperture radar with integrated radiometer, *IEEE Transactions on Aerospace and Electronic Systems*, vol. 17 (3), pp. 410-421, 1981.

- [15] F. De Zan and A.M. Monti Guarnieri, TOPSAR: Terrain Observation by Progressive Scans, *IEEE Transactions on Geoscience and Remote Sensing*, vol. 44 (9), pp. 2352-2360, 2006.
- [16] L. Brule and H. Baeggli, Radarsat-2 Program Update, *Proceedings of the IEEE International Geoscience and Remote Sensing Symposium (IGARSS)*, Toronto, Canada, 2002.
- [17] J. Mittermayer and H. Runge, Conceptual Studies for Exploiting the TerraSAR-X Dual Receiving Antenna, *Proceedings of the IEEE International Geoscience and Remote Sensing Symposium (IGARSS)*, Toulouse, France, 2003.
- [18] J. Curlander and R. McDonough, *Synthetic Aperture Radar – Systems and Signal Processing*, J. Wiley & Sons, Inc., 1991.
- [19] A. Freeman, W.T.K. Johnson, B. Huneycutt, R. Jordan, S. Hensley, P. Siqueira, and J. Curlander, The “Myth” of the minimum SAR antenna area constraint, *IEEE Transactions on Geoscience and Remote Sensing*, vol. 38 (1), pp. 320-324, 2000.
- [20] J. P. Claassen and J. Eckerman, A system concept for wide swath constant incident angle coverage, *Proceedings of Synthetic Aperture Radar Technology Conference*, Las Cruces, New Mexico, USA, 1978.
- [21] A. Jain, Multibeam synthetic aperture radar for global oceanography, *IEEE Transactions on Antennas and Propagation*, vol. 27 (4), pp. 535-538, 1979.
- [22] B. R. Jean and J. W. Rouse, A multiple beam synthetic aperture radar design concept for geoscience applications, *IEEE Transactions on Geoscience and Remote Sensing*, vol. 21 (2), pp. 201-207, 1983.
- [23] H. Griffiths and P. Mancini, Ambiguity suppression in SARs using adaptive array techniques, *Proceedings of the IEEE International Geoscience and Remote Sensing Symposium (IGARSS)*, Espoo, Finland, pp. 1015-1018, 1991.
- [24] A. Currie and M.A. Brown, Wide-Swath SAR, *IEE Proceedings – Radar Sonar and Navigation*, vol. 139 (2), pp. 122-135, 1992.
- [25] G.D. Callaghan and I.D. Longstaff, Wide Swath Spaceborne SAR Using a Quad Element Array, *IEE Proceedings – Radar Sonar and Navigation*, vol. 146 (3), pp. 159-165, 1999.
- [26] N. Goodman, D. Rajakrishna, and J. Stiles, Wide swath, high resolution SAR using multiple receive apertures, *Proceedings of the IEEE International Geoscience and Remote Sensing Symposium (IGARSS)*, Hamburg, Germany, vol. 3, pp. 1767-1769, 1999.
- [27] M. Younis and W. Wiesbeck, SAR with Digital Beamforming on Receive Only, *Proceedings of the IEEE International Geoscience and Remote Sensing Symposium (IGARSS)*, Hamburg, Germany, vol. 3, pp. 1773-1775, 1999.
- [28] J. Stiles, N. Goodman, and L. SiChung, Performance and processing of SAR satellite clusters, *Proceedings of the IEEE International Geoscience and Remote Sensing Symposium (IGARSS)*, Honolulu, Hawaii, USA, vol. 2, pp.883 – 885, 2000.
- [29] M. Suess and W. Wiesbeck, Side-looking synthetic aperture system, European Patent No. EP 1 241 487 A 1, filed 2001, published 2002.
- [30] J.T. Kare, Moving Receive Beam Method And Apparatus For Synthetic Aperture Radar, US Patent No. US 6,175,326 B1, filed 1998, published 2001.

- [31] M. Suess, B. Grafmüller, and R. Zahn, A Novel High Resolution, Wide Swath SAR System, *Proceedings of the IEEE International Geoscience and Remote Sensing Symposium (IGARSS)*, Sydney, Australia, pp. 1013-1015, 2001.
- [32] W. Wiesbeck, SDRS: software-defined radar sensors, *Proceedings of the IEEE International Geoscience and Remote Sensing Symposium (IGARSS)*, Sydney, Australia, pp. 3259-3261, 2001.
- [33] M. Suess, M. Zubler, and R. Zahn, Performance investigation on the high resolution, wide swath SAR system, *Proceedings of European Conference on Synthetic Aperture Radar (EUSAR)*, Cologne, Germany, pp. 187-191, 2002.
- [34] N. Goodman, S. Lin, D. Rajakrishna, and J. Stiles, Processing of Multiple-Receiver Spaceborne Arrays for Wide-Area SAR, *IEEE Transactions on Geoscience and Remote Sensing*, vol. 40 (4), pp. 841-852, Apr. 2002.
- [35] J.P. Aguttes, The SAR Train: Along track orientated formations of SAR satellites, *Proceedings of International Symposium on Formation Flying Missions & Technologies*, Toulouse, France, 2002.
- [36] G. Krieger, H. Fiedler, M. Rodriguez-Cassola, D. Hounam, and A. Moreira, System Concepts for Bi- and Multistatic SAR Missions, *Proceedings of the ASAR Workshop 2003*, Saint-Hubert, Quebec, Canada, Jun 2003.
- [37] G. Krieger and A. Moreira, Potentials of digital beamforming in bi- and multistatic SAR, *Proceedings of the IEEE International Geoscience and Remote Sensing Symposium (IGARSS)*, Toulouse, France, pp. 527-529, 2003.
- [38] C. Heer, F. Soualle, R. Zahn, and R. Reber, Investigations on a new high resolution wide swath SAR concept, *Proceedings of IEEE International Geoscience and Remote Sensing Symposium (IGARSS)*, Toulouse, France, pp. 521-523, 2003.
- [39] M. Younis, C. Fischer, and W. Wiesbeck, Digital Beamforming in SAR systems, *IEEE Transactions on Geoscience and Remote Sensing*, vol. 41 (7), pp. 1735-1739, Jul. 2003
- [40] M. Younis, Y. Venot, W. Wiesbeck, A Simulator for Digital Beam Forming SAR, *Proceedings of International Radar Symposium, (IRS)*, Dresden, Germany, 2003.
- [41] J.P. Aguttes, The SAR Train Concept: Required Antenna Area Distributed over N Smaller Satellites, Increase of performance by N, *Proceedings of the IEEE International Geoscience and Remote Sensing Symposium (IGARSS)*, Toulouse, France, 2003.
- [42] G. Krieger, N. Gebert, and A. Moreira, Unambiguous SAR Signal Reconstruction from Nonuniform Displaced Phase Center Sampling, *IEEE Geoscience and Remote Sensing Letters*, vol. 1 (4), pp. 260-264, 2004.
- [43] G. Krieger, N. Gebert, and A. Moreira, SAR Signal Reconstruction from Non-Uniform Displaced Phase Center Sampling, *Proceedings of the IEEE International Geoscience and Remote Sensing Symposium (IGARSS)*, Anchorage, Alaska, USA, Sep. 2004.
- [44] G. Krieger, N. Gebert, and A. Moreira, Digital Beamforming and Non-Uniform Displaced Phase Centre Sampling in Bi- and Multistatic SAR, *Proceedings of European Conference on Synthetic Aperture Radar (EUSAR)*, Ulm, Germany, 2004.

- [45] M. Younis, Digital Beam-Forming for High Resolution Wide Swath Real and Synthetic Aperture Radar, *Forschungsbericht aus dem Institut für Höchstfrequenztechnik und Elektronik der Universität Karlsruhe (Dissertation)*, vol. 42, Karlsruhe, Germany, 2004.
- [46] N. Gebert, G. Krieger, and A. Moreira, SAR Signal Reconstruction from Non-Uniform Displaced Phase Centre Sampling in the Presence of Perturbations, *Proceedings of the IEEE International Geoscience and Remote Sensing Symposium (IGARSS)*, Seoul, South-Korea, 2005.
- [47] N. Gebert, G. Krieger, and A. Moreira, High Resolution Wide Swath SAR Imaging – System Performance and Influence of Perturbations, *Proceedings of International Radar Symposium (IRS)*, Berlin, Germany, 2005.
- [48] Z. Li, H. Wang, T. Su, and Z. Bao, Generation of Wide-Swath and High-Resolution SAR Images From Multichannel Small Spaceborne SAR System, *IEEE Geoscience and Remote Sensing Letters*, vol. 2 (1), pp. 82-86, Jan. 2005
- [49] Z. Li, Z. Bao, H. Wang, and G. Liao, Performance Improvement for Constellation SAR Using Signal Processing Techniques, *IEEE Transactions on Aerospace and Electronic Systems*, vol. 42 (2), pp. 436-452, 2006.
- [50] Z. Li and Z. Bao, A novel approach for wide-swath and high-resolution SAR image generation from distributed small spaceborne SAR systems, *International Journal of Remote sensing*, vol. 27 (5), pp. 1015-1033, 2006.
- [51] C. Fischer, C. Heer, G. Krieger, and R. Werninghaus, A high resolution wide swath SAR, *Proceedings of European Conference on Synthetic Aperture Radar (EUSAR)*, Dresden, Germany, 2006.
- [52] N. Gebert, G. Krieger, and A. Moreira, High Resolution Wide Swath SAR Imaging with Digital Beamforming – Performance Analysis, Optimization and System Design, *Proceedings of European Conference on Synthetic Aperture Radar (EUSAR)*, Dresden, Germany, 2006.
- [53] N. Gebert, G. Krieger, and A. Moreira, Digital Beamforming for HRWS-SAR Imaging, *Proceedings of the IEEE International Geoscience and Remote Sensing Symposium (IGARSS)*, Denver, Colorado, USA, Jul. 2006.
- [54] G. Krieger and A. Moreira, Spaceborne Bi- and Multistatic SAR: Potential and Challenges, *IEE Proceedings – Radar, Sonar and Navigation*, vol. 153 (3), pp. 184-198, 2006.
- [55] N. Gebert, G. Krieger, and A. Moreira, Digital Beamforming on Receive: Techniques and Optimization Strategies for High-Resolution Wide-Swath SAR Imaging, *IEEE Transactions on Aerospace and Electronic Systems*, vol. 45 (2), pp. 564-592, 2009.
- [56] N. Gebert and G. Krieger, Synthetisk-Apertur-Radarsystem, German Patent No. DE 10 2007 041 373.6, filed 2007, published 2009.
- [57] N. Gebert and G. Krieger, Azimuth Phase Center Adaptation on Transmit for High-Resolution Wide-Swath SAR Imaging, *IEEE Geoscience and Remote Sensing Letters*, accepted for publication in 2009.
- [58] N. Gebert, G. Krieger, and A. Moreira, Multi-Channel ScanSAR for High-Resolution Ultra-Wide-Swath Imaging, *Proceedings of the European Conference on Synthetic Aperture Radar (EUSAR)*, Friedrichshafen, Germany 2008.



- [59] N. Gebert, G. Krieger, M. Younis, F. Bordoni, and A. Moreira, Ultra Wide Swath Imaging With Multi-Channel ScanSAR, *Proceedings of the IEEE International Geoscience and Remote Sensing Symposium (IGARSS)*, Boston, Massachusetts, USA, Jul. 2008.
- [60] G. Krieger, N. Gebert, M. Younis, F. Bordoni, A. Patyuchenko, and A. Moreira, Advanced Concepts for Ultra-Wide-Swath SAR Imaging with High Azimuth Resolution, *Proceedings of European Conference on Synthetic Aperture Radar (EUSAR)*, Friedrichshafen, Germany, 2008.
- [61] G. Krieger, N. Gebert, and A. Moreira, Digital Beamforming Techniques for Spaceborne Radar Remote Sensing, *Proceedings of European Conference on Synthetic Aperture Radar (EUSAR)*, Dresden, Germany, 2006.
- [62] M. Younis, S. Huber, A. Patyuchenko, F. Bordoni and G. Krieger, Performance Comparison of Reflector- and Planar-Antenna based Digital Beam-Forming SAR, *International Journal of Antennas and Propagation, Special Issue on Active Antennas for Space Applications*, accepted for publication in 2009.
- [63] G. Krieger, N. Gebert, and A. Moreira, Hochauflösendes Synthetik-Apertur-Seitensicht-Radarsystem mittels Digital Beamforming, German Patent No. DE 10 2006 022 814.6 / European Patent No. EP 2007 / 003921, filed 2006, published 2007.
- [64] G. Krieger, N. Gebert, and A. Moreira, Multidimensional Waveform Encoding: A New Digital Beamforming Technique for Synthetic Aperture Radar Remote Sensing, *IEEE Transactions on Geoscience and Remote Sensing*, vol. 46 (1), pp. 31-46, 2008.
- [65] M. Younis; F. Bordoni, N. Gebert, and G. Krieger, Smart Multi-channel Radar Techniques for Spaceborne Remote Sensing. *Proceedings of the IEEE International Geoscience and Remote Sensing Symposium (IGARSS)*, Boston, Massachusetts, USA, Jul. 2008.
- [66] Klausning, Holpp (Eds.), *Radar mit realer und synthetischer Apertur: Konzeption und Realisierung*, Oldenburg Verlag, 1999.
- [67] A. J. Lewis and F. M. Henderson (Eds.), *Principles and Applications of Imaging Radar: Principles and Applications of Imaging Radar (Manual of Remote Sensing, Volume 2)*, J. Wiley & Sons, Inc., 1998.
- [68] K. Raney, Considerations for SAR image quantification unique to orbital systems, *IEEE Transactions on Geoscience and Remote Sensing*, vol. 29 (5), pp. 754-760, 1991.
- [69] I.G. Cumming and F.H. Wong, *Digital Processing of Synthetic Aperture Radar Data – Algorithms and Implementation*, Artech House, 2005.
- [70] M. Soumekh, *Synthetic Aperture Radar Signal Processing With Matlab Algorithms*, J. Wiley & Sons, Inc., 1999.
- [71] C. E. Shannon, Communication in the presence of noise, *Proc. Institute of Radio Engineers*, vol. 37 (1), pp. 10-21, Jan. 1949.
- [72] A. Papoulis, Generalized Sampling Expansion, *IEEE Transactions on Circuits and Systems*, vol. 24 (11), pp. 652-654, 1977.
- [73] J. Brown, Multi-Channel Sampling of Low-Pass Signals, *IEEE Transactions on Circuits and Systems*, vol. 28 (2), pp. 101-106, 1981.
- [74] J.R. Guerci, *Space-Time Adaptive Processing*, Artech House, 2003.

- [75] H. L. van Trees, *Optimum Array Processing – Part IV of Detection, Estimation, and Modulation Theory*, J. Wiley & Sons, Inc., 2002.
- [76] A. Oppenheim, *Discrete-Time Processing*, Prentice Hall, 1999.
- [77] N. Gebert and A. Meta, Weiterentwicklung der Azimutprozessierung – Appendix: A general space-time framework for azimuth digital beamforming in SAR imaging, Technischer Bericht HRWSII-HR-TB2300 Analyse eines neuen SAR Konzeptes (Follow-on), DLR Förderkennzeichen 50 EP 0606, 2008.
- [78] G. Krieger et al., TanDEM-X: A Satellite Formation for High-Resolution SAR Interferometry. *IEEE Transactions on Geoscience and Remote Sensing*, vol. 45 (11, part 1), pp. 3317-3341, 2007.
- [79] F.G. Stremmer, *Introduction to Communication Systems*, Addison-Wesley, 1977.
- [80] T. Wang and Z. Bao, Improving the Image Quality of Spaceborne Multiple-Aperture SAR Under Minimization of Sidelobe Clutter and Noise, *IEEE Geoscience and Remote Sensing Letters*, vol. 3 (3), pp. 297-301, Jul. 2006.
- [81] J. Marquez-Martinez, J. Mittermayer, and M. Rodriguez Cassola, Radiometric Resolution Optimization for Future SAR Systems, *Proceedings of the IEEE International Geoscience and Remote Sensing Symposium (IGARSS)*, Anchorage, Alaska, USA, Sep. 2004.
- [82] R.K. Raney, SNR in SAR, *Proceedings of the IEEE International Geoscience and Remote Sensing Symposium (IGARSS)*, Amherst, Massachusetts, USA, Oct. 1985.
- [83] R.K. Raney, SNR Considerations For An Orbital SAR, *Proceedings of the IEEE International Geoscience and Remote Sensing Symposium (IGARSS)*, Washington, DC, USA, May 1990.
- [84] (June, 2008), German Aerospace Center (DLR), E-SAR – Das flugzeuggetragene SAR System des DLR , [Online], Available: [http://www.dlr.de/hr/desktopdefault.aspx/tabid-2326/3776\\_read-5679/](http://www.dlr.de/hr/desktopdefault.aspx/tabid-2326/3776_read-5679/)
- [85] (June, 2008), German Aerospace Center (DLR), F-SAR – Das neue flugzeuggetragene SAR System, [Online], Available: [http://www.dlr.de/hr/desktopdefault.aspx/tabid-2326/3776\\_read-5691/](http://www.dlr.de/hr/desktopdefault.aspx/tabid-2326/3776_read-5691/)
- [86] R. Horn, A. Nottensteiner, and R. Scheiber, F-SAR – DLR's advanced airborne SAR system onboard DO228, *Proceedings of the European Conference on Synthetic Aperture Radar (EUSAR)*, Friedrichshafen, Germany 2008.
- [87] S. Baumgartner, M. Gabele, N. Gebert, R. Scheiber, G. Krieger, K.-H. Bethke, and A. Moreira, Digital Beamforming and Traffic Monitoring Using the new F-SAR System of DLR, *Proceedings of International Radar Symposium (IRS)*, Cologne, Germany, 2007.
- [88] K. Camara de Macedo, R. Scheiber, and A. Moreira, An Autofocus Approach for Residual Motion Errors With Application to Airborne Repeat-Pass SAR Interferometry, *IEEE Transactions on Geoscience and Remote Sensing*, vol. 46 (10), pp. 3151-3162, 2008.
- [89] C. Schaefer, Nadir Echo Suppression for High-Resolution Wide-Swath SAR, Technical Note TN-DFE-2500-AED/01, Active Receive-Only Digital Frontend for Radar and SAR, ESA contract 19648/05/NL/JA, 2008.
- [90] J. Kraus, *Antennas*, McGraw-Hill, 1950.

- 
- [91] B. Grafmüller and C. Schaefer, Hochauflösende Synthetik-Apertur-Radarvorrichtung und Antenne für eine hochauflösende Synthetik-Apertur-Radarvorrichtung, German Patent No. DE 10 2005 062 031.0, filed 2005, published 2007.
- [92] C. Schaefer, System Study, Technical Note TN-DFE-1100-AED/01, Active Receive-Only Digital Frontend for Radar and SAR, ESA contract 19648/05/NL/JA, 2008.
- [93] J. Mittermayer et al., TerraSAR-X System Performance & Command Generation, *Proceedings of the European Conference on Synthetic Aperture Radar (EUSAR)*, Friedrichshafen, Germany 2008.
- [94] N. Gebert, Azimutprozessierung, Optimierung der Azimutperformance, Technischer Bericht DLR-HRWSTB2200\_2400/2 Analyse eines neuen SAR Konzeptes, dem sog. High Resolution Wide Swath SAR, DLR Förderkennzeichen PM-FA/DR-RE - 50 EP 0502 - AAK, 2006.
- [95] G. Krieger, N. Gebert, M. Younis; and A. Moreira, Advanced Synthetic Aperture Radar Based on Digital Beamforming and Waveform Diversity. *Proceedings of the IEEE Radar Conference (RadarCon)*, Rome, Italy, May 2008.
- [96] P. Prats, A. Meta, R. Scheiber, J. Mittermayer, J. Sanz-Marcos, and A. Moreira, A TOPSAR Processing Algorithm Based on Extended Chirp Scaling: Evaluation with TerraSAR-X Data. *Proceedings of the European Conference on Synthetic Aperture Radar (EUSAR)*, Friedrichshafen, Germany 2008.
- [97] P. Prats, R. Scheiber, J. Mittermayer, A. Meta, A. Moreira, and J. Sanz-Marcos, A SAR Processing Algorithm for TOPS Imaging Mode Based on Extended Chirp Scaling, *Proceedings of the IEEE International Geoscience and Remote Sensing Symposium (IGARSS)*, Barcelona, Spain, 2007.
- [98] J. Way and E.A. Smith, The evolution of synthetic aperture radar systems and their progression to the EOS SAR, *IEEE Transactions on Geoscience and Remote Sensing*, vol. 29 (6), pp. 962-985, Nov. 1991.
- [99] J.J. Lee, G/T and Noise Figure of Active Array Antenna, *IEEE Transactions on Antennas and Propagation*, vol. 41 (2), pp. 241-244, Feb. 1993.
- [100] R.A. Horn and C.R. Johnson, *Matrix Analysis*, Cambridge University Press, 1990.
- [101] G.H. Golub and C.F. Van Loan, *Matrix Computations*, The John Hopkins University Press, 1983.



## A History of Spaceborne SAR Missions

The following table lists various spaceborne SAR missions from the beginnings until 2007.

Name	Country	Organization	Date	Band	Link
Seasat	USA	NASA (JPL)	1978	L	<a href="http://southport.jpl.nasa.gov/scienceapps/seasat.html">http://southport.jpl.nasa.gov/scienceapps/seasat.html</a>
SIR-A	USA	NASA (JPL)	1981	L	<a href="http://southport.jpl.nasa.gov/scienceapps/sira.html">http://southport.jpl.nasa.gov/scienceapps/sira.html</a>
SIR-B	USA	NASA (JPL)	1984	L	<a href="http://southport.jpl.nasa.gov/scienceapps/sirb.html">http://southport.jpl.nasa.gov/scienceapps/sirb.html</a>
Magellan	USA	NASA (JPL)	1989	S	<a href="http://www2.jpl.nasa.gov/magellan/">http://www2.jpl.nasa.gov/magellan/</a>
ALMAZ-1	Russia		1991	S	<a href="http://www.russianspaceweb.com/almazt.html">http://www.russianspaceweb.com/almazt.html</a>
ERS-1	-	ESA	1991	C	<a href="http://earth.esa.int/ers/">http://earth.esa.int/ers/</a>
JERS-1	Japan	JAXA	1992	L	<a href="http://www.eorc.jaxa.jp/JERS-1">http://www.eorc.jaxa.jp/JERS-1</a>
SIR-C/X-SAR	USA Germany Italy	NASA (JPL) DLR ASI	1994	L, C, X	<a href="http://southport.jpl.nasa.gov/desc/SIRCdesc.html">http://southport.jpl.nasa.gov/desc/SIRCdesc.html</a>
Radarsat-1	Canada	CSA	1995	C	<a href="http://www.asc-csa.gc.ca/eng/satellites/radarsat1/">http://www.asc-csa.gc.ca/eng/satellites/radarsat1/</a>
ERS-2	-	ESA	1995	C	<a href="http://earth.esa.int/ers/">http://earth.esa.int/ers/</a>
Cassini-Huygens	USA - Italy	NASA (JPL) ESA ASI	1997	Ku	<a href="http://saturn.jpl.nasa.gov/spacecraft/inst-cassini-radar-details.cfm">http://saturn.jpl.nasa.gov/spacecraft/inst-cassini-radar-details.cfm</a> <a href="http://en.wikipedia.org/wiki/Cassini-Huygens">http://en.wikipedia.org/wiki/Cassini-Huygens</a>
SRTM	USA Germany Italy	NASA (JPL) DLR ASI	2000	C, X	<a href="http://www2.jpl.nasa.gov/srtm/">http://www2.jpl.nasa.gov/srtm/</a> <a href="http://www.dlr.de/srtm/">http://www.dlr.de/srtm/</a> <a href="http://srtm.det.unifi.it/index.htm">http://srtm.det.unifi.it/index.htm</a>
ENVISAT ASAR	-	ESA	2002	C	<a href="http://envisat.esa.int/">http://envisat.esa.int/</a>
ALOS PalSAR	Japan	JAXA	2006	L	<a href="http://www.jaxa.jp/projects/sat/alos/index_e.html">http://www.jaxa.jp/projects/sat/alos/index_e.html</a> <a href="http://www.eorc.jaxa.jp/ALOS/">http://www.eorc.jaxa.jp/ALOS/</a>
SAR-Lupe	Germany	German Armed Forces (Bundeswehr)	2006	X	<a href="http://www.dlr.de/desktopdefault.aspx/tabid-1/86_read-6647/">http://www.dlr.de/desktopdefault.aspx/tabid-1/86_read-6647/</a> <a href="http://www.ohb-system.de/Security/sarlupe.html">http://www.ohb-system.de/Security/sarlupe.html</a>
COSMO-Skymed	Italy	ASI	2007	X	<a href="http://www.telespazio.it/cosmo.html">http://www.telespazio.it/cosmo.html</a> <a href="http://www.e-geos.it/">http://www.e-geos.it/</a>
TerraSAR-X	Germany	DLR, Astrium	2007	X	<a href="http://www.dlr.de/TerraSAR-X/">http://www.dlr.de/TerraSAR-X/</a>
Radarsat-2	Canada	CSA	2007	C	<a href="http://www.radarsat2.info">http://www.radarsat2.info</a> <a href="http://www.asc-csa.gc.ca/eng/satellites/radarsat2/">http://www.asc-csa.gc.ca/eng/satellites/radarsat2/</a>

**Table 14. Overview of Spaceborne SAR Missions**

It should be noted that the list is not complete but includes the most important SAR sensors brought into orbit. A more detailed description of the early systems can be found in [98] which considers also airborne sensors. In addition, [69] gives a short description of most of the listed sensors. For explicit information, the reader is referred to these references and the given links.

## B Spherical SAR Geometry

This chapter derives the time varying distance between the sensor and a specific target for a monostatic spaceborne SAR geometry based on a spherical model for Earth as well as sensor trajectory. As illustrated below, the sensor moves with constant velocity  $v_s$  in a height  $h_s$  on a spherical flight track defined by  $p_s(t)$ .

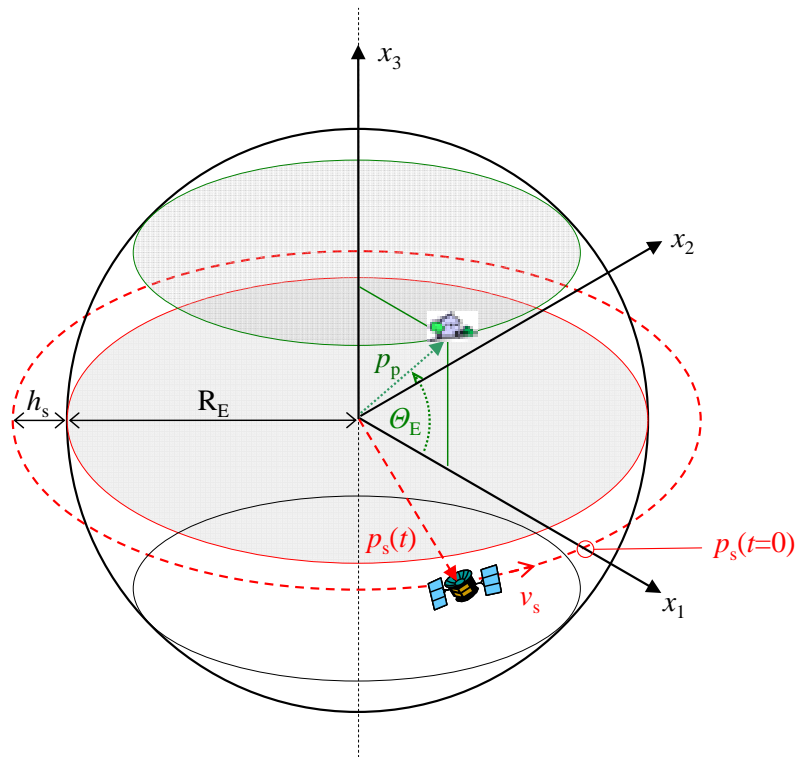


**Fig. 120.** SAR sensor on a spherical orbit defined by the trajectory  $p_s(t)$  (dashed red). The point-like target is given by the vector  $p_p$  (green). The coordinate system has its origin in the geocenter and is chosen such that the target is located in the  $x_1$ - $x_3$ -plane while the sensor travels in the  $x_1$ - $x_2$ -plane and passes the  $x_1$ -axis at  $t=0$ .

Without restriction of generality, the coordinate system is chosen according to Fig. 120, i.e. such that its origin is within the geocenter and the sensor trajectory is perpendicular to the  $x_3$ -

axis. Defining further  $x_2=0$  for time  $t=0$  for the sensor, its position is given by (153), where  $R_E$  is the mean Earth radius.

$$p_s(t) = \begin{pmatrix} (R_E + h_s) \cdot \cos\left(\frac{v_s \cdot t}{R_E + h_s}\right) \\ (R_E + h_s) \cdot \sin\left(\frac{v_s \cdot t}{R_E + h_s}\right) \\ 0 \end{pmatrix} \quad (153)$$

Assuming a target located in the  $x_1$ - $x_3$ -plane, the target position vector  $p_p$  is given as follows, where  $\Theta_E$  defines the angle between the straight lines from the geocenter to the target and the  $x_1$ -axis, respectively:

$$p_p = \begin{pmatrix} R_E \cdot \cos(\Theta_E) \\ 0 \\ R_E \cdot \sin(\Theta_E) \end{pmatrix} \quad (154)$$

Neglecting – accordingly to [68] – the rotation of the Earth yields the following expression for the slant range distance  $R(t)$  between the sensor and the target, which is defined in dependency on  $\Theta_E$ .

$$R(t) = |p_s(t) - p_p| = \sqrt{(R_E + h_s)^2 + R_E^2 - 2 \cdot (R_E + h_s) \cdot R_E \cdot \cos(\Theta_E) \cdot \cos\left(\frac{v_s}{R_E + h_s} \cdot t\right)} \quad (155)$$

The point of closest approach between sensor and target is given for  $x=0$ , i.e.  $t=0$ . Inserting into (155) then leads to the corresponding minimum slant range distance  $R_0$ :

$$R_0 = R(0) = \sqrt{(R_E + h_s)^2 + R_E^2 - 2 \cdot (R_E + h_s) \cdot R_E \cdot \cos(\Theta_E)} \quad (156)$$

Further, the following equation relates the angles  $\Theta_E$  and  $\Theta_i$ , as can be derived by simple geometric considerations or by applying the laws of cosine:

$$\cos(\Theta_E) = \frac{R_E + R_0 \cdot \cos(\Theta_i)}{R_E + h_s} \quad (157)$$

Inserting (157) into (156) and solving the resulting quadratic equation allows for the elimination of  $\Theta_E$  by replacing it by the incident angle  $\Theta_i$ . As a result,  $R_0$  is obtained in dependency on  $\Theta_i$  as shown below:

$$R_0 = R_E \left( \sqrt{\cos^2(\Theta_i) + 2 \frac{h_s}{R_E} + \frac{h_s^2}{R_E^2}} - \cos(\Theta_i) \right) \quad (158)$$

Equivalently, the time-varying slant range distance  $R(t)$  can be expressed depending on the local incident angle by insertion of (157) into (155).



$$R(t) = \sqrt{(\mathbf{R}_E + h_s)^2 + \mathbf{R}_E^2 - 2 \cdot \mathbf{R}_E \cdot (\mathbf{R}_E + R_0 \cdot \cos(\Theta_i)) \cdot \cos\left(\frac{v_s}{\mathbf{R}_E + h_s} \cdot t\right)} \quad (159)$$

In a further step,  $R_0$  as given in (158) is inserted in the above equation. After reforming it, one obtains the following expression for  $R(t)$ , only depending on system parameters and the Earth radius.

$$R(t) = \mathbf{R}_E \cdot \sqrt{\left(1 + \frac{h_s}{\mathbf{R}_E}\right)^2 + 1 - 2 \cdot \left(\sin^2(\Theta_i) + \cos(\Theta_i) \cdot \sqrt{\cos^2(\Theta_i) + 2 \frac{h_s}{\mathbf{R}_E} + \frac{h_s^2}{\mathbf{R}_E^2}}\right) \cdot \cos\left(\frac{v_s}{\mathbf{R}_E + h_s} \cdot t\right)} \quad (160)$$

In a further step, the relations for the slant range are simplified by quadratic approximation. This is achieved by applying a Taylor expansion of second order to (155), yielding the approximated signal path as follows:

$$R(t) \approx R_0 + \frac{\mathbf{R}_E \cdot \cos(\Theta_E) \cdot v_s^2}{2 \cdot R_0 \cdot (\mathbf{R}_E + h_s)} \cdot t^2 \quad (161)$$

In contrast to the flat-Earth approximation, the velocity of the antenna footprint on ground,  $v_g$ , is different from the sensor velocity  $v_s$  and has to be considered separately [67]. From (161),  $v_g$  can be derived as follows, thus ensuring the path approximation for spaceborne SAR systems with the well-known quadratic variation of the slant range distance between sensor and target according to (163).

$$v_g = \frac{\mathbf{R}_E \cdot \cos(\Theta_E)}{(\mathbf{R}_E + h_s)} \cdot v_s \quad (162)$$

$$R(t) \approx R_0 + \frac{v_g \cdot v_s}{2 \cdot R_0} \cdot t^2, \quad (163)$$

Again, the dependency on  $\Theta_E$  can be replaced by  $\Theta_i$  leading to the following expression for the footprint velocity:

$$v_g = \frac{\mathbf{R}_E \cdot (\mathbf{R}_E + R_0 \cdot \cos(\Theta_i))}{(\mathbf{R}_E + h_s)^2} \cdot v_s \quad (164)$$

By defining an equivalent velocity  $v_e$  in (165) and, introducing accordingly the equivalent azimuth dimension  $x_e(t) = v_e t$ , (163) can be reformed to (166):

$$v_e := \sqrt{v_s \cdot v_g} \quad (165)$$

$$R(t) \approx R_0 + \frac{v_e^2 \cdot t^2}{2 \cdot R_0} = R_0 + \frac{x_e(t)^2}{2 \cdot R_0} \quad (166)$$

The obtained result in (166) is identical to the description for the signal path in flat-Earth geometry. This implies that the spherical flight path can be approximated by a straight flight path  $R_{\text{straight}}(t)$ , if the “equivalent” geometry is used, i.e. a traveling velocity  $v_e$  is assumed and azimuth dimension is chosen accordingly.

$$R(t) \approx R_{\text{straight}}(t) = \sqrt{R_0^2 + v_e^2 \cdot t^2} = \sqrt{R_0^2 + x_e(t)^2} \quad (167)$$

Further considerations on the spaceborne geometry can be found in [69].

## C Quadratic Approximation of Range History

Recalling Appendix B, the results of (167) gives an approximation for the range history of a monostatic system in a spherical geometry. Based on this result, the present chapter extends the analysis of the range history to a multistatic configuration with a receive aperture separated by  $\Delta x$  from the transmitter. In the following, different approximations for the multistatic range history are derived and their validity is analyzed and confirmed.

Regarding separately the distance from the target to the transmitter,  $R_{\text{tx}}(t)$ , and back from the target to the receiver,  $R_{\text{rx}}(t)$ , the range history of a point target situated at  $x_e = 0$  on ground can be expressed by  $R_{\text{straight}}(t)$ :

$$R_{\text{straight}}(t) = R_{\text{tx}}(t) + R_{\text{rx}}(t) = \sqrt{R_0^2 + x_e(t)^2} + \sqrt{R_0^2 + (x_e(t) - \Delta x_e)^2} \quad (168)$$

In this context, it has to be noted that the time shift  $t_0$  introduced by a receiver separated with respect to the flight track by  $\Delta x = v_s \cdot t_0$  remains, of course, the same. Nevertheless in the equivalent geometry, the corresponding distance  $\Delta x$  translates into an equivalent shift  $\Delta x_e$  which is given as follows:

$$\Delta x_e = \sqrt{\frac{v_g}{v_s}} \cdot \Delta x \quad (169)$$

As a preliminary step for the approximation of (168), the first and second order derivatives for the transmit paths  $R_{\text{tx}}(t)$  and the receive path  $R_{\text{rx}}(t)$  are determined, respectively.

$$\frac{\partial}{\partial t} R_{\text{tx}}(t) = \frac{x_e(t)}{\sqrt{R_0^2 + x_e(t)^2}} \quad (170)$$

$$\frac{\partial^2}{\partial t^2} R_{\text{tx}}(t) = \frac{R_0^2}{\left(R_0^2 + x_e(t)^2\right)^{\frac{3}{2}}} \quad (171)$$

$$\frac{\partial}{\partial t} R_{\text{rx}}(t) = \frac{x_e(t) - \Delta x_e}{\sqrt{R_0^2 + (x_e(t) - \Delta x_e)^2}} \quad (172)$$

$$\frac{\partial^2}{\partial t^2} R_{\text{rx}}(t) = \frac{R_0^2}{\left(R_0^2 + (x_e(t) - \Delta x_e)^2\right)^{\frac{3}{2}}} \quad (173)$$

The above results then allow for deriving different approximations for the range history in a multistatic system. Firstly,  $R_{\text{straight}}(t)$  is expressed by the sum of the Taylor expansions of second order for  $R_{\text{tx}}(t)$  and  $R_{\text{rx}}(t)$ , respectively. This yields  $R_{\text{qa},1}(t)$  which consists of the well-known quadratic part around the effective phase center  $\Delta x_e/2$  and a constant slant range deviating by  $\Delta x_e^2/(4 \cdot R_0)$  from the monostatic two-way distance  $2 \cdot R_0$ .

$$R_{\text{straight}}(t) \approx R_{\text{qa},1}(t) = 2 \cdot R_0 + \frac{\Delta x_e^2}{4 \cdot R_0} + \frac{\left(x_e(t) - \frac{\Delta x_e}{2}\right)^2}{R_0} \quad (174)$$

A second approach describes the complete sum of receive and transmit path by a Taylor series of second order. As a result,  $R_{\text{qa},2}(t)$  is obtained, which is very similar to  $R_{\text{qa},1}(t)$  with respect to a constant slant range and a shifted quadratic component. But in contrast to (174), this result provides a slightly better approximation of the increased minimum slant range, and takes into account the changing curvature of the range history.<sup>30</sup>

$$R_{\text{straight}}(t) \approx R_{\text{qa},2}(t) = 2 \cdot \sqrt{R_0^2 + \frac{\Delta x_e^2}{4}} + \frac{R_0^2}{\left(R_0^2 + \frac{\Delta x_e^2}{4}\right)^{\frac{3}{2}}} \cdot \left(x_e(t) - \frac{\Delta x_e}{2}\right)^2 \quad (175)$$

In a next step, the validity of the above derived expressions will be demonstrated by selected system examples. For this, one single-platform and one multi-satellite system will be investigated, both for operation in X-band ( $\lambda = 0.031$  m) and L-band ( $\lambda = 0.25$  m). For the single-platform system, a maximum relative spacing of the receive apertures of 10 m is assumed, while the sparse array constellation is characterized by a maximum separation of 500 m. The maximum relative spacing refers to the largest offset of a receiver with respect to a reference receiver lo-

<sup>30</sup>In this context, it should be noted that the relative slant range offset assumes all apertures on the same track. Hence, this provides an accurate estimation for multi-platform constellations, but might cause small errors for single-platform systems on a spherical orbit. This is due to the fact that all apertures are located in a straight line, thus introducing for the outer apertures a small offset from the orbit of the – centered – transmit aperture. For the range of closest approach, this directly results in a difference governed by the “original” offset  $\Delta x^2/(4 \cdot R_0)$  as can be easily derived by basic geometric considerations. Nevertheless, the slant range offsets in single-platform systems can be neglected in any case, thus always leading to a valid approximation. Consequently this issue will not be investigated more extensively within the frame of this work.

cated at the same position as the transmitter. Further, an azimuth resolution of 1 m is considered, and as a consequence the synthetic aperture length is calculated for an antenna of 2 m length. Further system parameters are summarized in the following Table 15.

Parameter	Symbol	Value(s)	
Carrier wavelength	$\lambda$	3.1 cm	25 cm
Maximum relative receiver spacing	$\Delta x$	10 m	500 m
Geometric resolution in azimuth	$\delta_{az}$	1 m	
Slant range	$R_0$	$\sim 735$ km	
Sensor velocity	$v_s$	$\sim 7560$ m/s	
Footprint velocity	$v_g$	$\sim 6900$ m/s	

**Table 15. System parameters.**

As a reference, the exact range history for a spherical orbit is determined. Depending on the different extensions of the azimuth antenna footprint in X-band and L-band, respectively, the two subsequent results are obtained. Note that in order to focus on the relative range characteristic, the curves show only the relative variation with respect to the minimum slant range distance.

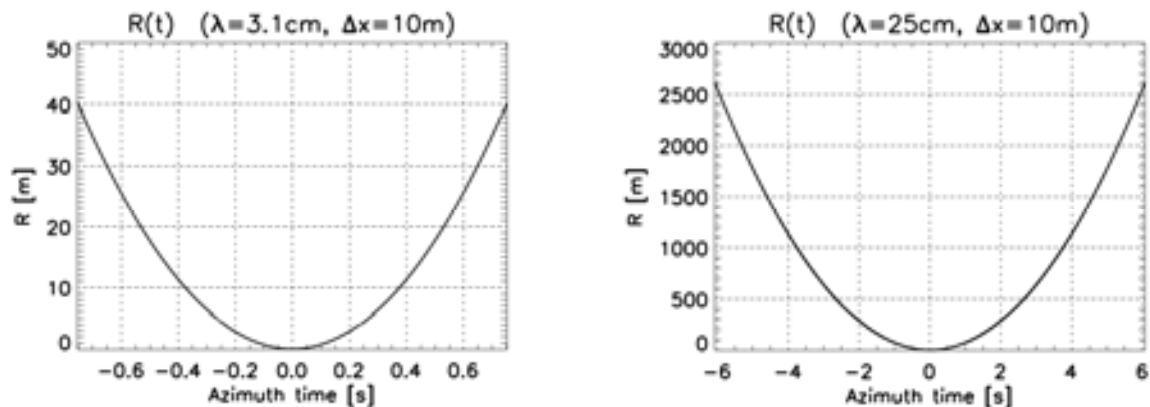


**Fig. 121. Range history  $R(t)$  for spherical flight path for X-band (left) and L-band (right).**

Next, the exact solution for the range history is compared to three following approximations. Firstly, the straight flight path approximation  $R_{\text{straight}}(t)$  according to (168) is applied, under consideration of the equivalent velocity  $v_e$  (cf. (165)) and the scaled receiver spacing  $\Delta x_e$  as defined in (169). Secondly, the Taylor expansion for the sum of the paths is analyzed, i.e.  $R_{\text{qa},2}(t)$  characterizes the range history. Last but not least, the estimation of the range history by the sum of separate Taylor expansions for transmit and receive path given by  $R_{\text{qa},1}(t)$  in (174) is evaluated.

The deviation of the respective approximations from the exact range history can be seen in the subsequent plots, where each of the figures is related to one of the specific systems.

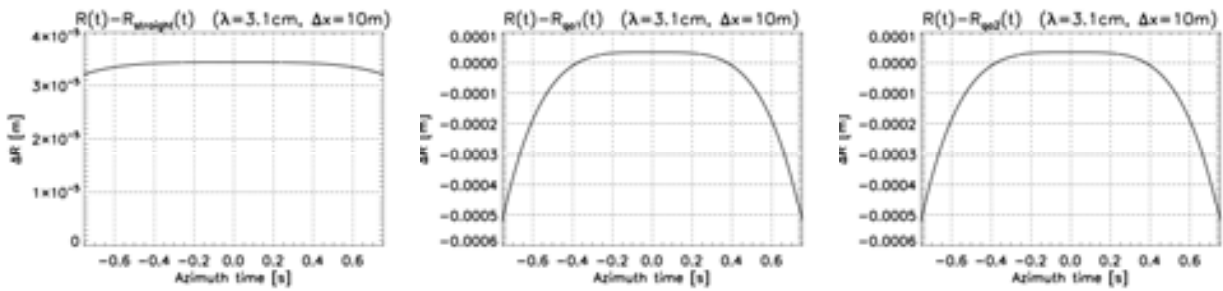


Fig. 122. Accuracy of different range history approximations in a single-platform X-band system.

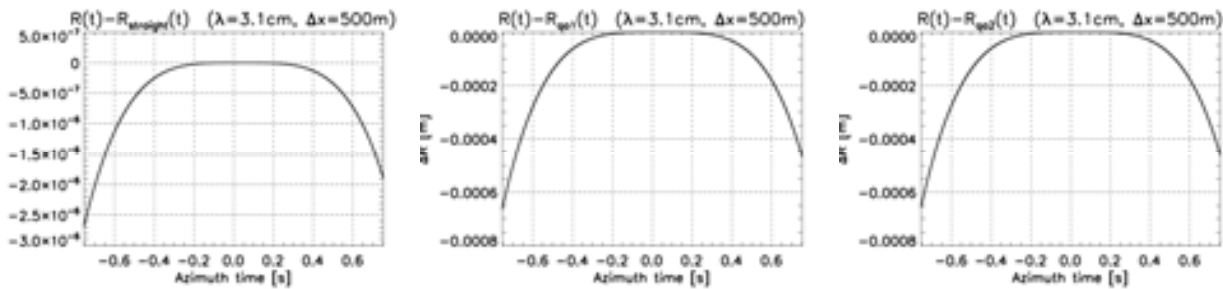


Fig. 123. Accuracy of different range history approximations in a multi-platform X-band system.

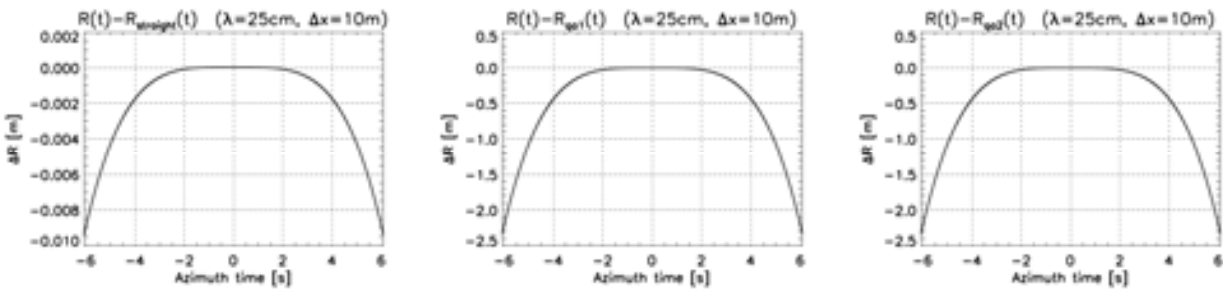


Fig. 124. Accuracy of different range history approximations in a single-platform L-band system.

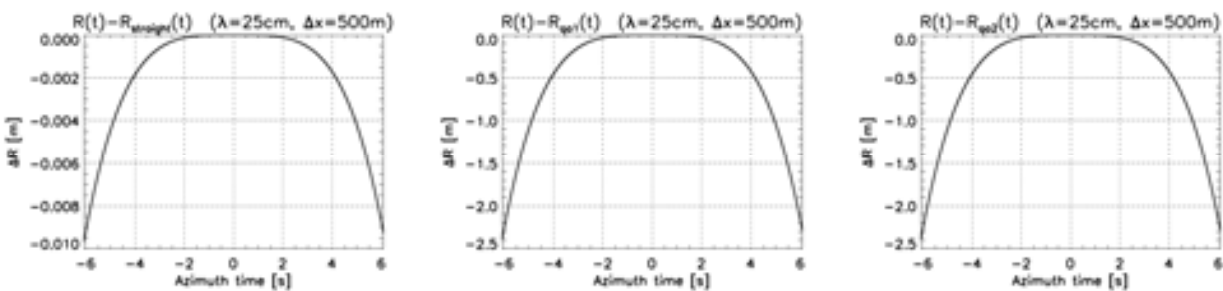
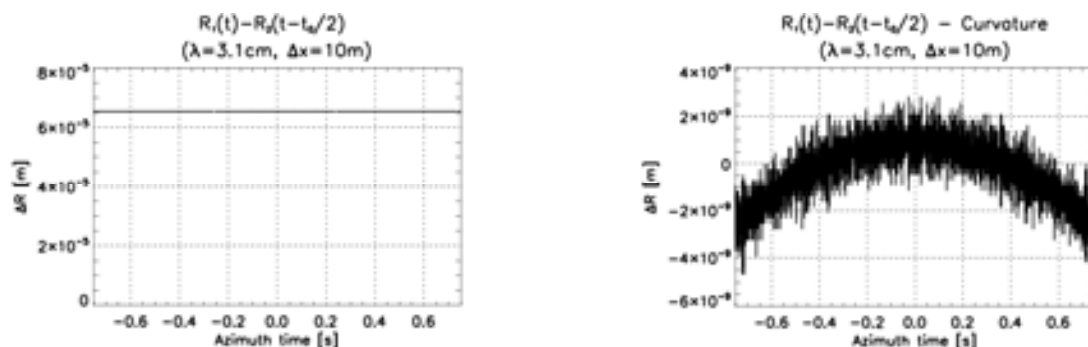


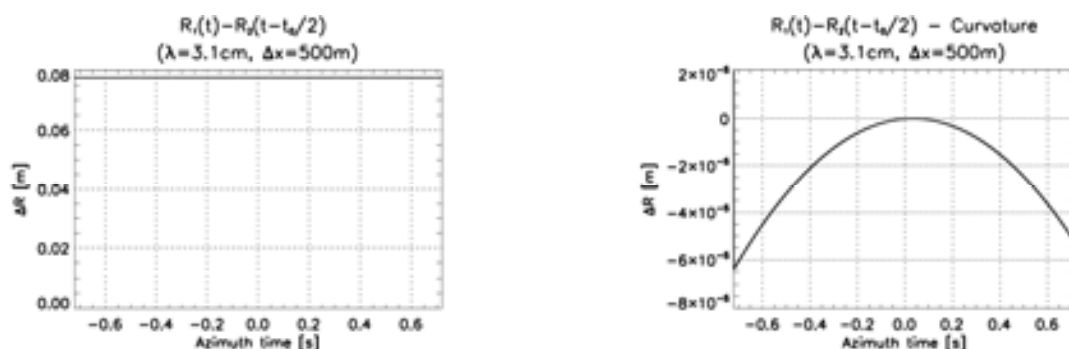
Fig. 125. Accuracy of different range history approximations in a multi-platform L-band system.

Fig. 122 to Fig. 125 allow for the conclusion that all approximations are valid in both X-band systems. Further, the approximation by a straight flight path is accurate and can be applied to both systems as well as both carrier wavelengths. Finally, both quadratic approximations in L-band systems yield only insufficient results, as the error increases with increasing synthetic aperture length which is typically large for L-band operation.

In any case, the approximations clearly show that the important relation of receiver spacing  $\Delta x$  and effective phase center positioned halfway at  $\Delta x/2$  is valid. This can be demonstrated by a comparison of a monostatic to a multistatic range history, which is shifted by  $t_0 = \Delta x/v_s$  according to the effective phase center definition. The results for the four different systems as discussed above are given in the subsequent plots. Thereby, the absolute offset between the two characteristics is shown (Fig. 126 to Fig. 129, left), as well as the remaining difference after compensating for the different minimum slant ranges, i.e. a constant value (Fig. 126 to Fig. 129, right).



**Fig. 126. Offset of shifted multistatic range history from monostatic reference in a single-platform X-band system (left). Right shows the remaining difference in curvature after correction of the respective constant slant range offsets.**



**Fig. 127. Offset of shifted multistatic range history from monostatic reference in a multi-platform X-band system (left). Right shows the remaining difference in curvature after correction of the respective constant slant range offsets.**

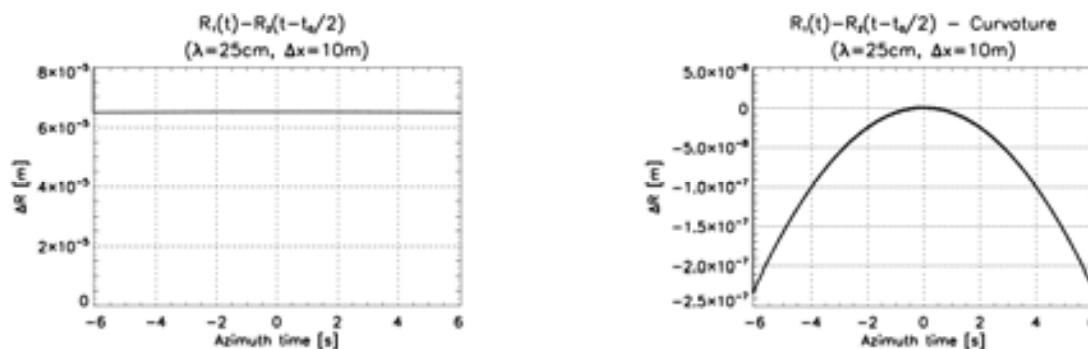


**Fig. 128. Offset of shifted multistatic range history from monostatic reference in a single-platform L-band system (left). Right shows the remaining difference in curvature after correction of the respective constant slant range offsets.**

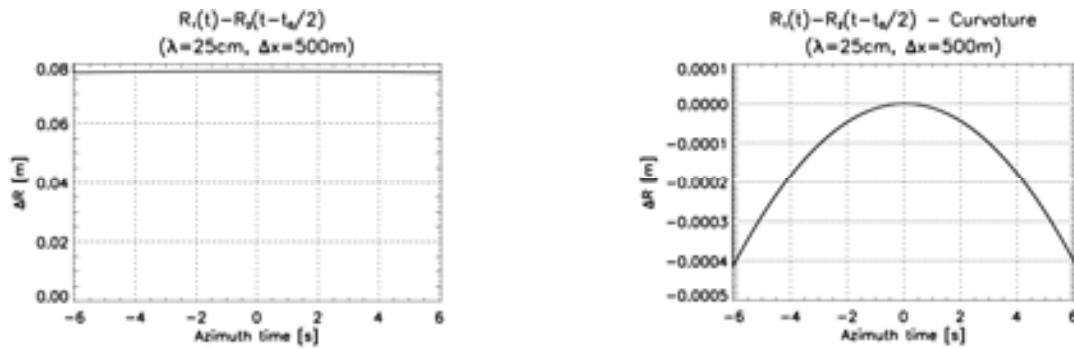


**Fig. 129. Offset of shifted multistatic range history from monostatic reference in a multi-platform L-band system (left). Right shows the remaining difference in curvature after correction of the respective constant slant range offsets.**

The simulation results allow for the conclusion that in any of the investigated systems the effective phase center definition is a valid approximation. In addition, the differences in range curvature can be neglected. Finally, the constant slant range offset is negligible only in the single-platform systems, but requires consideration in the multi-platform constellations. In any case, this offset can be estimated by the constant phase term of (174) and (175). Hence, as a final step the validity of the estimation is investigated by evaluating the expressions (174) and (175), and comparing them to the simulated values. Each approach yields a value of 7.76 cm, showing a very good coincidence, thus ensuring a valid approximation of the relative slant range offset. This is backed by the results in Fig. 122 to Fig. 125, which also demonstrated accurate estimation.

As a conclusion, the combination of the effective phase center definition and a constant slant range shift allows for relating the multistatic range history directly to a monostatic one.



## D Analogy of Null-Steering and Multi-Channel Reconstruction

A linear array of  $N$  receiving apertures is considered, where the distance of aperture  $j$  to aperture 1 is denoted by  $\Delta x_j$  and the look direction is designated by  $\theta$  (cf. Fig. 130). By definition  $\Delta x_1 = 0$  is set. After receiving the incident signal  $s_{\text{in}}(\theta)$ , an individual complex weighting coefficient  $a_j$  is applied to each of the channels' signals  $s_j(\theta)$ . Finally, these signals are combined coherently, which is indicated by the “ $\Sigma$ ”, yielding the output signal  $s(\theta)$ .

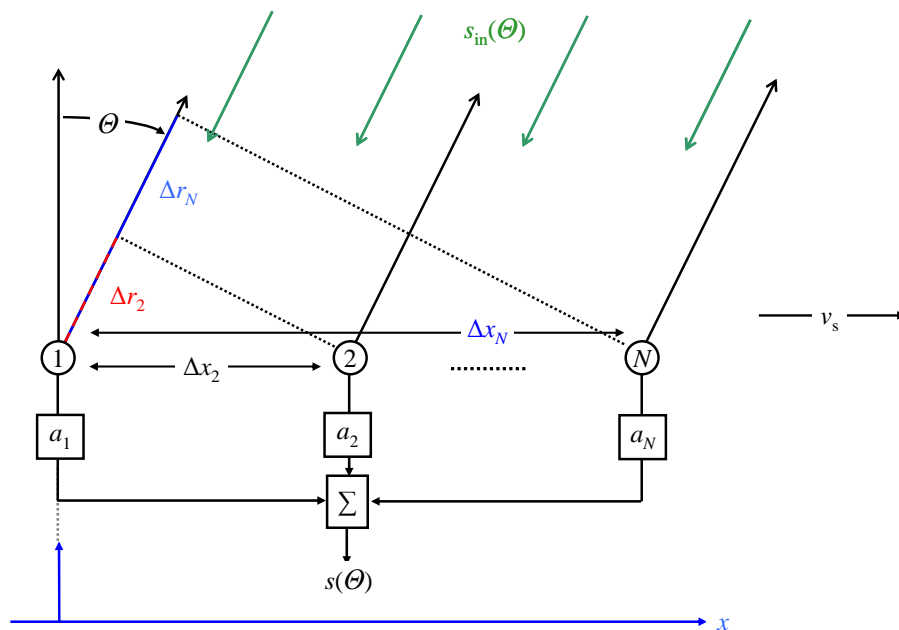


**Fig. 130.** Incident signal  $s_{\text{in}}(\theta)$ , arriving under angle  $\theta$  on linear array of  $N$  receiving apertures. After reception, each receiver's signal  $s_j(\theta)$  is weighted by  $a_j$  and summed up yielding the output signal  $s(\theta)$ .

Applying the quasi-parallel approximation, the well-known array manifold vector  $\underline{v}$  that characterizes the signal at each receiver  $j$  with respect to the signal at receiver 1 looks as follows[75]:

$$\underline{v}(\Theta) = \left[ 1, \exp\left[-j \cdot \frac{2 \cdot \pi}{\lambda} \cdot \Delta x_2 \cdot \sin \Theta\right], \dots, \exp\left[-j \cdot \frac{2 \cdot \pi}{\lambda} \cdot \Delta x_N \cdot \sin \Theta\right] \right]^T = [v_1, \dots, v_j, \dots, v_N]^T \quad (176)$$

Taking into account the weighting coefficients given by the vector  $\underline{a} = [a_1, \dots, a_N]^T$  and the subsequent coherent summation, the resulting output signal  $s(\Theta)$  is determined by (177), where  $s_1(\Theta)$  represents the signal at receiver 1.

$$s(\Theta) = \sum_{j=1}^N s_j(\Theta) \cdot a_j = s_1(\Theta) \cdot \sum_{j=1}^N (v_j \cdot a_j) = s_1(\Theta) \cdot \underline{v}^T(\Theta) \cdot \underline{a} \quad (177)$$

In a next step,  $N$  output signals are considered that are obtained from input signals arriving under  $N$  different angles  $\Theta_m$ ,  $m \in \{1, 2, \dots, N\}$ . The respective output signals are given by the vector  $\underline{s}$  that can be expressed by the matrix-vector operation of (178), where  $\mathbf{V}$  represents the manifold vectors for the different angles as given in (179).

$$\underline{s} = s_1(\Theta) \cdot \mathbf{V} \cdot \underline{a} \quad (178)$$

$$\mathbf{V} = \begin{bmatrix} v_1(\Theta_1) & \dots & v_N(\Theta_1) \\ \dots & v_j(\Theta_m) & \dots \\ v_1(\Theta_N) & \dots & v_N(\Theta_N) \end{bmatrix} \quad (179)$$

The weighting coefficients which are necessary to steer nulls in  $N-1$  directions  $\Theta_m$  in order to “extract” the signal from the  $N$ -th direction are then determined by the inversion of  $\mathbf{V}$ . One obtains a matrix  $\mathbf{A} = \mathbf{V}^{-1}$  that contains in its  $k$ -th column the respective weights to steer the nulls in the pattern to all directions  $\Theta_m$ ,  $m \neq k$ .

In a next step, consider a frequency  $f_1$  and its  $N-1$  ambiguous frequencies within the system azimuth bandwidth  $N \cdot PRF$ , that are separated by integer multiples of  $PRF$  (cf. (180)). Using the relation between angle  $\Theta$  and Doppler frequency  $f$  of (181), the variable  $\Theta_m$  in (179) can be replaced by the respective  $f_m$ , yielding  $\mathbf{V}(f)$  in (182). Then the matrix  $\mathbf{A}(f) = \mathbf{V}^{-1}(f)$  contains in its  $k$ -th column the respective weights to steer the nulls in the pattern to all ambiguous frequencies  $f_m$ ,  $m \neq k$ , while recovering  $f_k$ . Hence, calculating and applying  $\mathbf{A}(f)$  for all  $f_1$  within the interval  $I_1 = [-N \cdot PRF/2, -(N-2) \cdot PRF/2]$  and the respective ambiguous Doppler frequency sets in (180) allows for unambiguously recovering the original spectrum of bandwidth  $N \cdot PRF$ .

$$f_1 + [0, PRF, \dots, (N-1) \cdot PRF] = [f_1, \dots, f_m, \dots, f_N] \\ \text{with } f_1 \in \left[ -\frac{N \cdot PRF}{2}, -\frac{(N-2) \cdot PRF}{2} \right] \quad (180)$$

$$f(\Theta) = \frac{2 \cdot v_s}{\lambda} \cdot \sin(\Theta) \quad (181)$$

$$\mathbf{V}(f_1) = \begin{bmatrix} \exp\left[-j \cdot \frac{\pi \cdot \Delta x_1}{v_s} \cdot f_1\right] & \dots & \exp\left[-j \cdot \frac{\pi \cdot \Delta x_N}{v_s} \cdot f_1\right] \\ \dots & \exp\left[-j \cdot \frac{\pi \cdot \Delta x_j}{v_s} \cdot (f_1 + (m-1) \cdot PRF)\right] & \dots \\ \exp\left[-j \cdot \frac{\pi \cdot \Delta x_1}{v_s} \cdot (f_1 + (N-1) \cdot PRF)\right] & \dots & \exp\left[-j \cdot \frac{\pi \cdot \Delta x_N}{v_s} \cdot (f_1 + (N-1) \cdot PRF)\right] \end{bmatrix} \quad (182)$$

Finally, the matrix  $\mathbf{V}(f)$  shown above is compared to the system matrix  $\mathbf{H}(f)$  derived in Chapter 5. It is observed that under the assumed approximations  $\mathbf{V}(f)$  is nearly identical to  $\mathbf{H}(f)$ . The only difference is the constant phase term relating the bi- and monostatic sample position, that is accounted for in  $\mathbf{H}(f)$  while it is neglected in  $\mathbf{V}(f)$ . Hence the multi-channel reconstruction algorithm can be regarded as an extension of the classical null-steering approach that also accounts for large receiver spacing. In the case of a single-platform system, the distances between the receiving apertures are small, and consequently the resulting phase differences are negligible.



## E SNR in Multi- and Mono-Aperture Systems

The present chapter gives some considerations on the *SNR* value that is obtained in different multi- and mono-aperture scenarios.

Firstly, the **average transmit power**  $p_{\text{tx,av}}$  is considered. It is defined by the applied  $PRF_{\text{tx}}$  and the pulse length  $\tau$  according to (183). As  $\tau$  is determined by the inverse duty cycle which is assumed to be constant,  $p_{\text{tx,av}}$  remains constant if the transmit antenna is the same.

$$p_{\text{tx,av}} \propto PRF_{\text{tx}} \cdot \tau = \text{const.} \quad (183)$$

Then, the **power of the received samples** in channel  $j$  is taken into account in order to determine the *SNR*. The samples are given by the signals  $s_j(t)$  and the respective additive noise components  $n_j(t)$ . Further, a lossless *LNA*, i.e.  $F = 1$ , is assumed for the moment as well as constant receiver noise power  $p_{\text{n},j}$  independently of the channel, i.e.:

$$\text{E} \left[ |n_j(t)|^2 \right] = p_{\text{n},j} =: p_{\text{n}} \quad (184)$$

As a first system, a multi-channel configuration with exemplarily  $N=2$  channels is investigated. Fig. 131 on the left shows the system, respective signal and noise components and the resulting samples in azimuth dimension  $x$  for two (or more) subsequent pulses. As can be observed, the samples of the different channels are interleaved yielding a sampling rate of  $N \cdot PRF_{\text{tx}}$ . Note that the special case of uniform sampling is chosen as this represents the optimum scenario for the type of multi-channel systems which are primarily investigated in this work. If non-uniform sampling occurs, a possible degradation of the *SNR* described by  $\Phi_{\text{bf}}$  according to Section 5.7 has to be included in the following considerations. For the optimum  $PRF$ , the *SNR* of a single sample is denoted by  $SNR_{\text{el}}$  which is determined by the receiver noise power and the signal power transmitted and received by a single aperture.

Compared to a mono-aperture system of same aperture dimensions and twice (in general  $N$  times) the  $PRF_{\text{tx}}$  as in the first example, the same effective sampling on receive is obtained as shown in Fig. 131 on the right. Nevertheless, the *SNR* per sample is worsened by 3 dB (in general  $10 \cdot \log(N)$  dB), as the received transmit pulses show only half ( $1/N$ -th) the power with respect to the multi-channel example due to the reduced  $PRF$ . In other words, the gain of the multi-channel system with respect to mono-aperture reception results from the decreased  $PRF$  on

transmit that entails increased transmit power per pulse. A second “equivalent” system could be given by the system of Fig. 131 on the right but operated with the same  $PRF$  as the multi-channel system. This means that the transmit power per pulse and consequently the  $SNR$  per sample is equal to the multi-channel case, but only half ( $1/N$ -th) of the samples are received per time.

So, in any case, the energy gathered by the multi-channel system is increased by  $10 \cdot \log(N)$  dB compared to the mono-aperture system. In simple words, this corresponds to the increased antenna length when combining the  $N$  sub-apertures.

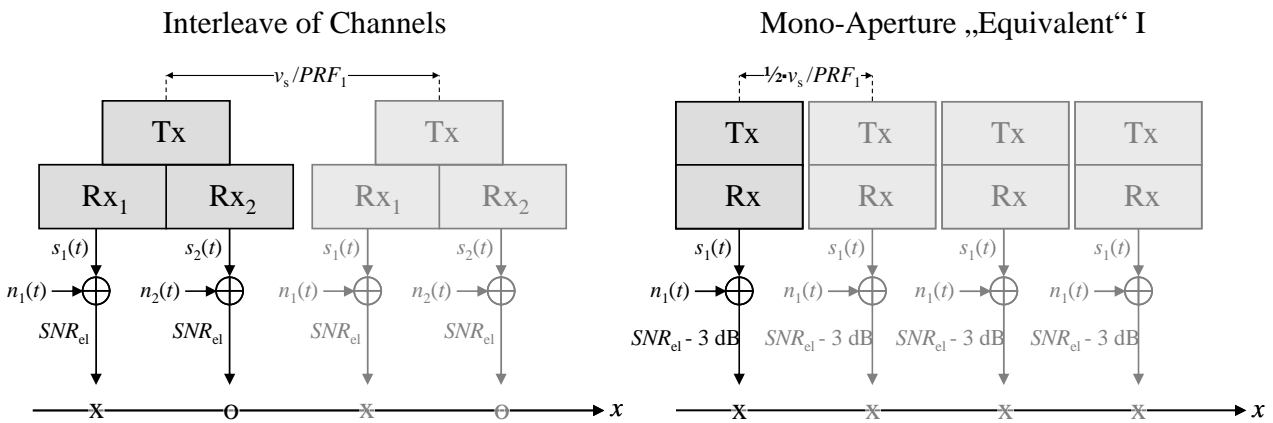


**Fig. 131. SNR of multi-channel system where samples are interleaved (left) and “equivalent” mono-aperture scenario, where the SNR per sample is worsened by 3 dB (right).**

Secondly, a multi-channel system is investigated, where the signals of the channels are summed as depicted in Fig. 132 on the left. In this case, the two digitized signals  $s_1(t)$  and  $s_2(t)$  are summed coherently resulting – in boresight – in twice the amplitude and consequently four times the signal power of a single channel.<sup>31</sup> The noise components  $n_1(t)$  and  $n_2(t)$  add incoherently yielding a noise power of twice the value of a single channel. Compared to the above scenario in Fig. 131 on the left, only half the samples per time are obtained but with twice the  $SNR$  per sample. This means that – again considered for boresight – the  $SNR$  per time remains constant. The respective equivalent mono-aperture system is shown on the right. It consists of a single receive aperture with the same size as the complete receiving antenna in the multi-channel case.

<sup>31</sup>Note that an analog interpretation of the summation would result in twice the signal power and constant noise power and consequently yield a  $SNR$  improved by 3 dB. This means that the  $SNR$  remains constant, independently of a digital or analog summation. For the investigation of the noise figure in analog beamforming networks, refer to [99]. Furthermore, if not only the peak value in boresight is considered, additionally one has to take into account the narrowed antenna pattern due to the doubled antenna dimension compared to the scenario where the samples of each aperture are interleaved.

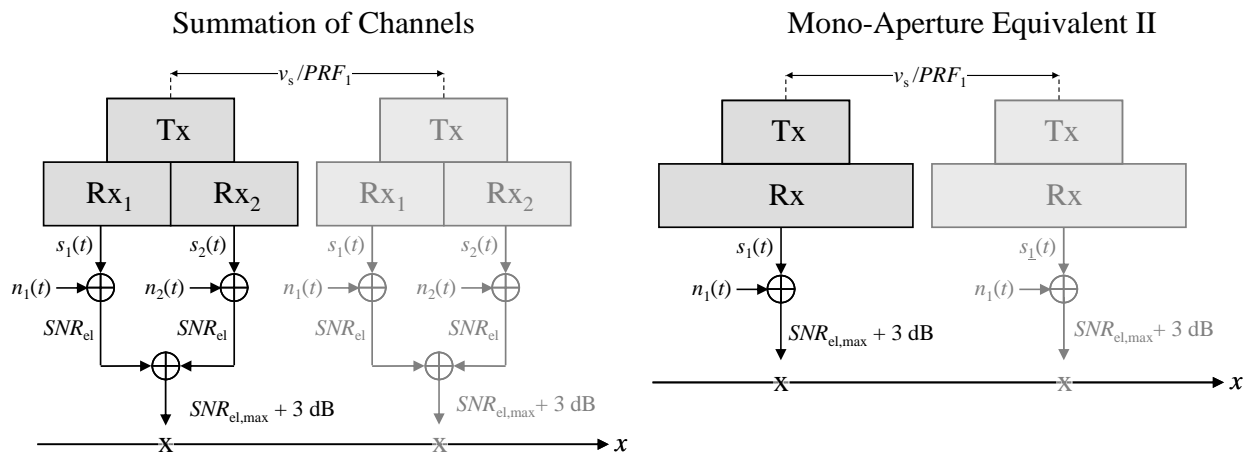


**Fig. 132.** SNR of a multi-channel system where samples are summed (left) and equivalent mono-aperture system of same SNR (right).

As a final remark, it should be noted that the effective sampling rate has to be considered when taking into account the focusing of the signals. Different sampling rates affect the noise power due to oversampling as well as the compression gain, i.e. the peak power obtained for point-like targets, which depends on the number of samples.





## F SNR Scaling – Further Interpretations

In Section 5.7 the impact of the multi-channel processing network on the *SNR* was discussed and (83) was derived which quantifies the scaling of the *SNR* induced by the applied processing algorithm. In order to complete this issue, two further ways of calculating the *SNR* scaling are presented subsequently.

### Eigenvalue Calculation

As given in (42), the filter have a constant magnitude on the respective sub-bands  $I_m$ , i.e.  $|P_{jm}(f)| = |P_{jm}|$ . This means that the necessity of calculating the mean value of  $|P_j(f)|^2$  is left out as it can be effectuated by summing the values of  $|P_{jm}|$  for all sub-bands, i.e.:

$$\sum_{j=1}^N \mathbb{E} \left[ |P_j(f)|^2 \right] = \sum_{j=1}^N \sum_{m=1}^N |P_{jm}|^2 \quad (185)$$

From a matrix theoretical point of view, (185) corresponds to the Hilbert-Schmidt norm [100] of a matrix  $\mathbf{P}_0(f_0)$  that is defined by specific values of  $\mathbf{P}(f)$  that are selected according to (186), where the frequency  $f_0$  can be chosen arbitrarily from the interval  $[0, PRF]$ .

$$\mathbf{P}_0(f_0) = \begin{bmatrix} P_{11}(f_0) & P_{12}(f_0 + PRF) & \dots & P_{N1}(f_0 + (N-1) \cdot PRF) \\ \dots & \dots & \dots & \dots \\ P_{1N}(f_0) & \dots & \dots & P_{NN}(f_0 + (N-1) \cdot PRF) \end{bmatrix} ; \mathbf{P}_0(f_0) \in \mathbb{C}^{N \times N} \quad (186)$$

Further, according to linear algebra [101], the Hilbert-Schmidt norm of  $\mathbf{P}_0(f_0)$  is equal to the trace of the matrix  $\mathbf{P}_0(f_0) \cdot \mathbf{P}_0^H(f_0)$ , where superscript  $\mathbf{H}$  indicates the conjugate transpose matrix. In a further step, that trace can be expressed by the sum of the eigenvalues  $\lambda_j(f_0)$  of the matrix  $\mathbf{P}_0(f_0) \cdot \mathbf{P}_0^H(f_0)$ . This means that the scaling of the receiver noise power in the data as quantified by (83) can be equivalently expressed by the summed eigenvalues  $\lambda_j$  and one obtains an equal representation of the *SNR* scaling factor given by (187). Note that for a given *PRF* the sum over all eigenvalues is independent of  $f_0$  and thus the *SNR* scaling factor  $\Phi_{\text{bf}}$  is not frequency dependent.

$$\Phi_{\text{bf}} = N \cdot \sum_{j=1}^N \lambda_j(f_0) \quad (187)$$

## Harmonic Functions

In 2006, [80] has shown that for the considered system and the approximations proposed in [36] the scaling of the noise by the reconstruction network as given in (82) can be expressed explicitly by harmonic functions as follows in (188), where the sample positions of receivers  $p$  and  $q$  are described by their respective sample times  $t_p$  and  $t_q$  normalized by  $1/PRF$ . Basically, the numerator gives the deviation of the samples from the optimum regular spaced positions given by  $2\pi \cdot n/N$ , while the denominator takes the mutual distances between the receivers into account.

$$\sum_{j=1}^N \mathbb{E} \left[ |P_j(f)|^2 \right] = \frac{1}{N^2} \sum_{p=1}^N \frac{\sum_{n=0}^{N-1} \prod_{\substack{q=1 \\ q \neq p}}^N \left( 1 - \cos \left( 2\pi \cdot \frac{n}{N} - 2\pi \cdot t_q \cdot PRF \right) \right)}{\prod_{\substack{q=1 \\ q \neq p}}^N \left( 1 - \cos \left( 2\pi \cdot PRF \cdot (t_p - t_q) \right) \right)} \quad (188)$$

# Curriculum Vitae

## Personal data

Name: Nicolas Gebert  
Date of birth: August 30<sup>th</sup>, 1978  
Place of birth: Munich, Germany  
Nationality: German

## Education and Professional Experience

**2009:** **Degree: Dr.-Ing.** (Doctorate)  
Fakultät für Elektrotechnik und Informationstechnik  
Universität Karlsruhe (TH), Karlsruhe, Germany

**Since 2003:** **PhD student / Researcher** at the Microwaves and Radar Institute  
German Aerospace Center (DLR), Oberpfaffenhofen, Germany  
**Field of Interest:** Multi-Channel Synthetic Aperture Radar (SAR) Systems, Azimuth Signal Processing, Digital Beamforming for SAR, High-Resolution Wide-Swath SAR Imaging

**1998-2003:** **Degree: Dipl.-Ing.** (Diploma)  
Graduate Studies With Focus on Electronics and Signal Processing  
Electrical Engineering and Information Technology  
Technische Universität München, Munich, Germany

**2001-2002:** **Semester Abroad**, Graduate Studies  
Ecole Nationale Supérieure de l'Aéronautique et de l'Espace (SUPAERO)  
Toulouse, France



### Corrigenda

This chapters summarizes corrections to *DLR Forschungsbericht 2009-13, "Multi-Channel Azimuth Processing for High-Resolution Wide-Swath SAR Imaging"*. It did not form part of the original Dissertation/Forschungsbericht. The dates when the respective corrections were added are indicated in the headings.

#### **5.6 Residual Reconstruction Error and Azimuth Ambiguities: *AASR<sub>N</sub>* (22 Apr 2013)**

Page 59, equation (69)

Summation of  $e_k(f)$  for all  $k>0$  leads to the correct complex spectrum  $e_\Sigma(f)$  for  $k>0$ . However, the factor of 2 in equation (69) is not the correct way to account for both signs of  $k$ .

As an auxiliary step, in order to ensure a compact notation for the corrected (69), the notation of (68) is modified such that the full index range of  $m$  is considered. As a result, one obtains (C.68), which is not only valid for  $k>0$ , but for both signs of  $k$ . Note that the results of (68) and (C.68) are identical for  $k>0$ .

$$e_k(f) = \sum_{j=1}^N e_{k,j}(f) = U_k(f) \cdot \sum_{m=1}^N \sum_{j=1}^N H_{jk}(f) \cdot P_{jm}(f) \quad (\text{C.68})$$

With  $e_k(f)$  as above, (69) should read:

$$e_\Sigma(f) = \sum_{\substack{k=-\infty \\ k \neq 0}}^{\infty} e_k(f) = \sum_{\substack{k=-\infty \\ k \neq 0}}^{\infty} \left( U_k(f) \cdot \sum_{m=1}^N \sum_{j=1}^N H_{jk}(f) \cdot P_{jm}(f) \right) \quad (\text{C.69})$$

Notably, this does not affect the presented results in Chapters 7.

### 8.7.2 Phase Center Adaptation (22 Apr 2013)

Page 120, figure 90.

Figures 89 and 90 were duplicated.

Figure 90 should be as depicted below.

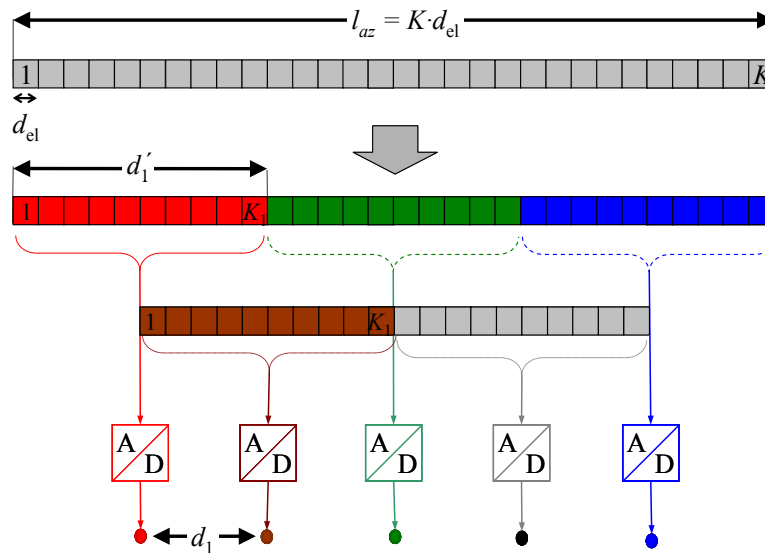


**Fig. 90. System with pre-processing network. Multiple use of certain elements yields mutually overlapping sub-apertures of increased length  $d'_1$ , but decreased phase center spacing  $d_1$ .**

**8.7.5 Residual Reconstruction Error and Azimuth Ambiguities:  $AASR_N$  (22 Apr 2013)**

Page 125, equations (127) and (130)

Equivalently to the corrections applicable to Chapter 5.6 (see first page of Corrigendum), the factor of two does not apply to the complex ambiguous spectrum, but to the power of it. Accordingly, (127) should be modified to read as follows:

$$p_{a,c} = 2 \cdot E \left[ \left| G \cdot \sum_{k=1}^{\infty} e_{c,k}(f) \right|^2 \right] \quad (\text{C.127})$$

Equivalently,  $p_{a,c, B_D}$  in (130) needs to be modified as follows:

$$p_{a,c, B_D} = 2 \cdot E \left[ \left| G \cdot \sum_{k=1}^{\infty} e_{c,k, B_D}(f) \right|^2 \right]$$

## 9.4 Azimuth Ambiguities in Burst Mode Operation: $AASR_{N,B}$ (22 Apr 2013)

Page 144, equation (148)

Equivalently to the corrections applicable to Chapter 5.6, the factor of two is not appropriate to represent the complex ambiguous spectrum, and (148) needs to be modified, in order to account for both signs of  $k$ .

$$p_{a,B_{s,i}} = E \left[ \left| \sum_{\substack{k=-\infty \\ k \neq 0}}^{\infty} \left( U_k(f) \cdot \sum_{m=1}^N \sum_{j=1}^N H_{jk}(f) \cdot P_{jm}(f) \right) \cdot W(B_{s,i}) \right|^2 \right] \quad (\text{C.148})$$